Effects of Stabilizing Binder on the Formability, Microstructure, and Mechanical Performance of Wet Compression Molded Unidirectional Non-Crimp Fabric Composites

by

Renan Miranda Portela

A thesis
presented to the University of Waterloo
in fulfillment of the
thesis requirement for the degree of
Doctor of Philosophy
in
Mechanical and Mechatronics Engineering

Waterloo, Ontario, Canada, 2025

© Renan Miranda Portela 2025

Examining Committee Membership

The following served on the Examining Committee for this thesis. The decision of the Examining Committee is by majority vote.

Supervisor:	John Montesano, PhD Associate Professor, University of Waterloo
Co-Supervisor:	Alfredo Rocha de Faria, PhD Adjunct Professor, University of Waterloo
External Member:	Scott E. Stapelton, PhD Professor, University of Massachusetts
Internal Member:	Clifford Butcher, PhD Associate Professor, University of Waterloo
Internal Member:	Peng Peng, PhD Assistant Professor, University of Waterloo
Internal-external Member:	Aiping Yu, PhD Professor, University of Waterloo

Author's Declaration

This thesis consists of material all of which I authored or co-authored: see Statement of Contributions included in the thesis. This is a true copy of the thesis, including any required final revisions, as accepted by my examiners.

I understand that my thesis may be made electronically available to the public.

Statement of Contributions

I would like to acknowledge my co-authors who contributed to this thesis.

Professor John Montesano: Supervision, Funding acquisition, Conceptualization, Writing - Review & Editing, Resources, Project administration, Validation and Investigation.

Professor Alfredo Rocha de Faria: Writing – Review & Editing, Validation, Supervision.

Professor Luise Kärger: Chapters 4, 5, and 6 - Writing – Review & Editing, Conceptualization, Resources.

Professor Garrett W. Melenka: Chapter 7 - Writing – Review & Editing, Validation, Resources.

Bastian Schäfer: Chapters 4, 5, and 6 - Writing – Review & Editing, Methodology, Formal Analysis.

Ayshan Soltansaleki: Chapter 7 - Writing – Review & Editing, Methodology, Formal Analysis.

The balance of the research work is my own work.

Abstract

Wet Compression Molding (WCM) with highly reactive resins is a manufacturing process capable of high-volume production that has recently gained interest in the automotive industry as an alternative to traditional methods for producing structural components. These components are subject to high loads and may experience impact loads during service; therefore, to achieve the desired mechanical properties and performance requirements, the structural components may require several layers and a significant amount of resin. For typical WCM processes utilizing molds with deep cavities, resin management can be challenging as the fabric stack may drape prematurely due to the mass of the resin; however, the use of binder-stabilized fabric can overcome this problem by enhancing the fabric bending stiffness. While the influence of stabilizing binder on the permeability of various fabrics and the flow characteristics of different resins has been previously studied, its impact on void formation and mechanical performance is less understood. This study focuses on the effects of stabilizing binders on the intra-ply draping mechanisms of wet, unidirectional, non-crimp fabric (UD-NCF), as well as on the microstructure and mechanical performance of the UD-NCF composite fabricated via WCM, which comprises PX35-UD300 carbon fiber fabric and EPIKOTE resin 06150 snap cure epoxy resin, through physical experiments. The objectives of this study are to investigate the influence of the stabilizing binder on the formability of infiltrated carbon-fiber UD-NCF (including membrane behaviour, bending, and compaction), to examine its effects on the microstructure and mechanical performance of UD-NCF composites manufactured via WCM, and to assess the impact of the stabilizing binder on the energy-absorption performance.

For Objective 1, the UD-NCF carbon fiber was characterized through a series of physical experiments, including membrane, bending, and compaction tests. An infiltrated bias-extension test setup was used to analyze the membrane mechanism, a rheometer bending test setup was employed to examine the bending mechanism, and a punch-to-plate setup was utilized to study the compaction mechanism. The fabric infiltration was found to influence the membrane and bending behaviors by reducing the friction between the carbon fiber and the stitching yarns, which consequently decreased the membrane stiffness and the bending stiffness up to 30%. However, impregnation was found to have no significant impact on the compaction response due to the low friction of the carbon fibers. In contrast to fabric impregnation, the pre-activation of the stabilizing binder was found to affect all three draping mechanisms by increasing fiber/fiber and fiber/yarn friction, thereby increasing membrane stiffness by up to 100% and bending stiffness by up to 50%.

For Objective 2, flat UD-NCF composite panels were fabricated by WCM to examine how the stabilizing binder and its state, as well as the vacuum application to the mold and

its duration, influence the formation of voids and mechanical properties. It was observed that the use of binder-stabilized fabrics decreased the void content of WCM parts by up to 70%, likely due to reduced relative layer movement and lower air entrapment. The void size decreases further when a vacuum is applied to the mold for more than 20 seconds, which partially removes air inside the mold. This reduction in void size leads to an increase in interlaminar shear strength. Additionally, applying a vacuum enhances preform compaction, resulting in more consistent panel thickness and a higher fiber volume fraction (FVF).

For Objective 3, UD-NCF composite hat channels were fabricated by WCM to examine the influence of the stabilizing binder and vacuum application on energy absorption during axial crush experiments. The use of binder-stabilized fabric and vacuum increased energy absorption; however, this increase was not statistically significant, possibly due to the high FVF of the components. The WCM hat channels achieved energy absorption levels comparable to those of similar hat channels comprising the same constituents and ply stacking sequence and fabricated by high-pressure resin transfer molding (HP-RTM) in a previous study. The WCM hat channels also showed a similar brittle fracture failure mode to the HP-RTM hat channels.

The main results of this investigation include a new dataset on the viscous draping mechanisms of the binder-stabilized UD-NCF. Additionally, mechanical tests provided strong evidence of the influence of the stabilizing binder on the mechanical performance of the UD-NCF composites. These results indicate the feasibility of using the WCM process as an alternative to HP-RTM in the manufacturing of structural components.

Acknowledgements

I would like to express my deepest gratitude to my supervisor, Professor John Montesano, for the opportunity to be a member of the Composites Research Group and contribute to this project. His patience, guidance, and unwavering support have been instrumental to my growth as a researcher and have made my doctoral experience both rewarding and enjoyable. I am especially thankful for his motivation and insightful direction throughout this endeavor. I would also like to extend my sincere appreciation to my co-supervisor, Professor Alfredo Rocha de Faria, for his valuable input and guidance.

I would also like to express my sincere gratitude to Professor Luise Kärger and her research group in Karlsruhe, Germany, for hosting me during an enriching and memorable four-month stay. Their exceptional support, generosity, and willingness to share their expertise and experimental setups were instrumental to the success of my research on fabric characterization. Furthermore, I wish to thank the members of my examining committee—Professor Scott E. Stapleton from the University of Massachusetts (USA), as well as Professors Clifford Butcher, Peng Peng, and Aiping Yu from the University of Waterloo—for their time, valuable feedback, and constructive comments on my research.

The successful completion of the experimental work in this research project would not have been possible without the invaluable assistance of the skilled research staff and technicians at the Forming and Crash Lab. I am deeply grateful to Dr. Imbert-Boyd, Mike Bustamante, Tom Gawel, Jason Benninger, Richard Gordon, and Karl Janzen for their exceptional expertise, dedication, and unwavering support throughout the experimental phase. Dr. Melenka for providing access to the X-ray CT scanner used in the thesis, as well as Ayshan Soltansaleki for performing the scans.

I wish to express my gratitude to the generous financial supporters. Zoltek Corp. and Westlake Epoxy are acknowledged for providing the unidirectional non-crimp fabric and the snap-cure resin system, respectively. Natural Sciences and Engineering Research Council of Canada (NSERC) for providing funding in support of the research.

Finally, I would like to extend my heartfelt thanks to the members of the Composites Research Group. Their willingness to discuss challenges, question methodologies, and offer constructive feedback greatly contributed to my growth and confidence as a researcher. Beyond their professional support, their encouragement, camaraderie, and sense of humor made even the most demanding stages of this doctoral journey genuinely enjoyable. I am also grateful to my roommates—Matheus Ota (Japa), Nathan Benedetto Proença, Thomás do Sul, Zeus Dantas, Santos-Dumont, and Dr. Lang—for the countless memorable moments shared over pizza, Ben & Jerry's, and pain au chocolat.

Dedication

In loving memory of my grandmothers, Eunice and Julieta, whose wisdom, kindness, and unwavering love continue to guide and inspire me every day. Though they are no longer with me, their strength and warmth remain deeply rooted in my heart and in all that I do. This work is dedicated to them, with eternal gratitude and affection.

Table of Contents

Examining Committee Membership **ii**

Author's Declaration **iii**

Statement of Contributions **iv**

Abstract **v**

Acknowledgements **vii**

Dedication **viii**

List of Figures **xv**

List of Tables **xxiv**

1 Introduction **1**

1.1 Research Motivation 1

1.2 Thesis Outline 4

References 4

2 Background and Literature Review **8**

2.1 Continuous reinforcement fabrics for fiber-reinforced composite materials . 8

2.1.1 Woven fabric 8
2.1.2 Non-Crimp Fabric (NCF) 10
2.2 Stabilizing Binder 11
2.3 Liquid composite molding (LCM) processes 12
2.3.1 Resin Transfer Molding (RTM) 13
2.3.2 HP-RTM 14
2.3.3 WCM 15
2.4 Characterization of Reinforcement Fabrics 16
2.4.1 Viscous Membrane Behavior 17
2.4.2 Viscous Bending Behavior 21
2.4.3 Viscous compaction behavior 25
2.4.4 Gaps in the literature 30
2.5 WCM Process Studies for FRP Composites 30
2.5.1 Gaps in the literature 31
2.6 Microstructural Assessment of Unidirectional FRP Composites 32
2.7 Performance characterization of energy absorbing FRP parts 33
2.7.1 Gaps in the literature 37
References 37

3 Research Objectives and Scope **55**
3.1 Research Objectives 55
3.2 Scope of Work 59
3.2.1 Task 1 59
3.2.2 Task 2 59
3.2.3 Task 3 60

4 Influence of Viscosity, Binder Activation, and Loading Rate on the Membrane Response of an Infiltrated UD-NCF 61

4.1 Overview . . . 61

4.2 Introduction . . . 62

4.3 Experimental Procedure . . . 63

4.3.1 Materials . . . 63

4.3.2 Infiltrated bias-extension test (IBET) . . . 64

4.4 Results and discussion . . . 65

4.4.1 Influence of fluid viscosity . . . 65

4.4.2 Influence of fabric binder pre-activation . . . 68

4.4.3 Influence of loading rate . . . 71

4.5 Summary and conclusion . . . 73

References . . . 73

5 Effect of loading rate, viscosity, and binder activation on the bending response of an infiltrated UD-NCF 76

5.1 Overview . . . 76

5.2 Introduction . . . 77

5.3 Fabric material and experimental methodology . . . 81

5.3.1 Fabric description and specimen preparation . . . 81

5.3.2 Rheometer bending test setup . . . 82

5.4 Results and Discussion . . . 85

5.5 Conclusions . . . 91

References . . . 92

6 Characterizing and modelling the time-dependent compaction response of an infiltrated binder-stabilized unidirectional non-crimp fabric 99

6.1 Overview . . . 99

6.2 Introduction . . . 100

6.2.1 Research motivation . . . 100
6.2.2 State-of-the-Art . . . 102
6.2.3 Research goal . . . 106
6.3 Methodology . . . 106
6.3.1 Materials and specimen preparation . . . 106
6.3.2 Punch-to-plate compaction test . . . 107
6.3.3 Implementation of rheological models . . . 110
6.4 Results and discussion . . . 114
6.4.1 Experimentally captured compaction response . . . 114
6.4.2 Model parameter identification . . . 122
6.5 Conclusions . . . 130
References . . . 131

7 High-fidelity fiber volume fraction estimation for UD-NCF composites using digital image processing technique 137
7.1 Overview . . . 137
7.2 Introduction . . . 138
7.3 Methodology . . . 144
7.3.1 Materials . . . 144
7.3.2 Panel fabrication . . . 144
7.3.3 Acid digestion . . . 146
7.3.4 Microscopic sample preparation . . . 146
7.3.5 Microscopic assessment . . . 147
7.3.6 Digital image processing . . . 148
7.4 Results and discussion . . . 150
7.4.1 Microstructural assessment of WCM and HP-RTM materials . . . 150
7.4.2 Fiber volume fraction estimation using the acid digestion method . 152
7.4.3 Fiber volume fraction estimation using DIP technique . . . 154
7.5 Conclusions . . . 159
References . . . 159

8 Effect of stabilizing binder on void morphology and mechanical performance of wet compression molded rapid-curing non-crimp fabric composites 164

8.1 Overview . . . 164

8.2 Introduction . . . 165

8.2.1 Motivation . . . 165

8.2.2 State-of-the-Art . . . 167

8.2.3 Objective of Study . . . 170

8.3 Materials and panel manufacturing . . . 171

8.3.1 Materials . . . 171

8.3.2 Panel manufacturing . . . 171

8.4 Mechanical testing and microstructural assessment . . . 173

8.4.1 Tensile testing . . . 174

8.4.2 Short-beam shear testing . . . 176

8.4.3 Microscopy . . . 177

8.4.4 Micro-CT imaging . . . 177

8.5 Results . . . 180

8.5.1 Microstructural Assessment . . . 180

8.5.2 Void Morphology . . . 183

8.5.3 Short-Beam Shear Tests . . . 189

8.5.4 Transverse Tension Tests . . . 191

8.5.5 Longitudinal Tension Tests . . . 193

8.5.6 Discussion . . . 195

8.6 Conclusions . . . 198

References . . . 199

9 Energy absorption capability of wet compression molded binder-stabilized UD-NCF composite hat channels **207**

9.1 Overview . . . 207

9.2 Introduction . . . 208

9.3 Fabric Material and Experimental Methodology . . . 210

9.3.1 Materials . . . 210

9.3.2 Hat Channel Fabrication . . . 211

9.3.3 Crushing test . . . 213

9.3.4 Microscopy . . . 215

9.4 Results and Discussion . . . 216

9.5 Conclusions . . . 224

References . . . 225

10 General Discussion **230**

11 Conclusions and Recommendations **233**

11.1 Conclusions . . . 233

11.2 Contributions . . . 236

11.3 Recommendations for Future Work . . . 237

11.3.1 Future material characterization work . . . 237

11.3.2 Future process studies work . . . 237

11.3.3 Future crush test work . . . 237

Letters of Copyright Permission **239**

Bibliography **244**

Appendix 1 **245**

Appendix 2 **248**

List of Figures

1.1 Total transportation GHG emissions from all modes from 2000 to 2019. . . 2

1.2 Schematic of the WCM process flow variants. 3

2.1 Schematic of fabrics with different weave patterns. 9

2.2 Schematic of non-crimp fabric with different tow orientations. 10

2.3 Schematic of most common stitching patterns (a) pillar, (b) tricot, and (c) plain. 11

2.4 Schematic of the RTM process flow. 13

2.5 Schematic of the HP-RTM process flow. 14

2.6 Mechanisms present during the WCM process. 16

2.7 Draping mechanisms present during the WCM process. 17

2.8 Shear extension characterization test setups for engineering fabrics: (a) and (b) Picture Frame Test setup and schematic of the specimen deformation during the test [12], (c) and (d) Schematic showing distinct shear zones in bias extension test for woven fabric and UD-NCF specimens [45]. 18

2.9 Comparison between pure and simple shear deformation. 19

2.10 Extension test setup and shear force vs. angle response. 20

2.11 Hemisphere punch simulation considering different data input. 22

2.12 Variation in wrinkle size for different bending stiffness values. 22

2.13 Scheme and setup of the modified cantilever beam test. 23

2.14 RBT setup, Anton Paar MCR501 rheometer coupled with an enlarged bending frame. 24

2.15 Compaction test setup. 26
2.16 Schematic three-branch Maxwell model, including the elastic and viscoelastic branches. 28
2.17 Fractional Zener model scheme and their rheological elements. 29
2.18 Microscopic analysis to investigate the presence of voids in HP-RTM (left) and WCM (right) parts. 30
2.19 Schematic of a quasi-static crush test performed with a universal testing machine [135]. 34
2.20 Types of failure in axial crushing 35

3.1 Binder stabilized carbon fiber UD-NCF, namely PX35-UD300, and its constituents: (a) tricot pattern stitching yarns and (b) supporting glass fiber. . 56
3.2 Schematic showing the research plan. 59

4.1 Binder stabilized uni-directional non-crimp fabric (PX35-UD300); left: Polyester stitching yarns in a tricot pattern; right: Glass fiber to improve the fabric handleability. 64
4.2 Experimental IBET setup. 65
4.3 Deformed UD-NCF specimens; left: 30° test specimen; right: 60° test specimen. 67
4.4 Experimental results for dry (blue) and impregnate (20 cSt in orange and 100 cSt in green) UD- NCF specimens; left: 30° specimens tested at 100 mm/min; right: 30° specimens tested at 500 mm/min. 67
4.5 Experimental results for dry (blue) and impregnated (20 cSt in orange and 100 cSt in green) UD-NCF specimens; left: 60° specimens tested at 100 mm/min; right: 60° specimens tested at 500 mm/min. 69
4.6 Binder-stabilized UD-NCF; left: Inactivated binder; right: Pre-activated binder in the oven at 120°C. 69
4.7 Experimental results for dry inactivated (IT) and pre-activated (AT) binder on the UD-NCF specimens; left: 30° specimens tested at 100 mm/min; right: 30° specimens tested at 500 mm/min. 70
4.8 Experimental results for dry inactivated (IT) and pre-activated (AT) binder on the UD-NCF specimens; left: 60° specimens tested at 100 mm/min; right: 60° specimens tested at 500 mm/min. 70

4.9 Experimental results for dry and impregnated UD-NCF specimens with activated binder system (AT); left: dry 30° specimens tested at 100 and 500 mm/min; center: impregnated 30° specimens under 20 cSt tested at 100 and 500 mm/min; right: impregnated 30° specimens under 100 cSt tested at 100 and 500 mm/min. 72

4.10 Experimental results for dry and impregnated UD-NCF specimens with activated binder system (AT); left: dry 60° specimens tested at 100 and 500 mm/min; center: impregnated 60° specimens under 20 cSt tested at 100 and 500 mm/min; right: impregnated 60° specimens under 100 cSt tested at 100 and 500 mm/min. 72

5.1 Schematic of the steps for a typical WCM process. 77

5.2 Draping mechanism present during the WCM process [21]. 79

5.3 Images of the PX35-UD300 UD-NCF showing different constituents and microstructure: (a) stitch tricot pattern surface, and (b) supporting glass fiber surface. 82

5.4 (a) Setup of the RBT with a fabric specimen mounted in the frame fixtures, including a prepared specimen and its measurements, (b) top-view schematic of the RBT setup. 83

5.5 Normalized moment–curvature plots for the four tested conditions, each including dry, impregnated with 20 cSt silicone oil, and impregnated with 100 cSt silicone oil infiltration cases: (a) Condition (1) – binder pre-activated and 0.1 RPM velocity, (b) Condition 2 – binder pre-activated and 1 RPM velocity, (c) Condition 3 – binder pre-activated and 10 RPM velocity, (d) Condition 4 – binder inactivated and 1 RPM velocity. 86

5.6 Normalized bending stiffness for the four tested conditions, each including impregnated with 20 cSt silicone oil, impregnated with 100 cSt silicone oil infiltration, and dry cases: (a) Condition (1) – binder pre-activated and 0.1 rpm velocity, (b) Condition 2 – binder pre-activated and 1 rpm velocity, (c) Condition 3 – binder pre-activated and 10 rpm velocity, and (d) Condition 4 – binder inactivated and 1 rpm velocity. (e) Normalized bending stiffness vs loading rate for the indicated infiltration case. 88

6.1 Schematic of the wet compression molding (WCM) process steps: (a) direct variant, and (b) indirect variant. 101

6.2 Schematic of the three-branch Maxwell model, including an elastic and three viscoelastic branches. The illustrated elements are defined as: springs (E_i) and dashpot (τ_j) [14]. 105

6.3 Schematics of: (a) Fractional Zener model, and (b) rheological elements. The illustrated elements are defined as: springs (E_i), dashpots (τ_j), stress (σ), strain (ε), fractional derivative order (α), proportionality factor (p) and the fractional derivative operator (D) [28]. 106

6.4 Specimens soaking procedure: (a) silicone bath for 15 minutes to fully impregnate the stack, (b) drain process to remove the silicone excess. 107

6.5 Punch-to-plate compaction test setup for the 8-layer carbon fiber UD-NCF. 108

6.6 Six-phase load-relaxation cycle for compaction characterization. 109

6.7 Compaction force response and punch height-time data for: (a) $[0]_8$ stacking sequence (Conditions 5–8), and (b) $[0/45]_4$ stacking sequence (Conditions 1–4). The Conditions cover different infiltration fluid viscosities as well as inactive (IT) and pre-activated (AT) binder states, see Table 6.1. (c) Schematic of the tow nesting phenomenon for $[0]_8$ specimens during Phase I. 116

6.8 Compression height-stress curves for the first compression cycle: (a) $[0]_8$, and (b) $[0/45]_4$ specimens, and the second compression cycle: (c) $[0]_8$, and (d) $[0/45]_4$ specimens 117

6.9 Maximum compression stress (σ_0) for each impregnated condition: (a) first compaction cycle (Phase I) for $[0]_8$ specimen, (b) first compaction cycle (Phase I) for $[0/45]_4$ specimen, (c) second compaction cycle (Phase V) for $[0]_8$ specimen, and (d) second compaction cycle (Phase V) for $[0/45]_4$ specimen. 118

6.10 Normalized relaxation stress for each impregnated condition: (a) first relaxation cycle for $[0]_8$ specimen, (b) first relaxation cycle for $[0/45]_4$ specimen, (c) second relaxation cycle for $[0]_8$ specimen, and (d) second relaxation cycle for $[0/45]_4$ specimen. 119

6.11 Stress relaxation ratio for each impregnated condition: (a) first relaxation cycle for $[0]_8$, (b) first relaxation cycle for $[0/45]_4$, (c) second relaxation cycle for $[0]_8$, and (d) second relaxation cycle for $[0/45]_4$. 120

6.12 Elastic recovery capacity for each impregnated condition during Phase IV: (a) $[0]_8$ and (b) $[0/45]_4$. 120

6.13 Phase II stress–time curve fitting using the Fractional Zener and Maxwell models: (a) dry inactivated $[0]_8$, (b) dry pre-activated $[0]_8$, (c) impregnated 20 cSt pre-activated $[0]_8$, (d) impregnated 100 cSt pre-activated $[0]_8$, (e) dry inactivated $[0/45]_4$, (f) dry pre-activated $[0/45]_4$, (g) impregnated 20 cSt pre-activated $[0/45]_4$, and (h) impregnated 100 cSt pre-activated $[0/45]_4$. . 125

6.14 A comparison between the experimental measurements of condition 4 during Phase VI and the curve derived from the material parameters obtained in Phase II using the Fractional Zener model 126

6.15 Phase VI stress–time curve fitting using the Fractional Zener and Maxwell models: (a) dry inactivated $[0]_8$, (b) dry pre-activated $[0]_8$, (c) impregnated 20 cSt pre-activated $[0]_8$, (d) impregnated 100 cSt pre-activated $[0]_8$, (e) dry inactivated $[0/45]_4$, (f) dry pre-activated $[0/45]_4$, (g) impregnated 20 cSt pre-activated $[0/45]_4$, and (h) impregnated 100 cSt pre-activated $[0/45]_4$. . 128

6.16 Phase I height-stress curve fitting by using the nonlinear Maxwell model for: (a) dry inactivated $[0]_8$, (b) dry pre-activated $[0]_8$, (c) impregnated 20 cSt pre-activated $[0]_8$, (d) impregnated 100 cSt pre-activated $[0]_8$, (e) dry inactivated $[0/45]_4$, (f) dry pre-activated $[0/45]_4$, (g) impregnated 20 cSt pre-activated $[0/45]_4$, and (h) impregnated 100 cSt pre-activated $[0/45]_4$. . 129

7.1 Schematic showing use of the line and area methods on the cross-section of a unidirectional composite to obtain FVF. 140

7.2 Schematic of a UD-NCF illustrating different constituents and microstructure: (a) stitch tricot pattern surface, and (b) supporting fiber surface. . . 143

7.3 WCM equipment used to manufacture flat panels: (a) 100-ton hydraulic press with heated platens, (b) a two-part mold featuring a vacuum port, and (c) an automated metering unit for rapid mixing and dispensing of resin and hardener. 145

7.4 Acid digestion procedure conducted with one HP-RTM sample: (a) initial sample weight measurement, (b) acid digestion in nitric acid bath on a hot plate in a fume hood, (c) sample partially digested in nitric acid, and (d) final weight measurement of the acid-digested sample. 146

7.5 Procedure to prepare samples for microcopy: (a) panel regions where samples were extracted, (b) cold-mounted sample, (c) Struers automatic polisher used to grind and polish the cold-mounted samples. 147

7.6 (a)Microscope used to assess the cold-mounted samples (Keyence VHX-5000 microscope) and (b) mosaic-image made through several microscopic figures assessed with an optical-digital microscope. 148

7.7 Image filtering process: (a) raw microscopic image, (b) definition of the pixel intensity threshold, (c) identification of the pixels that represent fibers. . . 149

7.8 Verification procedure for pixel selection: (a) the original microscopic image; (b) a magnified region within the original microscopic image, and (c) the visualization of pixels identified as carbon fiber, highlighted in red. 150

7.9 Microscopic assessment of a $[0]_7$ HP-RTM sample: (a) cross-sectional micrograph with laminate thickness measurements and region of interest indicated, and (b) magnified view of the region of interest. 151

7.10 Microscopic assessment of a $[0]_8$ WCM sample: (a) cross-sectional micrograph with laminate thickness measurements and region of interest indicated, and (b) magnified view of the region of interest. 152

7.11 Microscopic image of the (a) HP-RTM sample 02 with a designated region of interest highlighted in blue, (b) raw image of the selected region, and (c) processed image of the same area, with the pixels corresponding to carbon fiber identified in white. 155

7.12 Cross-sectional microscopic images of different WCM samples: (a) image of Sample 01, (b-c) magnified raw and processed images of Sample 01 with fibers identified for the latter (white regions), (d) image of Sample 02, and (e) image of Sample 03. 156

7.13 Microscopic assessment of WCM Sample 02 for regions of interest with varying widths (in blue): (a) single tow, (b) two tows, and (c) three tows. . . . 158

8.1 Schematic of the typical steps for a direct WCM process. 166

8.2 Schematic of UD-NCF: (a) stitching side with yarns in a tricot pattern, and (b) transversely oriented supporting fiber side. 166

8.3 Schematic demonstrating distinct draping characteristics between: (a) binder-stabilized fabric stack, and (b) non-bindered fabric stack with lower bending stiffness. 167

8.4 Schematic of in-plane resin flow and the resulting inter-tow void formation under low-velocity infiltration. 169

8.5 WCM equipment utilized for manufacturing flat panels: (a) 100-ton hydraulic press with heated platens, (b) lower half of two-part mold with wiper vacuum seal visible, and (c) electronic metering unit for quick mixing and dispensing of resin and hardener. 172

8.6 (a) Sketch of the manufactured panels showing the regions where the specimens were waterjet cut for mechanical tests and microscopic analysis, and (b) dimensions of each specimen. 174

8.7 Universal testing machines used in tensile tests: (a) Shimadzu AGS-X for testing transverse specimens and (b) Instron 1331 for testing longitudinal specimens. 175

8.8 Image of an SBS test showing the support span length, the direction of displacement of the loading pin, and a delamination region near the loading pin. 177

8.9 (a) μCT Sky Scan 1272 used to CT-scan the four samples, (b) schematic of the scanning procedure. 178

8.10 Microscopic analysis of an AT sample showing: (a) cross-sectional CT image with supporting glass fibers and voids shown, and (b) histogram with values for threshold for voids and glass fibers. 179

8.11 Microscopic images of samples extracted from panels manufactured by indicated processing condition, including a magnified view of a region of interest (ROI) in each image: (a-b) UNB sample, (c-d) IT sample, (e-f) AT sample, (g-h) VAC 10 s sample, (i-j) VAC 20 s sample, (k-l) HP-RTM sample. . . . 183

8.12 3D volumetric models generated from the CT scans of samples showing supporting glass fibers in grey and voids in blue: (a) AT, (b) IT, (c) UNB, and (d) VAC 20 s samples. 185

8.13 2D images from CT scanned samples highlighting the presence of voids in red around and adjacent to the supporting glass fibers: (a) AT, (b) IT, (c) UNB, and (d) VAC 20 s samples. 186

8.14 Position of the voids along the sample thickness with their volume categorized as small (<0.001 mm^3), medium (0.001 mm^3 – 0.005 mm^3), and large (>0.005 mm^3): (a) AT, (b) IT, (c) UNB, and (d) VAC 20 s samples. . . . 187

8.15 Void analysis in samples corresponding to each configuration: (a) volume of voids categorized by size, (b) number of voids categorized by size, and (c) void volume accumulation by layer. 188

8.16 SBS test shear stress-displacement plots for configurations: (a) UNB, (b) IT, (c) AT, (d) VAC 10 s, (e) VAC 20 s, and (f) HP-RTM. 189

8.17 ILSS obtained from SBS tests for indicated conditions. 190

8.18 Transversal tensile test stress-strain plots for configurations: (a) UNB, (b) IT, (c) AT, (d) VAC 10 s, (e) VAC 20 s, and (f) HP-RTM. 191

8.19 Mechanical properties in the transverse direction. 192

8.20 Longitudinal tensile test stress-strain plots for configurations: (a) UNB, (b) IT, (c) AT, (d) VAC 10 s, (e) VAC 20 s, and (f) HP-RTM. 194

8.21 Mechanical properties in the longitudinal direction. 194

8.22 Thickness measurements taken from all WCM samples ($[0]_8$ stacking sequence) and the HP-RTM samples $[0]_7$ stacking sequence. 196

9.1 Dimensions of the hat channel lower mold used in this study. 212

9.2 (a) Resin at room temperature with air bubbles (b) and resin heated at 85°C without air bubbles. 212

9.3 Illustration of the preform preparation steps: (a) cutting the fabric, (b) introducing it into the mold, (c) releasing from the T-shaped tool, and (d) preforming the fabric stack. 213

9.4 Specimen preparation steps procedure for quasi-static test. 214

9.5 (a) WCM hat channel specimen cut from one of the hat channels manufactured with vacuum applied for 20 seconds (230 mm length), and (b) hat channel cross-sectional dimensions. 215

9.6 Schematic of progressive failure for a fiber-reinforced composite part subjected to axial crush load, with typical load-displacement response. 216

9.7 Setup for the experimental quasi-static axial loading tests showing test specimen mounted to lower press platen using a fixture and adapter plate. . . . 217

9.8 Regions in hat channel parts where samples were extracted for microscopy. 218

9.9 Load-displacement responses obtained from quasi-static axial crush tests for each composite laminate configuration: (a) UNB, (b) AT, and (c) VAC 20s. 218

9.10 WCM hat channel with poorly impregnated regions within flanges and upper region. 219

9.11 Total energy absorbed vs displacement data for each configuration during the quasi-static axial crush tests. 219

9.12 Quantitative comparison between WCM and HP-RTM [28, 29] specimens: (a) Peak Crush Force, (b) Mean Crush Force, (c) Crush Force Efficiency, and (d) Specific Energy Absorption 220

9.13 Images of the $[0/45/90]_s$ WCM hat channels after quasi-static axial loading, showing similar brittle fracture in the (a) UNB (b) AT, and (c) VAC 20s hat channel configurations. 222

9.14 Microstructure of $[0/\pm 45/90]_s$ hat channels for three WCM manufacturing configurations: (a,b) UNB, (c,d) AT, and (e,f) VAC 20s, at regions A and B. 223

List of Tables

2.1 Comparison of composites with 3 different weave patterns and similar mass fractions. 10

3.1 PX35-UD300 textile constituents. Values given in $\frac{g}{m^2}$. 55

3.2 Research objectives, gaps, and tasks 57

5.1 Different conditions tested using the RBT setup. 84

5.2 Normalized bending stiffness values of the pre-activated samples (Conditions 1–3). 85

5.3 Normalized bending stiffness values of the inactivated samples (Condition 4). 85

5.4 P-values obtained through T-Test comparing the normalized bending stiffness for different loading rate pairs, for each impregnation case. 89

5.5 P-values obtained through T-Test comparing the normalized bending stiffness of pre-activated binder specimens for different fabric impregnation case pairs, for each loading rate. 90

5.6 P-values obtained through T-Test comparing the normalized bending stiffness of specimens with and without stabilizing binder pre-activation under different impregnation conditions at 1 RPM. 90

6.1 Conditions of the samples tested using the punch-to-plate compaction test setup, including different infiltrated fluid viscosities (dry, 20 cSt, and 100 cSt) and binder state (IT and AT). 108

7.1 Characteristics of the indicated samples, including panel thickness, average ply thickness, tow height, and tow width. Mean and standard deviation of all values are provided. 153

7.2 Mean and standard deviation of FVF measurement of each analyzed WCM sample with average result. 154

7.3 Mean and standard deviation of FVF measurement of each analyzed WCM sample with average result. 155

7.4 FVF measurements of the second HP-RTM and WCM samples for regions of interest with widths spanning one, two, and three fiber tows. 157

8.1 Configurations of panels fabricated using the WCM process, including fabric binder state and vacuum duration specified. 173

8.2 Parameter used for X-ray μCT scanning of the WCM samples. 179

8.3 Gray scale classification range for segmenting each sample type for voids only. 180

8.4 Panel and average ply thickness for each investigated configuration, along with FVF. Average values with standard deviation are tabulated. 181

8.5 Void content, glass fiber volumetric fraction, and the percentage of the mix comprising carbon fiber, matrix, and stitching. 187

8.6 Average ILSS with standard deviation for each studied configuration. . . . 190

8.7 P-values obtained through T-Test comparing the maximum shear stress values for different manufacturing parameters. 190

8.8 Average and standard deviation of Young's modulus, ultimate tensile strength, and ultimate strain values for each studied condition in the transverse direction. 192

8.9 P-values obtained through T-Test comparing the Young's modulus in the transverse direction for different manufacturing parameters. 192

8.10 P-values obtained through T-Test comparing the ultimate tensile strength in the transverse direction for different manufacturing parameters. 193

8.11 Average and standard deviation of Young's modulus, ultimate tensile strength, and ultimate strain values for each studied condition in the longitudinal direction. 195

8.12 P-values obtained through T-Test comparing the Young's modulus in the longitudinal direction for different manufacturing parameters. 195

8.13 P-values obtained through T-Test comparing the ultimate tensile strength in the longitudinal direction for different manufacturing parameters 195

9.1 Configurations of panels fabricated using the WCM process with fabric binder presence and vacuum duration specified. 213

9.2 Peak crush force, mean crush force, crush force efficiency, and specific energy absorption of each WCM hat channel and HP-RTM hat channel specimens. 221

9.3 P-values obtained through T-Test comparing the peak crush force for the different WCM hat channel specimens. 221

9.4 Thickness measurements obtained from regions A and B for each WCM sample. 222

11.1 Permissions, rights holders, and references for all figures used in the thesis. 240

2 P-values obtained through the T-Test comparing the maximum compression stress values of inactivated and pre-activated binder-stabilized specimens under different impregnation conditions, for each stacking sequence in both first and second compaction phases (Phases I and VI). 245

3 P-values obtained through T-Test comparing the maximum compression stress values for the first and second compaction phases (Phases I and VI), for each specimen condition. 245

4 : P-values obtained through the T-Test comparing the normalized relaxation stress values of inactivated and pre-activated binder-stabilized specimens under different impregnation conditions, for each stacking sequence in both first and second relaxation (Phases II and VI). 246

5 : P-values obtained through T-Test comparing the stress relaxation ratio values for the first and second relaxation cycles (Phases II and VI), for each specimen condition. 246

6 P-values obtained through the T-Test comparing the elastic recovery values of inactivated and pre-activated binder-stabilized specimens under different impregnation conditions, for each stacking sequence, during Phase IV. . . . 246

7 P-values obtained through T-Test comparing the maximum compression stress values of the specimens with different stacking sequences in both first and second compaction cycles (Phases I and V), for each condition. 246

8 P-values obtained through T-Test comparing the stress relaxation ratio values of two specimens with different stacking sequences in both first and second compaction cycles (Phases I and V), for each condition. 247

9 P-values obtained through the T-Test comparing the elastic recovery rate values for specimens with different stacking sequences, for each condition, during Phase IV. 247

10 Material parameter values for the fractional Zener model for each condition (Phase II). 249

11 Material parameter values for the Maxwell model for each condition (Phase II). 249

12 Material parameter values for the fractional Zener model for each condition (Phase VI). 250

13 Material parameter values for the Maxwell model for each condition (Phase VI). 250

14 Material parameter values for the nonlinear Maxwell model for each condition (Phase I). 251

Chapter 1

Introduction

1.1 Research Motivation

Over the past few years, governments worldwide have been working to decrease greenhouse gas (GHG) emissions. Countries such as Canada, along with regions like Europe and Asia, have committed to reducing their GHG emissions by at least 40% below 2005 levels by 2035 [1, 2]. A significant source of these emissions is the road transportation sector, which accounts for 21% of Canada's total GHG emissions and 84% of the country's transportation-related GHG emissions (see Figure 1.1), according to a recent report from the Canadian government [3]. In response to these governmental measures, the automotive industry is adopting innovative solutions, such as replacing traditionally heavy metal components with advanced, lighter materials—known as light-weighting—which helps improve fuel efficiency while maintaining vehicle performance [4].

The adoption of lightweight strategies is important for internal combustion engine (ICE) vehicles because it improves fuel efficiency. For electric vehicles (EVs), lightweighting offsets the additional weight introduced by the batteries and increases range [4, 5]. Achieving these improvements involves balancing system functions and reliability while minimizing total mass, leading to enhanced efficiency. As Henning et al. [6] highlight, realizing such advancements requires the development of new methods, materials, and manufacturing technologies focused on function preservation and weight reductions.

In the past, composite materials have been used in the automotive industry mainly to produce non-structural parts or to create a small number of components for sports cars [7]. In the 1970s, the Brazilian automaker Gurgel manufactured non-structural fiberglass-reinforced parts for their models, including the electric vehicle called Itaipu E150, which

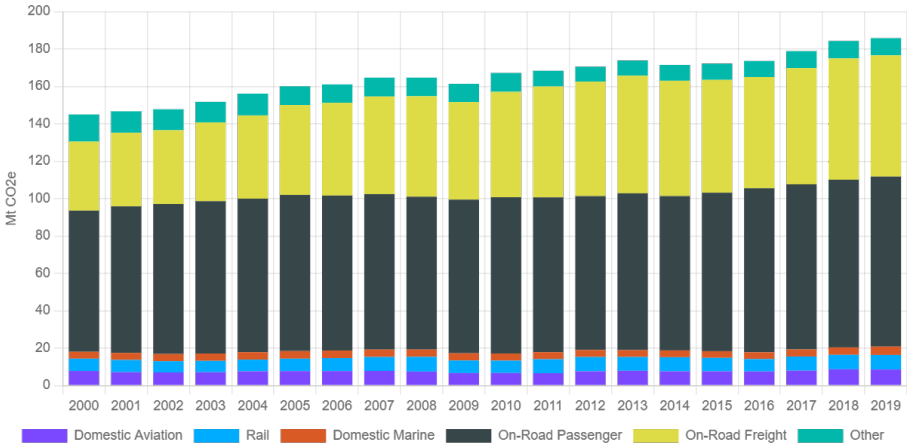


Figure 1.1: Total transportation GHG emissions from all modes from 2000 to 2019 [3].

weighed less than 500 kg [8]. A more recent example of cars utilizing composite materials is the BMW i3, which features structural components made of carbon fiber-reinforced plastic (CFRP) and was the first mass-produced zero-emission model by BMW [6, 9].

Henning et al. [6] have indicated that recent studies highlight the potential of composite materials for structural components in the automotive industry. These components exhibit significantly more intricate geometries than their aerospace counterparts. In summary, the manufacturing technology employed to produce structural parts in the next generation of EVs must be capable of delivering components with a high fiber volume fraction, support high-volume production to ensure short cycle times, and accommodate complex geometries. An alternative to delivering automotive structural components at high-scale production is to use one of the liquid composite molding (LCM) processes, including resin transfer molding (RTM), high-pressure resin transfer molding (HP-RTM), and wet compression molding (WCM). The HP-RTM process has the advantages of fabricating complex-shaped geometry parts with good surface finish and low void content; however, it requires an extra preforming tool, a metering unit, and a large press, which increases the manufacturing costs. The WCM process is an alternative to HP-RTM, producing parts with complex shapes of similar quality. The use of the WCM in the production of complex-shaped parts is still little explored within the industry.

The WCM is a manufacturing process with the potential for mass production with highly reactive resins, a requirement in the automotive industry. The WCM exhibits two variants: direct and indirect, as shown in Figure 1.2a. The direct variant consists of five steps: cutting and stacking the engineering textile, applying the resin, introducing the

impregnated stack into the preheated mold, forming and molding, and curing, followed by the removal of the final composite part. A distinguishing feature of this variant is the simultaneous stack-forming and resin-infiltration step. In contrast, the indirect variant (see Figure 1.2b) separates the forming and resin infiltration into two steps. In this approach, forming occurs before the resin is applied, and infiltration takes place during the molding step.

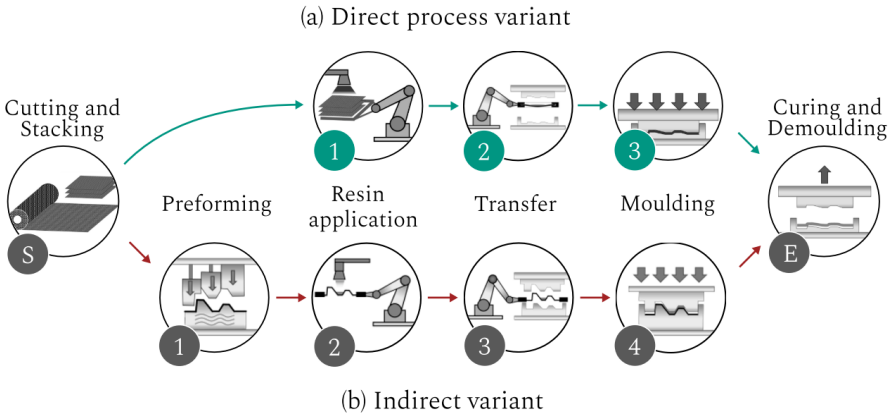


Figure 1.2: Schematic of the WCM process flow variants [10].

The application of the resin on the direct variant easies the manufacturing process. Consequently, WCM represents an economical option to HP-RTM due to the simultaneous draping and curing of the part because the resin can be applied to the stacking outside the hot mold which minimizes the risk of curing and the time loss of the resin injection [11, 12]. Another advantage of the WCM process is the low-pressure process as the resin is applied at atmospheric pressure which demands simpler machinery to reach similar outcomes [12].

However, the WCM has limitations regarding part thickness and geometric complexity, which may lead to local defects in the manufactured parts [13]. Additionally, the low-pressure gradient characteristic of the WCM may result in microscopic flow behavior that impregnates the fiber tows but poorly fills the spaces between them, leading to the formation of large voids between the fiber tows, known as inter-tow voids [14, 15]. These inter-tow voids are more likely to initiate damage compared to voids located within the fiber tows (micro-voids), which are smaller and less detrimental to the mechanical properties of the composite parts.

In addition to the manufacturing process, the selection of engineering textile is also important to deliver the desired mechanical properties to the final laminar composite part.

The unidirectional non-crimp fabric (UD-NCF) is a textile made of parallel straight fibres that can deliver higher lightweight potential, which satisfies the requirements of the lightweighting strategies, and can be used to manufacture structural parts due to the fibre orientation of each layer that can be designed independently [16, 17].

The UD-NCF is a textile that offers a wider range of orientations than woven fabric, enhancing design flexibility, allowing for better control of fiber orientation, and increasing performance [7, 17–19]. Additionally, UD-NCF can achieve load-bearing efficiency up to 15% higher than similar woven fabrics, providing greater lightweight potential. However, UD-NCF has lower handleability compared to woven fabric, making it more susceptible to defects such as gaping, fiber waviness, and wrinkling [20].

When manufacturing thick components in complex-shaped, deep-cavity molds via the WCM process, the low bending stiffness of the UD-NCF, combined with the significant amount of resin, can lead the stack to drape prematurely—prior to mold closure—resulting in resin pooling and undesired movement of the fabric stack within the mold. An effective alternative to prevent the impregnated stack from draping before mold closure is to use binder-stabilized UD-NCF, which can increase its bending stiffness and improve resin management [21, 22]. However, the effects of the stabilizing binder on the formability, microstructure, and mechanical performance of the final composite have not been widely studied and, thus, are not well understood.

1.2 Thesis Outline

This PhD thesis is presented in a manuscript-based format with content from papers included as main chapters in the body of the thesis. Chapter 2 provides a relevant background and a review of the literature related to liquid composite molding, continuous fiber-reinforced textiles, fabric characterization for viscous draping, and laminate characterization. The main objectives and scope of the thesis are outlined in Chapter 3. Chapters 4 through 9 include content from papers that present key findings from research conducted during the PhD program. Chapter 10 provides a general discussion of the key findings. Finally, Chapter 11 presents the conclusions and offers recommendations for future work.

References

[1] Government of Canada. “Canada’s next net-zero milestone: 2035 emissions reduction target.” Accessed: 2025-11-07, Environment and Climate Change Canada.

(2024), [Online]. Available: https://www.canada.ca/en/services/environment/weather/climatechange/climate-plan/2035-emissions-reduction-target/next-netzero-milestone.html.

[2] European Commission. "European climate law." Accessed: 2025-11-07, European Commission. (2024), [Online]. Available: https://climate.ec.europa.eu/eu-action/european-climate-law_en.

[3] Transport Canada. "Greenhouse gas emissions: 2021 annual report." Accessed: 2025-11-07, Transport Canada. (2021), [Online]. Available: https://tc.canada.ca/en/corporate-services/transparency/corporate-management-reporting/transportation-canada-annual-reports/2021/greenhouse-gas-emissions.

[4] National Research Council Canada. "Reducing the carbon footprint of vehicles: Nrc's snap composites industrial r&d group." Accessed: 2025-11-07, National Research Council Canada. (2024), [Online]. Available: https://nrc.canada.ca/en/stories/reducing-carbon-footprint-vehicles-nrcs-snap-composites-industrial-rd-group.

[5] C. B. Latham, "Federal Vehicle Fleets: Observations on the Transition to Electric Vehicles," Washington, DC, 2022. [Online]. Available: https://www.gao.gov/assets/gao-23-105635.pdf.

[6] F. Henning, L. Kärger, D. Dörr, F. J. Schirmaier, J. Seuffert, and A. Bernath, "Fast processing and continuous simulation of automotive structural composite components," *Composites Science and Technology*, vol. 171, pp. 261–279, Feb. 2019, ISSN: 0266-3538. DOI: 10.1016/J.COMPSCITECH.2018.12.007.

[7] C. D. Rudd, A. C. Long, K. N. Kendall, and C. G. E. Mangin, *Liquid Moulding Technologies*. Amsterdam, The Netherlands: Elsevier, 1997, ISBN: 0768000165. DOI: 10.1533/9781845695446.

[8] A. Schaun. "Gurgel itaipu foi o primeiro carro elétrico nacional, mas morreu por problemas que existem até hoje." (2021), [Online]. Available: https://autoesporte.globo.com/um-so-planeta/noticia/2021/04/gurgel-itaipu-foi-o-primeiro-carro-eletrico-nacional-mas-morreu-por-problemas%5C%5C-que-existem-ate-hoje.ghtml (visited on 04/02/2021).

[9] I. Boudway. "Bmw's discontinued i3 is already an ev cult classic." (2022), [Online]. Available: https://www.bloomberg.com/news/features/2022-12-12/bmw-s-discontinued-i3-is-already-an-ev-cult-classic (visited on 12/12/2022).

[10] C. Poppe, "Process simulation of wet compression moulding for continuous fibre-reinforced polymers," Ph.D. dissertation, Karlsruhe Institute of Technology, 2021.

[11] M. Karcher, M. Gerlitziki, B. Thoma, and F. Henning, "Evaluation of a new "inlineprepreg" process approch to establishe process for the manufacturing of structural components out of carbon fibre reinforced plastic," *Novi, MI*, 2015.

[12] J. Fels, G. Meirson, V. Ugresic, P. Dugsin, F. Henning, and A. Hrymak, "Mechanical property difference between composites produced using vacuum-assisted liquid compression molding and high-pressure injection resin transfer molding," in *Proceedings ACCE2017-17th Annual Automotive Composites Conference and Exhibition, Michigan*, Jun. 2017.

[13] P. Bussetta and N. Correia, "Numerical forming of continuous fibre reinforced composite material: A review," *Composites Part A: Applied Science and Manufacturing*, vol. 113, pp. 12–31, 2018, ISSN: 1359-835X. DOI: https://doi.org/10.1016/j.compositesa.2018.07.010. [Online]. Available: https://www.sciencedirect.com/science/article/pii/S1359835X18302732.

[14] N. R. Thompson, "Void formation during liquid composite molding under varied pressure with mechanical properties validation," M.S. thesis, Brigham Young University, 2024.

[15] M. Mehdikhani, L. Gorbatikh, I. Verpoest, and S. V. Lomov, "Voids in fiber-reinforced polymer composites: A review on their formation, characteristics, and effects on mechanical performance," *Journal of Composite Materials*, vol. 53, no. 12, pp. 1579–1669, 2019.

[16] B. Schäfer, R. Zheng, P. Boisse, and L. Kärger, "Investigation of the compaction behavior of uni-and bidirectional non-crimp fabrics," in *ESAFORM 2023 - 26th International Conference on Material Forming*, Kraków, Poland, Apr. 2023.

[17] F. J. Schirmaier, K. A. Weidenmann, L. Kärger, and F. Henning, "Characterisation of the draping behaviour of unidirectional non-crimp fabrics (UD-NCF)," *Composites Part A: Applied Science and Manufacturing*, vol. 80, pp. 28–38, Jan. 2016, ISSN: 1359-835X. DOI: 10.1016/J.COMPOSITESA.2015.10.004.

[18] J. Pourtier, B. Duchamp, M. Kowalski, X. Legrand, P. Wang, and D. Soulat, "Bias extension test on a bi-axial non-crimp fabric powdered with a non-reactive binder system," in *ESAFORM 2018 - 21st International Conference on Material Forming*, Palermo, Italy, 23. and 25. of April 2018.

[19] P. Quenzel *et al.*, "Material characterisation of biaxial glass-fibre non-crimp fabrics as a function of ply orientation, stitch pattern, stitch length and stitch tension," *Journal of Composite Materials*, vol. 56, no. 26, pp. 3971–3991, 2022. DOI: 10.1177/

00219983221127005. eprint: https://doi.org/10.1177/00219983221127005. [Online]. Available: https://doi.org/10.1177/00219983221127005.

[20] B. Schäfer, S. Haas, P. Boisse, and L. Kärger, "Investigation of the membrane behavior of ud-ncf in macroscopic forming simulations," *Key Engineering Materials*, vol. 926, pp. 1413–1422, 2022.

[21] R. Kumar, K. Rashvand, A. Fraisse, A. Sarhadi, and T. L. Andersen, "Experimental testing method to characterise the drapability of ud non-crimp fabrics used in wind turbine blades," *IOP Conference Series: Materials Science and Engineering*, vol. 1293, no. 1, p. 012 020, Nov. 2023. DOI: 10.1088/1757-899X/1293/1/012020. [Online]. Available: https://dx.doi.org/10.1088/1757-899X/1293/1/012020.

[22] P. H. Broberg *et al.*, "That's how the preform crumples: Wrinkle creation during forming of thick binder-stabilised stacks of non-crimp fabrics," *Composites Part B: Engineering*, vol. 273, p. 111 269, 2024, ISSN: 1359-8368. DOI: https://doi.org/10.1016/j.compositesb.2024.111269. [Online]. Available: https://www.sciencedirect.com/science/article/pii/S1359836824000805.

Chapter 2

Background and Literature Review

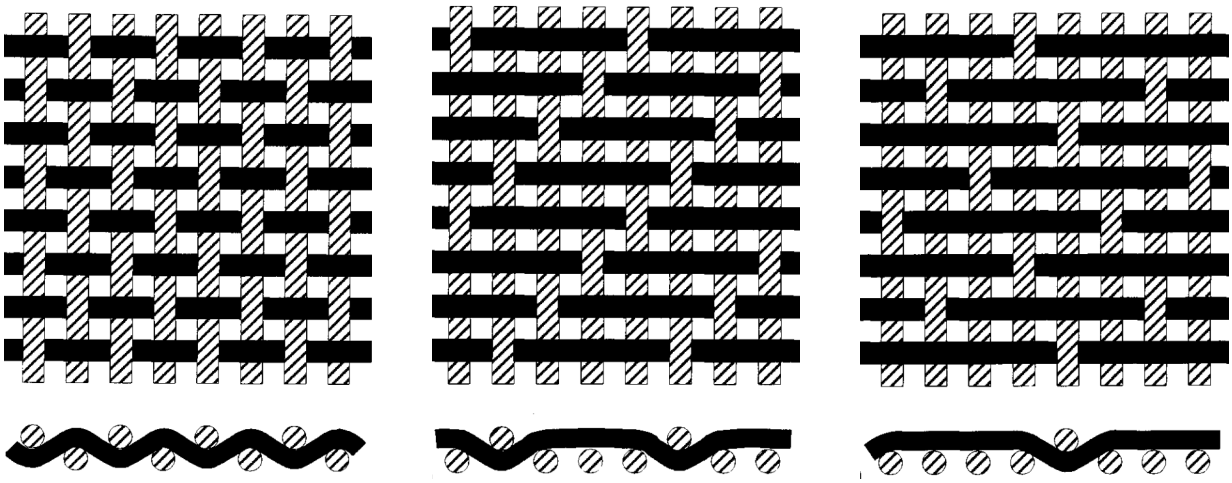
2.1 Continuous reinforcement fabrics for fiber-reinforced composite materials

Composite materials are formed by combining two or more distinct materials, resulting in a heterogeneous material with mechanical properties distinct from those of the individual reinforcement and matrix phases. This resultant material often exhibits superior mechanical properties, including increased specific stiffness and strength, when compared to the matrix phase (typically a polymer) and other conventional monolithic materials [1, 2].

Vinson [3] classify composites into five distinct categories based on the type of reinforcement they employ, which include particulate, fiber-reinforced, flake, filled, and laminar composites. The latter category consists of multiple layers of fiber-reinforced composites with different orientations and a specific stacking sequence. For liquid composite molded fiber-reinforced composites, such as those produced using WCM processes, these layers are composed of reinforcement fabrics with different fiber architectures, including woven, braided, or unidirectional.

2.1.1 Woven fabric

Woven fabric are widely used in the different liquid composite moulding (LCM) processes. The woven fabric is manufactured by applying traditional textile techniques to weave the fiber tows and create textile patterns such as plain weave, 3×1 twill weave, and 5 harness satin weave as presented in Figure 2.1.



(a) Plain weave. (b) 3×1 twill weave. (c) 5 harness satin weave.

Figure 2.1: Schematic of fabrics with different weave patterns [4].

The plain weave pattern, depicted in Figure 2.1a, involves a straightforward interlacing of weft and warp yarns, offering heightened stability during fabric manipulation but resulting in increased crimp that potentially compromises the in-plane mechanical properties of the composite part [4]. Conversely, the twill weave, as shown in Figure 2.1b, exhibits a modified interlacing frequency every three or more yarns, reducing fiber crimp and enhancing fabric drapability [4]. The satin weave, seen in Figure 2.1c, showcases minimal crimp due to the weft's passage across multiple yarns before alternating with the warp, boosting superficial fabric density and elevating the mechanical properties of the final composite compared to other weave patterns; however, its lower shear resistance and increased handling complexity may affect its suitability for intricate geometries [4].

Rudd et al. [4] compared the effects of the weave pattern on different mechanical properties. Table 2.1 presents this comparison between plain and two satin weave patterns and their respective mechanical properties such as flexural strength, flexural modulus, and tensile strength. As the degree of fiber crimp decreases from plain to satin weaves, some mechanical properties such as compressive and tensile strengths increase significantly while the flexural modulus reduces over 15% from plain to 8 harness satin. Henning et al. [5] states that the use of woven fabric compromises the structural performance of the final part due to crimping of the fibers, leading to misalignments of the fibers.

Table 2.1: Comparison of composites with 3 different weave patterns and similar mass fractions [4].

Fabric weave style	Plain	5 harness satin	8 harness satin
Fiber mass fraction (%)	62.90	63.50	62.40
Thickness (mm)	3.15	3.05	3.05
Flexural strength (MPa)	371.00	435.80	600.00
Flexural modulus (GPa)	26.80	26.30	22.30
Compressive strength (MPa)	177.20	331.00	443.30
Tensile strength (MPa)	316.50	404.70	413.70

2.1.2 Non-Crimp Fabric (NCF)

Non-crimp fabrics (NCF), as defined by Lomov [6], consist of parallel-oriented layers made up of reinforced tows. These reinforcement tows are held together by stitching yarns, which provide stability during handling and manufacturing processes [7–9]. Typically crafted from thermoplastic materials like polyester, the yarns secure the intersection points of the tows.

Figure 2.2 illustrates three variations of NCF: uniaxial, biaxial, and multiaxial configurations. Biaxial NCFs, as described by Zheng et al. [10], feature fibers arranged in two primary directions and bonded by stitching yarns, which can be tailored to meet specific requirements. Because the tows remain straight, biaxial NCFs offer enhanced mechanical properties compared to plain woven fabrics. The multiaxial configuration is similar to the biaxial variation but can include up to four layers, incorporating diagonal tows alongside weft and warp tows.

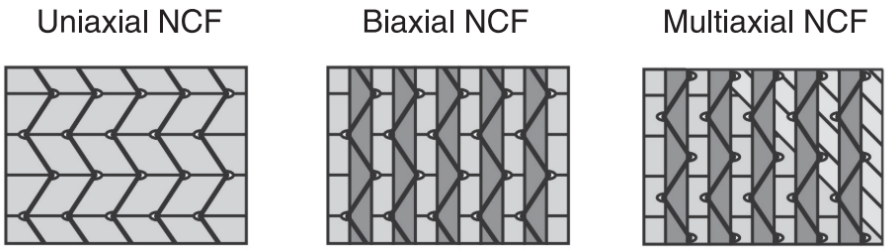


Figure 2.2: Schematic of non-crimp fabric with different tow orientations [6].

Although stitching yarns hold the fiber tows together, NCFs do not possess the interlacing pattern typical of woven fabrics. They may, however, feature various stitching patterns, such as pillar, tricot, and plain (Figure 2.3) [6]. The choice of stitch pattern

affects the drapability of the NCF. According to Lomov [6], increasing stitch length enhances the fabric's formability but may compromise its handling properties. To ensure symmetry and alignment in the NCF stack, the upper layers must be flipped and secured onto the lower layers using chemical adhesives, thermal bonding, or mechanical methods [6]. Chemical adhesives can be applied by either spraying a liquid onto the fabric or using a chemical bath. Additionally, Lomov [6] mentions a thermo-bonding polymer, also known as a stabilizing binder.

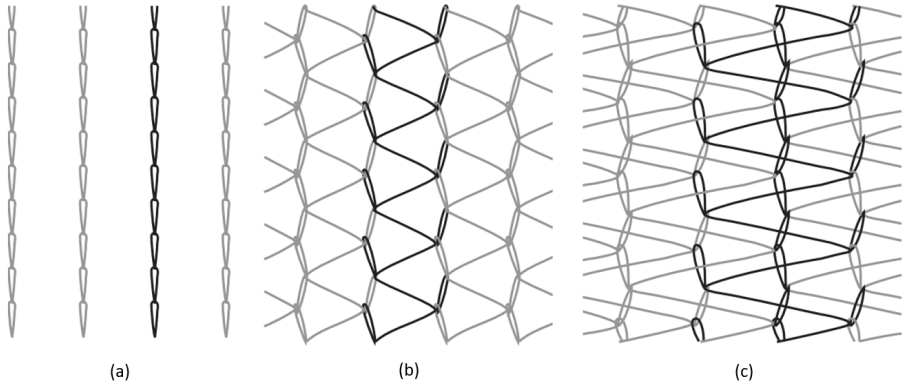


Figure 2.3: Schematic of most common stitching patterns (a) pillar, (b) tricot, and (c) plain [6].

Quenzel et al [11] highlight several advantages of NCFs, including low production costs and design flexibility, which allows for control over fiber orientation and improved performance. Table 2.1 further illustrates that the mechanical properties of the woven fabric, such as strength and stiffness, increase as the crimp level decreases [4, 11–13]. Rudd et al. [4] also notes that NCFs can achieve load-bearing efficiency up to 15% greater than similar woven fabrics, indicating that unidirectional NCFs (UD-NCF) offer significant lightweight potential. However, this lower crimp level can affect the fabric's handling stability, and due to their high stiffness in a single direction, UD-NCFs are more vulnerable to defects like gapping, fiber waviness, and wrinkling [14].

2.2 Stabilizing Binder

Stabilizing binders are polymers — typically thermoplastics or uncatalyzed epoxy resins — available in both solvent-based liquid and dry powder forms [15–17]. They are commonly used to enhance cohesion between adjacent layers and to maintain fabric integrity during

operations such as trimming and handling [15, 18]. Additionally, a stabilizing binder system is often applied onto the fabric stack to enable the preforming during the resin transfer molding (RTM) process. As explained by Rimmel et al. [18], the binder is melted during processing and, upon cooling, the adjacent layers are fixed. Binder-stabilized fabrics also help prevent fiber tow disorientation, which can occur during handling or impregnation [4, 5, 19, 20]. Pourtier et al. [13] compared fabrics with and without a binder system and found that the presence of a binder increases stiffness at small shear angles (less than 4°), due to stronger connections among fibers and between the fiber tows and stitches. However, while beneficial for handling, stabilizing binders may also introduce challenges in the manufacturing process by affecting processing conditions and reducing stack formability [6, 13, 18].

2.3 Liquid composite molding (LCM) processes

The LCM process is a group of manufacturing techniques that have been in use for over 50 years [21]. These methods are designed to produce fiber-reinforced plastic composite parts with complex shapes. Some of these processes can achieve high fiber volume fractions as well as high-volume production at a low manufacturing cost [22]. This group of processes is defined by the use of dry continuous reinforcement—comprising fibers such as glass or carbon—with a set layer stacking sequence known as a preform, which is then impregnated with liquid resin [21, 23, 24]. The preform is designed to meet the composite part's final mechanical properties [21]. The resin is consolidated and cured inside a mold cavity under a set pressure. The group of manufacturing processes includes RTM, its variation HP-RTM, and WCM.

The HP-RTM and WCM processes are examples of cost-effective technologies that have contributed to the rise in the production of composite structural parts in the automotive sector. Kruckenberg et al. [25] notes that, in general, the manufacturing costs for a composite part range from 20% to 50% greater per kilogram than the manufacturing processes designed for aluminum. Despite the higher production costs of composite parts, the industry remains interested in switching from conventional materials to composites due to a mass reduction of 20% to 25% in the final parts [5, 25]. The advent of these cost-effective manufacturing technologies has offset the higher costs of composite raw materials compared to aluminum due to their high-scale production capabilities [5, 21, 25, 26].

The LCM process results in lightweight and high-strength composite parts [21]. Additionally, LCM processes can be cost-effective, provide standardized repeatability, and be capable of high-scale production, especially when using snap-cure (highly reactive) resin

[21]. However, LCM may present challenges in avoiding defects such as wrinkling and the presence of voids, particularly in parts where the fiber volume fraction exceeds 50% [5, 21]

2.3.1 Resin Transfer Molding (RTM)

RTM is a manufacturing process that was initially used to manufacture boat and low-fiber content parts [25]. Later, RTM process was included in the automotive industry as low-scale production alternative [4, 25]. Today, some authors define RTM as medium-scale production process, delivering up to 15 thousand parts per year [21].

The RTM is a manufacturing process characterized by the separation of the reinforcement and the matrix and the use of the rigid mold, which has a cavity with the same geometry as the final part [21]. RTM consists of five steps, as shown in Figure 2.4, that includes the fabric cutting, lay-up and dry fabric draping, mold closure, the injection at low-pressure [21] and cure of the resin, and finally the part demolding. The filling velocity of the composite part is controlled during the injection to avoid the presence of voids either among or within the fiber tows and ensure quality [21]. The thickness of the final part and the fiber volume fractions can be controlled by the mold closure, so the parts may present consistent mechanical properties [27].

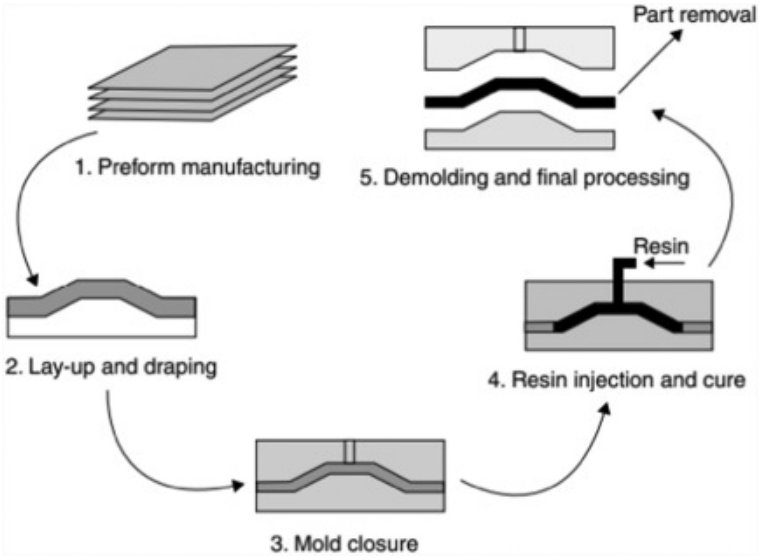


Figure 2.4: Schematic of the RTM process flow [28].

The RTM technology offers a distinct advantage in the surface quality of the final part,

eliminating the necessity for additional finishing operations. In addition, this technology enables the production of intricate geometries, a challenge often encountered in alternative manufacturing processes such as autoclave molding. A second benefit is the elimination of the need for autoclave usage in the flow control and consolidation stages of the RTM process, resulting in reduced cycle times. In production lines, the RTM process also exhibits lower defect rates compared to autoclave molding. Conversely, the RTM may exhibit some porosity and voidage in its final parts, a concern that can be addressed through adjustments to mold and process control parameters[27].

2.3.2 HP-RTM

While the RTM process has been a longstanding and established manufacturing technique in the industry for decades [5], this technology has limitations in terms of the annual production volume compared to the contemporary standards of high-scale production, surpassing what Rudd et al. [4] defined in 1997. According to Rosenberg et al [29], RTM technology is not well-suited for the large-scale production of vehicles containing a substantial number of composite parts, as seen in models like the BMW i3 and i8 series. An alternative to the RTM technology would be another process capable of working with highly reactive resin systems, short cycle times, high automation, and capable of deliver complex composite part shapes, known as high-pressure RTM (HP-RTM) and illustrated in Figure 2.5 [5, 20].

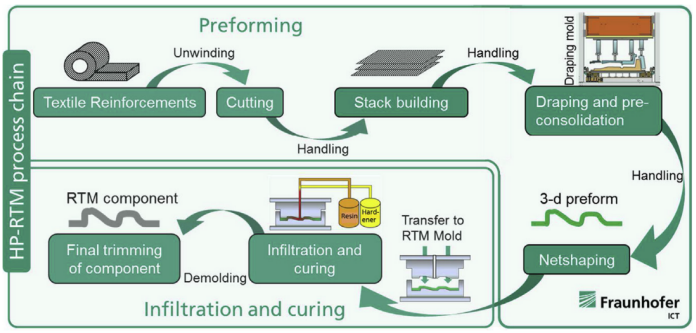


Figure 2.5: Schematic of the HP-RTM process flow [5].

HP-RTM increases production capability by injecting resin into the mold under high pressure. This manufacturing process also separates the fabric preforming from the resin infiltration and curing steps and requires the use of special equipment which is capable of mixing homogeneously the resin formulation, guaranteeing the reproducibility of the

process conditions and a fast filling by injecting the resin at a rate of 20 to 200 $\frac{g}{s}$. Because of these capabilities, use of this special equipment enables the application of fast-curing resins with a curing time shorter than 3 minutes which rises the production capability [5, 29].

2.3.3 WCM

WCM using highly reactive resins is a manufacturing process with a mass-scale production potential and is increasingly being adopted in the automotive industry to enhance production capacity. This method serves as an alternative to the established HP-RTM process [5, 30, 31]. The WCM process comprises two different variants, as illustrated in Figure 1.2: direct and indirect variants. The primary distinction between these methods lies in the moment when the forming process occurs.

In the direct process, forming occurs concurrently with resin infiltration, a technique commonly referred to as viscous draping. In contrast, the indirect method involves initially preforming a dry stack, followed by the application of resin onto this preformed stack. The additional procedural step in the indirect approach results in increased associated costs [5, 32].

The application of resin in the direct variant streamlines the manufacturing process. As a result, WCM emerges as a more economical option compared to HP-RTM due to the simultaneous draping and curing of the part; the resin can be applied to the stack outside the hot mold, minimizing the risk of premature curing and reducing the time lost during resin injection. Another advantage of the WCM process is that it operates at low pressure, with resin being applied at atmospheric pressure, which necessitates simpler machinery to achieve similar outcomes [30].

Karcher et al. [33] compares the WCM process to Inline Prepreg and Autoclave processes in their study. For instance, to manufacture a hat channel with a length of $0.8\,m$, WCM proves to be the most cost-effective option among the three processes, with a cost of approximately 49 euros, compared to 65 euros for the Inline Prepreg part and over 300 euros for an autoclave part. Unlike WCM, which operates at a pressure of 25 bar, the HP-RTM process requires high pressure (approximately 160 bar). This necessitates the use of sophisticated equipment for mixing and dispensing the resin, as well as heavy molds and presses [34]. All these specialized pieces of equipment contribute to higher costs for both the process and the final part.

2.4 Characterization of Reinforcement Fabrics

Although the WCM process is a simple manufacturing process, several mechanisms occur inside the mold simultaneously, which increases the complexity of the process and the development of numerical process simulation models. Poppe [32] illustrates in Figure 2.6 the mechanisms present in the WCM process which were divided in four groups: viscous draping, fluid progression, strong fluid-structure-interaction, and non-isothermal curing. The initial mechanism category, namely viscous draping, is associated with the forming process wherein the fabric is shaped in accordance with the mold geometry. The second group refers to the progression of the resin through the stacking thickness and the fabric surface. The third group of mechanisms involves all the interactions between fabric and fluid. The last group is related to the mechanisms that involve the curing process.

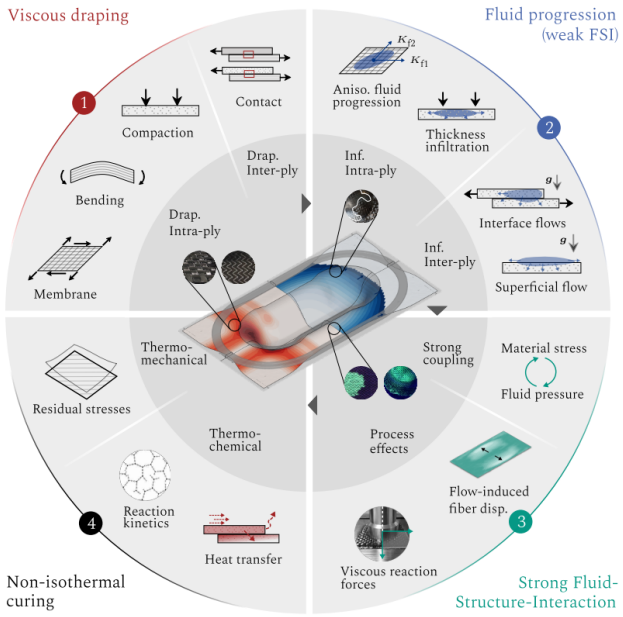


Figure 2.6: Mechanisms present during the WCM process [32].

The research project focused on characterizing the impregnated fabric to support future WCM forming simulations. Therefore, the mechanisms discussed in the following sections are specifically related to viscous draping, particularly the intra-ply draping behavior as shown in Figure 2.7. These mechanisms govern the fabric behavior during the forming process of complex geometries and dictate the development of deformations and wrinkles [5, 24]. Consequently, these deformations influence certain aspects of stacking, such as

fiber orientation, fiber volume fraction, and thickness, which affect the quality of the final part [5].

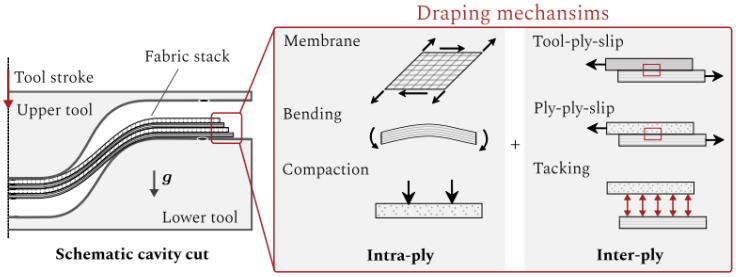


Figure 2.7: Draping mechanisms present during the WCM process [32].

Due to the importance of draping mechanisms in the WCM process and the objective of optimizing final parts, it is imperative to characterize the fabric employed in the manufacturing process [13].

2.4.1 Viscous Membrane Behavior

Ghazimoradi et al. [35] and Boisse et al. [24] identify in-plane shear as one of the main deformation mechanisms during fabric forming. This behavior is especially important during the draping phase, as excess shear can lead to defects such as wrinkling and gapping [36, 37]. Many researchers have addressed the behavior of woven fabric membranes [38–44], but fewer authors have considered unidirectional non-crimp fabrics (UD-NCF) [12, 14, 35, 36, 45, 46]. To the best of the author's knowledge, studies on binder-stabilized and impregnated fabrics remain scarce. For instance, Zhao et al [42] studied the effect of different stabilizing binder concentrations on the shear behavior of woven fabrics, while Poppe et al. [32] considered both dry and wet woven fabrics, as well as three off-axis dry UD-NCFs for membrane characterization.

To capture membrane behavior, most authors rely on either the Picture Frame Test (PFT) (Figures 2.8a and 2.8b) or the Bias Extension Test (BET) (Figures 2.8c and 2.8d) [8, 12, 32, 35, 47]. The PFT comprises a hinged frame in which the fabric is clamped. This frame consists of four equal-length bars. As shown in Figure 2.8b, a tensile force is exerted across diagonally opposing corners of the frame, inducing a transition from the initial square geometry to a lozenge shape [8, 12]. Conversely, the BET uses a simple setup with two horizontal bars to which a rectangular fabric specimen is clamped at both ends.

The length-to-width ratio of the fabric specimen must exceed 2. A tensile force is applied to the top bar, stretching the rectangular specimen as illustrated in Figures 2.8c and 2.8d [8, 35, 45, 47, 48].

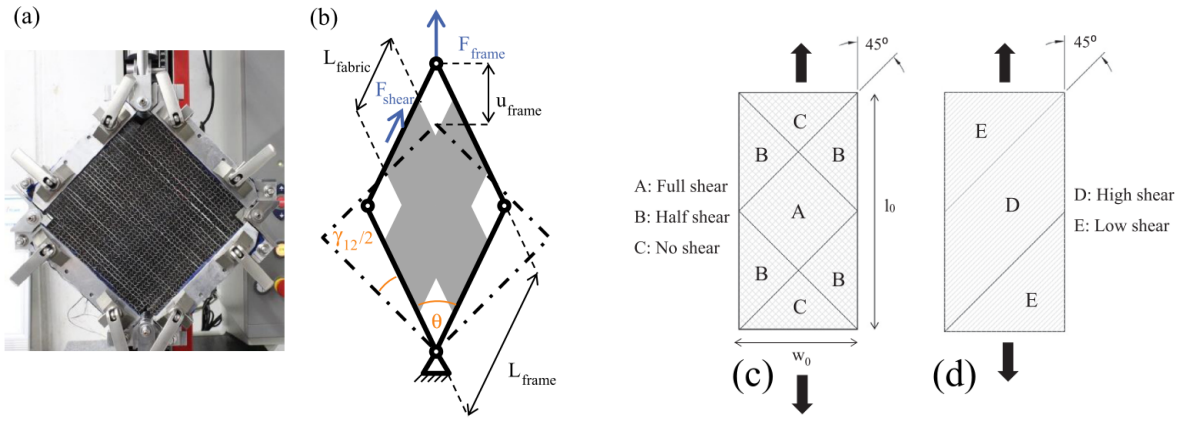


Figure 2.8: Shear extension characterization test setups for engineering fabrics: (a) and (b) Picture Frame Test setup and schematic of the specimen deformation during the test [12], (c) and (d) Schematic showing distinct shear zones in bias extension test for woven fabric and UD-NCF specimens [45].

The BET was originally created to characterize the membrane behavior of woven fabric and is performed under the assumptions that the tows are inextensible, that no crossover slip occurs within the sample, and that shear is defined by fiber rotation [12, 36, 48]. When characterizing woven fabric, the specimen is divided into three regions (A, B, C), as shown in Figure 2.8c. Region C presents no shear deformation, region A displays pure shear deformation, while region B experiences half of the shear found in region A [8, 45, 49]. However, UD-NCFs deform under a combination of deformation mechanisms, including relative fiber rotation (denoted as pure shear) and slippage between fiber rovings (also known as simple shear), as shown in Figure 2.9. The pure and simple shear deformations are nearly indistinguishable for angles below 10° [50]. Due to the absence of perfect pure shear, the regions of the specimen are distributed differently in NCF specimens compared to woven fabric, as illustrated in Figures 2.8c and 2.8d [12, 36, 45, 48, 50, 51].

In addition to the pure and simple shear deformation mechanisms, NCFs exhibit a shear locking mechanism that requires a different approach compared to the classical shear locking observed in woven fabric. Unlike the classical shear locking mechanism, the one present in UD-NCF cannot be captured by the PFT since this type of test induces out-of-plane buckling of the fabric [12]. Schirmaier et al. [12] mentions that the shear locking

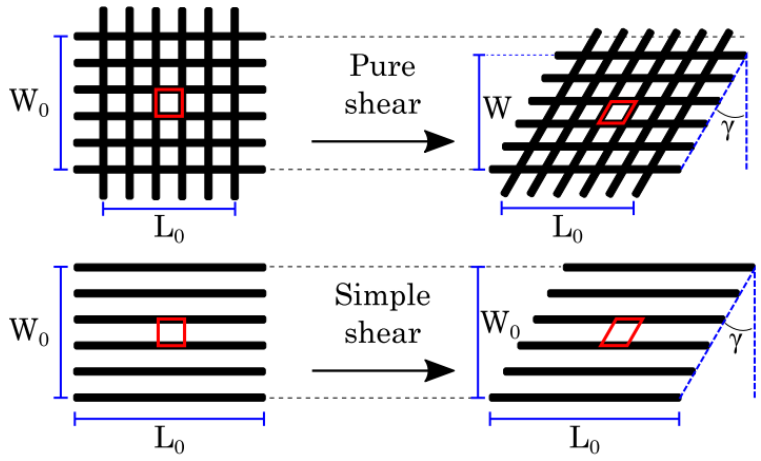
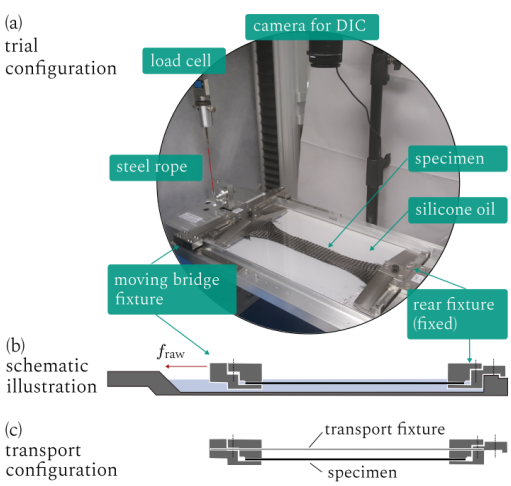


Figure 2.9: Comparison between pure and simple shear deformation [50].

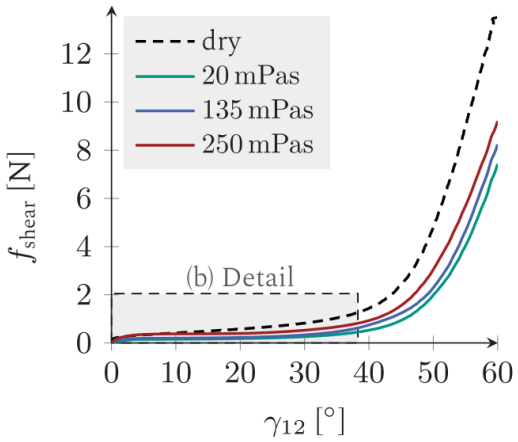
mechanism in UD-NCF occurs when the fabric shear strain reaches a certain limit. Beyond this limit, the sample undergoes normal strain deformation due to fiber contraction in the width direction.

Since the PFT and BET were developed primarily for characterizing dry fabric, Poppe et al. [38] proposed a test setup to evaluate infiltrated woven fabric, as illustrated in Figure 2.10a. This test setup includes the BET positioned horizontally and a reservoir that allows for the infiltration of the fabric using silicone oil to maintain a constant viscosity during trials. The significance of this test lies in the infiltration mechanisms, which may reduce internal friction between the fiber tows, leading to different shear behavior. Poppe et al. [38] indicates that the resin used in the manufacturing process can create lubrication coats between the fibers, altering the friction conditions. As a result, fabric impregnation can significantly reduce the shear force, depending on the loading rate, as presented in Figure 2.10b.

The membrane behavior of reinforcement fabrics has been characterized by several studies using both BET and PFT methods. Daghboudj and Satha [39] investigated the shear rigidity of three types of glass/propylene woven fabrics (BPW, BTW, and UBTW) and found that BPW and BTW exhibited greater stiffness, attributed to the highly unbalanced structure of the fabrics. Guan et al. [40] characterized unbalanced 3D interlock woven reinforcements (IWR) using BET and simulated the membrane behavior through finite element models. The study reported asymmetric deformation between the right and left B areas of the fabric (see Figure 2.8c). Büyükbayraktar et al. [41] performed BET on various woven fabrics with different weave types, analyzing properties such as shear



(a) Infiltrated bias extension test setup.



(b) Membrane shear force response for different fabric impregnation conditions.

Figure 2.10: Extension test setup and shear force vs. angle response [32].

angle, breaking load, and bias extension. The study found that both the test direction and structural parameters had statistically significant effects. Specifically, plain weave fabrics demonstrated the highest breaking load in the bias direction, while twill fabrics exhibited the lowest.

Some studies have also characterized the membrane behavior of dry UD-NCF. Pourtier et al. [48] investigated the deformation of NCF during the BET—including rotation and slippage—and the impact of these deformations on the test results. The authors concluded that the sample width directly impacts the modes of deformation during BET and reported that it is important for the engineering textile to present a significant width to ensure test reliability. Schirmaier et al. [46] characterized carbon UD-NCF through Off-axis-tension (OAT) tests and noted that pure shear is not an intrinsic deformation mode of UD-NCF. They also found that the OAT test is well-suited for model development and for obtaining material parameters, in contrast to PFT, which is not recommended for UD-NCF characterization. Schafer et al. [14] developed a forming model to capture the membrane behavior of UD-NCF based on superimposed shear, transverse tensile, and longitudinal compressive strains. The authors parametrized the developed model with experimental results obtained from OAT tests in different fabric orientations and compared their outcomes with the results from Schirmaier et al.[46]. Schafer et al. [36] characterized both UD-NCF and Biax-NCF under multiaxial strain conditions. They created a new method to capture fabric deformation by applying a dot pattern to the textile and measuring the strain field

with DIC frames. They reported that the 45°-OAT test is best suited to characterize the fabric's shear properties, while the 30 and 60°-OAT tests are better suited to investigate the transverse behavior.

As mentioned previously in this section, investigations on binder-stabilized and impregnated fabrics are very limited. Zhao et al. [42] examined the effect of varying binder concentrations on the membrane behavior of woven fabrics. They conducted experimental tests and developed a finite element model incorporating cohesive elements to simulate binder behavior. Their findings indicated that the primary influence of stabilizing binders is the formation of binder structures at gaps and weave intersections, which increases inter-tow friction as binder concentration rises.

2.4.2 Viscous Bending Behavior

A second behavior that is important to characterize is the bending, or flexural, behavior. Early research neglected this mechanism, focusing solely on the membrane behavior for the sake of simplicity in analysis [52, 53]. However, bending behavior is a critical mechanism that describes the curvature of the fiber and influences the formation of undesired wrinkles during the forming process, potentially affecting the mechanical performance of the final part [54–58]. Senner et al [59] note that low bending stiffness significantly impacts the deformation behavior of the fabric, resulting in large deformations from small bending loads.

Figure 2.11 illustrates the significance of bending behavior in the simulation process. Subfigure (b) depicts a draping simulation that considers only tensile stiffness, resulting in perfect draping without any wrinkles—an outcome that differs from real draping situations. Subfigure (c) represents a simulation that accounts for both tensile and in-plane shear stiffness, leading to the formation of small wrinkles, yet still not reflective of reality. Conversely, subfigure 2.11 (d) demonstrates the effect of bending stiffness, which contributes to larger wrinkles that are more akin to genuine draping. Finally, subfigure (e) shows the deformed shape of an isotropic material, which exhibits the same axial rigidity in all directions; thus, the reproduction of hemispherical geometry remains an unattainable objective in this context.

Wrinkling is a common issue during the textile draping process, often caused by relative motion among the fiber tows that form the textile. This relative motion results in low bending stiffness, creating conditions conducive for wrinkles that are prominent in the transverse direction of UD-NCF [12, 24, 55]. Various factors, including temperature, angular velocity, and stitching type in the case of UD-NCF, have been studied [60–62]

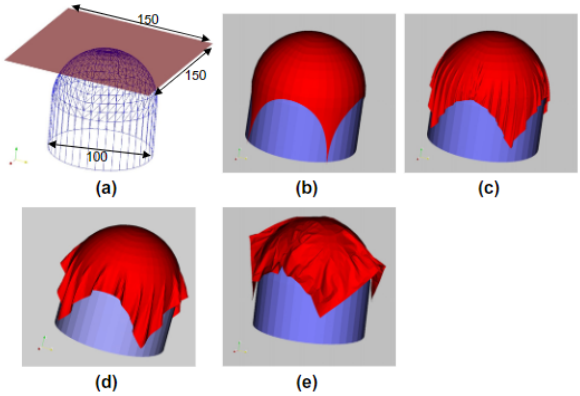


Figure 2.11: Hemisphere punch simulation considering different data input [54].

and may influence bending stiffness, resulting in variations in wrinkle size, as illustrated in Figure 2.12. An alternative to mitigate wrinkle formation is the use of forming constraints, such as blank holders. These constraints apply tension to the textile, helping to prevent compressive states within the fabric [43, 54, 63].

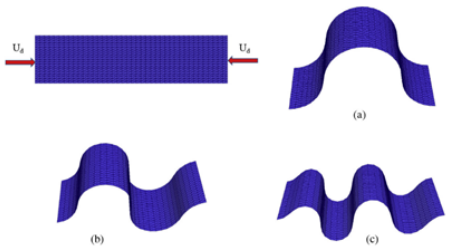


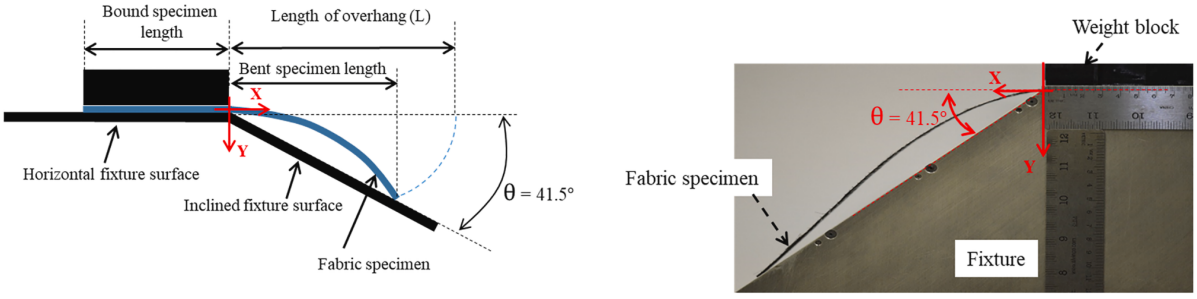
Figure 2.12: Variation in wrinkle size for different bending stiffness values [63].

In continuous materials such as metal or cured composite parts, the bending behavior can be related to the membrane using a chosen plate theory. However, textile fabrics exhibit low bending stiffness, which invalidates the relationship established by plate theory between extension and flexural stiffness [24, 55]. Consequently, these two characterization experiments should be performed separately. Several testing methods have been developed to characterize the bending behavior of engineering textiles, including various cantilever tests (e.g., Peirce, vertical, and free-hanging tests), the rheometer bending test (RBT), and buckling tests [64]. Traditional three- and four-point bending tests are generally not used for fabric characterization due to their low flexural stiffness, which results from relative slippage between fiber tows. These test setups are typically reserved for thicker reinforce-

ments or small composite samples with higher bending stiffness, and are therefore avoided in fabric studies [52, 55, 65].

In their study, Krogh et al. [64] examined various testing methods for assessing fabric bending stiffness. One of the primary methods, known as the Peirce cantilever test [66], involves a straightforward setup using an inclined plane over which a fabric strip hangs (refer to Figures 2.13a and 2.13b). This method estimates bending stiffness based on the contact point of the fabric tip with the plane, under the assumption of constant stiffness. However, this assumption may be overly simplistic, potentially failing to capture the nonlinear characteristics of fabric behavior [64].

Despite its drawbacks, the inherent simplicity of the Peirce method has made it a popular choice among researchers [52, 63, 64, 67, 68]. Poppe et al. [65] noted that some adaptations of the Peirce method incorporate a weight to clamp the non-overhanging end of the fabric strip. This added weight compresses the fabric to an indeterminate extent, thereby altering boundary conditions and possibly introducing inconsistencies into the test results.



(a) Modified cantilever test scheme.

(b) Modified cantilever test setup.

Figure 2.13: Scheme and setup of the modified cantilever beam test [35].

The Kawabata bending test (KES-FB2) utilizes a specialized apparatus equipped with two clamps that secure the specimen in place. One of these clamps rotates to apply a controlled curvature and loading rate. This method allows for the direct measurement of moment–curvature curves, even under cyclic loading conditions, effectively capturing nonlinear, hysteretic, and loading-rate-dependent behaviors. An adaptation of this setup was introduced by Sachs et al. [57], which modified the test for compatibility with rheometer equipment; this adaptation is known as the Rheometer Bending Test (RBT) (see Figure 2.14).

In the RBT configuration, the setup consists of two fixtures: the bottom fixture remains

stationary and secures the fabric, while the top fixture, attached to the rheometer shaft, rotates at a predetermined angular velocity to bend the fabric sample. The RBT is widely recommended in the literature due to its accuracy and effectiveness in characterizing rate-dependent, temperature-sensitive, and hysteretic responses of fabrics [64, 69].

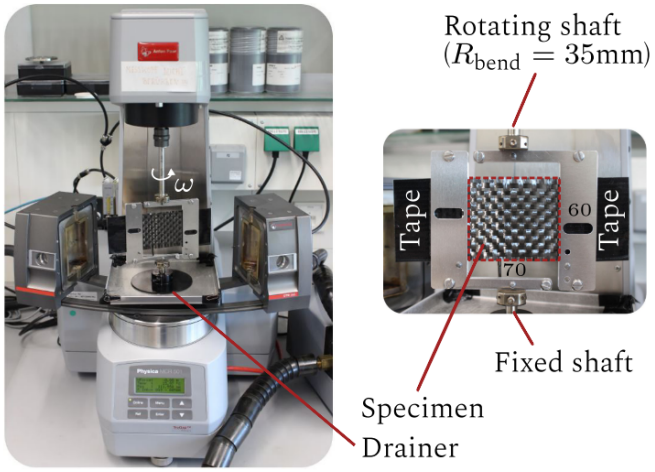


Figure 2.14: RBT setup, Anton Paar MCR501 rheometer coupled with an enlarged bending frame [65].

Recent studies have concentrated on the bending behavior of binder-stabilized fabrics. For instance, Broberg et al. [70] examined the forming process of binder-stabilized glass fiber non-crimp fabrics (NCF) used for manufacturing thick parts. They discovered that in transition regions, the stabilizing binder could actually increase wrinkle formation. Additionally, they noted that high compressive loads could lead to the creation of large wrinkles and damage to the binder material.

In a follow-up study, Broberg et al.[71] characterized the nonlinear behavior of glass fiber NCF through a modified cantilever test. Their findings indicated that including material nonlinearities in simulation models enhances the accuracy of wrinkle formation predictions. Likewise, Ghazimoradi et al. [35] employed the modified cantilever method to investigate the nonlinear bending behavior of dry and inactivated binder-stabilized carbon fiber UD-NCF. They reported significant anisotropy, showing low bending stiffness in the direction perpendicular to the fiber tows and greater stiffness along the fiber direction. The characterization data were subsequently utilized to calibrate an anisotropic material model in commercial finite element software [37].

While both Broberg et al.[71] and Ghazimoradi et al. [35] explored the properties

of binder-stabilized UD-NCF, neither considered the impacts of binder pre-activation or fabric impregnation, reflecting the specific manufacturing processes they targeted. Despite significant progress having been made in understanding the bending behavior of binder-stabilized UD-NCFs, it is crucial to recognize that in the WCM process, the forming occurs during the molding phase when the fabric is impregnated. Consequently, the mechanisms of draping, including bending behavior, may differ from those documented in earlier studies [35, 70], which did not account for fabric infiltration or the pre-activation of the binder due to the various manufacturing processes examined.

One relevant study that investigated the impact of infiltrated fluid viscosity on the bending response of reinforcement fabrics was conducted by Poppe et al. [69]. The researchers employed both the RBT test and a modified Peirce test to characterize the bending behavior of infiltrated woven fabric. Although Poppe et al. [69] were pioneers in studying the bending response of impregnated reinforcement fabrics, their research focused solely on non-binder-stabilized woven fabrics. This has created a gap in the literature regarding other binder-stabilized fabrics, particularly UD-NCFs, which may exhibit distinct behaviors.

2.4.3 Viscous compaction behavior

2.4.3.1 Experimental characterization

A third draping mechanism present in all LCM processes and important to be characterized is the compaction behaviour. Boisse et al [24] and Korkiakoski et al. [72] emphasize the significance of compaction testing for capturing fabric behavior under transverse loads, which is essential for ensuring the quality of the final part. According to Schafer et al [73], compaction has a considerable impact on the mechanical properties of the finished parts due to their fiber volume content. Bickerton et al [74] explain that during transverse compression, the stress-strain behavior of the fiber bed exhibits viscoelastic characteristics influenced by the lubrication state. Moreover, Yong et al. [75] assert that in manufacturing processes involving rigid-closed molds (e.g., WCM), determining whether the desired fiber volume fraction can be achieved relies on the reaction force on the tooling surface, which is contingent upon the compaction response. The compaction mechanism can also affect other stack characteristics, such as textile permeability. [76] clarify that during compaction, textile layers are pressed together, causing them to slide against each other and rearrange inside the mold, generating friction forces. In processes like WCM, lubrication of the textile may reduce friction between adjacent layers, facilitating relative sliding [75, 76].

Similar to the manufacturing process, the compaction test can be conducted by compressing a fabric stack using a universal testing machine, as illustrated in Figure 2.15. Various studies have investigated the influence of multiple parameters on compaction behavior, including compaction speed [77], lubrication conditions [32, 72, 75, 77], number of layers [73, 77–79], fabric architecture [72, 77], stack orientation [73], and number of cycles [72, 77, 78, 80]. However, studies on the influence of stabilizing binder on compaction behavior remain limited [81, 82].

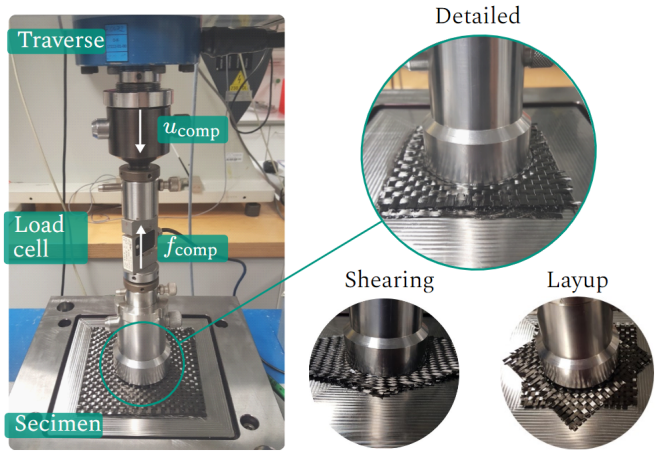


Figure 2.15: Compaction test setup [32].

Poppe et al. [83] studied the effects of shear angle, fabric impregnation, and nesting on the response of a carbon fiber woven fabric stack. They found that both shear angle and fabric impregnation lead to an increase in compaction force. The fluid saturating the fabric stack creates hydraulic pressure, which opposes the applied compaction force. Additionally, they investigated the impact of different stacking sequences (e.g., $[0]_4$ and $[0/45]_2$) and concluded that for woven fabric, stacking sequences with the fiber tows aligned in parallel ($[0]_4$) exhibited more overlap at the interfaces, a phenomenon known as nesting, which subsequently reduced the necessary compaction force. In contrast, Yong et al [75] discussed experiments involving wet woven and NCF fabrics that showed significant differences in compaction response, which were attributed to differences in fabric architecture.

Further studies have concentrated on the compaction mechanisms of non-crimp fabrics, considering various process parameters. Schafer et al. [73] characterized UD- and biaxial-NCFs with different stacking sequences and fiber orientations at their interfaces. They noted that resistance to compaction decreased with an increasing number of layers, although this effect diminished beyond a certain threshold. Limited nesting was observed

in UD-NCFs compared to biaxial-NCFs, which can be attributed to the supporting glass fibers orthogonal to the carbon fiber tows, inhibiting a more pronounced nesting effect in the UD-NCF layers. Li et al. [77] investigated the effects of cyclic compactions, number of layers, stitching patterns (such as tricot, chain, and tricot-chain), compression rates, and fabric impregnation for carbon fiber NCF. They concluded that lubrication had little impact on compaction behavior due to low friction, while impregnation influenced relaxation response. Furthermore, Droste et al. [80] noted nesting caused by sunken stitching yarns.

Recent research has explored the time-dependent compaction response of binder-stabilized fabrics. Wei et al. [82] analyzed how varying concentrations of liquid stabilizing binder (0%, 4%, 8%, and 12%) influence the compression of different carbon fiber textiles, including two types of woven fabric, a biaxial non-crimp fabric (NCF), and a multiaxial NCF. The authors found that as the binder concentration increased, the elastic modulus decreased while the normalized relaxation stress increased, indicating an improvement in stack relaxation ability.

In a separate study, Wei et al. [81] examined how process parameters—such as compression speed, maximum pressure, and holding time—affect the compaction behavior of binder-stabilized fabric at various binder weight concentrations. They reported that the initial stack thickness increased with higher binder concentrations. Additionally, they discovered that the recovery thickness also rose with increased maximum pressure, regardless of binder content. Another noteworthy finding was the potential for increasing the fiber volume fraction by lowering the compression rate.

While both studies provided valuable insights into the effects of the stabilizing binder, they focused solely on liquid stabilizing binders and did not investigate the impact of preactivating the binder. Furthermore, these studies did not address the importance of binder impregnation in the context of the WCM process.

2.4.3.2 Numerical modeling of compaction response

The compaction response of engineering textile stacks has been modeled in several previous studies. Poppe et al. [83] developed and validated coupled finite element forming and fluid-submodels to simulate the three-dimensional WCM process. They stated that the forming submodel can reproduce the non-linear viscoelastic compaction response of a woven fabric stack without numerical locking. Mitsch et al. [84] proposed and validated a computationally efficient 3D modeling approach that includes nonlinear compaction modeling, enabling the simulation of the thermoforming process of thermoplastic composites. This viscoelastic nature of the compaction mechanism has led several studies to adopt rhe-

ological models - such as Zener, Burguer and Maxwell - to fit the compaction parameters. These models consist of a combination of elastic springs and viscous dashpots as illustrated in Figure 2.16 [79, 85]. In the Maxwell model, the viscoelastic behavior of a given material is described by a combination in series of a spring and a dashpot. In the Burgers model, the viscoelasticity is characterized by the combination of a spring and a dashpot in series (Maxwell element) together with a spring and a dashpot in parallel (Kelvin–Voigt element) [86, 87]. Finally, the Zener model consists of a spring and a dashpot in series with a second spring in parallel [88].

Echaabi et al [89] compared all three rheological models and reported that the Maxwell model returned the most accurate results among the three for relaxation time. Danzi et al [85] proposed a three-branch Maxwell model with strain-dependent springs and strain-rate-dependent dashpots (Figure 2) to describe the time-dependent compaction response of a dry carbon fiber woven fabric bed. The authors reported that this model is valid across different fiber volume fractions and strain rates. The same three-branch Maxwell model was later adopted by Werlen et al. [76] to strike a balance between accuracy and complexity. They reported that the three-branch Maxwell model can yield accurate results for a wide range of experimental configurations (e.g., fabric architecture, fiber volume fraction, and fabric impregnation state). However, modelling the viscoelastic behavior is a challenging task and can require a considerable number of elastic springs and viscous dashpots to fit experimental data adequately. The three-branch Maxwell model for a one-dimensional stress case requires calibration of seven parameters (E_0, E_1, τ_1, E_2, τ_2, E_3, τ_3) [90, 91].

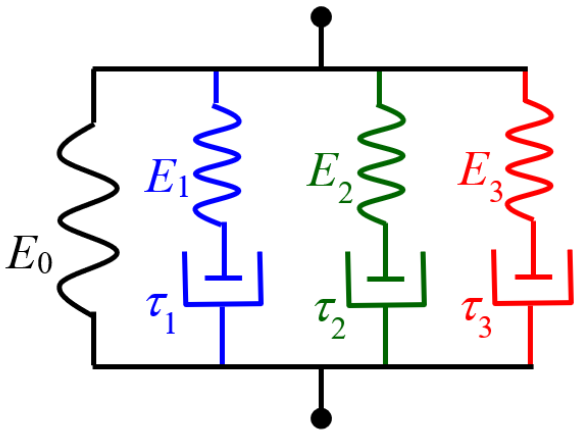
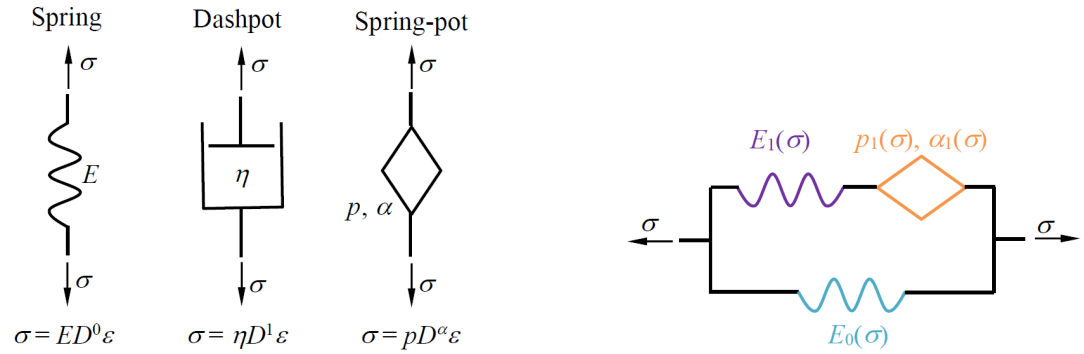


Figure 2.16: Schematic three-branch Maxwell model, including the elastic and viscoelastic branches.

Haveroth et al [91] state that these experiments can generate too many parameters to be identified and proposed the implementation of fractional derivatives to approach the problem. Fractional derivatives can describe the viscoelastic behavior and provide a good curve-fitting property by providing a lower mean square error with fewer input parameters [92, 93]. Hence, Haveroth et al [91] propose the fractional Zener model as an alternative to the Maxwell model, replacing the viscoelastic branches (Figure 2.16) by a spring-pot or Scott-Blair element, illustrated in Figure 2.17a. The result of this replacement is a system with four parameters (E_0, E_1, α, p) as shown in Figure 2.17b.



(a) Schematic representation of the rheological elements. (b) Schematic Fractional Zener model.

Figure 2.17: Fractional Zener model scheme and their rheological elements.

To obtain the material parameters that can accurately represent the time-dependent behavior captured during experiments, an optimization method should be applied to the problem. Several optimization methods have been adopted for this purpose, including Simplex [76] and Particle Swarm Optimization (PSO). Werlen et al [76] obtained the material parameters for the Maxwell model by applying a finite difference method, which was optimized with the Simplex optimization algorithm. This optimization approach was implemented, obtaining three parameters while the other four were fixed, which can make the optimization process time-consuming and computationally expensive. The PSO is a heuristic method extensively recommended for inverse optimization problems in which the material parameters are sought to fit experimental curves, as is the current investigated problem [90, 94]. The optimization process is heuristic due to a few or a lack of initial assumptions related to the optimized problem [90, 95]. Although the PSO can provide no guarantee of global minimum value, the optimization process is capable of searching large domains of possible solutions and requires no use of gradients. For this reason, the optimization problem has no requirement of differentiability, and the PSO is extensively applied in optimization problems that present irregularities or numerical noises [90].

2.4.4 Gaps in the literature

Research on binder-stabilized and impregnated fabric is quite limited due to the specific context of the manufacturing processes under investigation in this field. Unlike other WCM processes, the WCM process involves a forming step with an infiltrated engineering textile, and the use of binder-stabilized fabric is a potential alternative to address the challenge of resin management in the manufacturing of composite parts in complex, deep-cavity molds. Additionally, the UD-NCF has attracted the attention of the automotive industry due to its enhanced in-plane mechanical properties and the ability to tailor them as needed.

2.5 WCM Process Studies for FRP Composites

WCM is distinguished by the lower pressure applied to the resin in comparison to HP-RTM. During WCM trials, the pressure within the stacking sequence may be lower than the vapor pressure of moisture present between layers, which acts in opposition to the resin pressure [96, 97]. This pressure difference may form voids inside the parts, as illustrated in Figure 2.18, which represents one of the main challenges of WCM [30]. On the other hand, the higher pressure of HP-RTM may decrease both the size and the number of voids [97].

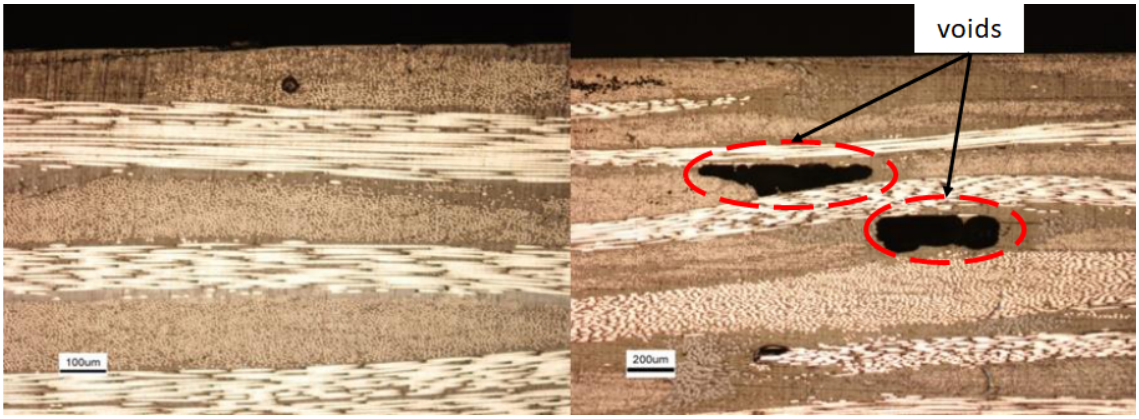


Figure 2.18: Microscopic analysis to investigate the presence of voids in HP-RTM (left) and WCM (right) parts. Adapted from [30].

The influence of stabilizing binders has been widely studied, mainly regarding their effects on processing. Increased binder content generally reduces fabric permeability and

can alter resin flow behavior through gradual dissolution or by forming interlayer films that block capillary channels [15–17, 98]. Fewer studies address mechanical performance, though existing work shows that binders may introduce defects such as voids and reduce properties like flexural strength and fracture toughness [99]. However, these results are limited by the absence of microstructural analysis and their focus on VARTM rather than other LCM processes such as WCM. This highlights a gap in understanding binder effects in UD-NCF composites produced via WCM.

Void formation and its impact on composite performance depend strongly on the manufacturing process [100]. In LCM, voids arise from mechanical entrapment or reaction gases [101–103]. In WCM, the low-pressure, thickness-dominated flow promotes rapid initial infiltration followed by slower in-plane progression [104], which can leave inter-tow voids that are more harmful than smaller intra-tow voids [101, 102]. Even small void contents (1.5–3%) substantially reduce matrix-dominated properties, ductility, and failure strain [105–107].

Although eliminating voids is impractical, controlling them can improve WCM part quality. Strategies include resin degassing and controlled mold vacuum. Vacuum can reduce void content and improve mechanical properties, but if mismanaged, it may also induce resin evaporation [102]. Studies have shown mechanical improvements with vacuum application, though void content and fiber volume fraction were not quantified, leaving uncertainty about the magnitude of these effects [108].

Recent WCM research identified key process parameters—resin and mold temperature and resin set time—that influence mechanical performance, whereas gap closure speed and curing time have minimal effect [109]. Additional work linked temperature gradients in the mold to property variations across panels [110]. However, these studies did not consider vacuum application or binder activation, leaving important process variables unexplored.

2.5.1 Gaps in the literature

Many studies have examined the effects of different types of stabilizing binders—thermoplastic and thermosetting—on processing parameters, particularly permeability, highlighting the potential for poor impregnation and defect formation, such as voids. However, most of the limited available research has focused on the influence of thermoplastic binders on the mechanical properties of the final composite part. Thermoplastic binders are generally used in vacuum-bag processes, which partly explains this emphasis. Consequently, there is a notable lack of studies investigating how thermosetting binders affect the mechanical performance of composites. Furthermore, since the use of binder-stabilized fabrics can

increase void content, applying a vacuum to the mold cavity may help remove entrapped air. Although some studies have reported that vacuum-assisted techniques improve part quality, these investigations were conducted using other manufacturing methods (e.g., the RTM process) and did not quantify the degree of improvement.

2.6 Microstructural Assessment of Unidirectional FRP Composites

The reinforcement phase in fiber-reinforced plastic (FRP) composites strongly influences their mechanical properties, making accurate fiber volume fraction (FVF) estimation essential for assessing structural performance [111, 112]. The three primary FVF measurement methods are acid digestion (AD), burn-off (BO), and non-destructive approaches [113]. These rely on sampling small regions of a part under the assumption of uniform fiber distribution. AD and BO, standardized in ASTM D3171 [114], are the most widely used, with AD being predominant.

In AD, the composite sample is weighed, the matrix is dissolved in acid, and the remaining fibers are re-weighed [113, 115]. The method is simple and low-cost but destructive, operator-dependent, and requires safe chemical handling [116]. A sample mass >0.5 g is required [114], and carbon fibers may degrade during digestion, making AD unsuitable for CFRPs [112]. BO removes the matrix thermally at temperatures above decomposition [114]. It is faster than AD but unsuitable for CFRPs due to fiber incineration risks [113]. Both destructive methods may introduce up to 2% error [116]. BO variants such as thermogravimetric analysis (TGA) measure mass continuously but require clearly separated decomposition temperatures, limiting their applicability [112].

Non-destructive techniques evaluate microstructure through optical microscopy, SEM, or micro-CT, followed by digital image processing (DIP) [113, 115]. DIP applied to cross-sections has been widely used to quantify FVF [117, 118]. Methods include fiber counting, line-intercept measurements, and area-based pixel segmentation [119]. DIP can estimate FVF and visualize fiber distribution [113], but it is best suited to unidirectional (UD) composites, is sensitive to section bias, and requires high-quality images for accuracy [120, 121].

Micro-CT generates 3D reconstructions from multiple slices and is less prone to section bias while enabling FVF estimation for fabric-reinforced and multidirectional laminates [120, 122]. It has been combined with microscopy for improved accuracy [123]. However,

micro-CT is expensive, limited in sample size due to resolution constraints, and cannot reliably distinguish carbon fibers from polymer matrices because of similar densities [102].

Additional nondestructive methods include ultrasonic, thermal diffusivity, and density-based approaches. Ultrasonic methods can estimate FVF by relating sound velocity to material composition [111], but require complex modeling and offer limited resolution. Thermal diffusivity methods infer FVF from material thermal properties but may produce large uncertainties [116]. The ASTM D3171 density-based method uses fabric areal weight, laminate thickness, and sample density but is sensitive to errors in thickness measurement and cannot account for tow spreading during compaction.

Most FVF measurement methods have been applied to UD tape, pultruded products, or woven composite systems. Liquid composite molding processes such as RTM and WCM integrate dry fabrics with resin inside a mold, enabling more controlled FVF [124]. UD non-crimp fabrics (UD-NCFs) are increasingly used due to superior in-plane properties and architecture [6, 35]. However, their multiple constituents complicate FVF measurement. In AD and BO, the removal of transverse support fibers and partial digestion of stitching yarns (often polyester) makes accurate fiber mass measurement difficult [116, 125].

DIP of cross-sectional images is more suitable for UD-NCFs. Mikkelsen et al. [118, 126] used SEM-based DIP to measure intra-tow FVF (59–66%) and an overall FVF of 55%. Zeng and Montesano [127] applied a two-step DIP method, combining intra-tow and impregnated-tow measurements, yielding an overall FVF of 54%, consistent with density-based values. Cherniaev et al. [128] reported a similar two-step approach resulting in a 45% FVF estimate. A key challenge of these methods is accurately defining the regions corresponding to impregnated tows, which often have irregular shapes [118].

2.7 Performance characterization of energy absorbing FRP parts

Besides enhancing the vehicle's system efficiency, composite parts often offer superior crashworthiness compared to metal components. This is because, through various failure mechanisms such as delamination, fibre-matrix debonding, matrix cracking, and fiber breakage, composites can absorb more energy per unit of weight during an impact than metal alloys. Consequently, this increases the vehicle's safety in the event of an accident [129–137]. As composite parts can be tailored accordingly to their use, the crashworthiness of a composite part can vary through a series of manufacturing parameters, including the material system, the part geometry, type of loading, and the manufacturing process [132]. Therefore, it is

important to understand how these parameters influence the crashworthiness of the final part.

Quasi-static tests are generally conducted in the axial direction, which is considered the most efficient configuration for energy absorption in structural design [132]. Figure 2.19 illustrates an axial crush test, which can be conducted in a universal testing machine or a hydraulic press. In general, the test is displacement-controlled, with force measured by load cells mounted to the testing equipment. As a result, the energy absorbed is represented by the area under the force-displacement curve [129, 130, 132, 134, 138, 139], and is given by

$$E_{\text{abs}} = \int_0^{d_c} F(\delta) d\delta, \tag{2.1}$$

where F is the load applied to the specimen and d_c represents crushing distance.

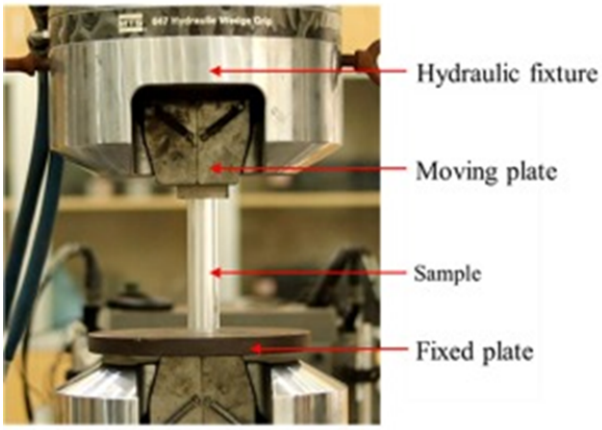


Figure 2.19: Schematic of a quasi-static crush test performed with a universal testing machine [135].

Although axial crush test is the most efficient configuration, the axial compression of composite parts can result in catastrophic failure, characterized by a high peak load (P_{max}) followed by a significantly lower mean load (P_{mean}), ultimately reducing the total energy absorbed (see Figure 2.20) [139, 140]. To mitigate this, a special geometry known as a trigger is often machined at one end of the composite specimen. The trigger acts as a stress concentrator that facilitates the initiation of failure, promoting a more stable and progressive crushing mode that enhances energy absorption [130, 138–140].

Figure 2.20 shows the typical load-displacement curve in the axial crushing tests for both types of failure. In the first region, the specimens present an elastic stage with a

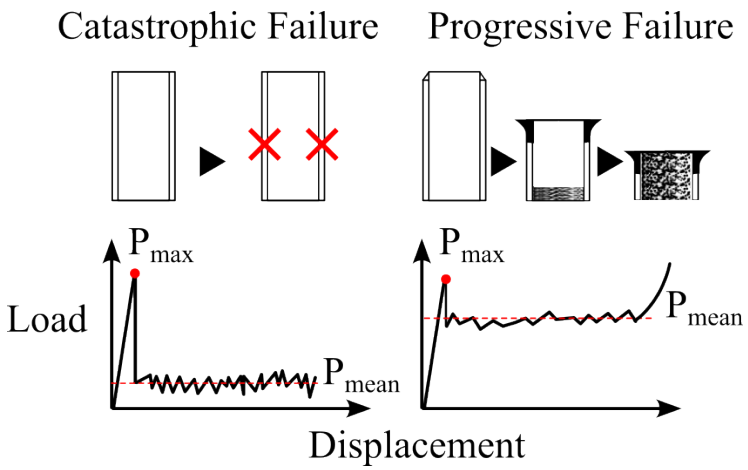


Figure 2.20: Types of failure in axial crushing

steady loading slope, also known as the pre-crush zone [129, 134], which ends when the load-displacement curve reaches its peak value, P_{max}. Mamalis et al. [132] state that the part geometry and the material system directly influence the peak load. Yang et al. [135] highlight that the smaller the P_{max} and the higher the absorbed energy, resulting in the maximum deceleration of the car, improving the vehicle's safety. Progressive failure is considered the safest design approach due to its superior energy absorption capacity. To maximize this, the difference between the peak and mean loads should be minimized, as a larger area under the force-displacement curve corresponds to greater deceleration and improved passenger safety [134, 139]. Jimenez et al. [139] note that machining the trigger at the end of the specimen is key to achieving high energy absorption.

The load-displacement curve from a crush test is typically divided into three zones, as illustrated in Figure 2.20 [129, 134]. The first zone, pre-crushing, represents the elastic behavior of the material and continues until the first failure, which occurs at the peak load P_{max}. The second zone, crushing, is defined by the mean crush force P_{mean}. The third, compaction or failure zone, is characterized by a sudden increase in crush force due to material debris accumulation [132, 134, 139].

In the literature, performance comparisons between different materials and geometries are often expressed using specific energy absorption (SEA), which is the energy absorbed per unit mass of the specimen [129, 134]. It is defined as

$$\text{SEA} = \frac{E_{\text{abs}}}{m}, \tag{2.2}$$

where m is the mass of the crushed specimen. Numerous studies have found that composite

parts generally absorb more energy per unit mass than metallic components [134]. This superior performance is attributed to failure mechanisms such as fiber breakage and ply delamination [135].

Due to the critical importance of safety in the automotive and aerospace industries, numerous studies have investigated various parameters of crush testing. A recent literature review by [141] highlights key parameters such as strain rate [130, 140], material system [134, 135, 142], trigger type [134, 139], and cross-section geometry [129, 143].

Among these studies, strain rate is one of the most studied parameters. However, there is no clear consensus on its effect on energy absorption. Some studies report a strain-rate dependency [130], while others claim no significant influence [132, 140]. Chiu et al. [140] suggest that the discrepancy is due to the limited sample sizes in previous studies. Their own results support the conclusion that energy absorption is independent of strain rate, aligning with the findings of other authors. However, some studies report reduced energy absorption under dynamic loading compared to quasi-static conditions [132].

In contrast, studies on part geometry consistently agree that circular cross-sections offer optimal energy absorption. Additionally, investigations on crush test have a consensus that sharp corners in rectangular profiles act as stress concentrators, reducing the energy absorption capacity [134, 143]. However, the influence of diameter remains debated: while Capretti et al [134] and Mamalis et al. [132] argue that a smaller diameter-to-thickness ratio maximizes energy absorption, Yang et al. [135] suggests that larger diameters lead to better performance. Moreover, the literature agrees on the importance of the trigger to avoid catastrophic failure in composite parts. Similarly, with respect to material systems, it is widely accepted that composites generally outperform metals in energy absorption. Jacob et al.[138] estimated the weight of different material systems needed to absorb energy during crashes at varying speeds. Lastly, Solaimurugan et al. [144] compared stitched and unstitched fabric composites and found that stitched fabrics can achieve up to 40% higher energy absorption.

Recently, Ajayi [145] conducted a series of quasi-static axial loading of HP-RTM double-hat channels and investigated the influence of two different stacking sequences ($[\pm 45/0_2]_S$ and $[0/\pm 45/90]_S$). The author reported an expected higher efficiency of the $[\pm 45/0_2]_S$ laminate with a 22% higher peak force under quasi-static load, 7.5% higher mean crush force and around 2% greater energy absorption. Ajayi [145] explains that the difference between both stack lays on sample failure mode: the laminate $[\pm 45/0_2]_S$ exhibited a mixture of splaying and lamina bending, while the sample $[0/\pm 45/90]_S$ ehxibited a brittle failure, a combination of fragmentation and lamina bending.

2.7.1 Gaps in the literature

In the literature, many studies often employ manufacturing methods that are limited in production volume or material costs (e.g., vacuum bag molding, hand lay-up, and autoclave curing). Consequently, there remains a clear gap in the literature regarding composite parts produced using WCM processes and the influence of process parameters—such as stabilizing binders and vacuum-assisted techniques—on their energy absorption performance.

References

[1] R. M. Portela, "Comparação de modelos de placa para simulação de laminados compósitos," M.S. thesis, Universidade Estadual de Campinas, 2020.

[2] I. M. Daniel and O. Ishai, *Engineering mechanics of composite materials*. Oxford university press New York, 2006, vol. 1994.

[3] J. R. Vinson and R. L. Sierakowski, Eds., *The Behavior Of Structures Composed Of Composite Materials*. Springer Netherlands, 2002, vol. 105, ISBN: 978-1-4020-0904-4. DOI: 10.1007/0-306-48414-5. [Online]. Available: http://link.springer.com/10.1007/0-306-48414-5.

[4] C. D. Rudd, A. C. Long, K. N. Kendall, and C. G. E. Mangin, *Liquid Moulding Technologies*. Amsterdam, The Netherlands: Elsevier, 1997, ISBN: 0768000165. DOI: 10.1533/9781845695446.

[5] F. Henning, L. Kärger, D. Dörr, F. J. Schirmaier, J. Seuffert, and A. Bernath, "Fast processing and continuous simulation of automotive structural composite components," *Composites Science and Technology*, vol. 171, pp. 261–279, Feb. 2019, ISSN: 0266-3538. DOI: 10.1016/J.COMPSCITECH.2018.12.007.

[6] A. Schnabel and T. Gries, "1 - production of non-crimp fabrics for composites," in *Non-Crimp Fabric Composites*, ser. Woodhead Publishing Series in Composites Science and Engineering, S. V. Lomov, Ed., Woodhead Publishing, 2011, pp. 3–41, ISBN: 978-1-84569-762-4. DOI: https://doi.org/10.1533/9780857092533.1.3. [Online]. Available: https://www.sciencedirect.com/science/article/pii/B9781845697624500011.

[7] L. Kärger, S. Galkin, E. Kunze, M. Gude, and B. Schäfer, "Prediction of forming effects in ud-ncf by macroscopic forming simulation–capabilities and limitations," in *ESAFORM 2021 - 24th International Conference on Material Forming*, Liège, Belgium, 14-16 April 2021.

[8] P. Boisse, N. Hamila, E. Guzman-Maldonado, A. Madeo, G. Hivet, and F. Dell'Isola, "The bias-extension test for the analysis of in-plane shear properties of textile composite reinforcements and prepregs: A review," *International Journal of Material Forming*, vol. 10, pp. 473–492, 2017.

[9] M. Ghazimoradi, E. A. Trejo, V. Carvelli, C. Butcher, and J. Montesano, "Deformation characteristics and formability of a tricot-stitched carbon fiber unidirectional non-crimp fabric," *Composites Part A: Applied Science and Manufacturing*, vol. 145, p. 106 366, Jun. 2021, ISSN: 1359-835X. DOI: 10.1016/J.COMPOSITESA.2021.106366.

[10] R. Zheng *et al.*, "Mesoscopic finite element modeling of biaxial non-crimp fabric including representative stitch pattern," *Composite Structures*, vol. 339, p. 118 126, 2024, ISSN: 0263-8223. DOI: https://doi.org/10.1016/j.compstruct.2024.118126. [Online]. Available: https://www.sciencedirect.com/science/article/pii/S026382232400254X.

[11] P. Quenzel *et al.*, "Material characterisation of biaxial glass-fibre non-crimp fabrics as a function of ply orientation, stitch pattern, stitch length and stitch tension," *Journal of Composite Materials*, vol. 56, no. 26, pp. 3971–3991, 2022. DOI: 10.1177/00219983221127005. eprint: https://doi.org/10.1177/00219983221127005. [Online]. Available: https://doi.org/10.1177/00219983221127005.

[12] F. J. Schirmaier, K. A. Weidenmann, L. Kärger, and F. Henning, "Characterisation of the draping behaviour of unidirectional non-crimp fabrics (UD-NCF)," *Composites Part A: Applied Science and Manufacturing*, vol. 80, pp. 28–38, Jan. 2016, ISSN: 1359-835X. DOI: 10.1016/J.COMPOSITESA.2015.10.004.

[13] J. Pourtier, B. Duchamp, M. Kowalski, X. Legrand, P. Wang, and D. Soulat, "Bias extension test on a bi-axial non-crimp fabric powdered with a non-reactive binder system," in *ESAFORM 2018 - 21st International Conference on Material Forming*, Palermo, Italy, 23. and 25. of April 2018.

[14] B. Schäfer, S. Haas, P. Boisse, and L. Kärger, "Investigation of the membrane behavior of ud-ncf in macroscopic forming simulations," *Key Engineering Materials*, vol. 926, pp. 1413–1422, 2022.

[15] G. Estrada, C. Vieux-Pernon, and S. G. Advani, "Experimental characterization of the influence of tackifier material on preform permeability," *Journal of Composite Materials*, vol. 36, no. 19, pp. 2297–2310, 2002. DOI: 10.1177/0021998302036019542. eprint: https://doi.org/10.1177/0021998302036019542. [Online]. Available: https://doi.org/10.1177/0021998302036019542.

[16] J. C. Brody and J. W. Gillespie, "The effects of a thermoplastic polyester preform binder on vinyl ester resin," *Journal of Thermoplastic Composite Materials*, vol. 18, no. 3, pp. 157–179, 2005. DOI: 10.1177/0892705705043535. eprint: https://doi.org/10.1177/0892705705043535. [Online]. Available: https://doi.org/10.1177/0892705705043535.

[17] H. M. Yoo, J. W. Lee, J. S. Kim, and M. K. Um, "Influence of non-reactive epoxy binder on the permeability and friction coefficient of twill-woven carbon fabric in the liquid composite molding process," *Applied Sciences*, vol. 10, no. 20, p. 7039, 2020, ISSN: 2076-3417. DOI: 10.3390/app10207039. [Online]. Available: https://www.mdpi.com/2076-3417/10/20/7039.

[18] O. Rimmel, D. Becker, and P. Mitschang, "Maximizing the out-of-plane-permeability of preforms manufactured by dry fiber placement," *Advanced Manufacturing: Polymer & Composites Science*, vol. 2, no. 3-4, pp. 93–102, 2016.

[19] T. Grundmann, "Automatisiertes preforming für schalenförmige komplexe faserverbundbauteile. aachen, rwth aachen, fakultät maschinenwesen," Ph.D. dissertation, RWTH Aachen, 2009.

[20] L. Moser, S. Heide, I. Swentek, U. Schmidt, and M. Seiz, "Thermoset technologies for cost efficient production of lightweight composites," in *Technologies for economic and functional lightweight design: Conference proceedings 2020*, Springer, 2021, pp. 35–41.

[21] P. Ermanni, C. Di Fratta, and F. Trochu, "Wiley encyclopedia of composites," in John Wiley and Sons, 2012, ch. Molding: Liquid Composite Molding (LCM), pp. 1–10. [Online]. Available: https://doi.org/10.1002/9781118097298.weoc153.

[22] J. Viisainen, A. Hosseini, and M. Sutcliffe, "Experimental investigation, using 3d digital image correlation, into the effect of component geometry on the wrinkling behaviour and the wrinkling mechanisms of a biaxial ncf during preforming," *Composites Part A: Applied Science and Manufacturing*, vol. 142, p. 106 248, 2021, ISSN: 1359-835X. DOI: https://doi.org/10.1016/j.compositesa.2020.106248. [Online]. Available: https://www.sciencedirect.com/science/article/pii/S1359835X20304838.

[23] S. Bickerton, Q. Govignon, and P. Kelly, "7 - resin infusion/liquid composite moulding (lcm) of advanced fibre-reinforced polymer (frp)," in *Advanced Fibre-Reinforced Polymer (FRP) Composites for Structural Applications*, ser. Woodhead Publishing Series in Civil and Structural Engineering, J. Bai, Ed., Woodhead Publishing, 2013, pp. 155–186, ISBN: 978-0-85709-418-6. DOI: https://doi.org/10.1533/

9780857098641.2.155. [Online]. Available: https://www.sciencedirect.com/science/article/pii/B9780857094186500077.

[24] P. Boisse, "Wiley encyclopedia of composites," in John Wiley and Sons, 2012, ch. Composite fiber reinforcement forming, pp. 1–16. [Online]. Available: https://doi.org/10.1002/9781118097298.weoc037.

[25] T. M. Kruckenberg and R. Paton, Eds., *Resin Transfer Moulding for Aerospace Structures*. Springer Netherlands, 1998, ISBN: 978-94-010-5906-0. DOI: 10.1007/978-94-011-4437-7. [Online]. Available: http://link.springer.com/10.1007/978-94-011-4437-7.

[26] P. Beardmore and C. Johnson, "The potential for composites in structural automotive applications," *Composites Science and Technology*, vol. 26, no. 4, pp. 251–281, 1986, ISSN: 0266-3538. DOI: https://doi.org/10.1016/0266-3538(86)90002-3. [Online]. Available: https://www.sciencedirect.com/science/article/pii/0266353886900023.

[27] K. Potter, "Rtm mould tool design," in *Resin Transfer Moulding*. Springer Netherlands, 1997, pp. 74–145, ISBN: 9789401064972. DOI: 10.1007/978-94-009-0021-9_4. [Online]. Available: http://link.springer.com/10.1007/978-94-009-0021-9_4.

[28] N. Razali, M. R. Mansor, G. Omar, S. A. F. S. Kamarulzaman, M. H. Zin, and N. Razali, "Chapter 15 - out-of-autoclave as a sustainable composites manufacturing process for aerospace applications," in *Design for Sustainability*, S. Sapuan and M. R. Mansor, Eds., Elsevier, 2021, pp. 395–413, ISBN: 978-0-12-819482-9. DOI: https://doi.org/10.1016/B978-0-12-819482-9.00011-3. [Online]. Available: https://www.sciencedirect.com/science/article/pii/B9780128194829000113.

[29] P. Rosenberg, R. Chaudhari, M. Karcher, F. Henning, and P. Elsner, "Investigating cavity pressure behavior in high-pressure rtm process variants," in *29th International Conference of the Polymer Processing Society*, Nuremberg, Germany, 15-19 July 2013.

[30] J. Fels, G. Meirson, V. Ugresic, P. Dugsin, F. Henning, and A. Hrymak, "Mechanical property difference between composites produced using vacuum-assisted liquid compression molding and high-pressure injection resin transfer molding," in *Proceedings ACCE2017-17th Annual Automotive Composites Conference and Exhibition, Michigan*, Jun. 2017.

[31] H. Yang, C.-C. Hsu, and C.-H. Hsu, "Three dimensional numerical simulations for wet-rtm process," in *35th Polymer Processing Society*, Cesme-Izmir, Turkey, 2019.

[32] C. Poppe, "Process simulation of wet compression moulding for continuous fibre-reinforced polymers," Ph.D. dissertation, Karlsruhe Institute of Technology, 2021.

[33] M. Karcher, M. Gerlitziki, B. Thoma, and F. Henning, "Evaluation of a new "inlineprepreg" process approch to establishe process for the manufacturing of structural components out of carbon fibre reinforced plastic," *Novi, MI*, 2015.

[34] S. Mannino, A. Latteri, G. Saccullo, R. Banatao, S. Pastine, and G. Cicala, "High pressure resin transfer moulding of epoxy resins from renewable sources," *Handbook of Composites from Renewable Materials*, p. 475, 2017.

[35] M. Ghazimoradi, E. A. Trejo, C. Butcher, and J. Montesano, "Characterizing the macroscopic response and local deformation mechanisms of a unidirectional non-crimp fabric," *Composites Part A: Applied Science and Manufacturing*, vol. 156, p. 106 857, May 2022, ISSN: 1359-835X. DOI: 10.1016/J.COMPOSITESA.2022.106857.

[36] B. Schäfer, R. Zheng, N. Naouar, and L. Kärger, "Membrane behavior of uni-and bidirectional non-crimp fabrics in off-axis-tension tests," *International Journal of Material Forming*, vol. 16, no. 6, p. 68, 2023.

[37] M. Ghazimoradi and J. Montesano, "Macroscopic forming simulation for a unidirectional non-crimp fabric using an anisotropic hyperelastic material model," *Applied Composite Materials*, pp. 1–23, 2023.

[38] C. Poppe, D. Dörr, F. Henning, and L. Kärger, "Experimental and numerical investigation of the shear behaviour of infiltrated woven fabrics," *Composites Part A: Applied Science and Manufacturing*, vol. 114, pp. 327–337, Nov. 2018, ISSN: 1359-835X. DOI: 10.1016/J.COMPOSITESA.2018.08.018.

[39] S. Daghboudj and H. Satha, "Experimental approach for determining the shear rigidity modulus of commingled glass/propylene woven fabrics," Bordj El Bahri, Mar. 2013.

[40] L. Guan, K. Hao, S. Mei, H. Yang, S. Lu, and Y. Yang, "In-plane shear behaviors of unbalanced 3d interlock woven reinforcement in bias extension test: Experiments and finite element modeling," *Polymer Composites*, vol. 43, no. 1, pp. 574–583, 2022. DOI: https://doi.org/10.1002/pc.26400. eprint: https://4spepublications.onlinelibrary.wiley.com/doi/pdf/10.1002/pc.26400. [Online]. Available: https://4spepublications.onlinelibrary.wiley.com/doi/abs/10.1002/pc.26400.

[41] R. B. Büyükbayraktar, "An investigation on shear properties of woven fabrics by bias-extension test," *The Journal of The Textile Institute*, vol. 112, no. 3, pp. 505–513, 2021. DOI: 10.1080/00405000.2020.1770011. eprint: https://doi.org/10.1080/00405000.2020.1770011. [Online]. Available: https://doi.org/10.1080/00405000.2020.1770011.

[42] X. Zhao, G. Liu, M. Gong, J. Song, Y. Zhao, and S. Du, "Effect of tackification on in-plane shear behaviours of biaxial woven fabrics in bias extension test: Experiments and finite element modeling," *Composites Science and Technology*, vol. 159, pp. 33–41, 2018, ISSN: 0266-3538. DOI: https://doi.org/10.1016/j.compscitech.2018.02.016. [Online]. Available: https://www.sciencedirect.com/science/article/pii/S0266353817332578.

[43] M. Moezzi, A. Haji-Badali, and F. Barez, "Analysis of the wrinkle geometry of the woven fabrics during uniaxial bias extension test using ricker wavelet algorithm," *Composites Part A: Applied Science and Manufacturing*, vol. 141, p. 106 230, 2021.

[44] P. Harrison, E. Taylor, and J. Alsayednoor, "Improving the accuracy of the uniaxial bias extension test on engineering fabrics using a simple wrinkle mitigation technique," *Composites Part A: Applied Science and Manufacturing*, vol. 108, pp. 53–61, 2018, ISSN: 1359-835X. DOI: https://doi.org/10.1016/j.compositesa.2018.02.025. [Online]. Available: https://www.sciencedirect.com/science/article/pii/S1359835X18300666.

[45] E. A. Trejo, M. Ghazimoradi, C. Butcher, and J. Montesano, "Assessing strain fields in unbalanced unidirectional non-crimp fabrics," *Composites Part A: Applied Science and Manufacturing*, vol. 130, Mar. 2020, ISSN: 1359835X. DOI: 10.1016/J.COMPOSITESA.2019.105758.

[46] F. J. Schirmaier, D. Dörr, F. Henning, and L. Kärger, "A macroscopic approach to simulate the forming behaviour of stitched unidirectional non-crimp fabrics (udncf)," *Composites Part A: Applied Science and Manufacturing*, vol. 102, pp. 322–335, 2017.

[47] P. Harrison, M. J. Clifford, and A. Long, "Shear characterisation of viscous woven textile composites: A comparison between picture frame and bias extension experiments," *Composites science and technology*, vol. 64, pp. 1453–1465, 2004.

[48] J. Pourtier, B. Duchamp, M. Kowalski, P. Wang, X. Legrand, and D. Soulat, "Two-way approach for deformation analysis of non-crimp fabrics in uniaxial bias extension tests based on pure and simple shear assumption," *International Journal of Material Forming*, vol. 12, pp. 995–1008, 2019.

[49] D. Zomer, S. Simaafrookhteh, K. Vanclooster, A. Dorigato, and J. Ivens, "Forming-behavior characterization of cross-ply carbon fiber/pa6 laminates using the bias-extension test," *Composites Part A: Applied Science and Manufacturing*, vol. 168, p. 107 436, 2023.

[50] C. Krogh, J. A. Kepler, and J. Jakobsen, "Pure and simple: Investigating the in-plane shear kinematics of a quasi-unidirectional glass fiber non-crimp fabric using the bias-extension test," *International Journal of Material Forming*, vol. 14, pp. 1483–1495, 2021.

[51] F. Härtel, P. Böhler, and P. Middendorf, "An integral mesoscopic material characterization approach," *Key Engineering Materials*, vol. 611, pp. 280–291, 2014.

[52] E. De Bilbao, D. Soulat, G. Hivet, and A. Gasser, "Experimental Study of Bending Behaviour of Reinforcements," *Experimental Mechanics*, vol. 50, pp. 333–351, 2010. DOI: 10.1007/s11340-009-9234-9.

[53] T. Martin, D. Bhattacharyya, and I. Collins, "Bending of fibre-reinforced thermoplastic sheets," *Composites Manufacturing*, vol. 6, no. 3, pp. 177–187, 1995, 3rd International Conference on Flow Processes in Composite Materials 94, ISSN: 0956-7143. DOI: https://doi.org/10.1016/0956-7143(95)95009-N. [Online]. Available: https://www.sciencedirect.com/science/article/pii/095671439595009N.

[54] P. Boisse, N. Hamila, E. Vidal-sallé, and F. Dumont, "Simulation of wrinkling during textile composite reinforcement forming . Influence of tensile , in-plane shear and bending stiffnesses," *Composites Science and Technology*, vol. 71, no. 5, pp. 683–692, 2011, ISSN: 0266-3538. DOI: 10.1016/j.compscitech.2011.01.011. [Online]. Available: http://dx.doi.org/10.1016/j.compscitech.2011.01.011.

[55] P. Boisse, J. Colmars, N. Hamila, N. Naouar, and Q. Steer, "Bending and wrinkling of composite fiber preforms and prepregs. A review and new developments in the draping simulations," *Composites Part B: Engineering*, vol. 141, pp. 234–249, May 2018, ISSN: 1359-8368. DOI: 10.1016/J.COMPOSITESB.2017.12.061.

[56] W. R. Yu, M. Zampaloni, F. Pourboghrat, K. Chung, and T. J. Kang, "Analysis of flexible bending behavior of woven preform using non-orthogonal constitutive equation," *Composites Part A: Applied Science and Manufacturing*, vol. 36, no. 6, pp. 839–850, 2005, ISSN: 1359835X. DOI: 10.1016/j.compositesa.2004.10.026.

[57] U. Sachs and R. Akkerman, "Viscoelastic bending model for continuous fiber-reinforced thermoplastic composites in melt," *Composites Part A: Applied Science and Manufacturing*, vol. 100, pp. 333–341, Sep. 2017, ISSN: 1359835X. DOI: 10.1016/J.COMPOSITESA.2017.05.032.

[58] R. Sourki, B. Khatir, S. S. Najar, R. Vaziri, and A. S. Milani, "Characterization of the dissipative large deformation bending response of dry fabric composites as occurs during forming," *Composite Structures*, vol. 310, p. 116 728, 2023.

[59] T. Senner, S. Kreissl, M. Merklein, M. Meinhardt, and A. Lipp, "Bending of unidirectional non-crimp-fabrics: experimental characterization, constitutive modeling and application in finite element simulation," *Production Engineering*, vol. 9, no. 1, pp. 1–10, Feb. 2015, ISSN: 18637353. DOI: 10.1007/S11740-014-0568-5/FIGURES/13. [Online]. Available: https://link.springer.com/article/10.1007/s11740-014-0568-5.

[60] T. Grieser, D. Becker, and P. Mitschang, "Investigation of the bending behaviour of multi-ply dry carbon fibre non-crimped fabrics," *The Journal of The Textile Institute*, vol. 109, no. 4, pp. 455–465, 2018.

[61] V. Eckers, S. Janetzko, and T. Gries, "Drape study on textiles for concrete applications," *AUTEX Research Journal*, vol. 12, no. 2, pp. 50–54, 2012.

[62] K. Vallons, "The behaviour of carbon fibre-epoxy ncf composites under various mechanical loading conditions," *Unpublished doctoral dissertation). Belgium: University Leuven*, 2009.

[63] B. Liang, N. Hamila, M. Peillon, and P. Boisse, "Analysis of thermoplastic prepreg bending stiffness during manufacturing and of its influence on wrinkling simulations," *Composites Part A: Applied Science and Manufacturing*, vol. 67, pp. 111–122, 2014, ISSN: 1359835X. DOI: 10.1016/j.compositesa.2014.08.020. [Online]. Available: http://dx.doi.org/10.1016/j.compositesa.2014.08.020.

[64] C. Krogh, P. H. Broberg, J. Kepler, and J. Jakobsen, "Comprehending the bending: A comparison of different test setups for measuring the out-of-plane flexural rigidity of a ud fabric," *Key Engineering Materials*, vol. 926, pp. 1257–1267, Jul. 2022, ISSN: 1662-9795. DOI: 10.4028/p-r883x4. [Online]. Available: https://www.scientific.net/KEM.926.1257.

[65] C. Poppe, T. Rosenkranz, D. Dörr, and L. Kärger, "Comparative experimental and numerical analysis of bending behaviour of dry and low viscous infiltrated woven fabrics," *Composites Part A: Applied Science and Manufacturing*, vol. 124,

p. 105 466, Sep. 2019, ISSN: 1359-835X. DOI: 10.1016/J.COMPOSITESA.2019.05.034.

[66] F. T. T. I. Peirce, "The 'handle' of cloth as a measurable quantity," *Journal of the Textile Institute Transactions*, 1930. DOI: 10.1080/19447023008661529. [Online]. Available: https://www.tandfonline.com/action/journalInformation?journalCode=jtit20.

[67] B. Liang, P. Chaudet, and P. Boisse, "Curvature determination in the bending test of continuous fibre reinforcements," *Strain*, vol. 53, no. 1, pp. 1–12, 2017, ISSN: 14751305. DOI: 10.1111/str.12213.

[68] P. H. Broberg *et al.*, "One-click bending stiffness: Robust and reliable automatic calculation of moment–curvature relation in a cantilever bending test," *Composites Part B: Engineering*, vol. 260, p. 110 763, 2023.

[69] C. Poppe, D. Dörr, F. Kraus, and L. Kärger, "Experimental and numerical investigation of the contact behavior during fe forming simulation of continuously reinforced composites in wet compression molding," in *ESAFORM 2019 - 22nd International Conference on Material Forming*, Vitoria-Gasteiz, Spain, Aug. 2019.

[70] P. H. Broberg *et al.*, "That's how the preform crumples: Wrinkle creation during forming of thick binder-stabilised stacks of non-crimp fabrics," *Composites Part B: Engineering*, vol. 273, p. 111 269, 2024, ISSN: 1359-8368. DOI: https://doi.org/10.1016/j.compositesb.2024.111269. [Online]. Available: https://www.sciencedirect.com/science/article/pii/S1359836824000805.

[71] P. H. Broberg, E. Lindgaard, A. J. Thompson, J. P.-H. Belnoue, S. R. Hallett, and B. L. Bak, "An accurate forming model for capturing the nonlinear material behaviour of multilayered binder-stabilised fabrics and predicting fibre wrinkling," *Composites Part B: Engineering*, vol. 274, p. 111 268, 2024, ISSN: 1359-8368. DOI: https://doi.org/10.1016/j.compositesb.2024.111268. [Online]. Available: https://www.sciencedirect.com/science/article/pii/S1359836824000799.

[72] S. Korkiakoski, M. Haavisto, M. R. Barouei, and O. Saarela, "Experimental compaction characterization of unidirectional stitched noncrimp fabrics in the vacuum infusion process," *Polymer Composites*, vol. 37, pp. 2692–2704, 9 Sep. 2016, ISSN: 02728397. DOI: 10.1002/pc.23464. [Online]. Available: https://onlinelibrary.wiley.com/doi/10.1002/pc.23464.

[73] B. Schäfer, R. Zheng, P. Boisse, and L. Kärger, "Investigation of the compaction behavior of uni-and bidirectional non-crimp fabrics," in *ESAFORM 2023 - 26th International Conference on Material Forming*, Kraków, Poland, Apr. 2023.

[74] S. Bickerton, M. J. Buntain, and A. A. Somashekar, "The viscoelastic compression behavior of liquid composite molding preforms," *Composites Part A: Applied Science and Manufacturing*, vol. 34, no. 5, pp. 431–444, 2003, ISSN: 1359835X. DOI: 10.1016/S1359-835X(03)00088-5.

[75] A. Yong *et al.*, "Experimental characterisation of textile compaction response: A benchmark exercise," *Composites Part A: Applied Science and Manufacturing*, vol. 142, p. 106 243, Mar. 2021, ISSN: 1359835X. DOI: 10.1016/j.compositesa.2020.106243. [Online]. Available: https://linkinghub.elsevier.com/retrieve/pii/S1359835X20304784.

[76] V. Werlen, C. Rytka, and V. Michaud, "A numerical approach to characterize the viscoelastic behaviour of fibre beds and to evaluate the influence of strain deviations on viscoelastic parameter extraction," *Composites Part A: Applied Science and Manufacturing*, vol. 143, p. 106 315, 2021.

[77] L. Li, Y. Zhao, J. Yang, J. Zhang, and Y. Duan, "An experimental investigation of compaction behavior of carbon non-crimp fabrics for liquid composite molding," *Journal of Materials Science*, vol. 50, pp. 2960–2972, 7 Apr. 2015, ISSN: 15734803. DOI: 10.1007/s10853-015-8860-0.

[78] J. Yang, J. Xiao, J. Zeng, D. Jiang, and C. Peng, "Compaction behavior and part thickness variation in vacuum infusion molding process," *Applied Composite Materials*, vol. 19, pp. 443–458, 3-4 Jun. 2012, ISSN: 0929189X. DOI: 10.1007/s10443-011-9217-8.

[79] B. Chen, E. J. Lang, and T.-W. Chou, "Experimental and theoretical studies of fabric compaction behavior in resin transfer molding," *Materials Science and Engineering: A*, vol. 317, no. 1, pp. 188–196, 2001, ISSN: 0921-5093. DOI: https://doi.org/10.1016/S0921-5093(01)01175-3. [Online]. Available: https://www.sciencedirect.com/science/article/pii/S0921509301011753.

[80] D. Droste *et al.*, "Investigation of the compaction behaviour of a quasi-unidirectional non-crimp fabric during the vacuum infusion process," *Journal of Composite Materials*, vol. 56, no. 16, pp. 2509–2524, 2022.

[81] K. Wei, D. Liang, M. Mei, D. Wang, X. Yang, and Z. Qu, "Preforming behaviors of carbon fiber fabrics with different contents of binder and under various process parameters," *Composites Part B: Engineering*, vol. 166, pp. 221–232, 2019, ISSN: 1359-8368. DOI: https://doi.org/10.1016/j.compositesb.2018.11.143. [Online]. Available: https://www.sciencedirect.com/science/article/pii/S1359836818326568.

[82] K. Wei, D. Liang, M. Mei, X. Yang, and L. Chen, "A viscoelastic model of compression and relaxation behaviors in preforming process for carbon fiber fabrics with binder," *Composites Part B: Engineering*, vol. 158, pp. 1–9, 2019, ISSN: 1359-8368. DOI: https://doi.org/10.1016/j.compositesb.2018.09.038. [Online]. Available: https://www.sciencedirect.com/science/article/pii/S1359836818328038.

[83] C. T. Poppe, C. Krauß, F. Albrecht, and L. Kärger, "A 3D process simulation model for wet compression moulding," *Composites Part A: Applied Science and Manufacturing*, vol. 145, p. 106 379, Jun. 2021, ISSN: 1359-835X. DOI: 10.1016/J.COMPOSITESA.2021.106379.

[84] J. Mitsch, B. Schäfer, and L. Kärger, "Rate-dependent 3d forming simulation of thermoplastic composite materials using visco-hyperelastic material modeling and 3d hexahedral solid-shell elements," *Composites Part A: Applied Science and Manufacturing*, vol. 200, p. 109 306, 2026, ISSN: 1359-835X. DOI: https://doi.org/10.1016/j.compositesa.2025.109306. [Online]. Available: https://www.sciencedirect.com/science/article/pii/S1359835X25006001.

[85] M. Danzi, C. Schneeberger, and P. Ermanni, "A model for the time-dependent compaction response of woven fiber textiles," *Composites Part A: Applied Science and Manufacturing*, vol. 105, pp. 180–188, Feb. 2018, ISSN: 1359835X. DOI: 10.1016/j.compositesa.2017.11.002.

[86] K. Ding and Y. Xiao, "Adaptability of burgers rheological model and its improved model to the creep properties of glue laminated bamboo," *Mechanika*, vol. 30, pp. 214–220, 3 2024, ISSN: 20296983. DOI: 10.5755/j02.mech.35600.

[87] M. Moutee, G. Student, M. Fafard, Y. Fortin, and A. Laghdir, "Modeling the creep behavior of wood cantilever loaded at free end during drying," *Wood and Fiber Science*, vol. 37, pp. 521–534, 3 2005.

[88] S. Jelić and D. Zorica, "Fractionalization of anti-zener and zener models via rheological analogy," *Acta Mechanica*, vol. 234, pp. 313–354, 2 Feb. 2023, ISSN: 16196937. DOI: 10.1007/s00707-022-03363-8.

[89] J. Echaabi, M. B. Nziengui, and M. Hattabi, "Compressibility and relaxation models for fibrous reinforcements in liquid composites moulding," *International Journal of Material Forming*, vol. 1, pp. 851–854, S1 Apr. 2008, ISSN: 1960-6206. DOI: 10.1007/s12289-008-0269-8. [Online]. Available: http://link.springer.com/10.1007/s12289-008-0269-8.

[90] T. C. D. C. Haveroth, "On the use of fractional derivatives for modeling nonlinear viscoelasticity," M.S. thesis, Universidade do Estado de Santa Catarina, 2015.

[91] T. da Costa-Haveroth *et al.*, "Aspects on viscoelasticity modeling of hdpe using fractional derivatives: Interpolation procedures and efficient numerical scheme," *Mechanics of Advanced Materials and Structures*, vol. 29, pp. 4343–4358, 25 Oct. 2022, ISSN: 1537-6494. DOI: 10.1080/15376494.2021.1928345. [Online]. Available: https://www.tandfonline.com/doi/full/10.1080/15376494.2021.1928345.

[92] J. Padovan, "Computational algorithms for fe formulations involving fractional operators," *Computational Mechanics*, vol. 2, pp. 271–287, 4 1987, ISSN: 0178-7675. DOI: 10.1007/BF00296422. [Online]. Available: http://link.springer.com/10.1007/BF00296422.

[93] M. Ferrante, "Viscoelastic models for the simulation of transients in polymeric pipes," *Journal of Hydraulic Research*, vol. 55, pp. 599–612, 5 2017. DOI: 10.1080/00221686.2017.1354935. [Online]. Available: https://doi.org/10.1080/00221686.2017.1354935.

[94] A. Kühl, "Uma formulação viscoelastoplástica não linear aplicada ao polietileno de alta densidade (pead)," M.S. thesis, Universidade do Estado de Santa Catarina, 2014.

[95] Q. Bai, "Analysis of particle swarm optimization algorithm," *Computer and Information Science*, vol. 3, 1 Jan. 2010, ISSN: 1913-8997. DOI: 10.5539/cis.v3n1p180. [Online]. Available: http://www.ccsenet.org/journal/index.php/cis/article/view/5131.

[96] S. F. M. de Almeida and Z. d. S. N. Neto, "Effect of void content on the strength of composite laminates," *Composite structures*, vol. 28, no. 2, pp. 139–148, 1994.

[97] T. Chang, L. Zhan, W. Tan, and S. Li, "Void content and interfacial properties of composite laminates under different autoclave cure pressure," *Composite Interfaces*, vol. 24, no. 5, pp. 529–540, 2017.

[98] S. Neunkirchen, M. Bender, and R. Schledjewski, "Effect of binder activation on in-plane capillary flow in multilayer stacks of carbon fiber fabrics," *Applied Composite Materials*, vol. 31, pp. 709–719, 2 Apr. 2024, ISSN: 0929-189X. DOI: 10.1007/s10443-023-10198-6. [Online]. Available: https://link.springer.com/10.1007/s10443-023-10198-6.

[99] M. Tanoğlu and A. T. Seyhan, "Investigating the effects of a polyester preforming binder on the mechanical and ballistic performance of e-glass fiber reinforced polyester composites," *International Journal of Adhesion and Adhesives*, vol. 23, pp. 1–8, 1 Jan. 2003, ISSN: 01437496. DOI: 10.1016/S0143-7496(02)00061-1. [Online]. Available: https://linkinghub.elsevier.com/retrieve/pii/S0143749602000611.

[100] I. R. Chowdhury, N. H. Nash, A. Portela, N. P. O'Dowd, and A. J. Comer, "Analysis of failure modes for a non-crimp basalt fiber reinforced epoxy composite under flexural and interlaminar shear loading," *Composite Structures*, vol. 245, Aug. 2020, ISSN: 02638223. DOI: 10.1016/j.compstruct.2020.112317.

[101] N. R. Thompson, "Void formation during liquid composite molding under varied pressure with mechanical properties validation," M.S. thesis, Brigham Young University, 2024.

[102] M. Mehdikhani, L. Gorbatikh, I. Verpoest, and S. V. Lomov, "Voids in fiber-reinforced polymer composites: A review on their formation, characteristics, and effects on mechanical performance," *Journal of Composite Materials*, vol. 53, no. 12, pp. 1579–1669, 2019.

[103] S. M. Sisodia, S. Garcea, A. George, D. Fullwood, S. Spearing, and E. Gamstedt, "High-resolution computed tomography in resin infused woven carbon fibre composites with voids," *Composites Science and Technology*, vol. 131, pp. 12–21, 2016.

[104] B. Muthuvel, D. Bhattacharyya, and S. Bickerton, "A parametric flow visualisation study on the impregnation and consolidation stages of the wet compression moulding process. part i: Process parameters," *Composites Part A: Applied Science and Manufacturing*, vol. 150, p. 106 634, Nov. 2021, ISSN: 1359-835X. DOI: 10.1016/J.COMPOSITESA.2021.106634. [Online]. Available: https://www.sciencedirect.com/science/article/pii/S1359835X21003523?via%3Dihub.

[105] S. R. Ghiorse, "Effect of void content on the mechanical properties of carbon/epoxy laminates," *SAMPE quarterly*, vol. 24, pp. 54–59, 2 1993, ISSN: 0036-0821.

[106] "Effects of void characteristics on the mechanical properties of carbon fiber reinforced polyetheretherketone composites: Micromechanical modeling and analysis," *Polymers*, vol. 17, p. 1721, 13 Jun. 2025, ISSN: 2073-4360. DOI: 10.3390/polym17131721. [Online]. Available: https://www.mdpi.com/2073-4360/17/13/1721.

[107] L. Luo *et al.*, "Identification of voids and interlaminar shear strengths of polymer-matrix composites by optical microscopy experiment and deep learning methodology," *Polymers for advanced technologies*, vol. 32, no. 4, pp. 1853–1865, 2021.

[108] C. Kaynak, E. Akgul, and N. A. Isitman, "Effects of rtm mold temperature and vacuum on the mechanical properties of epoxy/glass fiber composite plates," *Journal of Composite Materials*, vol. 42, pp. 1505–1521, 15 Aug. 2008, ISSN: 00219983. DOI: 10.1177/0021998308092204.

[109] S. Ayatollahi, "Effect of process parameters on the mechanical properties of carbon fiber epoxy composites by wet compression molding," M.S. thesis, The University of Western Ontario, 2023. [Online]. Available: https://ir.lib.uwo.ca/etdhttps://ir.lib.uwo.ca/etd/9144.

[110] J. Sears, "Predictive modelling of the effects of processing parameters on the mechanical properties of fiber reinforced composites using liquid composite molding," Ph.D. dissertation, University of Windsor, Sep. 2024.

[111] E. Duernberger, C. MacLeod, and D. Lines, "Fibre volume fraction screening of pultruded carbon fibre reinforced polymer panels based on analysis of anisotropic ultrasonic sound velocity," *Composites Part B: Engineering*, vol. 254, p. 110 577, Apr. 2023, ISSN: 1359-8368. DOI: 10.1016/J.COMPOSITESB.2023.110577. [Online]. Available: https://www.sciencedirect.com/science/article/pii/S135983682300080X.

[112] Y. Kim, C. Choi, S. K. S. Kumar, C.-G. Kim, S.-W. Kim, and J. H. Lim, "Thermogravimetric analysis method to determine the fiber volume fraction for pan-based cfrp considering oxidation of carbon fiber and matrix," *Composites Part A: Applied Science and Manufacturing*, vol. 102, pp. 40–47, Nov. 2017, ISSN: 1359835X. DOI: 10.1016/j.compositesa.2017.07.024. [Online]. Available: https://linkinghub.elsevier.com/retrieve/pii/S1359835X17302828.

[113] C. N. Morales, G. Claure, J. Álvarez, and A. Nanni, "Evaluation of fiber content in gfrp bars using digital image processing," *Composites Part B: Engineering*, vol. 200, p. 108 307, 2020.

[114] "Standard test methods for constituent content of composite materials," ASTM International, West Conshohocken (PA), Tech. Rep., 2022. DOI: 10.1520/D3171-22.

[115] L. Conklin, "Tutorial for collecting and processing images of composite structures to determine the fiber volume fraction," Tech. Rep., 2017.

[116] R. E. G. Jr., K. J. Kozaczek, and C. O. Ruud, Eds., *Nondestructive Characterization of Materials VI*. Springer US, 1994, vol. Voume 1. DOI: 10.1007/978-1-4615-2574-5.

[117] H. Yang and J. S. Colton, "Quantitative image processing analysis of composite materials," *Polymer composites*, vol. 15, no. 1, pp. 46–54, 1994.

[118] L. P. Mikkelsen, S. Fæster, S. Goutianos, and B. F. Sørensen, "Scanning electron microscopy datasets for local fibre volume fraction determination in non-crimp glass-fibre reinforced composites," *Data in Brief*, vol. 35, p. 106 868, Apr. 2021, ISSN: 23523409. DOI: 10.1016/j.dib.2021.106868. [Online]. Available: https://linkinghub.elsevier.com/retrieve/pii/S2352340921001529.

[119] L. A. Carlsson, D. F. Adams, and R. B. Pipes, *Experimental characterization of advanced composite materials*. CRC press, 2014.

[120] J. E. Little, X. Yuan, and M. I. Jones, "Characterisation of voids in fibre reinforced composite materials," *Ndt & E International*, vol. 46, pp. 122–127, 2012.

[121] M. T. Cann, D. O. Adams, and C. L. Schneider, "Characterization of fiber volume fraction gradients in composite laminates," *Journal of Composite Materials*, vol. 42, pp. 447–466, 5 Mar. 2008, ISSN: 00219983. DOI: 10.1177/0021998307086206.

[122] G. W. Melenka and A. Gholami, "Fiber identification of braided composites using micro-computed tomography," *Composites Communications*, vol. 27, p. 100 813, Oct. 2021, ISSN: 2452-2139. DOI: 10.1016/J.COCO.2021.100813. [Online]. Available: https://www.sciencedirect.com/science/article/pii/S2452213921001893.

[123] X. W. Yu, H. Wang, and Z. W. Wang, "Analysis of yarn fiber volume fraction in textile composites using scanning electron microscopy and x-ray micro-computed tomography," *Journal of Reinforced Plastics and Composites*, vol. 38, pp. 199–210, 5 Mar. 2019, ISSN: 15307964. DOI: 10.1177/0731684418811943.

[124] P. Mitschang and K. Hildebrandt, "Polymer and composite moulding technologies for automotive applications," *Advanced Materials in Automotive Engineering*, pp. 210–229, 2012. DOI: 10.1533/9780857095466.210.

[125] F. Mariano, "Development of an LCM process for rapid curing CFRP parts," M.S. thesis, Politecnico di Torino, Torino, Italy, 2019.

[126] L. P. Mikkelsen, S. Fæster, and V. A. Dahl, "Dataset for scanning electron microscopy based local fiber volume fraction analysis of non-crimp fabric glass fiber reinforced composites," *Data in Brief*, vol. 48, p. 109 058, Jun. 2023, ISSN: 23523409. DOI: 10.1016/j.dib.2023.109058. [Online]. Available: https://linkinghub.elsevier.com/retrieve/pii/S2352340923001762.

[127] Y. Zeng and J. Montesano, "Multiscale fe modelling and ann to predict mechanical properties of non-crimp fabric composites with manufacturing-induced defects," in *38th American Society for Composites (ASC) Technical Conference*, Sep. 2023.

[128] A. Cherniaev, Y. Zeng, D. Cronin, and J. Montesano, "Quasi-static and dynamic characterization of unidirectional non-crimp carbon fiber fabric composites processed by hp-rtm," *Polymer Testing*, vol. 76, pp. 365–375, Jul. 2019, ISSN: 01429418. DOI: 10.1016/j.polymertesting.2019.03.036.

[129] Z. Xiao, F. Mo, D. Zeng, and C. Yang, "Experimental and numerical study of hat shaped cfrp structures under quasi-static axial crushing," *Composite structures*, vol. 249, p. 112 465, 2020.

[130] A. Brighton, M. Forrest, M. Starbuck, D. Erdman, and B. Fox, "Strain rate effects on the energy absorption of rapidly manufactured composite tubes," *Journal of Composite Materials*, vol. 43, no. 20, pp. 2183–2200, 2009.

[131] Y. Peng, M. Li, X. Yang, J. Li, and C. Xiong, "Quasi-static crush response of lightweight sandwich composite tubes fabricated via newly designed internal thermal expansion technique," *Composites Science and Technology*, vol. 251, May 2024, ISSN: 02663538. DOI: 10.1016/j.compscitech.2024.110574.

[132] A. Mamalis, M. Robinson, D. Manolakos, G. Demosthenous, M. Ioannidis, and J. Carruthers, "Review Crashworthy capability of composite material structures," *Composite Structures*, vol. 37, no. 2, pp. 109–134, 1997, ISSN: 0263-8223. DOI: https://doi.org/10.1016/S0263-8223(97)80005-0. [Online]. Available: https://www.sciencedirect.com/science/article/pii/S0263822397800050.

[133] X. Liu *et al.*, "Experimental investigation of energy absorption behaviour of circular carbon/epoxy composite tubes under quasi-static and dynamic crush loading," *Composite Structures*, vol. 227, Nov. 2019, ISSN: 02638223. DOI: 10.1016/j.compstruct.2019.111266.

[134] M. Capretti *et al.*, "Crashworthiness of flax and hybrid composite tubes subjected to quasi-static axial crushing: Experimental and numerical results," *Composite Structures*, vol. 354, Jan. 2025, ISSN: 02638223. DOI: 10.1016/j.compstruct.2024.118785.

[135] C. Yang, Z. Chen, S. Yao, P. Xu, S. Li, and M. S. Alqahtani, "Quasi-static and low-velocity axial crushing of polyurethane foam-filled aluminium/CFRP composite tubes: An experimental study," *Composite Structures*, vol. 299, Nov. 2022, ISSN: 02638223. DOI: 10.1016/j.compstruct.2022.116083.

[136] P. Feraboli, B. Wade, F. Deleo, and M. Rassaian, "Crush energy absorption of composite channel section specimens," *Composites Part A: Applied Science and Manufacturing*, vol. 40, no. 8, pp. 1248–1256, Aug. 2009, ISSN: 1359835X. DOI: 10.1016/j.compositesa.2009.05.021.

[137] R. A. Eshkoor *et al.*, "Failure mechanism of woven natural silk/epoxy rectangular composite tubes under axial quasi-static crushing test using trigger mechanism," *International Journal of Impact Engineering*, vol. 64, pp. 53–61, 2014, ISSN: 0734743X. DOI: 10.1016/j.ijimpeng.2013.09.004.

[138] G. C. Jacob, J. F. Fellers, S. Simunovic, and J. M. Starbuck, "Energy absorption in polymer composites for automotive crashworthiness," *Journal of composite materials*, vol. 36, no. 7, pp. 813–850, 2002.

[139] M. Jimenez, A. Miravete, E. Larrode, and D. Revuelta, "Effect of trigger geometry on energy absorption in composite profiles," *Composite Structures*, vol. 48, no. 1-3, pp. 107–111, 2000.

[140] L. N. Chiu *et al.*, "Crush responses of composite cylinder under quasi-static and dynamic loading," *Composite Structures*, vol. 131, pp. 90–98, Nov. 2015, ISSN: 02638223. DOI: 10.1016/j.compstruct.2015.04.057.

[141] G. Sun, D. Chen, G. Zhu, and Q. Li, "Lightweight hybrid materials and structures for energy absorption: A state-of-the-art review and outlook," *Thin-Walled Structures*, vol. 172, p. 108 760, 2022, ISSN: 0263-8231. DOI: https://doi.org/10.1016/j.tws.2021.108760. [Online]. Available: https://www.sciencedirect.com/science/article/pii/S0263823121007564.

[142] S. Olhan, B. Antil, and B. K. Behera, "Low-velocity impact and quasi-static post-impact compression analysis of woven structural composites for automotive: Influence of fibre types and architectural structures," *Composite Structures*, vol. 352, Jan. 2025, ISSN: 02638223. DOI: 10.1016/j.compstruct.2024.118676.

[143] S. Palanivelu *et al.*, "Comparative study of the quasi-static energy absorption of small-scale composite tubes with different geometrical shapes for use in sacrificial cladding structures," *Polymer testing*, vol. 29, no. 3, pp. 381–396, 2010.

[144] S. Solaimurugan and R. Velmurugan, "Progressive crushing of stitched glass/polyester composite cylindrical shells," *Composites Science and Technology*, vol. 67, no. 3, pp. 422–437, 2007, ISSN: 0266-3538. DOI: https://doi.org/10.1016/j.compscitech.2006.09.002. [Online]. Available: https://www.sciencedirect.com/science/article/pii/S0266353806003381.

[145] V. A. O. Ajayi, "Experimental characterization and numerical modelling of the energy absorption capacity of ud-ncf carbon fibre/epoxy composite channels," M.S. thesis, University of Waterloo, 2025.

Chapter 3

Research Objectives and Scope

3.1 Research Objectives

The overarching goal of this research is to investigate the influence of stabilizing binder on the formability, microstructure, and mechanical performance of wet compression-molded UD-NCF composites. The fabric investigated in this study was a binder-stabilized UD-NCF, specifically PX35-UD300 (Zoltek, US) (see Figure 3.1). This UD-NCF consists of axially oriented, parallel tows, each containing 50K continuous PX35 carbon fibers with an areal weight of 333 $\frac{g}{m^2}$. The carbon fiber tows are stitched together with 76 dtex polyester yarn in a tricot pattern and are supported with low linear-density transversely oriented glass fiber yarns to enhance handleability. Lastly, a thermosetting (bisphenol-A-based epoxy) polymer powder binder with a density of 1.17-1.19 $\frac{g}{cm^3}$ is dispersed on the surface of the stitch tricot pattern. The areal weight of each constituent of the PX35-UD300 is listed in Table 3.1. The WCM parts were made using a three-part snap-cure resin system, Epikote 6150 (Westlake Epoxy, US). This system included a medium-viscosity snap-cure epoxy resin, a low-viscosity amine hardener, and an internal mold release agent.

Table 3.1: PX35-UD300 textile constituents. Values given in $\frac{g}{m^2}$.

Carbon fiber tow	Transverse supporting glass fiber yarns	Polyester stitching yarns	Thermosetting powder binder	Total
309	10	6	8	333

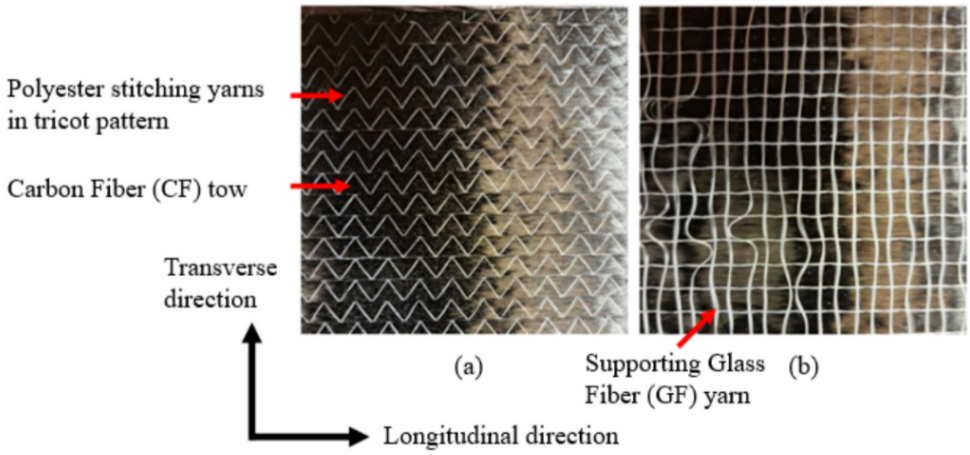


Figure 3.1: Binder stabilized carbon fiber UD-NCF, namely PX35-UD300, and its constituents: (a) tricot pattern stitching yarns and (b) supporting glass fiber.

Taking into account the gaps highlighted in the literature review (Chapter 2) and summarized in Table 3.2, the main objectives of this research project are:

1. Investigate the influence of stabilizing binder on the formability of an infiltrated carbon fiber UD-NCF, specifically the membrane, bending, and compaction behavior;
2. Study the influence of the stabilizing binder on the microstructure and mechanical properties of carbon fiber UD-NCF composite materials manufactured via WCM;
3. Assess the effect of stabilizing binder on the energy absorption performance of WCM UD-NCF composite hat channel components.

Table 3.2: Research objectives, gaps, and tasks

Objectives	Gaps in Literature	Tasks
1. Investigate the influence of stabilizing binder on the formability of an infiltrated carbon fiber UD-NCF, specifically the membrane, bending, and compaction behavior	Given the context of the investigated manufacturing processes (i.e., impregnated fabric), there is a clear gap in the literature regarding the characterization of the draping mechanisms of impregnated and binder-stabilized UD-NCF.	Characterization of viscous draping mechanisms: 1.1 Membrane behavior: Infiltrated bias extension test; 1.2 Bending behavior: RBT; 1.3 Compaction: Punch-to-plate test and identification of parameters.
2. Study the influence of the stabilizing binder on the microstructure and mechanical properties of carbon fiber UD-NCF composite materials manufactured via WCM	The literature lacks studies on the effects of thermosetting binders and the vacuum-assisted technique on the void content and mechanical performance of composites.	Microscopic assessment and evaluation of the mechanical properties of WCM panels: 2.1 Manufacture WCM panels; 2.2 Perform microscopy and CT scans on WCM parts to detect voids and assess fiber volume; 2.3 Perform mechanical tests to analyze the mechanical properties.

Objectives	Gaps in Literature	Tasks
3. Assess the effect of stabilizing binder on the energy absorption performance of WCM UD-NCF composite hat channel components.	There is a scarcity of publications addressing the energy absorption behavior of WCM parts under axial crush testing and the effects of stabilizing binders and vacuum-assisted techniques.	Evaluation of the energy absorption of WCM hat channels: 3.1 Manufacture WCM hat channels; 3.2 Perform quasi-static crush tests.

3.2 Scope of Work

The proposed research project consists of three main tasks, as listed in Table 3.2, each addressing a specific research objective. The workflow is illustrated in Figure 3.2 and is outlined in the following paragraphs.

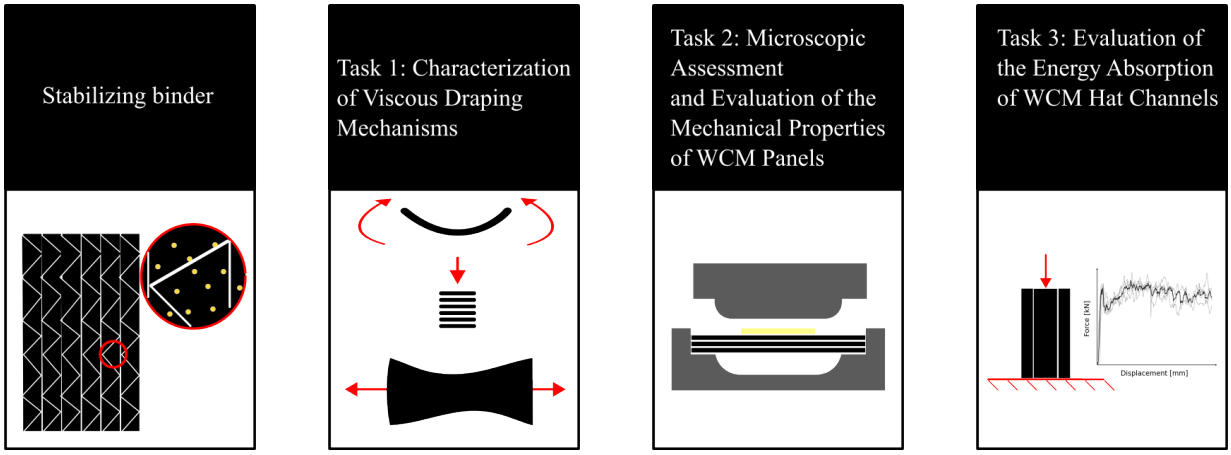


Figure 3.2: Schematic showing the research plan.

3.2.1 Task 1

Task 1 focuses on characterizing the mechanisms involved in the viscous draping process during the molding phase of the WCM process, including membrane, bending, and compaction behaviors. To fully characterize the binder-stabilized fabric for the WCM process, different fluid viscosities and both stabilizing binder states (inactivated and pre-activated) were considered for all three mechanisms. Additionally, the effects of loading rate on membrane (Task 1.1) and bending (Task 1.2) characterizations were examined. The stacking sequence was taken into account in the characterization of the compaction mechanism (Task 1.3). Finally, the compaction response curves were fitted to determine the compaction parameters using Maxwell and fractional Zener models.

3.2.2 Task 2

Task 2.1 focuses on manufacturing WCM panels by varying manufacturing parameters, including the stabilizing binder and its state, as well as the vacuum application. Task 2.2

involves assessing the WCM panels microscopically, verifying void content, size, and position using computed tomography scans, along with determining the fiber volume fraction through digital image processing. Lastly, Task 2.3 involves performing mechanical tests on specimens extracted from the WCM panels, such as tensile (longitudinal and transverse directions) and short-beam shear tests.

3.2.3 Task 3

Task 3.1 involves manufacturing WCM hat channels with distinct manufacturing parameters, including a stabilizing binder and vacuum application. Task 3.2 includes conducting a quasi-static crush test on the WCM hat channels produced in Task 3.1. Task 3.3 involves microscopic assessment of the WCM hat channels to check for the presence of voids in curved regions.

Chapter 4

Influence of Viscosity, Binder Activation, and Loading Rate on the Membrane Response of an Infiltrated UD-NCF

The contents of this chapter stem from the following paper: R. M. Portela, B. Schäfer, L. Kärger, A. R. de Faria, and J. Montesano, "Influence of viscosity, binder activation, and loading rate on the membrane response of an infiltrated UD-NCF," ESAFORM Conference, Toulouse, France, April 24-26, 2024. In: Materials Research Proceedings 2024;41:494-502.

This chapter presents the membrane characterization of dry and infiltrated binder-stabilized UD-NCF using an infiltrated bias-extension test setup.

4.1 Overview

Shear-tension coupling of engineering fabric is one of the most important behaviors during the draping phase of liquid composite molding (LCM) processes, including wet compression molding (WCM), which occurs with the infiltrated fabric and, in some cases, with the use of a stabilizing binder. In the present study, the membrane behavior of an impregnated and binder-stabilized uni-directional carbon fiber non-crimp fabric was characterized by performing off-axis tension tests. These tests allow the investigation of the influence of stabilizing binder, fluid viscosity and loading rate on the fabric membrane behavior. As

result of these experimental tests, an increase in membrane force is noticed when the stabilizing binder is activated, attributed to a greater shear stiffness. Additionally, a decrease in forces is observed for impregnated fabric compared to dry textiles caused by a lubrication layer between fiber tows. The study provides a better understanding of the membrane behavior of the impregnated and binder-stabilized UD-NCF, which is relevant for a potential high-volume production process.

4.2 Introduction

Automated wet compression molding (WCM) with fast-curing resin enables high-capacity production of continuous fiber-reinforced composite components [1]. The WCM process involves four simultaneously occurring physical mechanisms, which includes viscous draping, fluid progression, non-isothermal curing, and strong fluid-structure interaction [2]. Viscous draping of the fabric layers during mold closure is an inherent characteristic of the WCM process, involving complex mechanisms such as bending and membrane deformation, layer compaction, and frictions between adjacent layers and between layer and tool [2]. During engineering textile draping process, membrane deformation is critical, as it can directly influence the formation of defects and misalignment of fibers [3, 4]. For the WCM process, membrane deformation may be influenced by the varying resin viscosity within the mold and the deformation rate.

Unidirectional non-crimp fabrics (UD-NCF) have been increasingly used in structural applications and, in some cases, are preferred over more conventional woven fabrics. UD-NCFs comprise parallel-oriented reinforcing fiber tows and low density transversely oriented supporting fibers held together by stitching thread, providing stability during the handling and manufacturing process. Unlike woven fabrics, UD-NCFs have no tow interlacing, minimizing tow crimp and, as a result, increasing the in-plane mechanical properties of fabricated composite parts [4–8]. However, the elimination of tow interlacing leads to lower fabric handleability, which may affect the manufacturing automation and process time [9]. The addition of a stabilizing binder can improve the handling of UD-NCFs by providing higher cohesion between adjacent layers and mitigating ply slippage, while potentially reducing the manufacturing cost [4, 9]. For thick WCM parts with complex geometries, binder stabilized UD-NCFs may aid in increasing the fabric stack stiffness for improved resin management prior to mold closure. For binder stabilized UD- NCFs, the pre-activation of the binder may further influence the membrane deformation.

In general, membrane deformation is measured either by picture frame test (PFT) or bias- extension test (BET) setups [10, 11]. The PFT works by applying uniaxial tensile

forces to the low and top corners of the testing frame. It is conducted with a testing frame, initially in a square shape. During the experimental test, the testing frame deforms into a rhomboid while simultaneously imposing pure shear stress on the fabric sample. PFTs have been used for characterizing the shear deformation of woven fabrics due to their balanced nature [4, 12]. However, PFTs are not suitable for the characterization of UD-NCFs due to the fabric behavior that combines pure and simple shear [13, 14]. These two shear mechanisms are represented by the rotation and slippage of the fiber tows, respectively [13]. On the other hand, BET is performed with a rectangular shape fabric specimen that must have length to width ratio greater than 2. This type of test can be used to measure the extension-shear behavior with the fabric oriented in different directions, such as 30°, 45°, and 60°. In Ref [16], the authors indicated that 45° BET can be used to capture the UD-NCF shear response, while other studies suggest that 30° and 60° BET provide a more comprehensive understanding of the UD-NCF behavior [11, 13, 14].

Both the PFT and BET are suitable to characterize the membrane deformation of dry fabric. In Refs. [1, 2], an infiltrated bias-extension test (IBET) setup was designed to characterize the extension-shear deformation of impregnated woven fabric, which is representative of fabric draping during the WCM process. The IBET requires a horizontal frame with a reservoir, a rear fixture that holds the fabric, and a moving bridge that extends the engineering textile. In the reservoir, an amount of silicone oil is poured to fully impregnate the fabric before the test. Although impregnated woven fabrics were characterized in previous work [1, 2], the extension-shear behavior of impregnated UD-NCFs has not been studied. Furthermore, the influence of binder activation on the membrane deformation of UD-NCFs has not been studied.

In this work, the shear-tension behavior of an impregnated and binder stabilized carbon fiber UD-NCF is investigated through a series of IBETs. Thereby, the influence of the loading rate, fluid viscosity, and activation of binder on the membrane deformation response is investigated.

4.3 Experimental Procedure

4.3.1 Materials

A binder stabilized UD-NCF (Figure 4.1) was investigated, namely PX35-UD300 (Zoltek, US). This fabric consists of a single layer of axially oriented parallel tows each comprising 50K continuous PX35 carbon fibers (CFs) stitched together with a 76 dtex polyester yarn

in a tricot pattern. The fabric also consists of transversely oriented low linear density supporting glass fibers (GF) for improved handleability and a thermosetting polymer powder binder applied on one surface. The total areal density of the UD-NCF is 333 g/m^2. To impregnate the textiles and avoid additional temperature-related uncertainties, silicone oils with two different viscosities (20 and 100 cSt) were used.

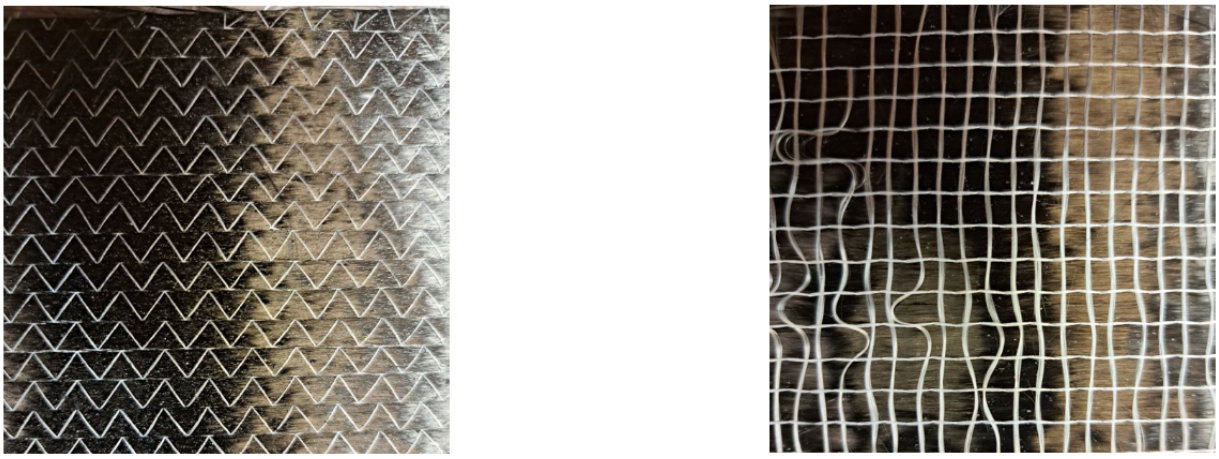


Figure 4.1: Binder stabilized uni-directional non-crimp fabric (PX35-UD300); left: Polyester stitching yarns in a tricot pattern; right: Glass fiber to improve the fabric handleability.

4.3.2 Infiltrated bias-extension test (IBET)

The IBET was performed on a servo-hydraulic test frame within the same fixture used by Poppe et al. [1], comprising a reservoir, a moving bridge attached to a 1 mm wire and a rear fixture as illustrated in Figure 4.2. When the IBET is conducted, the moving bridge is pulled, and the specimen, attached to both fixtures, is stretched. This setup was mounted on a servo-hydraulic test frame with a 1 kN load cell. Undeformed layers with a size of 280 mm × 140 mm and two different bias angles (30° and 60°) were tested at different loading rates of 100 and 500 mm/min under both dry and infiltrated conditions with two different liquid viscosities (20 cSt and 100 cSt), and with the binder pre-activated and inactivated. Each test was performed three times with a new UD-NCF specimen.

Similar to the evaluation methodology proposed by Poppe et al. [1], the shear resulting forces (f_{shear}) were found by:

$$f_{shear} = f_{raw} - f_{friction} - f_{fluid}(v, \mu) \tag{4.1}$$

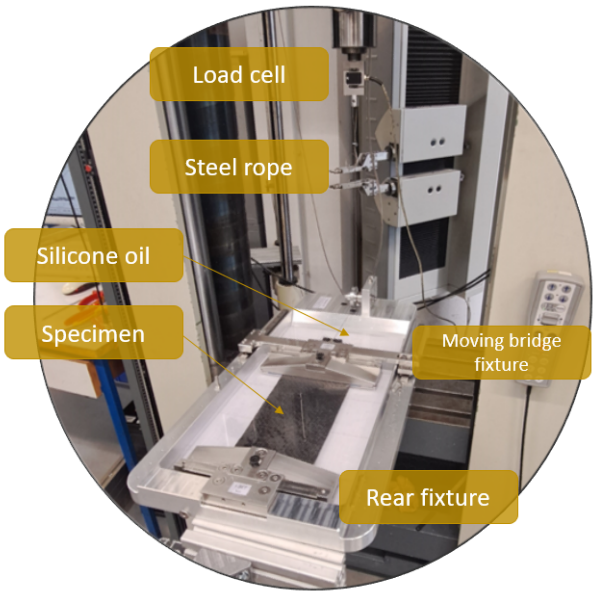


Figure 4.2: Experimental IBET setup.

where f_{raw} is the force measured by the universal testing machine, $f_{friction}$ is the frictional force within the linear bearings, and $f_{fluid}(v, \mu)$ is the fluid resistance on the moving, which is expressed as a function of fluid viscosity (μ) and loading rate or velocity (v). The last two forces were determined by performing the IBET with no specimen. For each configuration of viscosity and velocity, calibration tests were conducted 5 times.

4.4 Results and discussion

4.4.1 Influence of fluid viscosity

To investigate the influence of the fluid viscosity, two different fabric orientations (30° and 60°) were tested, both dry and impregnated with two different fluid viscosities (20 and 100 cSt). The displacement fields of both fabric orientations are illustrated in Figure 4.3. The results for the 30°-IBET and 60°-IBET are shown in Figure 4.4 and 4.5, respectively. For both considered fluid viscosities in the 30°-IBET, the average force of the dry specimens was up to 30% higher at the final displacement of approximately 50 mm (Figure 4.4). When the fabric is impregnated, it is observed a membrane force reduction, which is attributed to a lower friction between fibers within the tow and between the fiber tows and the stitching,

resulting from the lubrication layer on the fibers tows [1]. The same phenomenon occurs for an initial orientation of 60°, cf. Figure 4.5 (right), where the dry specimen has a higher membrane force. This force is reduced when the specimen is impregnated. On the other hand, an anomaly was observed in Figure 4.5 (left), showing higher membrane forces in the infiltrated specimens with 100 cSt compared to the dry specimens. This may be due to slippage of the sample during the experiment.

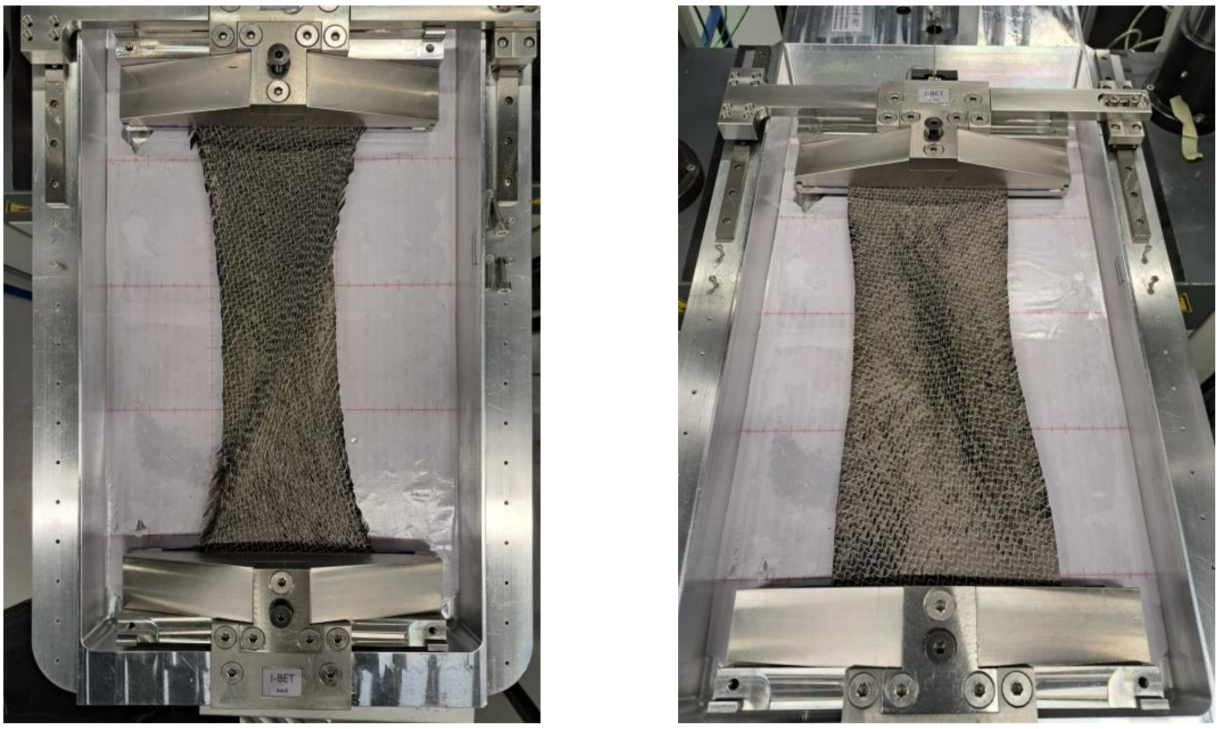


Figure 4.3: Deformed UD-NCF specimens; left: 30° test specimen; right: 60° test specimen.

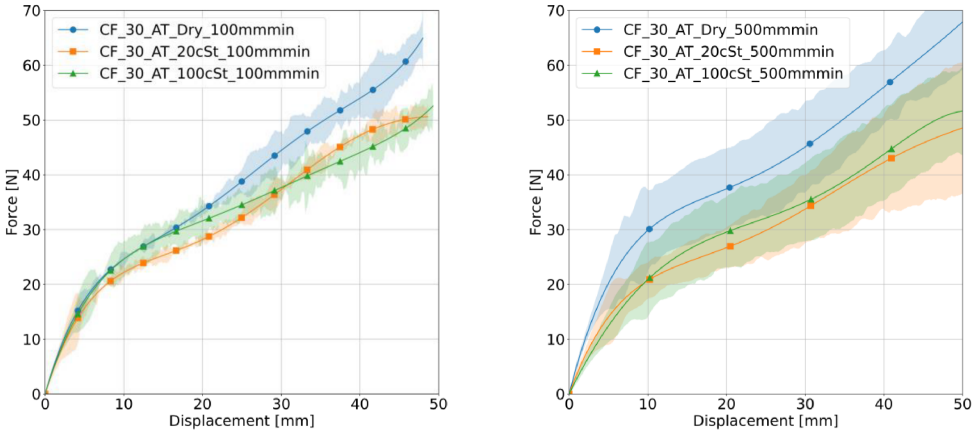


Figure 4.4: Experimental results for dry (blue) and impregnate (20 cSt in orange and 100 cSt in green) UD- NCF specimens; left: 30° specimens tested at 100 mm/min; right: 30° specimens tested at 500 mm/min.

4.4.2 Influence of fabric binder pre-activation

Figure 4.6 presents the fabric with inactivated binder (left) and the pre-activated binder (right). Figure 4.6 (left) shows the presence of polymer grains, which are pulverized over the fabric surface by the material supplier during the textile manufacturing process. When the binder is pre-activated in the oven at $120°C$, these grains melt and coat the nearest fibers and stitching. Figure 4.7 and 4.8 illustrate the influence of the pre-activated binder on the membrane force of the fabric initially oriented at 30° and 60°, respectively. The configurations with pre-activated binder are denoted by AT and without pre-activation of the binder as IT. The membrane force increases as the stabilizing binder is activated. This is due to the polymer binder that melts and coats the fiber tows and additionally increases cohesion between the tows and the stitching. This increases the shear stiffness of the fabric. In some cases, this phenomenon increases the membrane force up to 100% at different displacement values, including 20 mm and 40 mm, as shown in Figure 4.8 (right).

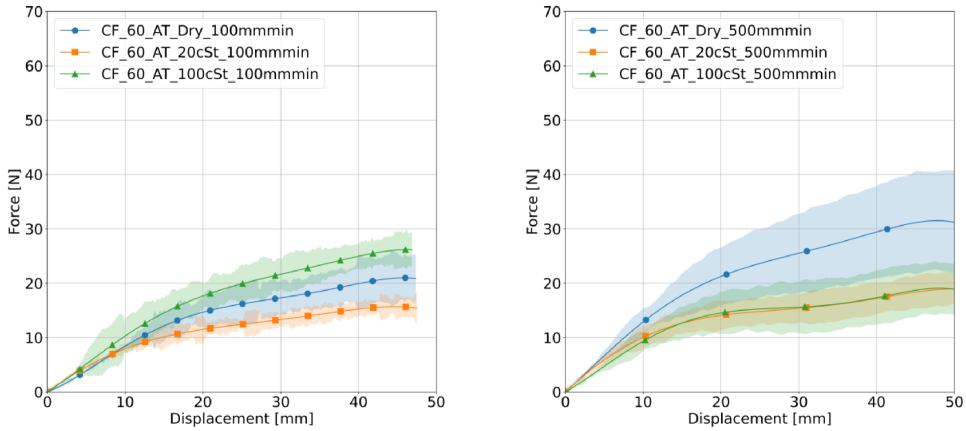


Figure 4.5: Experimental results for dry (blue) and impregnated (20 cSt in orange and 100 cSt in green) UD-NCF specimens; left: 60° specimens tested at 100 mm/min; right: 60° specimens tested at 500 mm/min.



Figure 4.6: Binder-stabilized UD-NCF; left: Inactivated binder; right: Pre-activated binder in the oven at 120°C.

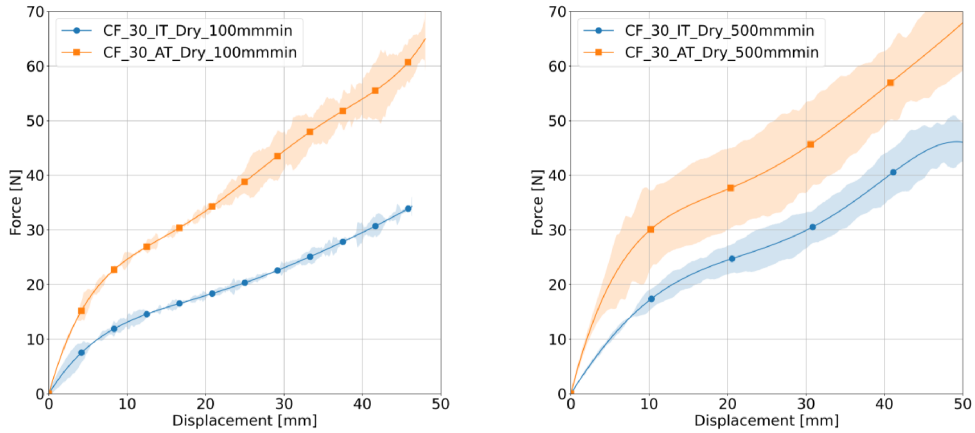


Figure 4.7: Experimental results for dry inactivated (IT) and pre-activated (AT) binder on the UD-NCF specimens; left: 30° specimens tested at 100 mm/min; right: 30° specimens tested at 500 mm/min.

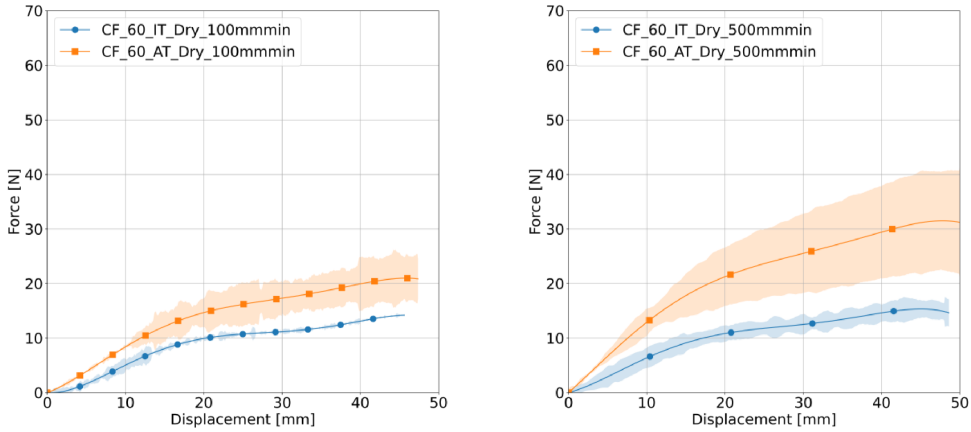


Figure 4.8: Experimental results for dry inactivated (IT) and pre-activated (AT) binder on the UD-NCF specimens; left: 60° specimens tested at 100 mm/min; right: 60° specimens tested at 500 mm/min.

4.4.3 Influence of loading rate

To understand the influence of the loading rate, the specimens were tested at two different rates. The 30°- and 60°-IBET specimens, presented in Figures 4.9 and 4.10, respectively, were tested under 100 and 500 mm/min. Figure 4.9 illustrates the results of the 30° specimens that overlap regardless of the infiltration state of the fabric, which means that for this orientation the loading rate has no influence over the membrane force. The results of the 60°-IBET specimens show an increase of the average membrane force when the specimens were dry (Figure 4.10 left); however, the standard deviation of both loading rates overlap, representing no significant difference between both loading rates. Analogously, the results of the infiltrated samples with 20 cSt silicone oil are similar, indicating no influence of the loading rate on the membrane force. Lastly, a higher membrane force was obtained at a slower loading rate when the specimens were infiltrated with 100 cSt silicone oil. The 60° bias angle is more complex because of the possible slippage of the specimen which can have affected the results presented in Figure 4.10 right.

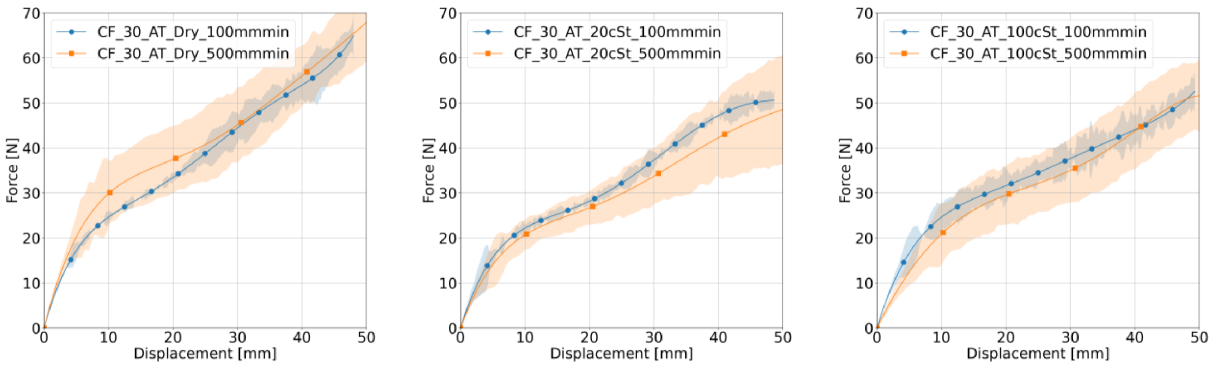


Figure 4.9: Experimental results for dry and impregnated UD-NCF specimens with activated binder system (AT); left: dry 30° specimens tested at 100 and 500 mm/min; center: impregnated 30° specimens under 20 cSt tested at 100 and 500 mm/min; right: impregnated 30° specimens under 100 cSt tested at 100 and 500 mm/min.

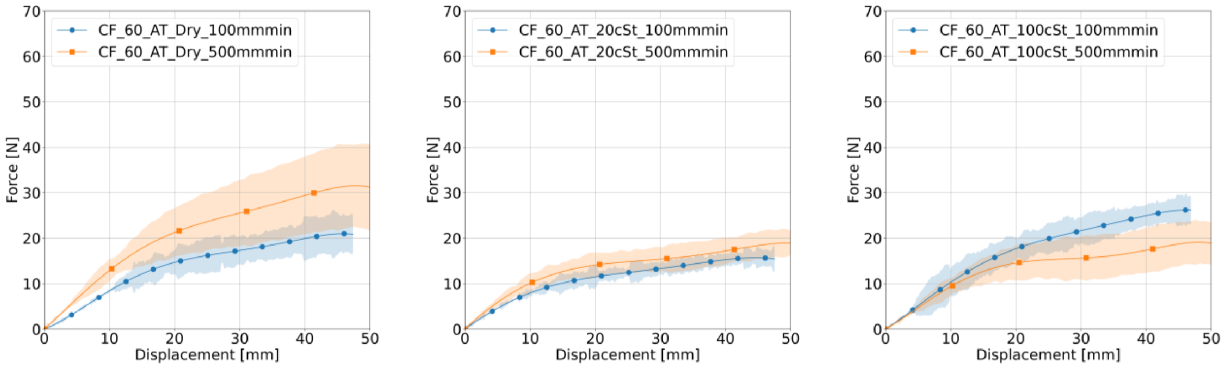


Figure 4.10: Experimental results for dry and impregnated UD-NCF specimens with activated binder system (AT); left: dry 60° specimens tested at 100 and 500 mm/min; center: impregnated 60° specimens under 20 cSt tested at 100 and 500 mm/min; right: impregnated 60° specimens under 100 cSt tested at 100 and 500 mm/min.

4.5 Summary and conclusion

In conclusion, the binder activation causes an increase of the fabric's membrane stiffness. The increase of the membrane stiffness happens because of the polymer binder that melts and, consequently, coats the fiber tows and increases cohesion with the stitching, increasing the fabric's membrane stiffness. On the other hand, the fluid viscosity creates a lubrication layer between the fiber tows and the stitching, reducing the friction, and consequently, decreasing the membrane stiffness. At last, no significant influence of the strain rate on the 30°- and 60°-IBET specimen results was found.

References

[1] C. Poppe, D. Dörr, F. Henning, and L. Kärger, "Experimental and numerical investigation of the shear behaviour of infiltrated woven fabrics," *Composites Part A: Applied Science and Manufacturing*, vol. 114, pp. 327–337, Nov. 2018, ISSN: 1359-835X. DOI: 10.1016/J.COMPOSITESA.2018.08.018.

[2] C. T. Poppe, C. Krauß, F. Albrecht, and L. Kärger, "A 3D process simulation model for wet compression moulding," *Composites Part A: Applied Science and Manufacturing*, vol. 145, p. 106 379, Jun. 2021, ISSN: 1359-835X. DOI: 10.1016/J.COMPOSITESA.2021.106379.

[3] M. Ghazimoradi, E. A. Trejo, C. Butcher, and J. Montesano, "Characterizing the macroscopic response and local deformation mechanisms of a unidirectional non-crimp fabric," *Composites Part A: Applied Science and Manufacturing*, vol. 156, p. 106 857, May 2022, ISSN: 1359-835X. DOI: 10.1016/J.COMPOSITESA.2022.106857.

[4] J. Pourtier, B. Duchamp, M. Kowalski, X. Legrand, P. Wang, and D. Soulat, "Bias extension test on a bi-axial non-crimp fabric powdered with a non-reactive binder system," in *ESAFORM 2018 - 21st International Conference on Material Forming*, Palermo, Italy, 23. and 25. of April 2018.

[5] A. Schnabel and T. Gries, "1 - production of non-crimp fabrics for composites," in *Non-Crimp Fabric Composites*, ser. Woodhead Publishing Series in Composites Science and Engineering, S. V. Lomov, Ed., Woodhead Publishing, 2011, pp. 3–41, ISBN: 978-1-84569-762-4. DOI: https://doi.org/10.1533/9780857092533.1.3. [Online]. Available: https://www.sciencedirect.com/science/article/pii/B9781845697624500011.

[6] B. Schäfer, R. Zheng, P. Boisse, and L. Kärger, "Investigation of the compaction behavior of uni-and bidirectional non-crimp fabrics," in *ESAFORM 2023 - 26th International Conference on Material Forming*, Kraków, Poland, Apr. 2023.

[7] P. Quenzel *et al.*, "Material characterisation of biaxial glass-fibre non-crimp fabrics as a function of ply orientation, stitch pattern, stitch length and stitch tension," *Journal of Composite Materials*, vol. 56, no. 26, pp. 3971–3991, 2022. DOI: 10.1177/00219983221127005. eprint: https://doi.org/10.1177/00219983221127005. [Online]. Available: https://doi.org/10.1177/00219983221127005.

[8] L. Kärger, S. Galkin, E. Kunze, M. Gude, and B. Schäfer, "Prediction of forming effects in ud-ncf by macroscopic forming simulation–capabilities and limitations," in *ESAFORM 2021 - 24th International Conference on Material Forming*, Liège, Belgium, 14-16 April 2021.

[9] P. H. Broberg, C. Krogh, E. Lindgaard, and B. L. V. Bak, "Simulation of wrinkling during forming of binder stabilized ud-ncf preforms in wind turbine blade manufacturing," *Key Engineering Materials*, vol. 926, pp. 1248–1256, Jul. 2022, ISSN: 1662-9795. DOI: 10.4028/p-165q46. [Online]. Available: https://www.scientific.net/KEM.926.1248.

[10] P. Boisse, N. Hamila, E. Guzman-Maldonado, A. Madeo, G. Hivet, and F. Dell'Isola, "The bias-extension test for the analysis of in-plane shear properties of textile composite reinforcements and prepregs: A review," *International Journal of Material Forming*, vol. 10, pp. 473–492, 2017.

[11] F. J. Schirmaier, D. Dörr, F. Henning, and L. Kärger, "A macroscopic approach to simulate the forming behaviour of stitched unidirectional non-crimp fabrics (ud-ncf)," *Composites Part A: Applied Science and Manufacturing*, vol. 102, pp. 322–335, 2017.

[12] G. Barbagallo, A. Madeo, I. Azehaf, I. Giorgio, F. Morestin, and P. Boisse, "Bias extension test on an unbalanced woven composite reinforcement: Experiments and modeling via a second-gradient continuum approach," *Journal of Composite Materials*, vol. 51, pp. 153–170, 2 Jan. 2017, ISSN: 1530793X. DOI: 10.1177/0021998316643577.

[13] B. Schäfer, R. Zheng, N. Naouar, and L. Kärger, "Membrane behavior of uni-and bidirectional non-crimp fabrics in off-axis-tension tests," *International Journal of Material Forming*, vol. 16, no. 6, p. 68, 2023.

[14] F. J. Schirmaier, K. A. Weidenmann, L. Kärger, and F. Henning, "Characterisation of the draping behaviour of unidirectional non-crimp fabrics (UD-NCF)," *Composites Part A: Applied Science and Manufacturing*, vol. 80, pp. 28–38, Jan. 2016, ISSN: 1359-835X. DOI: 10.1016/J.COMPOSITESA.2015.10.004.

Chapter 5

Effect of loading rate, viscosity, and binder activation on the bending response of an infiltrated UD-NCF

The contents of this chapter stem from the following paper: R. M. Portela, B. Schäfer, L. Kärger, A. R. de Faria, and J. Montesano, "Effect of loading rate, viscosity, and binder activation on the bending response of an infiltrated UD-NCF," Composites Part A: Applied Science and Manufacturing, vol. 200, p. 109347, 2026, doi: 10.1016/j.compositesa.2025.109347

This chapter presents the bending characterization of dry and infiltrated binder-stabilized UD-NCF using a rheometer bending test setup.

5.1 Overview

Assessing the bending response of infiltrated reinforcement fabrics is crucial in wet compression molding (WCM) as it affects macroscopic wrinkling. Binder-stabilized fabrics may be used in WCM to improve handleability and reduce defects, necessitating their characterization. This study examines the bending behavior of an infiltrated binder-stabilized carbon fiber unidirectional non-crimp fabric (UD-NCF), focusing on the effects of viscosity, loading rate, and binder pre-activation. Infiltration reduces bending stiffness compared to dry fabric owing to lubrication and lower tow-stitch friction, while higher loading rates increase bending stiffness for all considered conditions. Moreover, binder pre-activation

increases fabric stiffness by enhancing tow-stitch cohesion and friction. As the first investigation on infiltrated binder-stabilized UD-NCF bending, this work advances understanding of the complex bending response.

5.2 Introduction

Liquid composite molding (LCM) processes have been used for over 50 years [1] to manufacture fiber-reinforced plastic composite parts with complex shapes and high fiber volume fractions. LCM processes have the potential for high production volumes at relatively low manufacturing cost, which may compensate for high raw material costs [1–5]. This class of manufacturing processes includes Resin Transfer Molding (RTM), High Pressure-RTM (HP-RTM), and Wet Compression Molding (WCM). Among these processes, WCM using highly reactive resins is particularly promising for mass production. Unlike RTM processes, WCM does not require a fabric preforming step or use of sophisticated metering equipment to inject resin into the mold or use of a large press, which may increase processing throughput and decrease the cost of the final fabricated part [4, 6, 7]. A typical WCM process consists of five steps, as illustrated in Fig. 5.1. The fabric layers are first cut and stacked before being introduced into the preheated mold. Next, the resin is dispensed onto the fabric stack before the mold is closed. In automated setups, resin application may be conducted outside of the mold, and the impregnated fabric stack introduced into the mold. Thereafter, forming and infiltration of the fabric occur simultaneously during the molding phase, removing the need for a dedicated fabric preforming step. Finally, the resin cures, and the final part is removed from the mold.



Figure 5.1: Schematic of the steps for a typical WCM process.

Among the fabrics used in WCM processes, continuous re inforcements such as woven and unidirectional non-crimp fabrics (UD- NCF) are commonly employed. UD-NCFs have recently gained attention in the automotive industry owing to their excellent drapability, which is well-suited for LCM processes [8]. UD-NCFs consist of parallel-oriented fiber

tows held together by stitching threads, which ensure the structural integrity of the reinforcement and provide stability during handling and manufacturing [8–11]. Unlike woven fabrics that comprise varying de grees of interlacing, the aligned fiber tows in UD-NCFs are not inter laced, which enhances the in-plane mechanical properties of the fabricated composite material. According to Rudd et al. [12], NCF composites can achieve up to 15% greater load-bearing efficiency compared to similar woven fabrics, offering a higher potential for lightweight structures.

For structural components, many layers of UD-NCF oriented along different directions are required to meet desired anisotropic properties and performance requirements, which could result in thick components. For relatively large components comprising multidirectional layers, this would require the application of a significant quantity of resin to the flat fabric stack (i.e., step 3 in Fig. 5.1). However, producing such components using WCM processes—especially in molds with deep cavities—presents challenges related to resin management since the UD-NCF stack may drape under gravity due to the mass of the applied resin. Draping of the fabric stack prior to closing the mold may lead to resin pooling and fabric shifting within the mold, which could lead to defects such as dry spots, voids, and severe fabric wrinkling. A promising solution to address this issue is the use of binder-stabilized UD-NCF, where pre- activation of the binder before insertion of the flat stack into the mold may provide increased fabric bending stiffness [13] and enable improved resin management. Stabilizing binders are either thermo plastic or uncatalyzed epoxy resins, available in either solvent-based liquid or dry powder form [14–16]. Stabilizing binders are typically used to keep fabric layers adhered to one another and maintain fabric integrity during operations such as trimming and handling [14]. At the same time, stabilizing binders are necessary for preforming of UD-NCF stacks during RTM processes. However, the use of binder-stabilized fabrics may also introduce challenges, as they can affect processing conditions and fabric formability.

Most studies focused on characterizing binder-stabilized fabrics investigated the influence of the stabilizing binder on fabric perme ability and resin viscosity. Estrada et al. [14] reported that increasing the binder concentration leads to reduced fabric permeability. Brody and Gillespie [15] examined the effects of thermoplastic binder on vinyl ester resin and found that the binder powder gradually dissolved in the resin, decreasing in particle size over time. Additionally, they observed a significant delay in resin curing and an increase in viscosity. Yoo et al.[16] investigated the influence of epoxy binder on the permeability and friction coefficients of woven fabric, revealing that the stabilizing binder can reduce permeability by up to 98% and increase the fabric friction coefficient by as much as 200%. Neunkirchen et al. [17] reported that the molten stabilizing binder forms an interlayer film, which blocks some capillary channels and slows down capillary flow.

Several studies have concentrated on evaluating the impact of sta bilizing binders on intra-ply draping mechanisms, including membrane and compaction behaviors (see Fig. 5.2). Wei et al. [18] examined the compaction behavior of woven fabrics and NCFs, noting that the application of stabilizing binder increases the initial thickness and relaxation of the stack. However, it also reduces the elastic recovery, enhancing the viscoelastic properties of the fabric stack. Portela et al. [19] analyzed the effect of pre-activating the stabilizing binder on the membrane performance of both dry and impregnated UD-NCF. Their findings indicate that the molten binder coats the fiber tows, increasing cohesion between the tows and stitching yarns, which in turn enhances membrane stiffness. Broberg et al. [20] investigated the transverse shear behavior of a binder-stabilized glass UD-NCF to better comprehend the forming process in the manufacture of wind turbine blades. Their results demonstrated an increase in load corresponding with an increase in deformation rate.

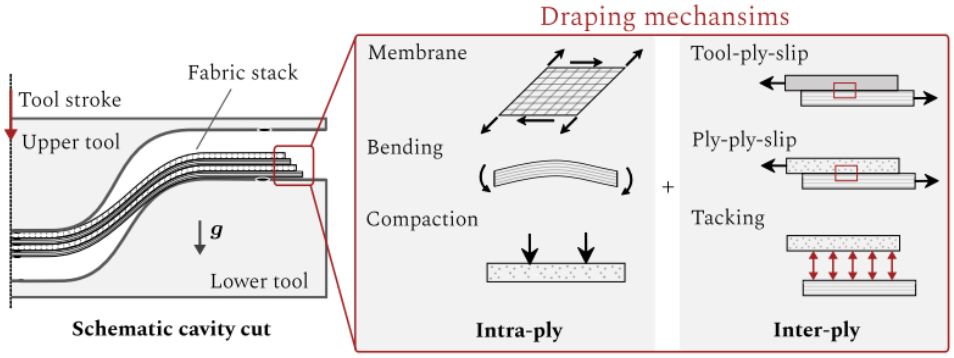


Figure 5.2: Draping mechanism present during the WCM process [21].

Given the critical importance of draping mechanisms within the WCM process and the objective of optimizing the final components, it is essential to thoroughly characterize the fabric utilized in manufacturing [22]. In previous studies, the bending mechanism was frequently neglected due to the low stiffness characteristic of fabrics, with primary focus on membrane behavior [23, 24]. However, flexural behavior plays a key role in describing fiber curvature and can significantly influence the wrinkle formation during the forming stage, compromising the mechanical performance of the final part [25–29]. Senner et al. [30] emphasized that low bending stiffness can lead to substantial fabric deformation under minimal bending loads.

Several test methods have been developed to characterize the bending behavior of engineering textiles, including variations of the cantilever test (e.g., Peirce, vertical, and free-hanging tests), rheometer bending test (RBT), and buckling tests [31]. Traditional

three- and four- point bending tests are, in general, not employed for fabric character ization due to their low flexural stiffness caused by relative slippage between fiber tows. These test setups are typically reserved for thick reinforcements or small composite samples with higher bending stiffness and are therefore avoided in fabric studies [23, 26, 32]. Krogh et al. [31] compared various testing methods for characterizing fabric bending stiffness. The first method, known as the Peirce cantilever test [33], involves a simple setup with an inclined plane over which a fabric strip overhangs. Bending stiffness is estimated when the tip of the fabric contacts the plane, assuming a constant stiffness. However, this assumption may oversimplify fabric behavior and fail to capture nonlinear responses [31]. Despite its limitations, the simplicity of the Peirce method has contributed to its popularity among researchers [23, 31, 34–37]. Poppe et al. [32] observed that some Peirce method variations use a weight to clamp the non-overhanging end of the fabric strip. This weight compresses the fabric under an undetermined degree of compaction, altering boundary conditions and potentially introducing inconsistencies in the results. Alternatively, the Kawabata bending test (KES-FB2) employs a specialized device with two clamps securing the specimen, while one clamp rotates to impose a controlled curvature and loading rate. This method enables direct measurement of moment–curvature curves, even under cyclic loading conditions, and effectively captures nonlinear, hysteretic, and loading-rate-dependent behaviors. An adaptation of this setup was introduced by Sachs and Akkerman [28], which modifies the test for compatibility with rheom eter equipment—referred to as the Rheometer Bending Test (RBT). The RBT is widely recommended in the literature for its accuracy and capability to characterize rate-dependent, temperature-sensitive, and hysteretic responses of fabrics [31, 32].

Recent studies in the literature have focused on the bending behavior of binder-stabilized fabrics. Broberg et al. [38] investigated the forming of binder-stabilized glass fiber NCF for manufacturing thick parts and found that, in transition regions, the stabilizing binder may increase wrinkle formation. They also observed that large compressive loads can cause the formation of large wrinkles and damage to the binder material. In a subsequent study, Broberg et al. [39] characterized the nonlinear behavior of glass fiber NCF using a modified cantilever test. They concluded that incorporating material nonlinearities in the simulation model improves the prediction of wrinkle formation. Similarly, Ghazi moradi et al. [40] used the modified cantilever method to characterize the nonlinear bending behavior of a dry and inactivated binder- stabilized carbon fiber UD-NCF. They reported significant anisotropy, with low bending stiffness in the direction transverse to the fiber tows and notable stiffness along the fiber direction. The characterization data were later used to calibrate an anisotropic material model implemented in commercial finite element software [41]. Broberg et al. [39] and Ghazimoradi et al. [40] investigated the behavior of a

binder-stabilized UD-NCF; however, neither considered the effect of binder pre-activation nor the impregnation of the fabric, due to the targeted manufacturing processes.

Despite advancements in understanding the bending behavior of binder-stabilized UD-NCFs, it is important to note that in the WCM process, forming occurs during the molding phase (Fig. 5.1) when the fabric is impregnated. Therefore, all draping mechanisms, including bending behavior (Fig. 5.2), may behave differently from those reported in previous studies [38, 40], which did not consider fabric infiltration or pre-activation of the binder due to the different manufacturing processes that were investigated. One study that did consider the influence of infiltrated fluid viscosity on the bending response of reinforcement fabrics was conducted by Poppe et al. [32]. An RBT test and a variation of the Peirce test were used to characterize the bending behavior of an infiltrated woven fabric. Although Pope et al. [32] were the first to study the bending response of an impregnated reinforcement fabric, their study exclusively considered a non-binder-stabilized woven fabric. This left a gap in the literature for other binder-stabilized fabrics, particularly UD-NCFs, which may influence the fabric's behavior. To date, no studies have focused on characterizing the bending response of infiltrated binder-stabilized UD-NCFs and the corresponding influence of binder pre-activation. In this study, the bending behavior of an impregnated binder-stabilized carbon fiber UD-NCF is investigated through a series of RBTs. Consequently, the influence of the loading rate, fluid viscosity, and activation of binder on the bending response is investigated.

5.3 Fabric material and experimental methodology

5.3.1 Fabric description and specimen preparation

The studied binder stabilized UD-NCF, namely PX35-UD300 (Zoltek, US), comprised axially oriented parallel tows, each composed of 50 K continuous PX35 carbon fibers (CF). The tows were stitched together with a 76 dtex polyester yarn in a tricot pattern. In addition, the textile included transversely oriented supporting glass fibers (GF) with low linear density to improve handleability, while a thermosetting polymer powder binder was dispersed on the stitch tricot pattern surface (Fig. 3). The textile has a total areal density of $333 g/m^2$. Fabric specimens with dimensions 140 mm $\times$ 60 mm (with CF aligned along the longer dimension) were cut from a roll using an automated cutting table (Zünd Systemtechnik AG, Switzerland). Lastly, 20 cSt and 100 cSt silicone oils were used to impregnate a subset of the specimens, as they represent the viscosities of various epoxy resins under elevated temperature process ing conditions.

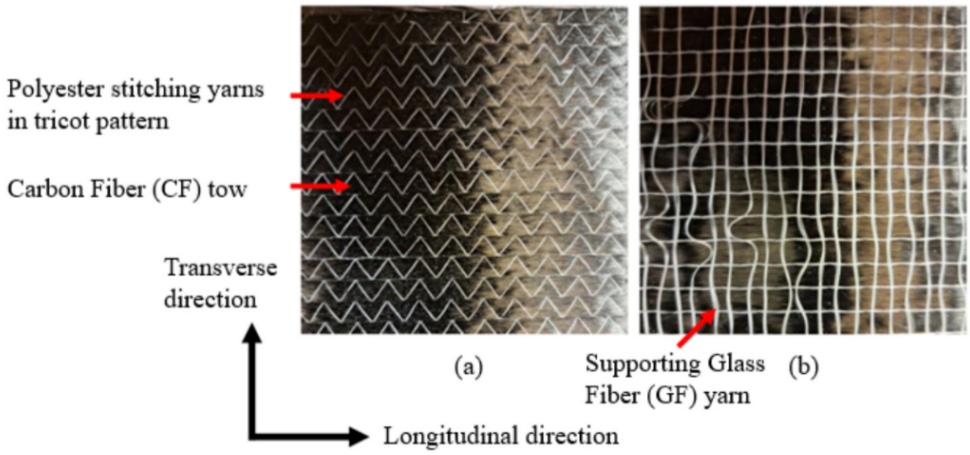


Figure 5.3: Images of the PX35-UD300 UD-NCF showing different constituents and microstructure: (a) stitch tricot pattern surface, and (b) supporting glass fiber surface.

5.3.2 Rheometer bending test setup

Fig. 5.4 illustrates the test setup used for the RBTs, comprising a customized MCR501 rheometer (Anton Paar, Austria), an oil collector plate, and an enlarged frame utilized for supporting and bending the fabric specimen over the angular range from 0 to 60°. The use of an enlarged frame enhanced the reproducibility of the tests. This frame is subdivided into two fixtures: a fixed fixture that supports the rectangular fabric specimen on one side and a rotating fixture that supports the specimen on the opposite side. Teflon tape was applied to the frame fixtures to mitigate friction with the fabric specimen. Additionally, industrial duct tape was fixed on both ends of each specimen to maintain the CF tow orientation along the horizontal direction. For the infiltrated samples, 2 ml of silicon oil was dispensed with a syringe onto the central region (approximately 70 mm × 60 mm), where the bending occurs, to avoid wetting the contact interfaces. Following impregnation, the specimens rested for 2 min prior to testing to ensure complete saturation.

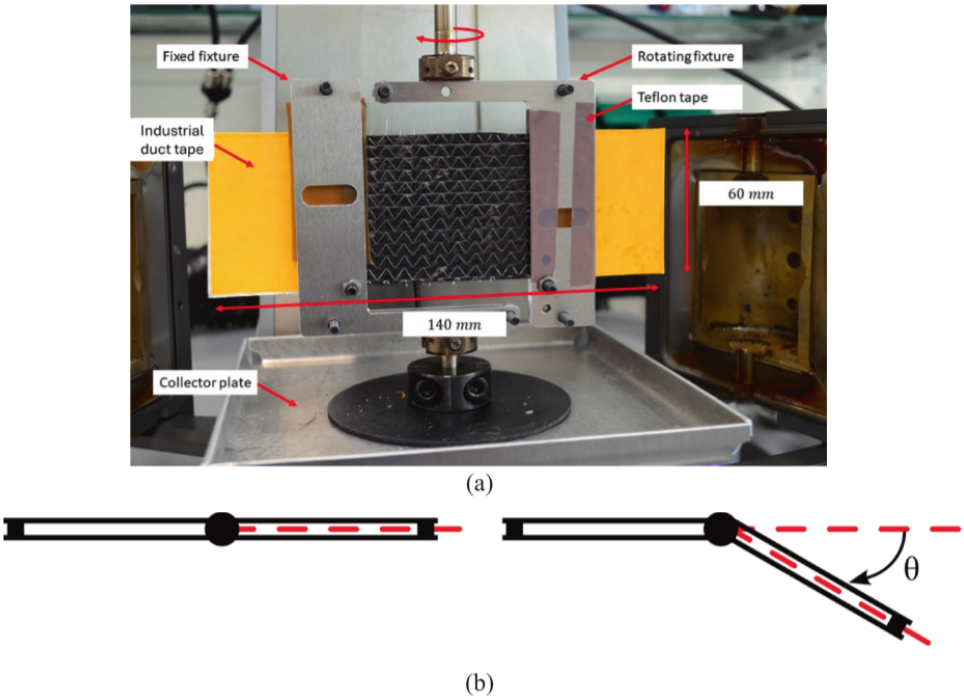


Figure 5.4: (a) Setup of the RBT with a fabric specimen mounted in the frame fixtures, including a prepared specimen and its measurements, (b) top-view schematic of the RBT setup.

Bending tests were performed at room temperature under four distinct conditions (refer to Table 5.1). While typical WCM processes are performed at elevated temperatures in a pre-heated mold, the fabric is usually formed before reaching the mold temperature. Consequently, tests at elevated temperatures were not considered herein as they are not representative of WCM processes. For the first three conditions, specimens had their binder system pre-activated at 120°C for 20 min prior to being supported in the fixtures. These specimens were subjected to an applied angular velocity of either 0.1, 1.0, or 10.0 RPM. The binder present in the investigated fabric is a thermosetting polymer, which, when thermally activated, melts and coats the fabric. Following pre-activation, subsequent variations in temperature would have a low influence on the binder, given that this process is irreversible; however, this factor was not considered in the study. For the fourth condition, specimens with no binder pre-activation were utilized, and an angular velocity of 1.0 RPM was applied. For all conditions, three viscosity cases were considered: dry, silicone oil with a viscosity of 20 cSt, and silicone oil with a viscosity of 100 cSt, yielding a total of 12 test cases. Both

Table 5.1: Different conditions tested using the RBT setup.

Condition	Bider state	Angular velocity [RPM]	Viscosity [cSt]	Number of specimens
1	Pre-activated	0.1	Dry	8
			20	8
			100	8
2	Pre-ativacted	1	Dry	8
			20	8
			100	8
3	Pre-activated	10	Dry	8
			20	8
			100	8
4	Inactivated	1	Dry	8
			20	8
			100	8

oil viscosities mimic the viscosity of typical resins during the manufacturing process. Note, a total of 8 repeated tests were performed for all test cases (i.e., 96 tests in total).

The rheometer was set to move from 0∘ to 60∘ for every test, considering the different bending rates. Data acquisition was performed at intervals of 0.5 s, 0.05 s, and 0.01 s for the tests at 0.1, 1.0, and 10.0 RPM, respectively. The bending moment, M(θ), and rotation angle, θ, were recorded for each experimental test. For every condition, the rotation angle was converted to curvature κ using [31, 32]:

$$\kappa = \frac{\tan(\frac{\theta_i^{Rheo}(t)}{2})}{R}, \tag{5.1}$$

where R is the rheometer bending radius, assumed to be constant throughout the test. Next, the moment M(κ) was divided by the sample width. The width-normalized bending stiffness (i.e., bending stiffness per unit width) was defined as the slope of the width-normalized moment–curvature plot.

To verify the statistical significance of the influence of loading rate, impregnation fluid viscosity, and binder pre-activation on the fabric bending stiffness, pairwise analyses were conducted on width- normalized bending stiffness for two conditions using a two-sample T- test. The null hypothesis for a T-test assumes no difference between the sample data

and is accepted when the corresponding p-value is greater than 0.05. Otherwise, the null hypothesis is rejected, indicating a statistically significant difference.

5.4 Results and Discussion

To ensure consistent analysis of all collected data for each condition (Table 5.1), the moment values were interpolated within the range from 0° to 60° to align the angle measurements across all eight specimens. Then, the angle measurements were converted to curvature, and the moments were normalized. The mean and standard deviation values for the normalized moment were calculated for the set of specimens for each investigated condition, represented by solid lines and shaded regions in Fig. 5.5, respectively. It is worth noting that, across all conditions, the results were repeatable with minimal scatter, and the normalized moment values exhibited a linear increase with increasing curvature. A small number of specimens exhibited responses that deviated from the majority of repeated tests for each condition. These outliers were omitted from the analysis, as they were not considered to be representative. Additionally, the normalized bending stiffness for each condition was determined as described in the previous section, utilizing the full range of curvature data from 0 to 0.0165 mm^{-1}. Tables 5.2 and 5.3 present the normalized bending stiffness values for the activated and inactivated specimens, respectively, while these data are also plotted in Fig. 5.6.

Table 5.2: Normalized bending stiffness values of the pre-activated samples (Conditions 1–3).

Loadig rate [RPM]	Dry [N.mm]	Viscosity 20 cSt [N.mm]	Viscosity 100 cSt [N.mm]
0.1	5.44	3.77	3.35
1	5.53	3.41	3.83
10	6.29	4.49	5.12

Table 5.3: Normalized bending stiffness values of the inactivated samples (Condition 4).

Loadig rate [RPM]	Dry [N.mm]	Viscosity 20 cSt [N.mm]	Viscosity 100 cSt [N.mm]
1	3.95	2.91	2.88

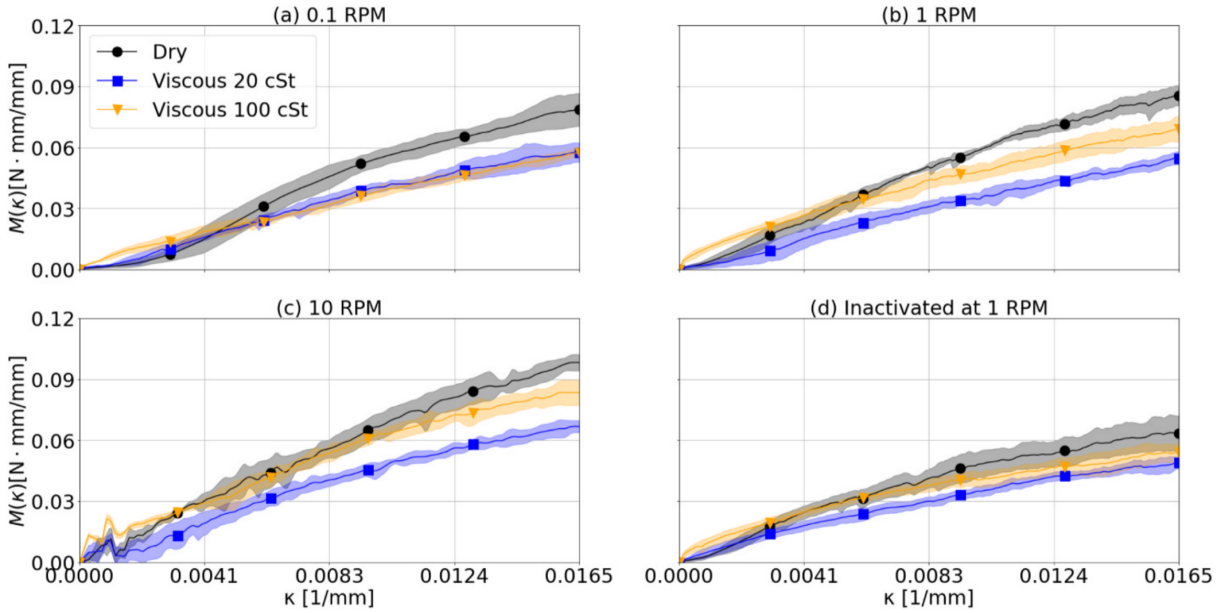


Figure 5.5: Normalized moment–curvature plots for the four tested conditions, each including dry, impregnated with 20 cSt silicone oil, and impregnated with 100 cSt silicone oil infiltration cases: (a) Condition (1) – binder pre-activated and 0.1 RPM velocity, (b) Condition 2 – binder pre-activated and 1 RPM velocity, (c) Condition 3 – binder pre-activated and 10 RPM velocity, (d) Condition 4 – binder inactivated and 1 RPM velocity.

As mentioned in the previous section, the fabric samples were extracted from the same binder-stabilized fabric roll with a CNC table machine. The relatively minor variability of the bending test results may be attributed to several factors, including material defects, sample preparation, and the testing procedure. Previous studies observed that stitching yarn cross-over points in NCFs can be unevenly distributed, which may lead to in-plane tow misalignment and out-of-plane crimp [42–44]. Uneven stitching yarn patterns may influence the size of the fiber tow and the thickness of the layer. Thus, it is plausible that these variations may lead to some degree of scatter in the bending stiffness, albeit deemed to be minor in this study. In addition, the application of stabilizing binder powder may also vary across different regions of the roll. This variation may lead to higher bending stiffness in specimens with greater binder content. Moreover, although the amount of silicone oil was carefully measured before impregnating each specimen, some minor variations in the amount of oil and impregnation uniformity may have also affected the bending response of the specimen and contributed to scatter in the presented data. Variations could have

also been induced during the fabric specimen preparation, particularly during cutting with the CNC table machine. The cutting procedure involved several steps, including aligning the fabric on the cutting table. The fabric may have been slightly misaligned, resulting in slightly off-axis specimens and lower fabric bending responses. Lastly, data scatter may also be attributed to positioning of the fabric specimens during the tests. As the fabric specimens were not clamped to the fixture, they may have exhibited some inclination at the beginning of the tests or minor shifting as the moving frame rotated.

The normalized bending stiffness of the dry UD-NCF along the fiber direction for the condition with inactivated binder at 1 RPM angular velocity (see Table 5.3) is approximately 64% greater than the normalized bending stiffness of 2.41 N.mm for a dry non-bindered 12 K carbon fiber plain woven fabric studied by Poppe et al. [32], using the same RBT setup. The comparatively lower bending stiffness of this woven fabric is presumably attributable to the presence of yarn interlacing and the smaller tow size, when contrasted with the UD-NCF examined herein. Additionally, the normalized bending stiffness of the dry UD-NCF along the fiber direction for the same condition is approximately 7.34% greater than the normalized bending stiffness of 3.68 N mm for a binder-stabilized UD glass fabric with a tricot stitching pattern and an areal density of 1322 g/m^2 investigated by Krogh et al. [31] using an RBT setup. This difference can be attributed to several factors, including the lower angular velocity used in Ref. [31] (i.e., 0.75 RPM) and differences in the fabric composition and architecture. Although a one-to-one comparison with a similar fabric is not feasible, these comparisons reveal that the bending stiffness of the studied carbon fiber UD-NCF along the fiber direction is relatively high in comparison to other common reinforcement fabrics. More generally, the findings also highlight a significant influence of loading rate, viscosity, and binder pre-activation on the fabric's bending behavior, which will be discussed hereafter.

The effect of loading rate on the fabric bending stiffness is illustrated qualitatively in Fig. 5.5 (a), (b), and (c). As the angular velocity increased from 0.1 RPM to 1 RPM and from 1 RPM to 10 RPM for the dry-activated binder case, the average normalized bending stiffness increased by 1.65% and 13.74%, respectively (Table 5.2). This observation aligns with previous studies indicating the dependency of bending stiffness on loading rate for dry woven fabrics [32, 45]. The bending stiffness of UD-NCFs is influenced by the interaction between fiber tows and stitching yarns [40]. As the fabric bends, the stitching yarns slide over the fiber tows, generating friction between the fabric constituents. Bending occurs once all the frictional resistance is overcome [46, 47]. At higher loading rates, there is less time for the fabric constituents to overcome static friction, resulting in reduced relative sliding and consequently higher measured fabric bending stiffness. Additionally, since the fabric specimens were not clamped to the RBT fixture, some slippage was observed, as

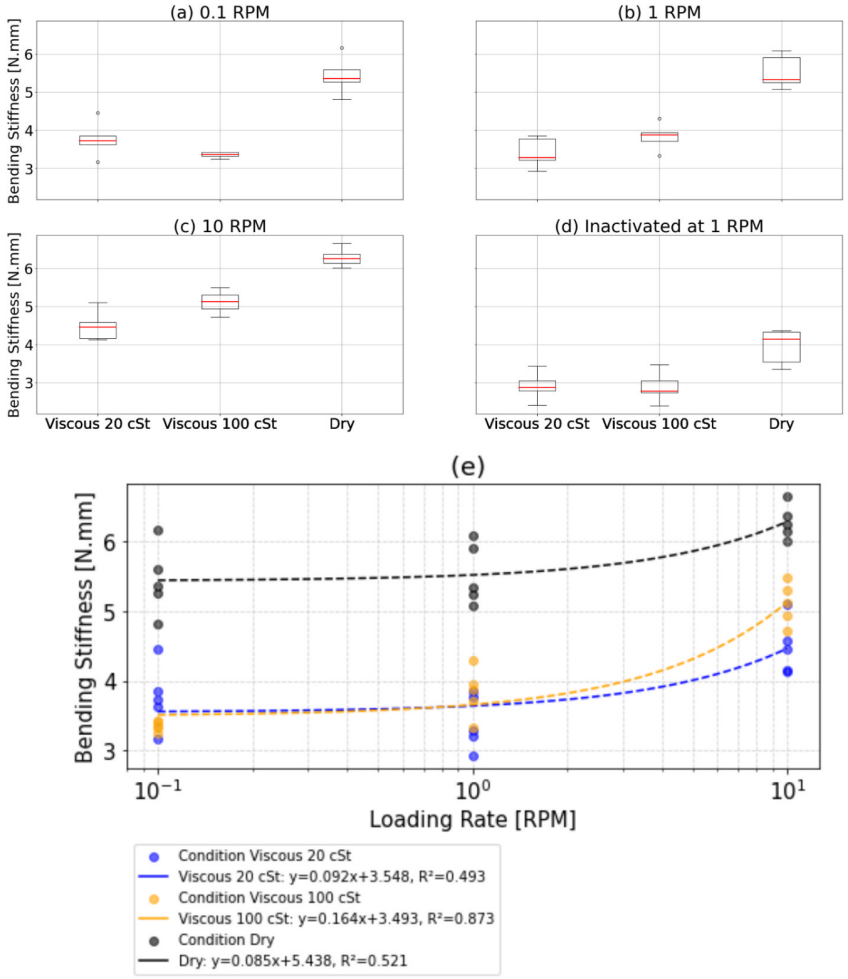


Figure 5.6: Normalized bending stiffness for the four tested conditions, each including impregnated with 20 cSt silicone oil, impregnated with 100 cSt silicone oil infiltration, and dry cases: (a) Condition (1) – binder pre-activated and 0.1 rpm velocity, (b) Condition 2 – binder pre-activated and 1 rpm velocity, (c) Condition 3 – binder pre-activated and 10 rpm velocity, and (d) Condition 4 – binder inactivated and 1 rpm velocity. (e) Normalized bending stiffness vs loading rate for the indicated infiltration case.

reported in Ref. [32], with this effect being more pronounced at an angular velocity of 0.1 RPM. Consequently, lower loading rates resulted in lower apparent bending stiffness because of the easier overcoming of static friction. Interestingly, the effect of loading rate on the specimens impregnated with a 20 cSt viscosity oil was much less noticeable

Table 5.4: P-values obtained through T-Test comparing the normalized bending stiffness for different loading rate pairs, for each impregnation case.

	0.1 RPM × 1 RPM	0.1 RPM × 10 RPM	1 RPM × 10 RPM
Dry	7.64×10^{-1}	8.99×10^{-3}	9.79×10^{-3}
Viscous 20 cSt	2.29×10^{-1}	2.99×10^{-2}	2.55×10^{-3}
Viscous 100 cSt	1.80×10^{-2}	1.50×10^{-6}	2.75×10^{-4}

(Table 5.2). The impregnation of the fabric with a low- viscosity oil has reduced friction between the fiber tows and stitching and enabled increased relative movement, which has reduced the degree of the influence of loading rate on fabric bending stiffness. Moreover, for the specimens impregnated with a 100 cSt viscosity oil, the normalized bending stiffness increased by 14.32% and 33.68% (Table 5.2) as the angular velocity increased from 0.1 to 1 RPM and from 1 RPM to 10 RPM, respectively (i.e., a similar trend to that of the dry pre-activated binder specimens). However, the stronger influence of loading rate on specimens infiltrated with higher viscosity oil may be because the frictional bending restraint is relatively greater compared to specimens infiltrated with lower viscosity oil. Table 5.4 lists the p-values associated with each pair of normalized bending stiffness data for each loading rate and impregnation condition. Only two of the nine comparisons yielded p-values greater than 0.05, confirming that an increase in loading rate results in a statistically significant increase in fabric bending stiffness.

The impregnated fabric specimens exhibited lower bending stiffness when compared to dry specimens for each condition, which is shown qualitatively in Fig. 5.5. For example, the normalized bending stiffness of the dry specimens and specimens impregnated with 100 cSt viscosity oil tested at an angular velocity of 1 RPM (Fig. 5.5b, Table 5.2) were, respectively, 62.17% and 12.32% greater than that of the specimens impregnated with a 20 cSt viscosity oil. Similar findings were reported in Ref. [32] for a carbon fiber woven fabric, where it was determined that the silicone oil acts as a lubricant, reducing friction among the fiber tows and supporting yarns, which resulted in lower fabric stiffness. Similarly, in this study, the friction between the carbon fiber tows and the polyester stitching yarns was reduced for impregnated specimens, leading to a reduction in the fabric's bending stiffness. The observed increase in bending stiffness for the specimens impregnated with the higher viscosity oil may be due to greater friction caused by the 100 cSt oil in comparison to 20 cSt oil [32]. It must be noted that at higher angular velocities (Fig. 5.5c, Table 5.2), the bending behavior of the sample impregnated with 100 cSt silicone oil converged with that of the dry fabric samples, possibly due to the comparable frictional resistance between the fabric constituents and, thus, similar bending restriction when compared to the dry samples

[48, 49]. Another interesting observation is that the bending stiffness of the specimens with inactivated binder (Fig. 5.5d, Table 5.3) was notably less influenced by the presence of viscous oil. This finding might be due to the relatively low friction between the fiber tows with inactivated stabilizing binder and the stitching, which led to reduced sensitivity to impregnation oil viscosity on the bending stiffness. Similar two-sample T-tests were performed (Table 5.5), revealing that for all but two test case comparisons, there were statistically significant differences in the normalized bending stiffness.

Table 5.5: P-values obtained through T-Test comparing the normalized bending stiffness of pre-activated binder specimens for different fabric impregnation case pairs, for each loading rate.

	Dry × Viscous 20	Dry × Viscous 100	Viscous 20 × Viscous 100
0.1 RPM	5.83×10^{-4}	1.48×10^{-5}	8.59×10^{-2}
1 RPM	4.17×10^{-5}	1.47×10^{-4}	1.13×10^{-1}
10 RPM	2.45×10^{-5}	1.52×10^{-4}	2.25×10^{-2}

Lastly, the effect of binder pre-activation on the bending behavior was evaluated by comparing the results illustrated in Fig. 5.5(b) and 5.5(d) as well as Tables 5.2 and 5.3. It was observed that binder pre-activation enhances bending stiffness, attributable to the improved cohesion provided by the molten binder [19]. When the fabric is subjected to heat, the binder melts and coats the fiber tows, increasing inter- and intra-tow friction and consequently bending stiffness. This effect was more pronounced in the dry samples, indicating that the impregnation fluid viscosity tends to counteract the influence of the activated binder. Broberg et al. [38] also reported variations in bending stiffness in binder-stabilized non-crimp fabric, which could potentially lead to an increased propensity for wrinkle formation. Once again, two-sample T-tests were conducted, and none of the comparisons failed to reject the null hypothesis (Table 5.6).

Table 5.6: P-values obtained through T-Test comparing the normalized bending stiffness of specimens with and without stabilizing binder pre-activation under different impregnation conditions at 1 RPM.

Dry	Viscous 20	Viscous 100
5.63×10^{-4}	4.82×10^{-2}	4.24×10^{-3}

5.5 Conclusions

This study has shown that the applied angular velocity, pre- activation of the stabilizing binder, and the viscosity of the impregna tion fluid significantly influence the bending behavior of a carbon fiber unidirectional non-crimp fabric (UD-NCF), particularly at large curva tures, which are likely to occur in components with complex geometries fabricated via wet compression molding (WCM) process. More specif ically, pre-activation of the stabilizing binder and increased loading rate contributed to an increase in bending stiffness across all three infiltrated conditions (i.e., dry, infiltrated with 20 cSt silicone oil, and infiltrated with 100 cSt silicone oil), owing to increased friction between the car bon fiber tows and stitching yarns. However, infiltration of the fabric with a low viscosity fluid resulted in a decrease in bending stiffness relative to the dry condition due to decreased tow-stitch friction. In contrast, the decrease was less pronounced for the higher-viscosity oil infiltration condition considered in this study. The influence of pre- activated stabilizing binder and fabric impregnation observed in this investigation for the studied UD-NCF is expected to be similar for other types of binder-stabilized fabrics, although the magnitude of these ef fects may vary depending on the specific fabric architectures. It is important to note that for a WCM process, an additional binder pre- activation step will be required prior to dispensing resin on the fabric stack, which would increase process complexity to some extent due to heating requirements. In an industrial setting, the addition of this step would not affect the overall process cycle time, so long as the binder pre- activation time is less than the cure and demolding time.

The generated test data fills a critical gap in the literature and can help improve material models for future forming simulations of binder- stabilized UD-NCFs. An improved understanding of the bending behavior of UD-NCFs achieved in this study can also be used for opti mizing WCM processes. Optimizing the press closing speed and the resin viscosity may aid in suppressing the formation of macroscopic wrinkles. At the same time, the use of a binder-stabilized fabric will increase stiffness, which could lead to better resin management before mold closing while also influencing fabric formability. As shown, the use of a stabilizing binder notably influences the bending response of the studied UD-NCF, where an increase in bending stiffness may potentially reduce the number of wrinkles during forming at the expense of increasing their size as reported by Boisse et al. [11]. Similar findings were reported in Ref. [38], where the authors studied a binder-stabilized glass UD-NCF and observed an increase in wrinkle size due to higher fabric bending stiffness. However, forming of continuous reinforcements on complex- shaped molds induces in-plane shear deformation, which can also contribute to the formation of wrinkles on the fabric depending on the forming process boundary conditions. Haanappel et al. [49] investigated the

drapability of two fiber-reinforced thermoplastic materials on a mold with a double-curved surface, highlighting that bending stiffness, as well as intra-ply deformation and friction, significantly influence drapability. Significant wrinkling in the double-curved regions was observed, where the authors noted that the number and size of wrinkles are dependent on the fabric properties. Specifically, it was stated that fabrics with greater bending stiffness were more sensitive to wrinkle formation. Nevertheless, these studies have not identified an optimal range of bending stiffness, as the drapability of an engineering textile is influenced by multiple parameters. Despite the important contributions made through the study herein, the connection between bending stiff ness, formability, and associated defect formation remains unclear as it likely depends on additional factors, such as the number of layers, ply orientation, and mold shape. Therefore, establishing such a relationship for the studied binder-stabilized UD-NCF is left for future work. Broadly, this work aims to assess the potential trade-offs between increased fabric stiffness and formability for complex shapes typical of real-world applications.

Additional future work is planned that is worth mentioning. The bending behaviour of the UD-NCF along the transverse direction was not studied herein, given that the fabric bending stiffness along this direc tion is anticipated to be orders of magnitude lower than that along the longitudinal direction. The resolution of the rheometer would not adequately capture the low-magnitude transverse bending stiffness. Future work will focus on modifying the rheometer bending test setup to enable testing along the transverse direction. Finally, future studies will explore whether binder type, concentration, and form, fiber tow count, and stitching pattern influence the bending stiffness of the UD-NCFs. The rate-dependent bending response of the UD-NCF will also be studied, since related data is important for developing rate-dependent forming models.

References

[1] P. Ermanni, C. Di Fratta, and F. Trochu, "Wiley encyclopedia of composites," in John Wiley and Sons, 2012, ch. Molding: Liquid Composite Molding (LCM), pp. 1–10. [Online]. Available: https://doi.org/10.1002/9781118097298.weoc153.

[2] J. Viisainen, A. Hosseini, and M. Sutcliffe, "Experimental investigation, using 3d digital image correlation, into the effect of component geometry on the wrinkling behaviour and the wrinkling mechanisms of a biaxial ncf during preforming," *Composites Part A: Applied Science and Manufacturing*, vol. 142, p. 106 248, 2021, ISSN: 1359-835X. DOI: https://doi.org/10.1016/j.compositesa.2020.106248.

[Online]. Available: https://www.sciencedirect.com/science/article/pii/S1359835X20304838.

[3] P. Beardmore and C. Johnson, "The potential for composites in structural automotive applications," *Composites Science and Technology*, vol. 26, no. 4, pp. 251–281, 1986, ISSN: 0266-3538. DOI: https://doi.org/10.1016/0266-3538(86)90002-3. [Online]. Available: https://www.sciencedirect.com/science/article/pii/0266353886900023.

[4] F. Henning, L. Kärger, D. Dörr, F. J. Schirmaier, J. Seuffert, and A. Bernath, "Fast processing and continuous simulation of automotive structural composite components," *Composites Science and Technology*, vol. 171, pp. 261–279, Feb. 2019, ISSN: 0266-3538. DOI: 10.1016/J.COMPSCITECH.2018.12.007.

[5] T. M. Kruckenberg and R. Paton, Eds., *Resin Transfer Moulding for Aerospace Structures*. Springer Netherlands, 1998, ISBN: 978-94-010-5906-0. DOI: 10.1007/978-94-011-4437-7. [Online]. Available: http://link.springer.com/10.1007/978-94-011-4437-7.

[6] H. Yang, C.-C. Hsu, and C.-H. Hsu, "Three dimensional numerical simulations for wet-rtm process," in *35th Polymer Processing Society*, Cesme-Izmir, Turkey, 2019.

[7] J. Fels, G. Meirson, V. Ugresic, P. Dugsin, F. Henning, and A. Hrymak, "Mechanical property difference between composites produced using vacuum-assisted liquid compression molding and high-pressure injection resin transfer molding," in *Proceedings ACCE2017-17th Annual Automotive Composites Conference and Exhibition, Michigan*, Jun. 2017.

[8] M. Ghazimoradi, E. A. Trejo, V. Carvelli, C. Butcher, and J. Montesano, "Deformation characteristics and formability of a tricot-stitched carbon fiber unidirectional non-crimp fabric," *Composites Part A: Applied Science and Manufacturing*, vol. 145, p. 106 366, Jun. 2021, ISSN: 1359-835X. DOI: 10.1016/J.COMPOSITESA.2021.106366.

[9] A. Schnabel and T. Gries, "1 - production of non-crimp fabrics for composites," in *Non-Crimp Fabric Composites*, ser. Woodhead Publishing Series in Composites Science and Engineering, S. V. Lomov, Ed., Woodhead Publishing, 2011, pp. 3–41, ISBN: 978-1-84569-762-4. DOI: https://doi.org/10.1533/9780857092533.1.3. [Online]. Available: https://www.sciencedirect.com/science/article/pii/B9781845697624500011.

[10] L. Kärger, S. Galkin, E. Kunze, M. Gude, and B. Schäfer, "Prediction of forming effects in ud-ncf by macroscopic forming simulation–capabilities and limitations," in *ESAFORM 2021 - 24th International Conference on Material Forming*, Liège, Belgium, 14-16 April 2021.

[11] P. Boisse, N. Hamila, E. Guzman-Maldonado, A. Madeo, G. Hivet, and F. Dell'Isola, "The bias-extension test for the analysis of in-plane shear properties of textile composite reinforcements and prepregs: A review," *International Journal of Material Forming*, vol. 10, pp. 473–492, 2017.

[12] C. D. Rudd, A. C. Long, K. N. Kendall, and C. G. E. Mangin, *Liquid Moulding Technologies*. Amsterdam, The Netherlands: Elsevier, 1997, ISBN: 0768000165. DOI: 10.1533/9781845695446.

[13] R. Kumar, K. Rashvand, A. Fraisse, A. Sarhadi, and T. L. Andersen, "Experimental testing method to characterise the drapability of ud non-crimp fabrics used in wind turbine blades," *IOP Conference Series: Materials Science and Engineering*, vol. 1293, no. 1, p. 012 020, Nov. 2023. DOI: 10.1088/1757-899X/1293/1/012020. [Online]. Available: https://dx.doi.org/10.1088/1757-899X/1293/1/012020.

[14] G. Estrada, C. Vieux-Pernon, and S. G. Advani, "Experimental characterization of the influence of tackifier material on preform permeability," *Journal of Composite Materials*, vol. 36, no. 19, pp. 2297–2310, 2002. DOI: 10.1177/0021998302036019542. eprint: https://doi.org/10.1177/0021998302036019542. [Online]. Available: https://doi.org/10.1177/0021998302036019542.

[15] J. C. Brody and J. W. Gillespie, "The effects of a thermoplastic polyester preform binder on vinyl ester resin," *Journal of Thermoplastic Composite Materials*, vol. 18, no. 3, pp. 157–179, 2005. DOI: 10.1177/0892705705043535. eprint: https://doi.org/10.1177/0892705705043535. [Online]. Available: https://doi.org/10.1177/0892705705043535.

[16] H. M. Yoo, J. W. Lee, J. S. Kim, and M. K. Um, "Influence of non-reactive epoxy binder on the permeability and friction coefficient of twill-woven carbon fabric in the liquid composite molding process," *Applied Sciences*, vol. 10, no. 20, p. 7039, 2020, ISSN: 2076-3417. DOI: 10.3390/app10207039. [Online]. Available: https://www.mdpi.com/2076-3417/10/20/7039.

[17] S. Neunkirchen, M. Bender, and R. Schledjewski, "Effect of binder activation on in-plane capillary flow in multilayer stacks of carbon fiber fabrics," *Applied Composite Materials*, vol. 31, pp. 709–719, 2 Apr. 2024, ISSN: 0929-189X. DOI: 10.1007/s10443-023-10198-6. [Online]. Available: https://link.springer.com/10.1007/s10443-023-10198-6.

[18] K. Wei, D. Liang, M. Mei, D. Wang, X. Yang, and Z. Qu, "Preforming behaviors of carbon fiber fabrics with different contents of binder and under various process parameters," *Composites Part B: Engineering*, vol. 166, pp. 221–232, 2019, ISSN: 1359-8368. DOI: https://doi.org/10.1016/j.compositesb.2018.11.143. [Online]. Available: https://www.sciencedirect.com/science/article/pii/S1359836818326568.

[19] R. M. Portela, B. Schäfer, L. Kärger, A. R. de Faria, and J. Montesano, "Influence of viscosity, binder activation, and loading rate on the membrane response of an infiltrated ud-ncf," in *ESAFORM 2024 - 27th International Conference on Material Forming*, Apr. 2024.

[20] P. H. Broberg, F. Shakibapour, J. Jakobsen, E. Lindgaard, and B. L. V. Bak, "Characterisation of the transverse shear behaviour of binder-stabilised preforms for wind turbine blade manufacturing," 2023. DOI: 10.17632/9m78sg3zwn.1. [Online]. Available: http://creativecommons.org/licenses/by/4.0/.

[21] C. T. Poppe, C. Krauß, F. Albrecht, and L. Kärger, "A 3D process simulation model for wet compression moulding," *Composites Part A: Applied Science and Manufacturing*, vol. 145, p. 106 379, Jun. 2021, ISSN: 1359-835X. DOI: 10.1016/J.COMPOSITESA.2021.106379.

[22] J. Pourtier, B. Duchamp, M. Kowalski, X. Legrand, P. Wang, and D. Soulat, "Bias extension test on a bi-axial non-crimp fabric powdered with a non-reactive binder system," in *ESAFORM 2018 - 21st International Conference on Material Forming*, Palermo, Italy, 23. and 25. of April 2018.

[23] E. De Bilbao, D. Soulat, G. Hivet, and A. Gasser, "Experimental Study of Bending Behaviour of Reinforcements," *Experimental Mechanics*, vol. 50, pp. 333–351, 2010. DOI: 10.1007/s11340-009-9234-9.

[24] T. Martin, D. Bhattacharyya, and I. Collins, "Bending of fibre-reinforced thermoplastic sheets," *Composites Manufacturing*, vol. 6, no. 3, pp. 177–187, 1995, 3rd International Conference on Flow Processes in Composite Materials 94, ISSN: 0956-7143. DOI: https://doi.org/10.1016/0956-7143(95)95009-N. [Online]. Available: https://www.sciencedirect.com/science/article/pii/095671439595009N.

[25] P. Boisse, "Wiley encyclopedia of composites," in John Wiley and Sons, 2012, ch. Composite fiber reinforcement forming, pp. 1–16. [Online]. Available: https://doi.org/10.1002/9781118097298.weoc037.

[26] P. Boisse, J. Colmars, N. Hamila, N. Naouar, and Q. Steer, "Bending and wrinkling of composite fiber preforms and prepregs. A review and new developments in the draping simulations," *Composites Part B: Engineering*, vol. 141, pp. 234–249, May 2018, ISSN: 1359-8368. DOI: 10.1016/J.COMPOSITESB.2017.12.061.

[27] W. R. Yu, M. Zampaloni, F. Pourboghrat, K. Chung, and T. J. Kang, "Analysis of flexible bending behavior of woven preform using non-orthogonal constitutive equation," *Composites Part A: Applied Science and Manufacturing*, vol. 36, no. 6, pp. 839–850, 2005, ISSN: 1359835X. DOI: 10.1016/j.compositesa.2004.10.026.

[28] U. Sachs and R. Akkerman, "Viscoelastic bending model for continuous fiber-reinforced thermoplastic composites in melt," *Composites Part A: Applied Science and Manufacturing*, vol. 100, pp. 333–341, Sep. 2017, ISSN: 1359835X. DOI: 10.1016/J.COMPOSITESA.2017.05.032.

[29] R. Sourki, B. Khatir, S. S. Najar, R. Vaziri, and A. S. Milani, "Characterization of the dissipative large deformation bending response of dry fabric composites as occurs during forming," *Composite Structures*, vol. 310, p. 116 728, 2023.

[30] T. Senner, S. Kreissl, M. Merklein, M. Meinhardt, and A. Lipp, "Bending of unidirectional non-crimp-fabrics : experimental characterization , constitutive modeling and application in finite element simulation," pp. 1–10, 2015. DOI: 10.1007/s11740-014-0568-5.

[31] C. Krogh, P. H. Broberg, J. Kepler, and J. Jakobsen, "Comprehending the bending: A comparison of different test setups for measuring the out-of-plane flexural rigidity of a ud fabric," *Key Engineering Materials*, vol. 926, pp. 1257–1267, Jul. 2022, ISSN: 1662-9795. DOI: 10.4028/p-r883x4. [Online]. Available: https://www.scientific.net/KEM.926.1257.

[32] C. Poppe, T. Rosenkranz, D. Dörr, and L. Kärger, "Comparative experimental and numerical analysis of bending behaviour of dry and low viscous infiltrated woven fabrics," *Composites Part A: Applied Science and Manufacturing*, vol. 124, p. 105 466, Sep. 2019, ISSN: 1359-835X. DOI: 10.1016/J.COMPOSITESA.2019.05.034.

[33] F. T. T. I. Peirce, "The 'handle' of cloth as a measurable quantity," *Journal of the Textile Institute Transactions*, 1930. DOI: 10.1080/19447023008661529. [Online]. Available: https://www.tandfonline.com/action/journalInformation?journalCode=jtit20.

[34] B. Liang, P. Chaudet, and P. Boisse, "Curvature determination in the bending test of continuous fibre reinforcements," *Strain*, vol. 53, no. 1, pp. 1–12, 2017, ISSN: 14751305. DOI: 10.1111/str.12213.

[35] B. Liang, N. Hamila, M. Peillon, and P. Boisse, "Analysis of thermoplastic prepreg bending stiffness during manufacturing and of its influence on wrinkling simulations," *Composites Part A: Applied Science and Manufacturing*, vol. 67, pp. 111–122, 2014, ISSN: 1359835X. DOI: 10.1016/j.compositesa.2014.08.020. [Online]. Available: http://dx.doi.org/10.1016/j.compositesa.2014.08.020.

[36] T. G. Clapp, H. Peng, T. K. Ghosh, and J. W. Eischen, "Indirect measurement of the moment-curvature relationship for fabrics," *Textile Research Journal*, vol. 60, pp. 525–533, 9 1990, ISSN: 00405175. DOI: 10.1177/004051759006000906.

[37] P. H. Broberg *et al.*, "One-click bending stiffness: Robust and reliable automatic calculation of moment–curvature relation in a cantilever bending test," *Composites Part B: Engineering*, vol. 260, p. 110 763, 2023.

[38] P. H. Broberg *et al.*, "That's how the preform crumples: Wrinkle creation during forming of thick binder-stabilised stacks of non-crimp fabrics," *Composites Part B: Engineering*, vol. 273, p. 111 269, 2024, ISSN: 1359-8368. DOI: https://doi.org/10.1016/j.compositesb.2024.111269. [Online]. Available: https://www.sciencedirect.com/science/article/pii/S1359836824000805.

[39] P. H. Broberg, E. Lindgaard, A. J. Thompson, J. P.-H. Belnoue, S. R. Hallett, and B. L. Bak, "An accurate forming model for capturing the nonlinear material behaviour of multilayered binder-stabilised fabrics and predicting fibre wrinkling," *Composites Part B: Engineering*, vol. 274, p. 111 268, 2024, ISSN: 1359-8368. DOI: https://doi.org/10.1016/j.compositesb.2024.111268. [Online]. Available: https://www.sciencedirect.com/science/article/pii/S1359836824000799.

[40] M. Ghazimoradi, E. A. Trejo, C. Butcher, and J. Montesano, "Characterizing the macroscopic response and local deformation mechanisms of a unidirectional non-crimp fabric," *Composites Part A: Applied Science and Manufacturing*, vol. 156, p. 106 857, May 2022, ISSN: 1359-835X. DOI: 10.1016/J.COMPOSITESA.2022.106857.

[41] M. Ghazimoradi and J. Montesano, "Macroscopic forming simulation for a unidirectional non-crimp fabric using an anisotropic hyperelastic material model," *Applied Composite Materials*, pp. 1–23, 2023.

[42] K. Rouf, M. J. Worswick, and J. Montesano, "A multiscale framework for predicting the mechanical properties of unidirectional non-crimp fabric composites with manufacturing induced defects," *Journal of Composite Materials*, vol. 55, pp. 741–757, 6 Mar. 2021, ISSN: 1530793X. DOI: 10.1177/0021998320958189.

[43] S. V. Lomov, I. Verpoest, T. Peeters, D. Roose, and M. Zako, "Nesting in textile laminates: Geometrical modelling of the laminate," *Composites Science and Technology*, vol. 63, pp. 993–1007, 7 2003, ISSN: 02663538. DOI: 10.1016/S0266-3538(02)00318-4.

[44] H. Heß and N. Himmel, "Structurally stitched ncf cfrp laminates. part 1: Experimental characterization of in-plane and out-of-plane properties," *Composites Science and Technology*, vol. 71, pp. 549–568, 5 Mar. 2011, ISSN: 02663538. DOI: 10.1016/j.compscitech.2010.11.012.

[45] J. Wang, H. Lin, A. Long, M. Clifford, and P. Harrison, "Predictive modelling and experimental measurement of the bending behaviour of viscous textile composites," in *International ESAFORM Conference on Materials Forming*, Glasgow, U.K., Apr. 2006.

[46] G. Abbott and P. Grosberg, "The fabric cantilever," *Textile Research Journal*, vol. 36, pp. 930–932, 10 Oct. 1966, ISSN: 0040-5175. DOI: 10.1177/004051756603601013. [Online]. Available: https://journals.sagepub.com/doi/10.1177/004051756603601013.

[47] P. Grosberg, "The mechanical properties of woven fabrics part ii: The bending of woven fabrics," *Textile research journal*, vol. 36, no. 3, pp. 205–211, 1966.

[48] T. J. Lahey and G. R. Heppler, "Mechanical modeling of fabrics in bending," *Journal of Applied Mechanics*, vol. 71, pp. 32–40, 1 Jan. 2004, ISSN: 0021-8936. DOI: 10.1115/1.1629757. [Online]. Available: https://asmedigitalcollection.asme.org/appliedmechanics/article/71/1/32/465514/Mechanical-Modeling-of-Fabrics-in-Bending.

[49] S. P. Haanappel, R. H. Ten Thije, U. Sachs, B. Rietman, and R. Akkerman, "Formability analyses of uni-directional and textile reinforced thermoplastics," *Composites Part A: Applied Science and Manufacturing*, vol. 56, pp. 80–92, 2014, ISSN: 1359835X. DOI: 10.1016/j.compositesa.2013.09.009. [Online]. Available: http://dx.doi.org/10.1016/j.compositesa.2013.09.009.

Chapter 6

Characterizing and modelling the time-dependent compaction response of an infiltrated binder-stabilized unidirectional non-crimp fabric

The contents of this chapter stem from the following paper: R. M. Portela, B. Schäfer, L. Kärger, A. R. de Faria, and J. Montesano, "Characterizing and modelling the time-dependent compaction response of an infiltrated binder-stabilized unidirectional non-crimp fabric," Manuscript submitted (under review).

This chapter presents the compaction characterization of dry and infiltrated binder-stabilized UD-NCF using a punch-to-plate test setup. Finally, the time-dependent compaction behavior was modeled using rheological models.

6.1 Overview

In wet compression molding (WCM), understanding the compaction behavior of infiltrated engineering textiles is essential, as it impacts the microstructure and fiber volume fraction of the finished part. Incorporating binder-stabilized reinforcements may be necessary in WCM to improve material handling and enhance part quality. This research aims to characterize and model the time-dependent compaction behavior of an infiltrated, binder-stabilized carbon fiber unidirectional non-crimp fabric (UD-NCF) through multi-phase

experiments, specifically focusing on effects of resin viscosity, stacking sequence, and binder pre-activation. Findings indicate that infiltrated fabric requires lower compaction forces compared to dry fabric, mainly due to the lubrication of tows and stitching, which reduces tow-stitch friction and provides less resistance to tow spreading. Furthermore, compaction forces increase with binder pre-activation across all conditions tested, while the degree of relaxation is reduced with pre-activation of the binder. Lastly, the stacking sequence has a minor influence on the compaction response as reported in previous studies. Maxwell and fractional Zener models are considered to capture the fabric time-dependent response, with the latter providing an improved fit to the experimental data. This is the first detailed investigation on compaction behavior of infiltrated binder-stabilized UD-NCFs, offering new and important insights into their complex mechanical response.

6.2 Introduction

6.2.1 Research motivation

Wet Compression Molding (WCM) is a manufacturing process that is especially advantageous for mass production with highly reactive resins, owing to low cycle times. Specialized equipment such as metering units for resin injection or large presses is not required, which simplifies the process and lowers overall manufacturing costs. Poppe et al. [1] describe the direct variant of the WCM process (Figure 6.1a). The direct variant involves five steps: fabric cutting and stacking, resin application, inserting the stack into the pre-heated mold, forming and molding, and curing, followed by demolding the final composite component. A key characteristic of the direct variant is a simultaneous fabric forming and resin infiltration step. Conversely, the WCM process also has an indirect variant (refer to Figure 6.1b) that separates the forming and resin infiltration steps, resulting in an additional preforming step before resin application.

The manufacturing of WCM parts involves continuous reinforcement materials such as woven and unidirectional non-crimp fabrics (UD-NCF). Overall, woven fabrics typically offer better drapability compared to UD-NCFs. However, UD-NCFs have gained attention in several industry sectors as a suitable alternative for various liquid composite molding processes, including WCM. UD-NCF composites exhibit improved in-plane mechanical properties and greater anisotropic property tailorability when compared to woven fabric, resulting in a greater lightweight performance [2]. UD-NCFs comprise aligned fiber tows that are held together by stitching yarns that ensure the structural integrity of the reinforcement and stabilize the textile [2–5]. Moreover, UD-NCFs are characterized by the

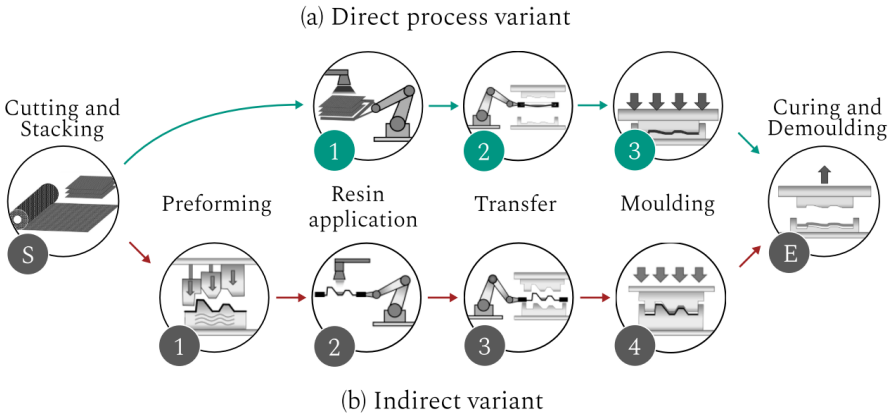


Figure 6.1: Schematic of the wet compression molding (WCM) process steps: (a) direct variant, and (b) indirect variant [1].

absence of interlacing, unlike woven fabrics. This property results in aligned fiber tows and enhances in-plane mechanical properties [6].

When producing structural components that require multiple layers of UD-NCF oriented in different directions to meet specific performance requirements, the resulting WCM components can be relatively thick. Manufacturing such thick parts using the direct WCM process variant involves applying a substantial amount of resin onto the fabric stack and transferring it into the mold. However, producing such components—especially in molds with deep cavities—presents challenges related to resin management, as the UD-NCF stack may drape under gravity prior to closing the mold due to its limited bending stiffness. A promising solution to address this issue is the use of binder-stabilized UD-NCF, where preactivation of the binder before applying resin onto the flat stack and transferring into the mold may provide increased fabric bending stiffness [7, 8] and enable improved resin management. Stabilizing binders are either thermoplastic or uncatalyzed epoxy resins, available in either solvent-based liquid or dry powder form [9–11]. Stabilizing binders are typically used to keep fabric layers adhered to one another and maintain fabric integrity during operations such as trimming and handling [9], while they are necessary for preforming UD-NCF stacks. However, the use of binder-stabilized fabrics may also introduce challenges, as they can affect processing conditions and the formability of the fabric. Some of these challenges would also apply to the indirect WCM variant, where the binder-stabilized UD-NCF is preformed prior to introducing resin on the fabric within the mold.

The study of fabric compaction is important due to its influence on the mold filling behavior, especially for the WCM process, and on the final composition of the final com-

posite part, including the fiber volume fraction, and the resulting mechanical performance. Bickerton et al. [12] outline that during transverse compression, the stress-strain behavior of the fiber bed exhibits viscoelastic characteristics, which are influenced by the lubrication state. Yong et al. [13] state that in manufacturing processes with rigid-closed molds (i.e., WCM), the determination of whether the desired fiber volume fraction can be achieved is given by the reaction force on the tooling surface, which depends on the compaction response. Other characteristics of the stack can also be affected by the compaction mechanism, like the textile permeability. Werlen et al. [14] explain that during the compaction process, the textile layers are pressed together, forcing them to slide against each other and rearrange inside the mold, generating friction forces. In manufacturing processes like WCM the textile might be lubricated, which tends to reduce the friction between adjacent layers and ease the relative sliding between layers [13, 14].

6.2.2 State-of-the-Art

6.2.2.1 Compaction behavior

Previous investigations explored the compaction behavior of infiltrated woven fabrics, aiming to understand the influencing parameters. Poppe et al. [15] investigated the influence of shear angle, fabric impregnation, and nesting on the response of a carbon fiber woven fabric stack. They found that both shear angle and fabric impregnation contribute to an increase in the compaction force. The fluid saturating the fabric stack creates hydraulic pressure that opposes the applied compaction force. They also studied the impact of different stacking sequences (e.g., $[0]_4$ and $[0/45]_2$) and concluded that for woven fabric, the stacking sequences with the fiber tows aligned in parallel ($[0]_4$) exhibited a greater overlapping at interface, also known as nesting, thereby decreasing the necessary compaction force.

Additional studies have focused on the compaction mechanisms of non-crimp fabrics, considering various process parameters. Schäfer et al. [16] characterized UD- and biaxial-NCFs with different stacking sequences and fiber orientations at interfaces. It was noted that resistance to compaction decreases as the number of layers increases, although this effect diminishes beyond a certain number of layers. They also observed limited nesting in UD-NCFs compared to biaxial-NCFs, which can be attributed to the supporting glass fibers that are orthogonal to the carbon fiber tows, thereby preventing a more pronounced nesting effect in the UD-NCF layers. Li et al. [17] investigated the effects of cyclic compactions, number of layers, stitching patterns (such as tricot, chain, and tricot-chain),

compression rate, and fabric impregnation for carbon fiber NCF. They found that lubrication has little impact on the compaction behavior due to low friction, but impregnation influences relaxation response. Nesting caused by sunken stitching yarns was also noted by Droste et al. [18].

Recent research has examined the time-dependent compaction response of binder-stabilized fabrics. Wei et al. [19] analyzed how different concentrations of liquid stabilizing binder (0%, 4%, 8%, and 12%) affect the compression of various carbon fiber textiles, including two variations of woven fabric, a biaxial NCF, and a multiaxial NCF. The authors observed that as the binder concentration increases, the elastic modulus decreases, while the normalized relaxation stress increases, indicating an improvement of the stack relaxation ability. In another study, Wei et al. [20] investigated the influence of process parameters (e.g., compression speed, maximum pressure, and holding time) on the compaction behavior of binder-stabilized fabric in different weight concentrations of binder. The authors reported an increase in the initial stack thickness with the increase in binder concentration. Another finding in this investigation was the increase in the recovery thickness with the increase of maximum pressure, regardless of the binder content. Additionally, they also reported a possibility of raising the fiber volume fraction by reducing the compression rate. Although both studies reported important findings regarding the influence of the stabilizing binder, they were limited to a liquid stabilizing binder; therefore, they were unable to investigate the effect of pre-activating the stabilizing binder. These studies also did not consider the influence of the impregnation of binder-stabilized fabric, which is critical for the WCM process.

6.2.2.2 Compaction modeling

The compaction response of engineering textile stacks has been considered in several previous studies. Poppe et al. [15] developed and validated coupled finite element forming and fluid-submodels to simulate the three-dimensional WCM process. They stated that the forming submodel can reproduce the non-linear viscoelastic compaction response of a woven fabric stack without numerical locking. Mitsch et al. [21] proposed and validated a computationally efficient 3D modeling approach that includes nonlinear compaction modeling, enabling the simulation of the thermoforming process of thermoplastic composites. The nonlinear time-dependent nature of fabric compaction prompted the use of rheological-based material models, combining elastic springs and viscous dashpots, such as Maxwell, Burgers, and Zener models. In the Maxwell model, the viscoelastic behavior of a given material is described by a combination in series of a spring and a dashpot. In the Burgers model, the viscoelasticity is characterized by the combination of a spring and a dashpot in

series (Maxwell element) together with a spring and a dashpot in parallel (Kelvin–Voigt element) [22, 23]. Finally, the Zener model consists of a spring and a dashpot in series with a second spring in parallel [24]. Echaabi et. al. [25] compared all three rheological models and reported that the Maxwell model returned the most accurate results among the three for relaxation time. Danzi et al. [26] proposed a three-branch Maxwell model with strain-dependent springs and strain-rate-dependent dashpots (Figure 6.2) to describe the time-dependent compaction response of a dry carbon fiber woven fabric bed. The authors reported that this model is valid across different fiber volume fractions and strain rates. The same three-branch Maxwell model was later adopted by Werlen et al. [14] to strike a balance between accuracy and complexity. They reported that the three-branch Maxwell model can yield accurate results for a wide range of experimental configurations (e.g., fabric architecture, fiber volume fraction, and fabric impregnation state). However, modelling the viscoelastic behavior is a challenging task and can require a considerable number of springs and dashpots to fit experimental data adequately. The three-branch Maxwell model for a one-dimensional stress case requires calibration of seven parameters (E_0, E_1, τ_1, E_2, τ_2, E_3, τ_3) [27, 28]. Da Costa-Haveroth et al. [28] state that these experiments can generate too many parameters to be identified and proposed the implementation of fractional derivatives to approach the problem. Fractional derivatives can describe the viscoelastic behavior and provide a good curve-fitting property by providing a lower mean square error with fewer input parameters [29, 30]. Hence, Da Costa-Haveroth et al. [28] propose the fractional Zener model as an alternative to the Maxwell model, replacing the viscoelastic branches (Figure 6.2) by a spring-pot or Scott-Blair element, illustrated in Figure 6.3a. The result of this replacement is a system with four parameters (E_0, E_1, α, p) as shown in Figure 6.3b.

To obtain the material parameters that can accurately represent the time-dependent behavior captured during experiments, an optimization method should be applied to the problem. Several optimization methods have been adopted for this purpose, including Simplex [14] and Particle Swarm Optimization (PSO). Werlen et al. [14] obtained the material parameters for the Maxwell model by applying a finite difference method, which was optimized with the Simplex optimization algorithm. This optimization approach was implemented, obtaining three parameters while the other four were fixed, which can make the optimization process time-consuming and computationally expensive. The PSO is a heuristic method extensively recommended for inverse optimization problems in which the material parameters are sought to fit experimental curves, as is the current investigated problem [27, 31]. The optimization process is heuristic due to a few or a lack of initial assumptions related to the optimized problem [28, 32]. Although the PSO can provide no guarantee of global minimum value, the optimization process is capable of searching

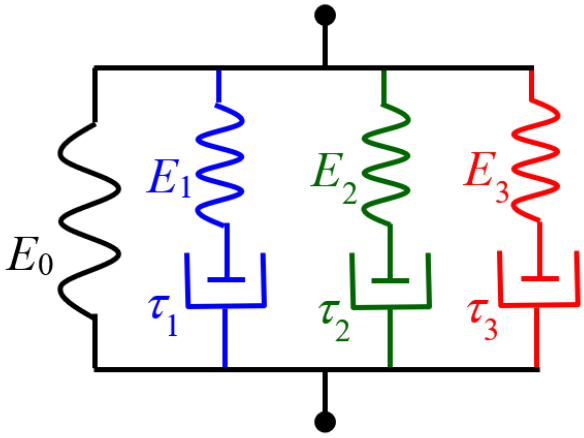
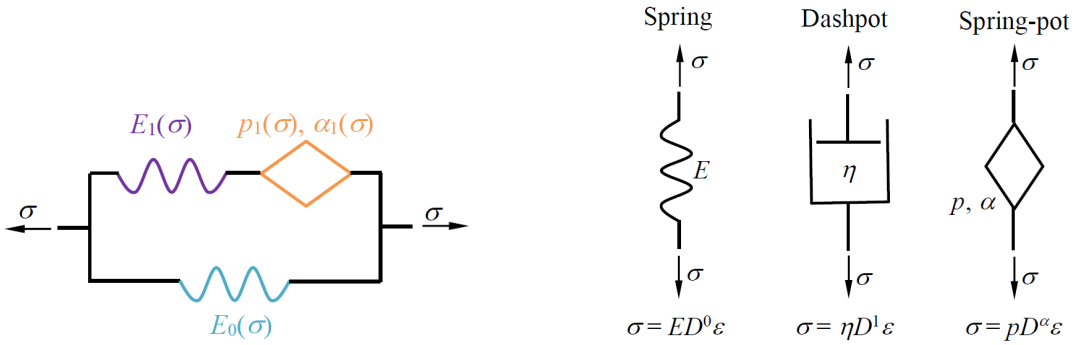


Figure 6.2: Schematic of the three-branch Maxwell model, including an elastic and three viscoelastic branches. The illustrated elements are defined as: springs (E_i) and dashpot (τ_j) [14].

large domains of possible solutions and requires no use of gradients. For this reason, the optimization problem has no requirement of differentiability, and the PSO is extensively applied in optimization problems that present irregularities or numerical noises [27].



(a) . (b) .

Figure 6.3: Schematics of: (a) Fractional Zener model, and (b) rheological elements. The illustrated elements are defined as: springs (E_i), dashpots (τ_j), stress (σ), strain (ε), fractional derivative order (α), proportionality factor (p) and the fractional derivative operator (D) [28].

6.2.3 Research goal

The overall goal of this investigation is to characterize and model the time-dependent compaction response of an infiltrated binder-stabilized unidirectional non-crimp fabric stack, focusing on the effects of viscosity, binder pre-activation, and stacking sequence. A set of experiments was conducted whereby 8-layer bindered fabric stacks were subjected to compaction load relaxation cycles for eight distinct conditions. Both Maxwell and fractional Zener rheological models are fit to the compaction response data using the PSO method to establish the fabric stack compaction behavior parameters.

6.3 Methodology

6.3.1 Materials and specimen preparation

A binder-stabilized UD-NCF, specifically PX35-UD300 (Zoltek, US), was examined. The fabric comprises aligned 50K continuous PX35 carbon fiber (CF) tows that are secured with a 76 dtex polyester yarn in a tricot pattern and supported with low linear density transversely oriented glass fiber (GF) yarns to enhance handleability. The textile also contains a thermosetting polymer powder binder dispersed on the side with the stitch tricot pattern, resulting in a total areal density of 333 g/m^2 (see Ghazimoradi et al. [2]

for further details). Square specimens measuring 100 mm × 100 mm were cut from a roll using an automated cutting table (Zünd Systemtechnik AG, Switzerland) in both 0° and 45° orientations. These layers were stacked with either a $[0]_8$ or $[0/45]_4$ sequence to mimic compaction of an 8-layer stack during the WCM process. A subset of the stacks was placed on trays in an industrial oven at 120°C for 20 minutes to pre-activate the stabilizing binder present on each layer of the stack. Additionally, some specimens were impregnated with silicone oils with either 20 cSt or 100 cSt viscosities—similar to that of various resins at elevated temperatures. The impregnation involved soaking the stack in a silicone oil bath for 15 minutes, then draining excess oil for another 15 minutes, as shown in Figure 6.4.

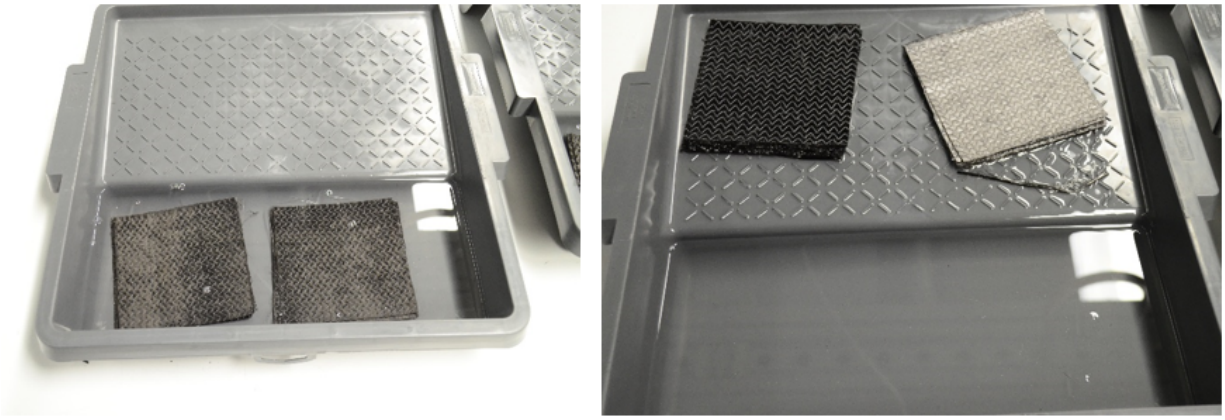


Figure 6.4: Specimens soaking procedure: (a) silicone bath for 15 minutes to fully impregnate the stack, (b) drain process to remove the silicone excess.

6.3.2 Punch-to-plate compaction test

The compaction tests were performed using an Inspekt universal testing machine equipped with a 5 kN load cell and a 56 mm diameter metal punch and flat plate to compress the fabric sample (Figure 6.5). The load cell measured the force, which was later converted into nominal stress by dividing the force by the punch area, and the displacement was converted into strain by calculating the change in height divided by the initial stack height. The stress-strain values were used to obtain the compaction parameters. All compaction tests were conducted at room temperature under eight different conditions, four per stacking sequence (Table 6.1). For each stacking sequence, one condition involved dry samples without pre-activation of the stabilizing binder (IT), while for the other three conditions,

the binder was pre-activated (AT). For two of these conditions, the samples were impregnated in silicone oil with a viscosity of 20 or 100 cSt. For each condition, four repeat tests were performed, yielding a total of 32 tests.

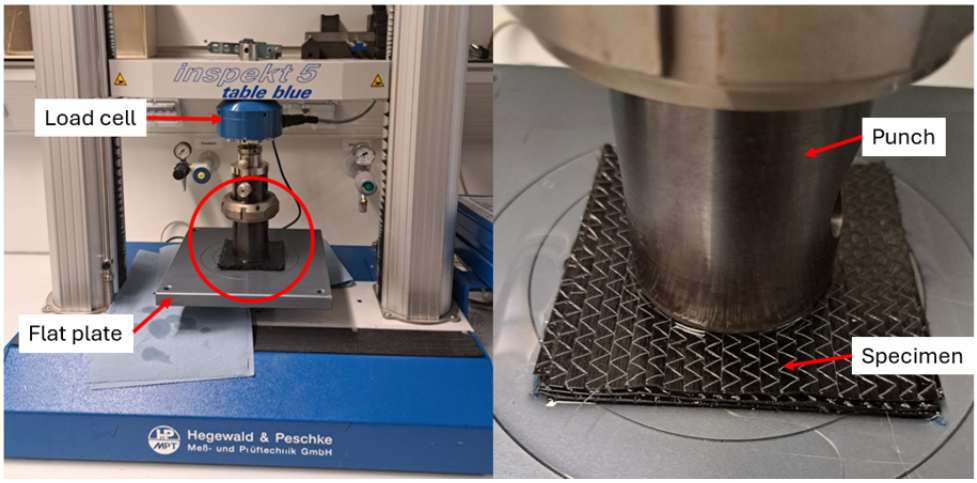


Figure 6.5: Punch-to-plate compaction test setup for the 8-layer carbon fiber UD-NCF.

Table 6.1: Conditions of the samples tested using the punch-to-plate compaction test setup, including different infiltrated fluid viscosities (dry, 20 cSt, and 100 cSt) and binder state (IT and AT).

Condition	Stacking sequence	Viscosity	Binder state	Number of tested specimens
1	$[0/45]_4$	Dry	Inactivated	4
2	$[0/45]_4$	Dry	Pre-activated	4
3	$[0/45]_4$	20 cSt	Pre-activated	4
4	$[0/45]_4$	100 cSt	Pre-activated	4
5	$[0]_8$	Dry	Inactivated	4
6	$[0]_8$	Dry	Pre-activated	4
7	$[0]_8$	20 cSt	Pre-activated	4
8	$[0]_8$	100 cSt	Pre-activated	4

The compaction load-relaxation cycle applied to the fabric stacks was similar to that used by Droste et al. [18]. The load-relaxation cycle was conducted in six phases (Figure 6.6) to analyse the compaction mechanism response of both WCM variants presented in Figure 1.2. This includes the pre-forming phase for the indirect variant, which features an

additional step compared to the direct variant. Each test was performed in displacement control with a rate of 1 mm/min and a precision of displacement measurement of 0.01 mm. During Phase I (i.e., first compaction), the punch was initially positioned 6 mm above the flat plate without contacting the stack specimen and displaced downwards to a pre-determined height of 2.5 mm to compact the sample. The first vertical dashed line in the figure indicates the moment of contact between the punch and the stack, at which point the compaction force begins to increase. Phase II (i.e., first relaxation) commences at the second dashed line and involves maintaining the stack at a constant height of 2.5 mm for a specific duration of 2 minutes. Phase III (i.e., first recovery) begins with the reduction of force to virtually 0 N, allowing a partial recovery of the stack's initial height. This reduced force is sustained during Phase IV for 5 minutes. In Phase V, the stack is compressed for a second time to a height of 2.5 mm. Finally, Phase VI involves holding the pre-assigned height constant for 3 minutes.

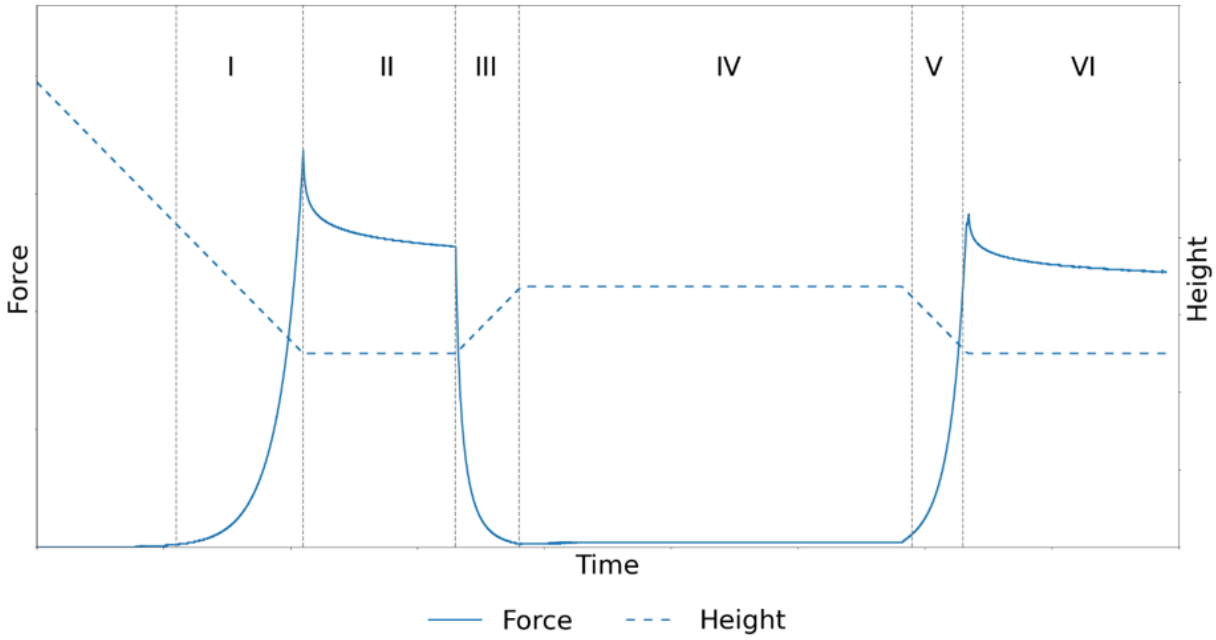


Figure 6.6: Six-phase load-relaxation cycle for compaction characterization.

The eight conditions were compared using different characterization metrics to better understand the influence of each parameter (e.g., pre-activation of the stabilizing binder and fabric impregnation). The first metric is the maximum nominal compressive stress, which is defined by the maximum compressive load divided by the punch area. Another

metric used in this study was the normalized relaxation stress λ, which is determined by:

$$\lambda = \frac{\sigma(t)}{\sigma_0} \tag{6.1}$$

where $\sigma(t)$ is the variation of the nominal stress during the relaxation phase, and σ_0 is the maximum nominal compression stress at the end of the compression phase. A third metric used was the stress relaxation ratio (r), which characterizes the degree of stress relaxation and is defined by:

$$r = \frac{\sigma_0 - \sigma_f}{\sigma_0} \tag{6.2}$$

where σ_f is the minimum nominal compression stress at the end of the relaxation phase. Lastly, the elastic recovery ratio (e) represents the percentage of elastic compression deformation to the total deformation and is defined as:

$$e = \frac{h_e - h_f}{h_i - h_f} \tag{6.3}$$

where h_i is the height where the punch touches the stack, h_e is the height where the punch returns at the end of the recovery phase, and h_f is the height where the punch is set to compress the stack ($h_e = 2.50$ mm).

To verify the statistical significance of the impregnation fluid viscosity, binder preactivation, and stacking sequence on the compaction response, pairwise analyses were conducted on compaction response metrics for two conditions using a two-sample T-test. The null hypothesis for a T-test assumes no difference between the sample data and is accepted when the corresponding p-value is greater than 0.05. Otherwise, the null hypothesis is rejected, indicating a statistically significant difference.

6.3.3 Implementation of rheological models

Fitting of experimental data was divided into two parts: the compaction and relaxation phases. The compaction phase was modelled with a nonlinear three-branch Maxwell model implemented by Bublitz et al [33] for the case of uniaxial stress. The first step involves calculating the elastic strain of each j branch (ε_j^e)

$$\varepsilon_j^{e,n+1} = \varepsilon_j^{e,n} \exp\left(-\frac{\Delta t}{\tau_j}\right) + \frac{\Delta\varepsilon}{\frac{\Delta t}{\tau_j}}\left(1 - \exp\left(-\frac{\Delta t}{\tau_j}\right)\right) \tag{6.4}$$

where τ_j denotes the damper parameters and Δt the time step size. The elastic modulus of each viscoelastic branch is defined as

$$E_j = a_j \exp\left((\varepsilon - \varepsilon^e) b_j\right), \tag{6.5}$$

where a_j and b_j are constant to be found, and ε is the total strain. Next, the stress in each viscoelastic branch is found by:

$$\sigma_j^{(n+1)} = \sigma_j^{(n)} \exp\left(-\frac{\Delta t}{\tau_j}\right) + \frac{\Delta \epsilon}{\frac{\Delta t}{\tau_j}} \left(E_j^{(n+1)} - E_j^{(n)} \left(-\frac{\Delta t}{\tau_j}\right)\right) \tag{6.6}$$

The j stress values are summed to the stress in the elastic branch, which varies with the fiber volume fraction (V_f). The V_f is defined as:

$$V_f = \frac{N A_w}{\rho_{fiber} h}, \tag{6.7}$$

where N denotes the number of layers, A_w represents the areal weight, ρ_{fiber} is the fabric density, and h the stack thickness. In this model, the fiber volume fraction influences the elastic modulus of the elastic branch, which is defined as:

$$E_0 = \frac{A}{V_f} \exp\left(B V_f^2\right), \tag{6.8}$$

where A and B are constant parameters to be determined. Finally, the stresses are defined as:

$$\sigma^{(n+1)} = E_0 \varepsilon^{(n+1)} + \sum_{j=1}^{N} \sigma_j^{(n+1)}, \tag{6.9}$$

The time-dependent compaction behavior or relaxation was captured using both the Maxwell and fractional Zener one-dimensional viscoelastic models. The Maxwell model, shown in Figure 2, involves seven parameters ($E_0, E_1, \tau_1, E_2, \tau_2, E_3, \tau_3$). Conversely, the fractional Zener model replaces the three spring and damper branches with a spring-pot element (see Figure 3a), reducing the number of parameters to four (E_0, E_1, p, α), as illustrated in Figure 3b. To capture the viscoelastic behavior using the Maxwell model, the time-dependent one-dimensional stress is defined as [26, 31, 34, 35]:

$$\sigma(t) = \sigma_0 + \sum_{j=1}^{n} \sigma_j(t), \tag{6.10}$$

where σ_0 represents the elastic stress, $\sigma_j(t)$ are the time-dependent stress terms, and n is the number of viscoelastic branches. Eq. (6.10) can be rewritten to represent the viscoelastic stress in terms of the spring constants (k_j), damper parameters, and the fabric strain, given by:

$$\sigma(t) = \left\{ k_0 + \sum_{j=1}^{n} k_j \exp\left(-\frac{t}{\tau_j}\right) \right\} \varepsilon(t). \tag{6.11}$$

Haveroth et al [27, 28] presented in detail the fractional Zener method as an alternative to capture nonlinear viscoelasticity, where the one-dimensional constitutive equation is given by:

$$\sigma(t) + \frac{p}{E_1} D_t^{\alpha} \sigma(t) = E_0 \varepsilon(t) + p \frac{E_0 + E_1}{E_1} D_t^{\alpha} \varepsilon(t), \tag{6.12}$$

where α, E_0, E_1, and p are material parameters that must be determined. E_0 and E_1 represent the sprigs of the elastic and viscoelastic portion of the fractional Zener model, respectively (see Figure 6.3b). Schmidt and Gaul [36] highlight that the value of α varies from 0 to 1. When $\alpha = 0$, the spring-pot element behaves as a spring, and the parameter p represents the spring stiffness. On the other hand, when $\alpha = 1$, the spring-pot element assumes a damper behavior, and the material parameter p represents the damper viscosity. D_t^{α} is the fractional derivative defined by Grünwald-Letnikov (GL) as:

$$D_t^{\alpha} f(t) = (\Delta t)^{-\alpha} \sum_{m=0}^{N-1} A_{m+1} f_m, \tag{6.13}$$

where $f(t)$ is a regular function with $f_m = f(t - mt/N)$, $\Delta t = t/N\,, (N > 0)$ is the time increment, and $A_{(m+1)}$ are the GL coefficients defined as:

$$A_{m+1} = \frac{\Gamma(m - \alpha)}{\Gamma(-\alpha)\Gamma(m + 1)}. \tag{6.14}$$

where Γ represents the usual Gamma function and $A_0 = 1$. Substituting Eq.(6.13) into Eq.(6.12):

$$\sigma(t) + \frac{p}{E_1} \Delta t^{-\alpha} \sum_{m=0}^{N-1} A_{m+1} \sigma_m = E_0 \varepsilon(t) + p\Big(\frac{E_0 + E_1}{E_1}\Big) \Delta t^{-\alpha} \sum_{m=0}^{N-1} A_{m+1} \varepsilon_m. \tag{6.15}$$

with $\sigma_m := \sigma(t - m\Delta t)$ and $\varepsilon_m := \varepsilon(t - m\Delta t)$. Separating the first term of the sum on both sides:

$$\sum_{m=0}^{N-1} A_{m+1} \beta_m = \beta_t + \sum_{m=1}^{N-1} A_{m+1} \beta_m, \quad \beta = \sigma, \epsilon, \tag{6.16}$$

where β denotes either σ or ε. With such a relation, Eq. (6.15) can be rewritten as:

$$\sigma(t)\Big(1+\frac{p}{E_1}\Delta t^{-\alpha}\Big)+\frac{p}{E_1}\Delta t^{-\alpha}\sum_{m=1}^{N-1}A_{m+1}\sigma_m = \tag{6.17}$$
$$\varepsilon(t)\Big(E_0+p\Big(\frac{E_0+E_1}{E_1}\Big)\Delta t^{-\alpha}\Big)+p\Big(\frac{E_0+E_1}{E_1}\Big)\Delta t^{-\alpha}\sum_{m=1}^{N-1}A_{m+1}\varepsilon_m,$$

and simplified to:

$$\sigma(t)(1+a)+aS_\sigma=\varepsilon(t)(E_0+b)+bS_\varepsilon, \tag{6.18}$$

where

$$a=\frac{p}{E_1}\Delta t^{-\alpha}, \tag{6.19}$$

$$b=p\Big(\frac{E_0+E_1}{E_1}\Big)\Delta t^{-\alpha}, \tag{6.20}$$

$$S_\sigma=\sum_{m=1}^{N-1}A_{m+1}\sigma_m, \tag{6.21}$$

$$S_\varepsilon=\sum_{m=1}^{N-1}A_{m+1}\varepsilon_m. \tag{6.22}$$

By solving Eq. (6.18) for $\sigma(t)$, the following is obtained:

$$\sigma(t)=\varepsilon(t)\frac{E_0+b}{1+a}+\frac{b}{1+a}S_\varepsilon-\frac{a}{1+a}S_\sigma. \tag{6.23}$$

The Maxwell and fractional Zener models were fitted to the compaction test data, and their respective parameters were determined using an optimization procedure. To save computational time, the material parameters were optimized using a vector of twenty-two experimental force values, spaced five seconds apart. These values were taken from Phase II of the compaction tests (Figure 6.6), and stresses were computed. The inverse optimization problem was defined as:

$$\text{Minimize } f:\mathbb{R}^n\longrightarrow\mathbb{R} \tag{6.24}$$

where f is the objective function given by:

$$\ell^2 \text{ norm} : f(X) = \sqrt{\sum_{n=1}^{N} (\sigma_{exp}^{(n)} - \sigma_{num}^{(n)}(X))^2}, \tag{6.25}$$

with $\sigma_{exp}^{(n)}$, and $\sigma_{num}^{(n)}$ being the experimental and numerical stresses, respectively. N represents the number of points, and $\bar{X}$ is the design variable vector. For the Maxwell model, the design vector is given by $\bar{X} = \left\{E_0, E_1, \tau_1, E_2, \tau_2, E_3, \tau_3\right\}^T$, also known as Prony-7. This design vector can be reduced to four variables (Prony-4) by setting the $\tau_i, i = 1, 2, 3$ to constant values, as suggested in Ref. [37]. However, this approach with variables may present greater error, as shown in Ref. [28]. For the fraction Zener model, the design vector is given by $\bar{X} = \left\{\alpha, p, E_0, E_1\right\}^T$. To obtain the material parameters, both rheological models were optimized by using the PSO method, where the Python library pymoo [38] was used. The optimization process was performed with a population size of 7,000 points distributed in the search region by the latin hypercube sampling method [39]. The optimization was performed with a maximum of 60,000 evaluations and 100 generations.

6.4 Results and discussion

6.4.1 Experimentally captured compaction response

To ensure data consistency across all conditions (Table 6.1), force and height values were interpolated within the relevant time range for the four specimens tested. For each condition, the mean and standard deviation of force were computed from the sample sets, represented as solid lines and shaded regions in Figure 6.7. The results across all tested conditions showed high repeatability with minimal variation in all phases. During the first compaction cycle (i.e., Phase I), all the samples exhibited a similar nonlinear deformation response with the forces nearly overlapping prior to reaching the peak force. Variation in the maximum compressive force was observed for the samples corresponding to the different conditions tested. The relaxation response during Phase II was also pronounced for each condition considered. During subsequent unloading (i.e., Phase III), both force and height measurements exhibited minimum variation. On the other hand, during the first dwell (i.e., Phase IV), samples for each condition exhibited a slightly different elastic recovery capacity. Additionally, it was observed that the specimens were not homogeneous in terms of the duration of their elastic recovery, which was evident through the shift in the height

measurements with time among the different conditions. This variation with respect to time was more evident during the second compaction cycle (i.e., Phase V). Moreover, in the second compaction cycle, the measurements of maximum force exhibited notable variation among the different conditions, as in the first compaction cycle. For each condition, the magnitude of the peak force was lower during the second compaction cycle when compared to the first cycle. This result is due to the exhibited tow nesting ($[0]_8$ specimens, see Figure 6.7c) and/or crimping ($[0/45]_4$ specimens) during the first compaction cycle, which required a greater magnitude of force. During the second compaction cycle, less force was required to achieve the same punch height. Lastly, the extent of stress relaxation during the second relaxation cycle (i.e., Phase VI) was notably less pronounced when compared to the first relaxation cycle for all conditions. Additional nesting/crimping of tows during Phase VI led to increased resistance to specimen deformation and, thus, a lower degree of relaxation during this phase. The subsequent sections provide an in-depth quantitative analysis of the results for each loading phase, with emphasis on the influence of binder pre-activation, stacking sequence, and infiltrated fluid viscosity on the compaction response of the samples.

6.4.1.1 Influence of the stabilizing binder pre-activation

During the first and fifth stages of loading, i.e., the initial and second compaction cycles, the Dry AT specimens exhibited greater average maximum compression stress in comparison to the Dry IT specimens for both stacking sequences considered (Figure 6.9). Figure 6.9 depicts the maximum compression stress (σ_0) for each of the eight conditions for the first (Figure 6.9(a) and 6.9(b)) and second (Figure 6.9(c) and 6.9(d)) compaction cycles. A difference in the average maximum stress between the Dry AT and Dry IT specimens of 15% and 13% was observed for the first compression cycle, and 15% and 14% for the second compression cycle for $[0]_8$ and $[0/45]_4$ specimens, respectively. Increased peak stress for the Dry AT specimens is due to the increased resistance to tow deformation caused by the activated binder that has coated the tows. However, these differences were not statistically significant, as shown in Table 2. The average maximum compression stresses for the second compaction cycle were less than that of the first compaction cycle for each of the Dry IT and Dry AT specimens owing to tow nesting/crimping, although the difference was not statistically significant (Table 3). The similarity between the maximum stress measurements in different compression cycles has been reported by Li et al. [17] for a carbon fiber non-crimp fabric. Some permanent deformation during the first two cycles was reported; however, the maximum stress remained within a similar range, which could be attributed to the capacity of the stack to recover. Grieser et a [40] have also reported

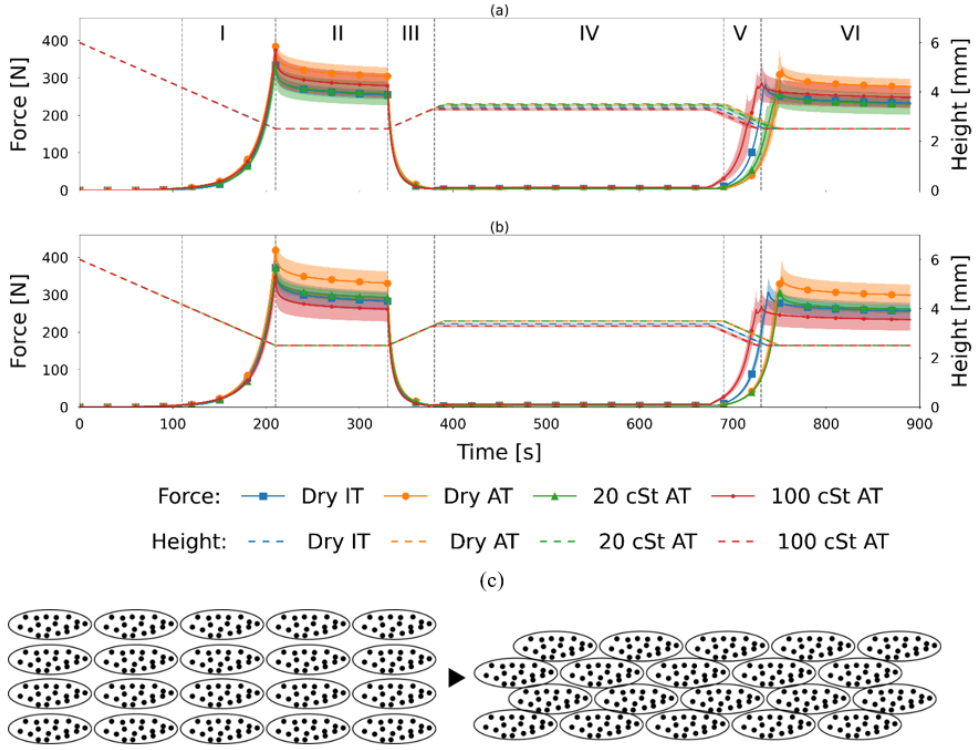


Figure 6.7: Compaction force response and punch height-time data for: (a) $[0]_8$ stacking sequence (Conditions 5–8), and (b) $[0/45]_4$ stacking sequence (Conditions 1–4). The Conditions cover different infiltration fluid viscosities as well as inactive (IT) and pre-activated (AT) binder states, see Table 6.1. (c) Schematic of the tow nesting phenomenon for $[0]_8$ specimens during Phase I.

a reduction in compaction stress as a result of repetitive compaction cycles.

Next, a comparison is conducted between the relaxation responses during Phases II and VI (Figure 6.7(a)), where the relaxation stress was normalized per Eq.(6.1). Figure 6.10 illustrates the normalized relaxation stress for each relaxation cycle for both stacking sequences. It is observed that for all four cases, the degree of relaxation for the Dry IT specimens was greater than that of the Dry AT specimens. A difference in the stress relaxation ratio of 15% and 14% was observed between the Dry IT and Dry AT specimens during the first relaxation cycle and 12% and 10% during the second relaxation cycle for the stacking sequences $[0]_8$ and $[0/45]_4$, respectively (Figure 6.11). Activation of the stabilizing binder resulted in a statistically significant difference in the degree of relaxation (Table 4).

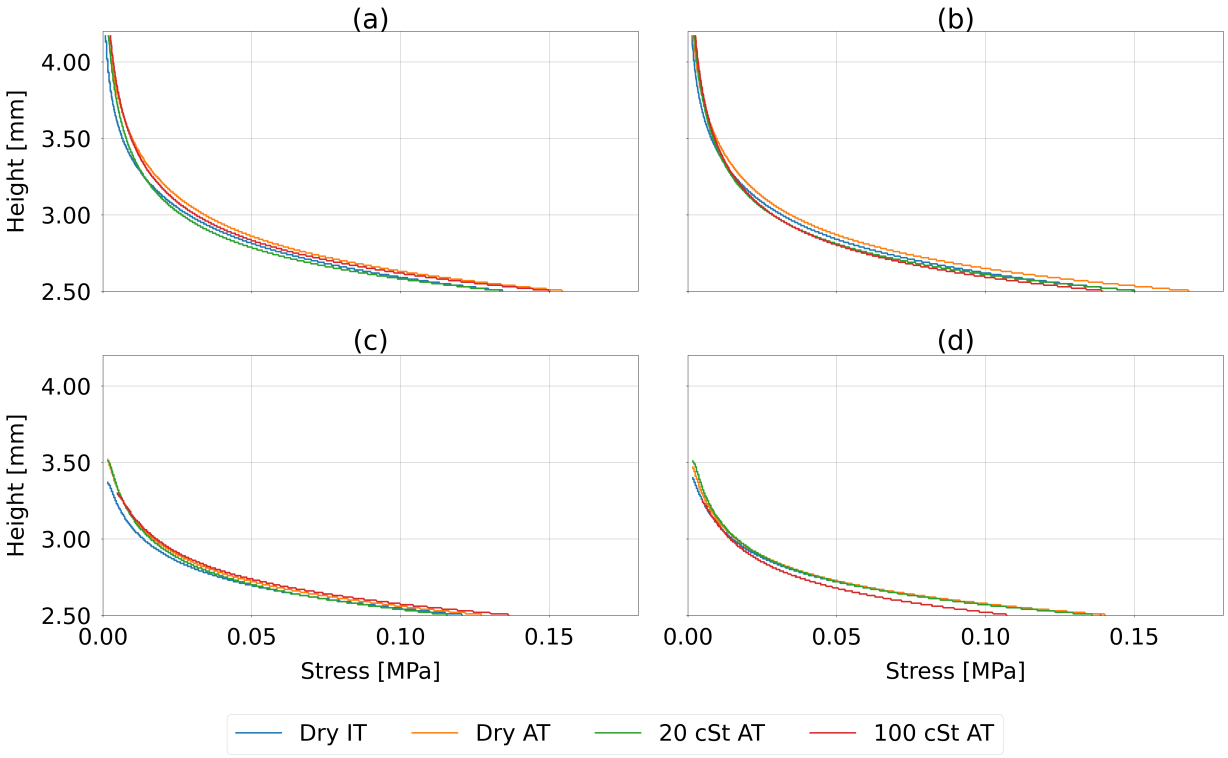


Figure 6.8: Compression height-stress curves for the first compression cycle: (a) $[0]_8$, and (b) $[0/45]_4$ specimens, and the second compression cycle: (c) $[0]_8$, and (d) $[0/45]_4$ specimens

The reduced degree of relaxation observed for the Dry AT specimens can be attributed to the increased cohesion between the fiber tows resulting from the melting of the stabilizing binder. Conversely, for the Dry IT specimens, the layers were allowed to more readily shift relative to one another, thereby enabling greater relaxation. It is also observed that the degree of stress relaxation during the first relaxation cycle for the Dry IT and Dry AT specimens (Figures 6.10 (a) and (b)) is greater than that during the second relaxation cycle (Figures 6.10 (c) and (d)), which was shown to be statistically significant (Table 5). Similar outcomes were reported by Li et al [17], where minor relaxation during the eighth cycle was attributed to a process that weakens the fabric stiffness after several cycles.

The elastic recovery of the Dry IT and Dry AT specimens after the recovery phase (i.e., Phase IV) was also compared (Figure 6.12). Dry IT specimens for both stacking sequences exhibited a greater elastic recovery than the Dry AT specimens, specifically 20% greater for the $[0]_8$ stack and 4% greater for the $[0/45]_4$ stacking sequence. The reduced elastic recovery for the Dry AT specimens is due to increased resistance to deformation owing to

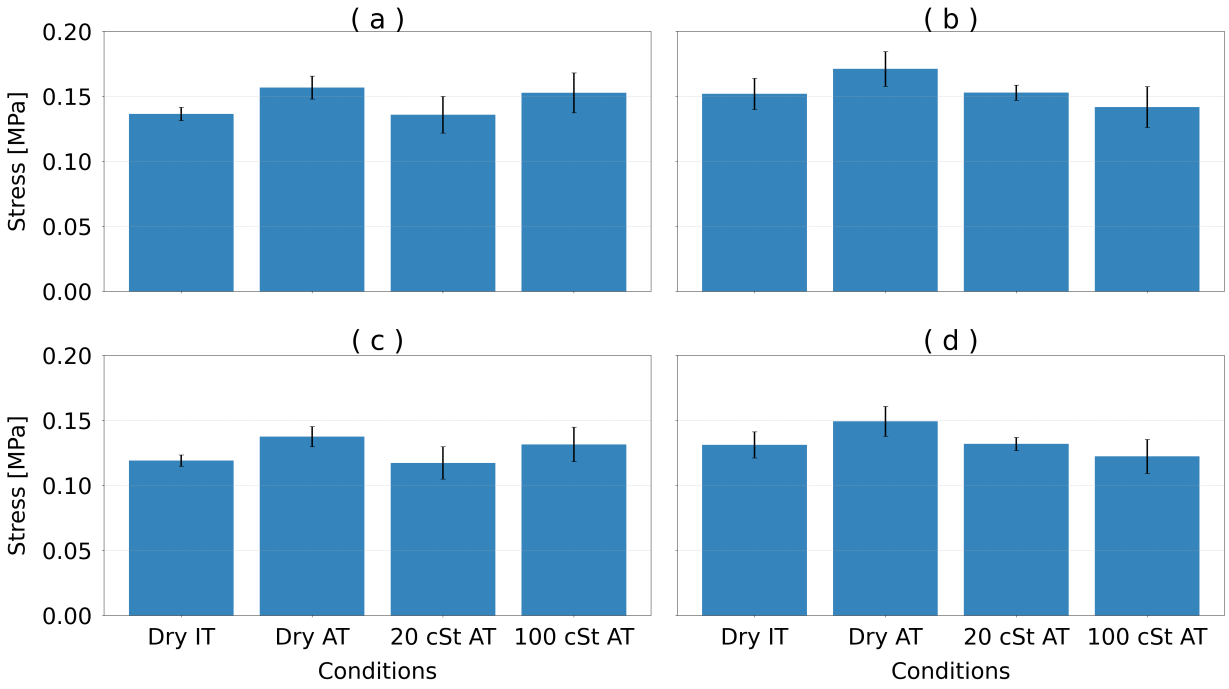


Figure 6.9: Maximum compression stress (σ_0) for each impregnated condition: (a) first compaction cycle (Phase I) for $[0]_8$ specimen, (b) first compaction cycle (Phase I) for $[0/45]_4$ specimen, (c) second compaction cycle (Phase V) for $[0]_8$ specimen, and (d) second compaction cycle (Phase V) for $[0/45]_4$ specimen.

cohesion between the layers caused by the activated binder. Statistical analysis points out that the elastic recovery of the Dry AT specimens is significantly different from that of the Dry IT specimens (Table 6). Note, although the height of the punch was greater for the Dry AT specimens during the dwell phase when compared to the Dry IT specimens (Figure 6.7(a)), the initial contact height of the punch was also higher for the former specimens. This finding is analogous with the results reported in Ref. [20], which emphasized that the addition of a stabilizing binder increases the initial stack thickness.

In the current study, the fabric stack was compressed to 2.5 mm, which is equivalent to a fiber volume fraction of 55% based on a calculation using the fabric areal weight. Schafer et al [16] investigated the same type of fabric without a stabilizing binder, which allows a better understanding of the influence of the thermosetting powder on the compaction response of the fabric. They indicate that the compression of a $[0]_8$ stacking sequence by up to 55% should result in a maximum stress of approximately 0.08 MPa. This stress mag-

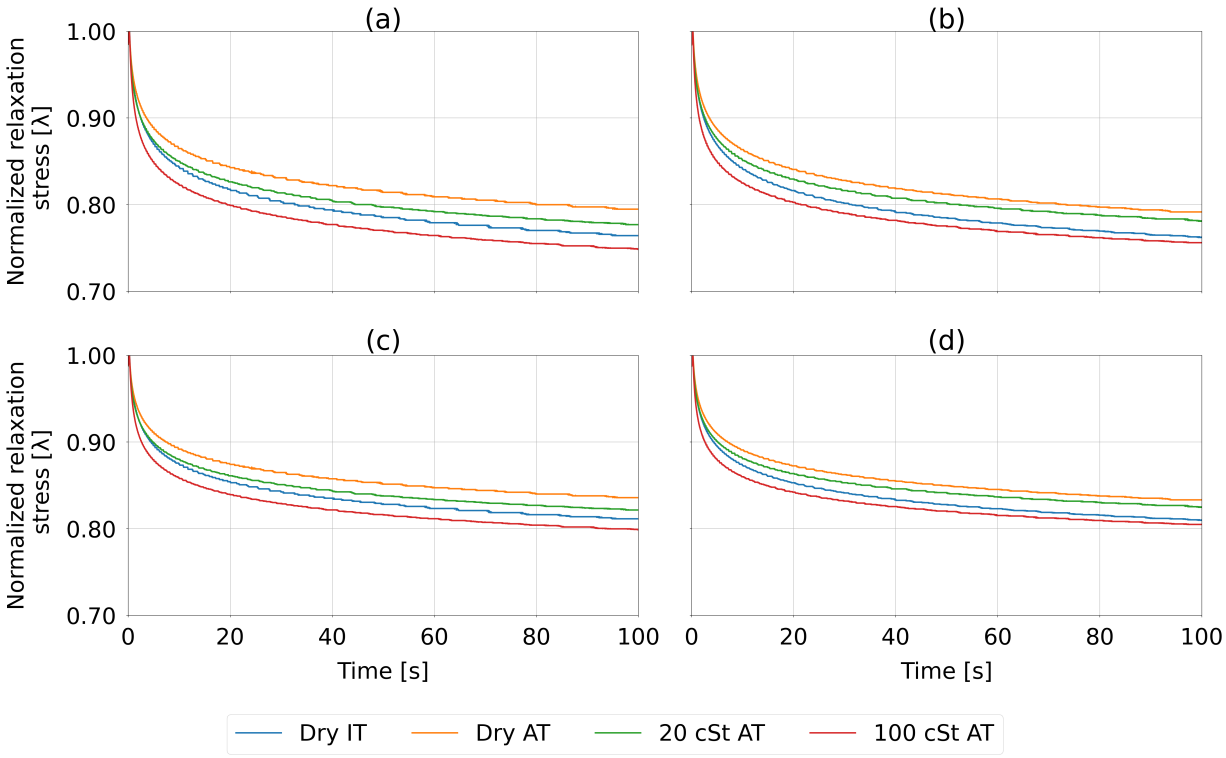


Figure 6.10: Normalized relaxation stress for each impregnated condition: (a) first relaxation cycle for $[0]_8$ specimen, (b) first relaxation cycle for $[0/45]_4$ specimen, (c) second relaxation cycle for $[0]_8$ specimen, and (d) second relaxation cycle for $[0/45]_4$ specimen.

nitude is approximately 60% of the maximum compression stress for the Dry IT specimens with the same stacking sequence and half of the stress of the Dry AT specimens. This difference in maximum stress revealed the influence of the thermosetting powder binder on the compaction behavior of the studied fabric and is due to greater resistance to deformation for binder-stabilized fabrics. These findings align with the results in Ref. [20], which states that maximum compression stress increases with increasing binder content for the same thickness.

6.4.1.2 Influence of the stacking sequence

The influence of stacking sequence on the overall compaction response is demonstrated through the force response and punch height-time results in Figures 6.7 (a) and (b). By comparing the maximum compression stress for the first compaction cycle (Figures 6.9

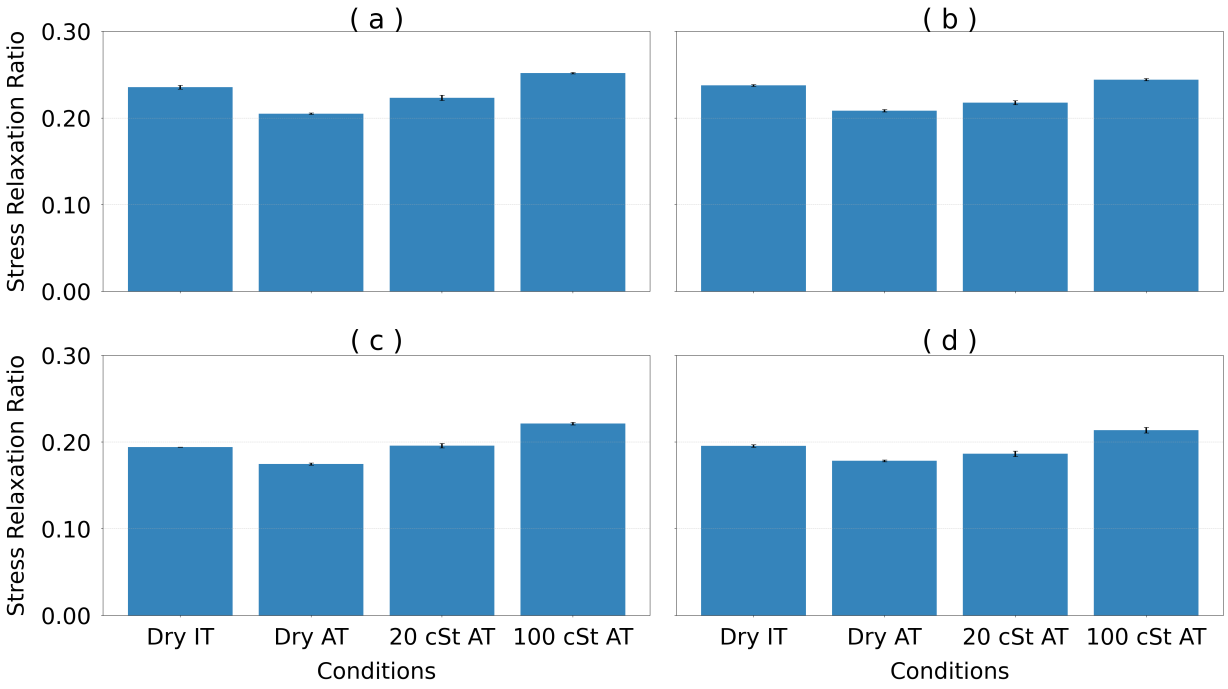


Figure 6.11: Stress relaxation ratio for each impregnated condition: (a) first relaxation cycle for $[0]_8$, (b) first relaxation cycle for $[0/45]_4$, (c) second relaxation cycle for $[0]_8$, and (d) second relaxation cycle for $[0/45]_4$.

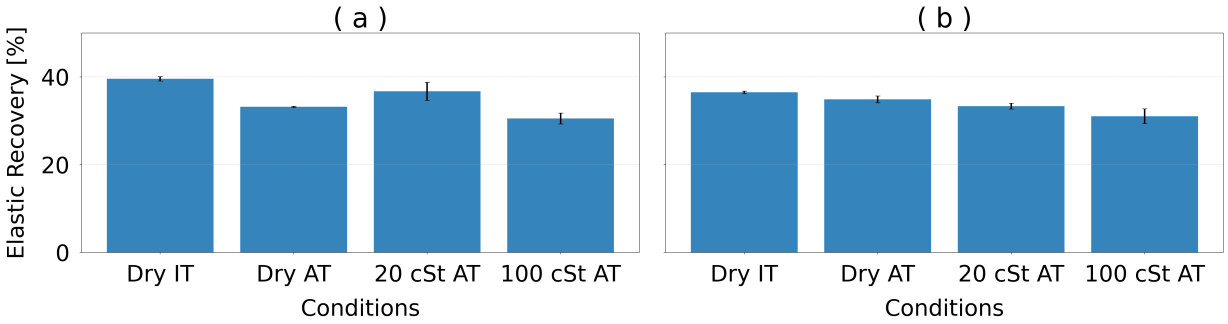


Figure 6.12: Elastic recovery capacity for each impregnated condition during Phase IV: (a) $[0]_8$ and (b) $[0/45]_4$.

(a) and (b))) and second compaction cycle (Figures 6.9 (c) and (d)) for all conditions considered, the influence of stacking sequence is deemed to be minor. Table 7 presents the p-values derived from the T-Test comparing the maximum compression stress values for

both stacking sequences, with no statistical significance identified in any comparison.

The degree of relaxation for specimens with each stacking sequence was found to be similar for each condition, for both loading cycles (compare Figures 6.11a and 6.11b, and Figures 6.11c and 6.11d). However, for the configurations in which the fabric stack was infiltrated with a 100 cSt oil, a statistical difference (see Table 8) between the degree of relaxation for specimens with different stacking sequences was observed. Given that the difference was observed in specimens impregnated with 100 cSt oil in both cycles, exhibiting greater relaxation for the $[0]_8$ specimens, it can be inferred that this phenomenon may be attributable to the higher viscosity of the oil.

The final comparison between specimens with different stacking sequences focuses on the difference in elastic recovery during Phase IV (Figure 6.12). Specimens with a $[0]_8$ stacking sequence exhibited an 8% increase in elastic recovery compared to specimens with a $[0/45]_4$ stacking sequence for the Dry IT condition. This phenomenon observed for the $[0]_8$ specimens can be attributed to enhanced recovery caused by the supporting glass fiber and stitching yarns that tended to aid with de-nesting of fiber tows. Statistical analysis (Table 9) indicates that the stacking sequence has no influence on the recovery of the stack thickness for the remaining conditions.

The three analyses indicate a minor influence of the stacking sequence on compaction responses (i.e., maximum compression stress, degree of relaxation, and elastic recovery). This outcome aligns with the results documented in Refs. [16, 41] that studied the compaction response of UD-NCF stacks. Both studies indicate that the low influence of the stacking sequence on the compaction response is due to the stitching yarns, especially when arranged in a tricot pattern. Lomov et al [41] explain that the nesting process in non-crimp fabric is associated with the presence of gaps between fabric layers; however, tricot stitching yarns limit a pronounced nesting effect when all the layers are aligned (i.e., $[0]_n$), leaving gaps between the layers.

6.4.1.3 Influence of the infiltrated fluid viscosity

The effect of fluid viscosity was also analyzed by comparing the maximum compression stress, relaxation response, and elastic recovery for the associated stages of loading. Generally, the maximum compression stress for the infiltrated specimens (20 and 100 cSt) was less than that of the Dry AT specimens and comparable to the Dry IT specimens for both compaction cycles and stacking sequences (Figure 6.9). The peak compaction force for the Dry AT specimens exceeded those of the 20 cSt and 100 cSt specimens by 15.45% and 2.72% for the $[0]_8$ stack, and by 11.95% and 20.65% for the $[0/45]_4$ stack. The p-values

presented in the last three columns of Table 2 demonstrate that specimen impregnation does not result in a statistically significant influence on the maximum compression stress values. This result aligns with the findings documented in Ref. [17], which investigated the compaction of a 16-layer carbon fiber UD-NCF stack. It was concluded that lubrication does not significantly influence the peak compaction stress, which is attributed to the inherently low coefficient of friction of carbon fiber. Given that the carbon fiber already possesses a low friction coefficient, the impregnation of the fabric did not reduce friction substantially further, this only slightly affecting the peak stress values.

Figures 6.10 (a) and (b) illustrate a comparison between dry samples and specimens impregnated with 20 cSt and 100 cSt silicone oil during the initial relaxation phase for each stacking sequence. The Dry AT specimens exhibited less relaxation compared to the infiltrated specimens for all stacking sequences and both compaction cycles, with the specimens infiltrated with 100 cSt oil exhibiting the greatest relaxation for every case (Figure 6.11). Also, the degree of relaxation for the Dry IT specimens was comparable to that of the infiltrated specimens for all cases. This is explained by the increase in the friction coefficient in the Dry AT, which prevents the movement of adjacent layers and results in lower stress relaxation. On the other hand, the fabric impregnation reduces the friction coefficient caused by the melting of the stabilizing binder, easing the relaxation. These variations in relaxation are corroborated by the statistical analysis. Table 4 presents the p-values obtained through the T-test, indicating a statistically significant difference among the conditions.

Finally, the influence of fluid viscosity on elastic recovery was examined, where Dry AT and infiltrated specimens exhibited similar elastic recovery (Figure 6.12), with statistically minor differences for most cases (Table 6).

6.4.2 Model parameter identification

As mentioned in Section 2.3, the stress values extracted from the average curve of the first compaction (Phase I) and relaxation (Phase II) cycle were used to obtain the material parameters and fit the time-dependent curve using the fractional Zener and Maxwell models (Figure 6.13). First, the relaxation phase was modelled. Table 10 shows the parameters for the fractional Zener model obtained under each investigated condition during the first relaxation phase, and Table 11 lists the material parameters for the Maxwell model for each condition during the first relaxation phase. For the first relaxation phase, both models fitted the experimental curves well with R^2 greater than 0.92 (Table 10 and 11). Both Tables 10 and 11 reveal variations in the material parameter values from one condition to another.

Wei et al [19] suggested that the relaxation time (τ) increases with the concentration of liquid stabilizing-binder in weight. However, it was observed in these experiments and the curve-fitting process that the pre-activation of the stabilizing binder in powder form causes a reduction in the relaxation time.

As the fractional Zener has fewer variables, it is easier to attribute physical meaning to the values and compare the influence of each condition. Conditions 1 and 5 represent the inactivated stabilizing binder conditions for the stacking sequences $[0/45]_4$ and $[0]_8$, respectively, while conditions 2 and 6 represent the conditions with the binder activated thermally. Comparing the main elastic modulus (E_0) for both stacking sequences, an increase of 18% is observed from condition 1 to 2 and 20% from condition 5 to 6. Additionally, the elastic modulus of the spring in the viscoelastic branch (E_1) increased by 213% and 48% from the Dry IT to the Dry AT specimens for the $[0/45]_4$ and $[0]_8$, respectively. Those increases in the elastic moduli represent a greater resistance of the binder-activated stack in comparison to the inactivated stack. This is due to the molten binder [42], which, as it melts, coats the fiber tows and enhances the cohesion between the adjacent layers. This enhanced cohesion prevents the layers from shifting relative to one another, resulting in greater resistance to the compression applied by the punch. A comparison of the derivative order values (α) revealed reductions of 3.34% and 5.30% from the Dry IT to the Dry AT specimens for the $[0/45]_4$ and $[0]_8$, respectively. This implies that by activating the stabilizing binder, the stack assumes a behavior more akin to that of a spring, whereas the Dry IT specimens exhibit behavior more akin to a dashpot, which is characterized by greater stress relaxation.

Although the parameters listed in Tables 10 and 11 fit the curves Phase II of the experiment for each condition, they do not accurately reproduce the curve seen in Phase VI, as shown in Figure 6.14 for the fractional Zener for Condition 4. This deviation can be attributed to the nesting of the fabrics after the first compression-relaxation cycle, which affects the compaction behavior during the second cycle (Section 6.3.1), as well as the permanent deformation of the stack that causes the relaxation curves to flatten [17].

Reproducing the procedure conducted to obtain the material parameters in Phase II, the curve in Phase VI was fitted with each model, as illustrated in Figures 6.15 (a) and (b). The parameters obtained for each condition are listed in Tables 12 and 13. This difference in arrangement exhibited a greater elastic modulus during the second relaxation, $E_0^{6th} > E_0^{2nd}$, which explains the greater compaction stress when comparing the experimental values in Phase VI and the stress estimation using values extracted from Phase II (Figure 6.14). For Phase V, both rheological models adequately fit the curves, albeit with a lower efficiency compared to the first relaxation cycle (R^2 >0.8). However, the Maxwell model poorly captured some of the studied conditions (Figures 6.15 (g) and (h)), in which R^2 was less than 0.8. Although both rheological models can generally be well fit to the experimental data, the Maxwell model is computationally more expensive due to the number of variables to be extracted, resulting in longer optimization processes. Additionally, the Fractional Zener has proven to be more efficient compared to the three-branch Maxwell model, with

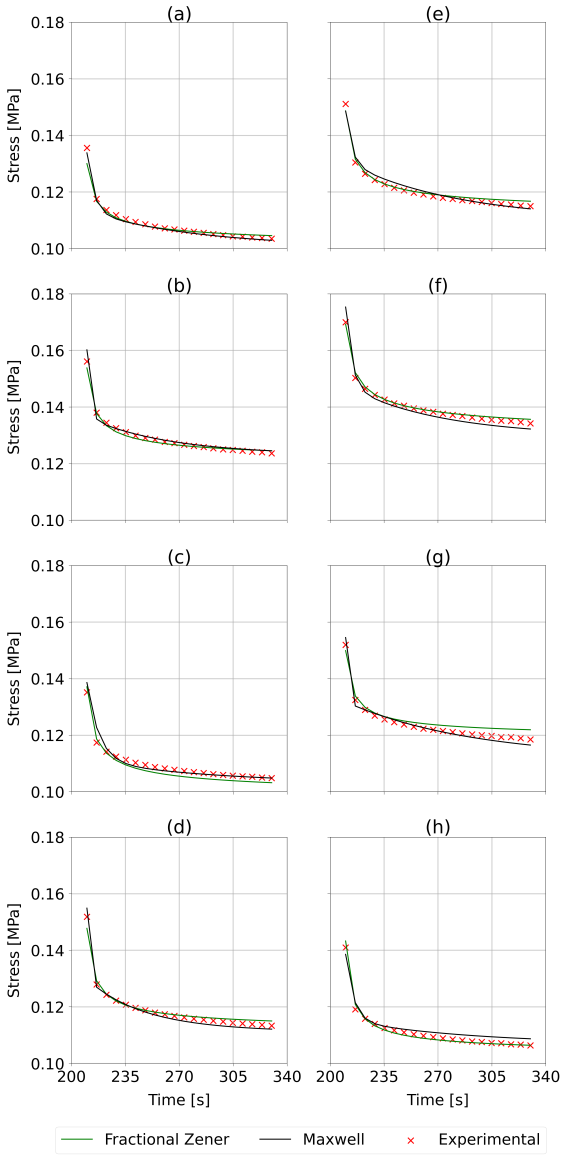


Figure 6.13: Phase II stress–time curve fitting using the Fractional Zener and Maxwell models: (a) dry inactivated $[0]_8$, (b) dry pre-activated $[0]_8$, (c) impregnated 20 cSt pre-activated $[0]_8$, (d) impregnated 100 cSt pre-activated $[0]_8$, (e) dry inactivated $[0/45]_4$, (f) dry pre-activated $[0/45]_4$, (g) impregnated 20 cSt pre-activated $[0/45]_4$, and (h) impregnated 100 cSt pre-activated $[0/45]_4$.

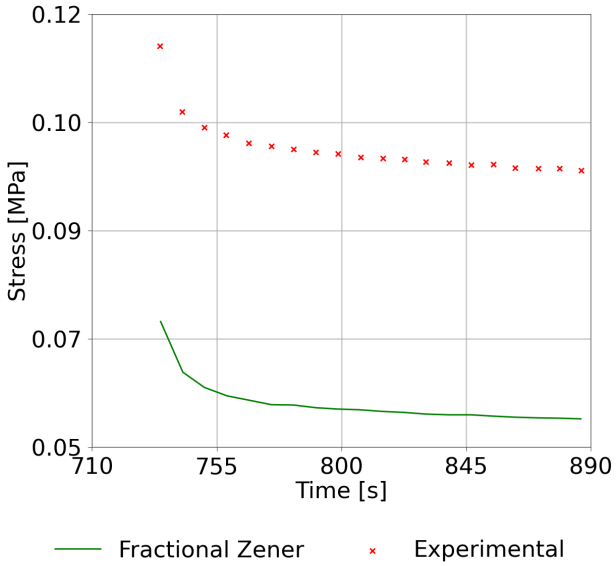


Figure 6.14: A comparison between the experimental measurements of condition 4 during Phase VI and the curve derived from the material parameters obtained in Phase II using the Fractional Zener model

higher coefficients of determination (R^2).

Lastly, a generalized Maxwell model with nonlinear terms, which was developed by Kaliske et al [43] and adapted by Bublitz [33], was utilized to fit the compaction response of the fabric specimens during Phase I. Figure 6.16 illustrates the stress-height curve during the first compaction (Phase I) with the nonlinear Maxwell model for the eight configurations. Table 14 lists the 11 material parameters obtained for each stacking sequence. In general, the model was well fitted with 7,000 experimental data points and 60,000 evaluations over the compaction phase. However, in some cases (refer to Figure 6.16b, 6.16e, and 6.16f), the model did not achieve good agreement with the experimental data, overshooting the stress values. The greater difference between the experimental and numerical values in those three cases can be attributed to the significant number of parameters to be optimized and the large search area for each parameter. An alternative would be to optimize those curves using additional experimental data points and/or evaluations to achieve better agreement with the experimental data, highlighting the challenges of fitting the model due to the high number of material parameters.

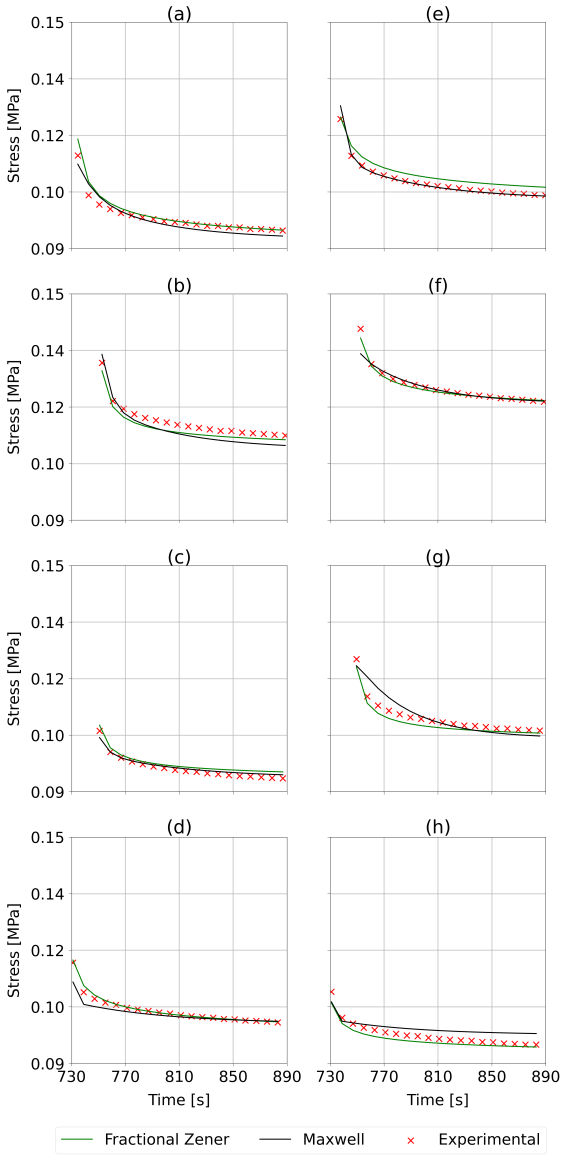


Figure 6.15: Phase VI stress–time curve fitting using the Fractional Zener and Maxwell models: (a) dry inactivated $[0]_8$, (b) dry pre-activated $[0]_8$, (c) impregnated 20 cSt pre-activated $[0]_8$, (d) impregnated 100 cSt pre-activated $[0]_8$, (e) dry inactivated $[0/45]_4$, (f) dry pre-activated $[0/45]_4$, (g) impregnated 20 cSt pre-activated $[0/45]_4$, and (h) impregnated 100 cSt pre-activated $[0/45]_4$.

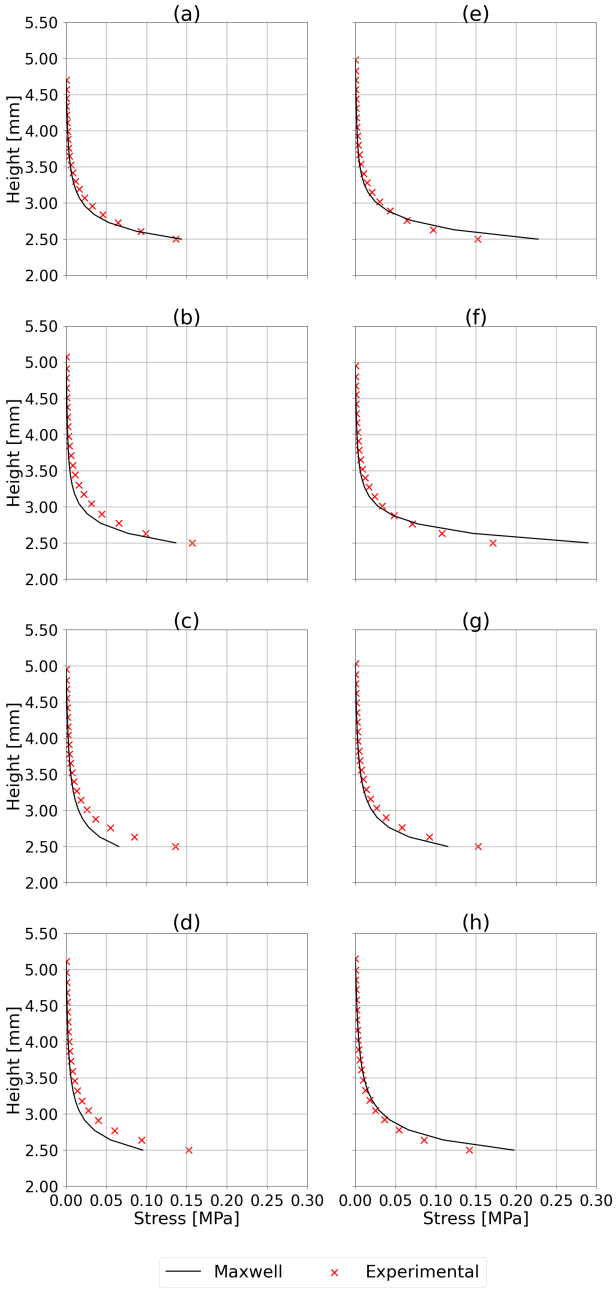


Figure 6.16: Phase I height-stress curve fitting by using the nonlinear Maxwell model for: (a) dry inactivated $[0]_8$, (b) dry pre-activated $[0]_8$, (c) impregnated 20 cSt pre-activated $[0]_8$, (d) impregnated 100 cSt pre-activated $[0]_8$, (e) dry inactivated $[0/45]_4$, (f) dry pre-activated $[0/45]_4$, (g) impregnated 20 cSt pre-activated $[0/45]_4$, and (h) impregnated 100 cSt pre-activated $[0/45]_4$.

6.5 Conclusions

The influence of binder pre-activation, stacking sequence, and impregnation fluid viscosity on the compaction response of an eight-layer carbon fiber unidirectional non-crimp fabric (UD-NCF) stack was investigated. Pre-activating the stabilizing binder increased the peak compaction stress by 10% when compared to a non-activated bindered fabric stack, owing to the increased resistance to tow deformation and enhanced cohesion among fabric layers, which restricted relative deformation. Additionally, pre-activating the stabilizing binder reduced the degree of relaxation of the stack by up to 15% and the recovery of the stack by up to 20%. Moreover, the stacking sequence was found to have minimal influence on the compaction response for the conditions considered, which is aligned with the literature. The stitching yarns and supporting glass fibers limited pronounced tow nesting, for both stacking sequences considered, which ultimately limited inter-layer interactions and led to similar peak compressive forces and relaxation response. Moreover, the fabric impregnation had no significant impact on the peak compaction stress due to the inherently low friction of the carbon fibers, rendering any reduction in friction between the fibers and stitching caused by the fluid to be minimal. On the other hand, the degree of relaxation was influenced by the infiltration of the fabric stack, which reduced the tow friction and resistance to spreading by acting as a lubricant.

The experimental outcomes from this study have enabled an improved understanding of the compaction behavior of binder-stabilized carbon fiber UD-NCFs under different conditions. These outcomes may aid in improving wet compression molding (WCM) processes by guiding the selection of parameters (e.g., binder state and resin viscosity), which can improve the precision in establishing part thickness and, thus, the desired fiber volume fraction. The use of binder-stabilized UD-NCFs in direct WCM processes was proposed in previous work by the authors to enhance resin management, based on an observed increase in bending stiffness of the fabric. Building on this, the present study investigated the effect of binder activation on compaction behavior and found that the time-dependent compaction response is significantly reduced for specimens with pre-activated binder. Thus, future research will investigate the impact of various binder types and binder quantity on the compaction response of similar UD-NCFs, as well as the interaction of compaction and bending behavior. The experimental data and parameters derived for the rheological Maxwell and fractional Zener models provide new and important data that can be used as input for future forming simulations of binder-stabilized UD-NCFs. Future research will also center on investigating the formability of dry and infiltrated UD-NCF stacks with pre-activated binder.

References

[1] C. Poppe, "Process simulation of wet compression moulding for continuous fibre-reinforced polymers," Ph.D. dissertation, Karlsruhe Institute of Technology, 2021.

[2] M. Ghazimoradi, E. A. Trejo, V. Carvelli, C. Butcher, and J. Montesano, "Deformation characteristics and formability of a tricot-stitched carbon fiber unidirectional non-crimp fabric," *Composites Part A: Applied Science and Manufacturing*, vol. 145, p. 106 366, Jun. 2021, ISSN: 1359-835X. DOI: 10.1016/J.COMPOSITESA.2021.106366.

[3] A. Schnabel and T. Gries, "1 - production of non-crimp fabrics for composites," in *Non-Crimp Fabric Composites*, ser. Woodhead Publishing Series in Composites Science and Engineering, S. V. Lomov, Ed., Woodhead Publishing, 2011, pp. 3–41, ISBN: 978-1-84569-762-4. DOI: https://doi.org/10.1533/9780857092533.1.3. [Online]. Available: https://www.sciencedirect.com/science/article/pii/B9781845697624500011.

[4] L. Kärger, S. Galkin, E. Kunze, M. Gude, and B. Schäfer, "Prediction of forming effects in ud-ncf by macroscopic forming simulation–capabilities and limitations," in *ESAFORM 2021 - 24th International Conference on Material Forming*, Liège, Belgium, 14-16 April 2021.

[5] P. Boisse, N. Hamila, E. Guzman-Maldonado, A. Madeo, G. Hivet, and F. Dell'Isola, "The bias-extension test for the analysis of in-plane shear properties of textile composite reinforcements and prepregs: A review," *International Journal of Material Forming*, vol. 10, pp. 473–492, 2017.

[6] C. D. Rudd, A. C. Long, K. N. Kendall, and C. G. E. Mangin, *Liquid Moulding Technologies*. Amsterdam, The Netherlands: Elsevier, 1997, ISBN: 0768000165. DOI: 10.1533/9781845695446.

[7] R. Kumar, K. Rashvand, A. Fraisse, A. Sarhadi, and T. L. Andersen, "Experimental testing method to characterise the drapability of ud non-crimp fabrics used in wind turbine blades," *IOP Conference Series: Materials Science and Engineering*, vol. 1293, no. 1, p. 012 020, Nov. 2023. DOI: 10.1088/1757-899X/1293/1/012020. [Online]. Available: https://dx.doi.org/10.1088/1757-899X/1293/1/012020.

[8] R. M. Portela, B. Schafer, L. Karger, A. R. de Faria, and J. Montesano, "Effect of loading rate, viscosity, and binder activation on the bending response of an infiltrated ud-ncf," *Composites Part A: Applied Science and Manufacturing*, vol. 200, p. 109 347, Jan. 2026, ISSN: 1359-835X. DOI: 10.1016/J.COMPOSITESA.

2025.109347. [Online]. Available: https://www.sciencedirect.com/science/article/pii/S1359835X25006414.

[9] G. Estrada, C. Vieux-Pernon, and S. G. Advani, "Experimental characterization of the influence of tackifier material on preform permeability," *Journal of Composite Materials*, vol. 36, no. 19, pp. 2297–2310, 2002. DOI: 10.1177/0021998302036019542. eprint: https://doi.org/10.1177/0021998302036019542. [Online]. Available: https://doi.org/10.1177/0021998302036019542.

[10] J. C. Brody and J. W. Gillespie, "The effects of a thermoplastic polyester preform binder on vinyl ester resin," *Journal of Thermoplastic Composite Materials*, vol. 18, no. 3, pp. 157–179, 2005. DOI: 10.1177/0892705705043535. eprint: https://doi.org/10.1177/0892705705043535. [Online]. Available: https://doi.org/10.1177/0892705705043535.

[11] H. M. Yoo, J. W. Lee, J. S. Kim, and M. K. Um, "Influence of non-reactive epoxy binder on the permeability and friction coefficient of twill-woven carbon fabric in the liquid composite molding process," *Applied Sciences*, vol. 10, no. 20, p. 7039, 2020, ISSN: 2076-3417. DOI: 10.3390/app10207039. [Online]. Available: https://www.mdpi.com/2076-3417/10/20/7039.

[12] S. Bickerton, M. J. Buntain, and A. A. Somashekar, "The viscoelastic compression behavior of liquid composite molding preforms," *Composites Part A: Applied Science and Manufacturing*, vol. 34, no. 5, pp. 431–444, 2003, ISSN: 1359835X. DOI: 10.1016/S1359-835X(03)00088-5.

[13] A. Yong *et al.*, "Experimental characterisation of textile compaction response: A benchmark exercise," *Composites Part A: Applied Science and Manufacturing*, vol. 142, p. 106 243, Mar. 2021, ISSN: 1359835X. DOI: 10.1016/j.compositesa.2020.106243. [Online]. Available: https://linkinghub.elsevier.com/retrieve/pii/S1359835X20304784.

[14] V. Werlen, C. Rytka, and V. Michaud, "A numerical approach to characterize the viscoelastic behaviour of fibre beds and to evaluate the influence of strain deviations on viscoelastic parameter extraction," *Composites Part A: Applied Science and Manufacturing*, vol. 143, p. 106 315, 2021.

[15] C. T. Poppe, C. Krauß, F. Albrecht, and L. Kärger, "A 3D process simulation model for wet compression moulding," *Composites Part A: Applied Science and Manufacturing*, vol. 145, p. 106 379, Jun. 2021, ISSN: 1359-835X. DOI: 10.1016/J.COMPOSITESA.2021.106379.

[16] B. Schäfer, R. Zheng, P. Boisse, and L. Kärger, "Investigation of the compaction behavior of uni-and bidirectional non-crimp fabrics," in *ESAFORM 2023 - 26th International Conference on Material Forming*, Kraków, Poland, Apr. 2023.

[17] L. Li, Y. Zhao, J. Yang, J. Zhang, and Y. Duan, "An experimental investigation of compaction behavior of carbon non-crimp fabrics for liquid composite molding," *Journal of Materials Science*, vol. 50, pp. 2960–2972, 7 Apr. 2015, ISSN: 15734803. DOI: 10.1007/s10853-015-8860-0.

[18] D. Droste *et al.*, "Investigation of the compaction behaviour of a quasi-unidirectional non-crimp fabric during the vacuum infusion process," *Journal of Composite Materials*, vol. 56, no. 16, pp. 2509–2524, 2022.

[19] K. Wei, D. Liang, M. Mei, X. Yang, and L. Chen, "A viscoelastic model of compression and relaxation behaviors in preforming process for carbon fiber fabrics with binder," *Composites Part B: Engineering*, vol. 158, pp. 1–9, 2019, ISSN: 1359-8368. DOI: https://doi.org/10.1016/j.compositesb.2018.09.038. [Online]. Available: https://www.sciencedirect.com/science/article/pii/S1359836818328038.

[20] K. Wei, D. Liang, M. Mei, D. Wang, X. Yang, and Z. Qu, "Preforming behaviors of carbon fiber fabrics with different contents of binder and under various process parameters," *Composites Part B: Engineering*, vol. 166, pp. 221–232, 2019, ISSN: 1359-8368. DOI: https://doi.org/10.1016/j.compositesb.2018.11.143. [Online]. Available: https://www.sciencedirect.com/science/article/pii/S1359836818326568.

[21] J. Mitsch, B. Schäfer, and L. Kärger, "Rate-dependent 3d forming simulation of thermoplastic composite materials using visco-hyperelastic material modeling and 3d hexahedral solid-shell elements," *Composites Part A: Applied Science and Manufacturing*, vol. 200, p. 109 306, 2026, ISSN: 1359-835X. DOI: https://doi.org/10.1016/j.compositesa.2025.109306. [Online]. Available: https://www.sciencedirect.com/science/article/pii/S1359835X25006001.

[22] K. Ding and Y. Xiao, "Adaptability of burgers rheological model and its improved model to the creep properties of glue laminated bamboo," *Mechanika*, vol. 30, pp. 214–220, 3 2024, ISSN: 20296983. DOI: 10.5755/j02.mech.35600.

[23] M. Moutee, G. Student, M. Fafard, Y. Fortin, and A. Laghdir, "Modeling the creep behavior of wood cantilever loaded at free end during drying," *Wood and Fiber Science*, vol. 37, pp. 521–534, 3 2005.

[24] S. Jelić and D. Zorica, "Fractionalization of anti-zener and zener models via rheological analogy," *Acta Mechanica*, vol. 234, pp. 313–354, 2 Feb. 2023, ISSN: 16196937. DOI: 10.1007/s00707-022-03363-8.

[25] J. Echaabi, M. B. Nziengui, and M. Hattabi, "Compressibility and relaxation models for fibrous reinforcements in liquid composites moulding," *International Journal of Material Forming*, vol. 1, pp. 851–854, S1 Apr. 2008, ISSN: 1960-6206. DOI: 10.1007/s12289-008-0269-8. [Online]. Available: http://link.springer.com/10.1007/s12289-008-0269-8.

[26] M. Danzi, C. Schneeberger, and P. Ermanni, "A model for the time-dependent compaction response of woven fiber textiles," *Composites Part A: Applied Science and Manufacturing*, vol. 105, pp. 180–188, Feb. 2018, ISSN: 1359835X. DOI: 10.1016/j.compositesa.2017.11.002.

[27] T. C. D. C. Haveroth, "On the use of fractional derivatives for modeling nonlinear viscoelasticity," M.S. thesis, Universidade do Estado de Santa Catarina, 2015.

[28] T. da Costa-Haveroth *et al.*, "Aspects on viscoelasticity modeling of hdpe using fractional derivatives: Interpolation procedures and efficient numerical scheme," *Mechanics of Advanced Materials and Structures*, vol. 29, pp. 4343–4358, 25 Oct. 2022, ISSN: 1537-6494. DOI: 10.1080/15376494.2021.1928345. [Online]. Available: https://www.tandfonline.com/doi/full/10.1080/15376494.2021.1928345.

[29] J. Padovan, "Computational algorithms for fe formulations involving fractional operators," *Computational Mechanics*, vol. 2, pp. 271–287, 4 1987, ISSN: 0178-7675. DOI: 10.1007/BF00296422. [Online]. Available: http://link.springer.com/10.1007/BF00296422.

[30] M. Ferrante, "Viscoelastic models for the simulation of transients in polymeric pipes," *Journal of Hydraulic Research*, vol. 55, pp. 599–612, 5 2017. DOI: 10.1080/00221686.2017.1354935. [Online]. Available: https://doi.org/10.1080/00221686.2017.1354935.

[31] A. Kühl, "Uma formulação viscoelastoplástica não linear aplicada ao polietileno de alta densidade (pead)," M.S. thesis, Universidade do Estado de Santa Catarina, 2014.

[32] Q. Bai, "Analysis of particle swarm optimization algorithm," *Computer and Information Science*, vol. 3, 1 Jan. 2010, ISSN: 1913-8997. DOI: 10.5539/cis.v3n1p180. [Online]. Available: http://www.ccsenet.org/journal/index.php/cis/article/view/5131.

[33] D. Bublitz, D. Colin, and K. Drechsler, "Implementation of a viscoelastic material model to predict the compaction response of dry carbon fiber preforms," *Composites Part A: Applied Science and Manufacturing*, vol. 153, p. 106 718, Feb. 2022, ISSN: 1359-835X. DOI: 10.1016/J.COMPOSITESA.2021.106718. [Online]. Available: https://www.sciencedirect.com/science/article/pii/S1359835X21004334?via%3Dihub#b0120.

[34] C. A. Careglio, C. Canales, L. Papeleux, J.-P. Ponthot, and A. E. Mirasso, "An implementation of the generalized maxwell viscoelastic constitutive model," *Mecánica Computacional*, vol. XXXIII, pp. 1179–1192, 1215 2014.

[35] D. Roylance, *Engineering viscoelasticity*, 2001.

[36] A. Schmidt and L. Gaul, "On the numerical evaluation of fractional derivatives in multi-degree-of-freedom systems," *Signal Processing*, vol. 86, pp. 2592–2601, 10 Oct. 2006, ISSN: 01651684. DOI: 10.1016/j.sigpro.2006.02.006. [Online]. Available: https://linkinghub.elsevier.com/retrieve/pii/S0165168406000454.

[37] H. Liu, M. A. Polak, and A. Penlidis, "A practical approach to modeling time-dependent nonlinear creep behavior of polyethylene for structural applications," *Polymer Engineering and Science*, vol. 48, pp. 159–167, 1 Jan. 2008, ISSN: 00323888. DOI: 10.1002/pen.20942.

[38] J. Blank and K. Deb, "Pymoo: Multi-objective optimization in python," *IEEE Access*, vol. 8, pp. 89 497–89 509, 2020, ISSN: 2169-3536. DOI: 10.1109/ACCESS.2020.2990567.

[39] C. Song and R. Kawai, "Monte carlo and variance reduction methods for structural reliability analysis: A comprehensive review," *Probabilistic Engineering Mechanics*, vol. 73, p. 103 479, Jul. 2023, ISSN: 02668920. DOI: 10.1016/j.probengmech.2023.103479. [Online]. Available: https://linkinghub.elsevier.com/retrieve/pii/S0266892023000681.

[40] T. Grieser and P. Mitschang, "Investigation of the compaction behavior of carbon fiber ncf for continuous preforming processes," *Polymer Composites*, vol. 38, pp. 2609–2625, 11 Nov. 2017, ISSN: 15480569. DOI: 10.1002/pc.23854.

[41] S. V. Lomov, I. Verpoest, T. Peeters, D. Roose, and M. Zako, "Nesting in textile laminates: Geometrical modelling of the laminate," *Composites Science and Technology*, vol. 63, pp. 993–1007, 7 2003, ISSN: 02663538. DOI: 10.1016/S0266-3538(02)00318-4.

[42] R. M. Portela, B. Schäfer, L. Kärger, A. R. de Faria, and J. Montesano, "Influence of viscosity, binder activation, and loading rate on the membrane response of an infiltrated ud-ncf," in *ESAFORM 2024 - 27th International Conference on Material Forming*, Apr. 2024.

[43] M. Kaliske and H. Rothert, "Formulation and implementation of three-dimensional viscoelasticity at small and finite strains," *Computational Mechanics*, vol. 19, pp. 228–239, 3 Feb. 1997, ISSN: 0178-7675. DOI: 10.1007/s004660050171. [Online]. Available: http://link.springer.com/10.1007/s004660050171.

Chapter 7

High-fidelity fiber volume fraction estimation for UD-NCF composites using digital image processing technique

The contents of this chapter stem from the following paper: R. M. Portela, A. R. de Faria, and J. Montesano, "High-fidelity fiber volume fraction estimation for carbon fiber UD-NCF composites using digital image processing technique," Manuscript submitted (under review).

This chapter presents a procedure for estimating the fiber volume fraction (FVF) from microscopic images, applied to samples extracted from panels fabricated by WCM and from HP-RTM panels from a previous study, using an in-house processing script.

7.1 Overview

The study aims to accurately estimate the fiber volume fraction (FVF) of two carbon fiber unidirectional non-crimp fabric (UD-NCF) composites with distinct process-induced microstructures through application of a digital image processing (DIP) technique, and to determine the appropriate width of the region of interest. The DIP methodology analyzes high-resolution cross-sectional microscopic images of samples that span their entire thickness. Initially, images are converted to grayscale, assigning an intensity value to each

pixel. Subsequently, an intensity threshold is set, and all pixels exceeding it are classified as carbon fiber. Finally, the pixels identified as fiber are aggregated, and the ratio of fiber area to the total area (i.e., total sample FVF) is computed. The capability of the DIP technique to accurately estimate FVF for the studied material systems is demonstrated, while the method is deemed to be less time-consuming and less operator-dependent than established methods such as acid digestion. Furthermore, it is recommended to analyze a region of interest that spans two-tow widths as a viable option to balance accuracy and computational efficiency.

7.2 Introduction

The reinforcement phase in fiber-reinforced plastic (FRP) composite materials strongly influences their mechanical properties, where the fiber volume fraction (FVF) plays an important role. Therefore, an accurate estimation of the FVF of FRP composites is critical in determining whether an associated structure can withstand a given load [1, 2]. The three main methods for measuring FVF in FRP composites are acid digestion (AD), burn-off (BO), and non-destructive approaches [3]. These methods assume that the fiber distribution is consistent throughout the material and estimate the FVF based on a small sample extracted from a manufactured part. The AD and BO methods have been standardized in ASTM D3171 [4]; thus, they are more widely used, with AD being the most common.

AD is performed by initially measuring the mass of a sample of the FRP composite material with known volume, followed by complete digestion of the matrix phase in acid and measurement of the bare fiber mass after drying [3–5]. This method requires a sample with a mass of at least 0.5 g for measuring the FVF [4]. While the AD method is frequently employed due to its simplicity, low-cost equipment requirements, and standardized procedure, there are some disadvantages. The AD method is destructive, rendering the sample unusable for any subsequent characterization [5]. Furthermore, the AD method necessitates the proper disposal of chemical waste and is known to be operator-dependent [6]. An alternative to improve the efficiency of the method and reduce dependence on the operator is to use a digester [7]. Kim et al. [2] explain that the AD method is not recommended for determining the FVF of carbon fiber-reinforced plastic (CFRP) composites, as the carbon fibers may degrade and lose a significant amount of weight during the process, affecting the final FVF estimation.

The BO method is analogous to the AD method, where instead the matrix phase of an FRP composite sample is removed through burning, typically in an oven or furnace, at temperatures exceeding the decomposition temperature [4]. The BO method is also

simplistic and enables a more rapid determination of the FVF when compared to the AD method. However, this method is not recommended for CFRP composites due to the possibility of fiber incineration at extreme temperatures, which can lead to inaccurate results [2, 3]. Lastly, destructive methods like AD and BO are known to introduce errors in FVF measurements of up to 2% [6]. Variants of the BO method include Thermo-Gravimetric Analysis (TGA), which combines the incineration of the matrix phase, or in some cases all phases, with continuous mass measurements. Kim et al. [2] explain that the procedure for the latter is divided into three steps: matrix, char, and fiber incineration, which are characterized by the differential weight of the sample curve. The FVF is defined by the ratio of the weight before the fiber incineration to the initial mass of the composite sample. Nonetheless, this technique is not recommended for materials comprising phases that exhibit similar decomposition temperatures.

The non-destructive approaches typically assess material microstructure and measure FVF by processing images captured using a variety of techniques, e.g., optical microscopy (OM), scanning electron microscopy (SEM), and micro-computed tomography (micro-CT)[3, 5, 8]. The microscopy techniques involve capturing cross-sectional images of the sample, followed by digital image processing (DIP) which enables quantification of microstructural features semi-manually or via an algorithm. DIP of obtained cross-sectional images has been widely used in the literature to quantify the FVF of FRP composites [9–12]. Yang and Colton [9] employed a fiber counting approach within an area of interest under the assumption that all fibers shared identical dimensions and perfect circular shapes, which is not entirely accurate. The FVF was estimated by:

$$v_f = \frac{\pi r_f^2 N_f}{A_t}, \tag{7.1}$$

where r_f is the average fiber radius, N_f the total number of fibers within the assessed area, and A_t the total area of the image. Cann et al. [13] highlight that the fiber counting technique demands previous knowledge of the fiber diameter size; however, this technique is insensitive to the image quality and can be conducted with lower magnification images, leading to increased sample sizes and improved statistical power. Another approach described in the literature is the Line Method, shown in Figure 7.1, where several lines are randomly placed over the microscopic image. The measurement is calculated as the ratio of the total fiber length along these lines to the overall fiber length. Carlsson et al. [12] recommend taking the FVF measurement from multiple lines and averaging these values to derive a representative measurement result. The Area Method (Figure 7.1) has also been employed and involves processing highly magnified cross-sectional images to establish the pixel intensity associated with each phase for estimation of the FVF within a region

of interest. A series of image processing steps is required, including thresholding and noise filtering to discretize the pixels associated with each phase and to smear surface artefacts from the polishing process. Among others, Morales et al. [3] conducted DIP analysis of SEM images of pultruded FRP bars and compared the results with those obtained using the BO technique. The authors used ImageJ to analyze the SEM images. The images were converted to grayscale, and a threshold function was used to define the pixels as fibers, resin-rich areas, or voids. The authors reported that the DIP method quantified the FVF and the resin fraction, which were comparable to the values obtained via the BO method. It was stated that DIP approaches provide an advantage over matrix separation methods as they additionally yield information on fiber distribution [3]. However, DIP techniques utilizing cross-sectional images are constrained to unidirectional (UD) composites as the FVF cannot be accurately determined when fibers are not perpendicular to the evaluated section plane (i.e., fabric-reinforced composites or multidirectional laminates) [2]. Additionally, these techniques are prone to section bias because the thickness and the fiber distribution may change from one region to another, which would result in varying FVF measurements [14–16]. Lastly, accurate FVF measurements using the described area method demand a high-quality image obtained at higher magnification to obtain accurate results [13].

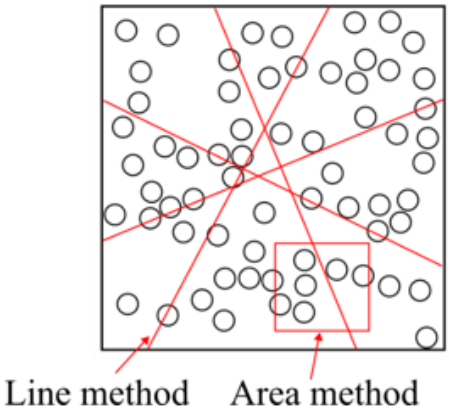


Figure 7.1: Schematic showing use of the line and area methods on the cross-section of a unidirectional composite to obtain FVF.

The methods employing micro-CT scans of the sample involve obtaining multiple cross-sectional images that are then reconstructed to form a three-dimensional visualization of the material. Similar to the microscopy techniques, the micro-CT method considers the intensity of the pixels to distinguish the phases of the composite (i.e., reinforcement, matrix,

and voids) and enables computation of the ratio of each [17]. The micro-CT methods are deemed to be more reliable than those based on processing cross-sectional images, as micro-CT is less prone to section bias and has lower location-based errors [14, 15, 18]. These methods also enable FVF estimates for fabric-reinforced composites and are not restricted to UD composites. For example, Yu et al. [19] combined SEM image analysis for fiber cross-sectional area measurement with micro-CT to capture the yarn cross-sectional dimensions for evaluation of FVF in plain-weave fiber-reinforced composites. Variations in intra-tow FVF at discrete locations throughout the samples were considered in the two-step FVF estimates for the FRP composite material. However, micro-CT is a costly technique owing to the equipment. Mehdikhani et al. [20] emphasized the challenge related to the sample size, where the spatial resolution is inversely proportional to the sample size; therefore, a high-resolution image restricts the sample to a few millimeters at most. Furthermore, distinguishing between carbon fibers and polymers from micro-CT scans is not typically feasible, given that their densities are similar, which inhibits accurate FVF estimation.

Additional nondestructive approaches include ultrasonic techniques, thermal diffusivity techniques, and the density-based approach. Ultrasonic techniques are typically used to assess defects in large sample volumes, including voids, and utilize a single transducer or an array of transducers on the sample surface. Duernberger et al. [1] recently developed a new technique to estimate the FVF of pultruded CFRP composites using an ultrasonic sound velocity concept. The FVF was computed by measuring ultrasonic sound velocity as a function of propagation angle, modeling wave paths through the composite, and correlating angular velocity patterns to FVF using calibration curves. However, this technique is highly complex, requiring the application of ray-tracing and imaging algorithms to consider the angular dependence of ultrasound velocity. Failure to account for this inherent anisotropy may result in overlooking defects or inaccurately determining their location [1]. Furthermore, ultrasonic techniques have limited resolution when compared to the other FVF measurement techniques and are limited to providing a range of FVF values. The thermal diffusivity techniques consist of a heat source that emits radiation towards the composite sample. The radiation is focused by using an optical lens and an electronic shutter. The radiation passes through the composite sample and is detected by a pyro-electric detector, which measures changes in infrared radiation. The FVF measurement is conducted assuming the void content in the part is negligible, and with some calculations that consider the physical properties of the composite components, like thermal conductivity and density [6]. The thermal diffusivity technique requires a relatively accurate and inexpensive setup; however, this technique may present a significant uncertainty when compared to standardized methods [6]. Finally, the density-based approach is applicable for estimating FVF for fabric-reinforced composite samples, including multidirectional

laminates, and is described in ASTM D3171 [4]. The FVF of composites is estimated by:

$$v_f = \frac{A_r N}{\rho_c t}, \tag{7.2}$$

where A_r denotes the areal weight of the fabric, N corresponds to the number of layers, ρ_c is the density of the sample, and t represents the thickness of the sample. Nonetheless, using a non-representative density of the composite or a poor measurement of thickness may result in inaccurate FVF calculation. Furthermore, the method does not account for the spreading of the fiber tows/yarns during compaction, which would inevitably alter the fabric areal density and potentially lead to inaccuracies in FVF estimation.

The different methods reviewed for estimating the FVF of FRP composites have been generally applied to either UD tape-based or pultruded composites and/or woven fabric-reinforced composites. Liquid composite molding processes, such as resin transfer molding and wet compression molding (WCM), combine continuous dry fabric layers with liquid resin into a mold, leading to improved FVF control [21]. Liquid molded FRP composite comprising unidirectional non-crimp fabrics (UD-NCFs) has recently been more widely used owing to improved in-plane mechanical properties and anisotropic property tailoring compared to woven composites [22]. UD-NCFs are characterized by parallel-oriented fiber tows, which are supported by transversely oriented fibers (typically low linear density glass fibers) and held together by polymeric stitching yarns in a variety of patterns (Figure 7.2) [23], thus, ensuring stability during the manufacturing process [24, 25]. Assessing the FVF of UD-NCF composites using the methods reviewed may pose a challenge due to multiple fabric constituents. For the AD method, once the matrix is digested, the transversely oriented supporting fibers must be removed prior to weighing the fiber tows, rendering this process exceedingly time-consuming and tedious [6, 7]. Given that the stitching yarns are typically polyester (i.e., a thermoplastic polymer), they may not fully digest and may adhere to the fiber tows, making removal difficult [26]. Use of the BO method to estimate the FVF of UD-NCF will lead to similar challenges.

DIP techniques utilizing cross-sectional images present a viable option for UD-NCF composites given that the reinforcing fiber tows are unidirectional. Mikkelsen et al. [10, 11] utilized a DIP-based method to estimate the FVF of glass fiber UD-NCF composite samples via cross-sectional SEM images. The Otsu threshold was used to distinguish between pixels related to fiber and resin-rich areas [10]. Initially, measurements of the local intra-tow FVF were performed using small regions of interest, which revealed notable variation in the intra-tow FVF (59% - 66%). The study also directly measured the overall FVF from several high-resolution images stitched together, where the region of interest encompassed the total sample thickness (i.e., multiple toes in all layers). The overall FVF

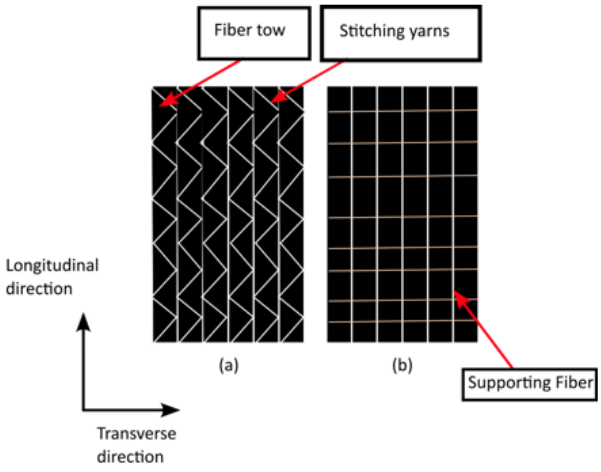


Figure 7.2: Schematic of a UD-NCF illustrating different constituents and microstructure: (a) stitch tricot pattern surface, and (b) supporting fiber surface.

was found to be 55%, which is notably lower than the intra-tow FVF. Zeng and Montesano [30] also utilized a DIP technique with microscopic cross-sectional images to estimate the FVF of a carbon fiber UD-NCF composite. A two-step approach was used involving estimation of the intra-tow FVF (65%) from several local high-resolution images, followed by estimation of the impregnated tow FVF (84%) from a region of interest spanning the entire sample thickness and comprising multiple tows along the width. The overall FVF of the composite material was then calculated to be 54%, which was similar in magnitude to the value determined using the density-based approach. Cherniaev et al. [27] also used a two-step DIP approach for a similar carbon fiber UD-NCF composite, whereby the FVF estimation of 45% was deemed to be accurate. One of the challenges using this two-step approach for UD-NCF composites is accurately defining the regions corresponding to the impregnated tows, which may have irregular shapes [11]. Although a few recent studies have employed DIP techniques for estimation of the FVF of UD-NCF composites, the robustness of these techniques for these materials has not been investigated, particularly for carbon fiber UD-NCF composites.

The primary objective of this study is to determine the FVF of carbon fiber UD-NCF composites employing a DIP technique, and to determine the size of the region of interest that enables high-fidelity FVF estimation. Several flat panels were manufactured utilizing a WCM process. High-resolution cross-sectional images of samples from both the manufactured WCM panels and panels manufactured in a previous study using a High-

Pressure Resin Transfer Molding (HP-RTM) process were examined using an opto-digital microscope. A custom script was developed to threshold and discretize the pixels associated with each phase, enabling calculation of the FVF for each sample.

7.3 Methodology

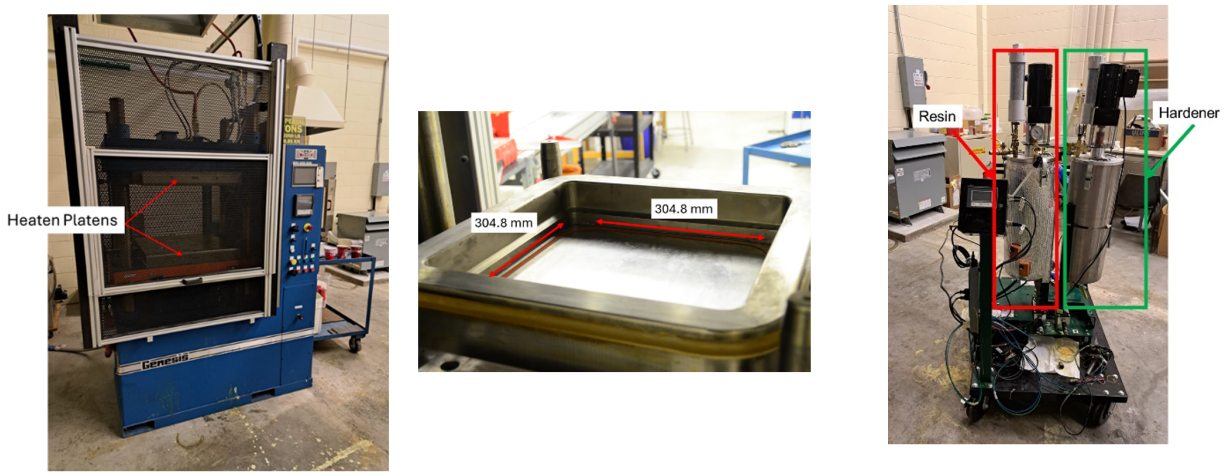
7.3.1 Materials

The material investigated comprised a UD-NCF, specifically PX35-UD300 (Zoltek, US), and the three-part snap-cure resin system Epikote 6150 (Westlake Epoxy, US). The UD-NCF was composed of axially oriented parallel tows each containing 50K continuous PX35 carbon fibers. The tows were stitched together with a 76 dtex polyester yarn in a tricot pattern. In addition, the textile included low linear density transversely oriented supporting glass fibers to improve handleability, while a thermosetting polymer powder binder was dispersed on the stitch tricot pattern surface. The textile has a total areal density of 333 g/m2 [32]. The three-component resin system consisted of a medium-viscosity snap-cure epoxy resin, a low-viscosity amine hardener, and an internal mold release agent [28].

7.3.2 Panel fabrication

The equipment used to manufacture flat panels via a WCM process included a Genesis G100H-24-CPX 100-ton hydraulic press (Wabash MPI, US), a custom two-part steel mold with variable thickness cavity measuring 304.8 mm $\times$ 304.8 mm (Laval, Canada), and a Super E metering unit for rapid mixing and dispensing of the resin system (Michael Engineering Ltd., US) (Figure 7.3). The upper half of the mold featured a vacuum port that can be connected to a vacuum pump, while the lower half of the mold included a vacuum seal as well as a silicon fiber pinch seal to mitigate fiber wash. The mold was mounted onto the press platens, which consisted of integrated cartridge heating elements. The metering unit consisted of a heated tank for the resin and a second tank for the hardener, each connected to a tube that fed into an electronically controlled dispensing gun. A static mixing nozzle was connected to the dispensing gun, where resin and hardener were rapidly mixed before dispensing. Further details of the WCM setup are provided in Ref. [26].

Panels comprising eight layers of the UD-NCF with stacking sequence $[0]_8$ were produced. Prior to fabricating the panels, the mold cavity was cleaned and sealed, and Loctite



(a) (b) (c)

Figure 7.3: WCM equipment used to manufacture flat panels: (a) 100-ton hydraulic press with heated platens, (b) a two-part mold featuring a vacuum port, and (c) an automated metering unit for rapid mixing and dispensing of resin and hardener.

Frekote 770NC release agent (Henkle, Germany) was applied. The press platens were preheated with a set temperature of 135°C and 115°C for the lower and upper press platens, respectively. The platen temperatures were held constant during the manufacturing trials. The resin and internal mold release were poured into the heated tank of the metering unit and premixed, and the hardener was poured into the second tank, with a mixing ratio of 100:29:1.7 for resin, hardener, and internal mold release. The metering unit was calibrated to dispense 104.52 ml of the three-part resin mixture for each panel.

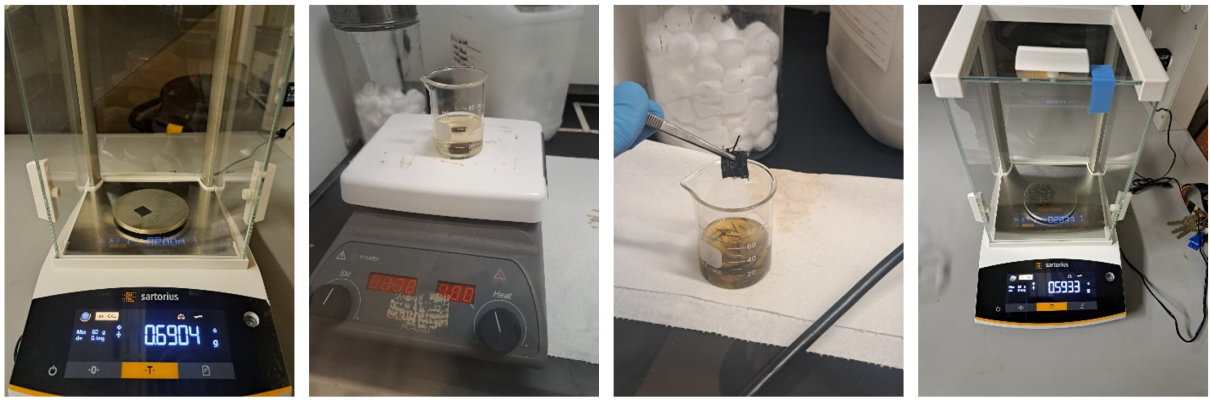
Eight layers of the UD-NCF, each measuring 300 mm × 300 mm, were cut, stacked and placed into the lower cavity of the preheated mold. The three-part resin system was subsequently mixed and dispensed onto the fabric stack and the mold closed with a constant force set to achieve 15 bar pressure within the mold cavity. The panel was allowed to cure for 5 minutes prior to demolding without a cooling cycle.

In addition, flat panels comprising seven layers of the same UD-NCF fabric ($[0]_7$) and epoxy resin system fabricated in a previous study [27] using an HP-RTM process were also investigated herein. Although both panels were manufactured using the same fabric and resin system, variations in microstructure and void content were anticipated due to differences in the manufacturing processes. The accuracy of the DIP technique was intended to

be evaluated on both panels.

7.3.3 Acid digestion

Acid digestion tests on 12 mm × 12 mm samples extracted from the HP-RTM panels followed Procedure A in ASTM Standard D3171-22 [4]. First, the mass of the extracted sample was measured to the nearest 0.0001 g using a high-precision scale (Figure 7.4 (a)). Next, the sample was placed into a beaker containing 40 mL of 70% nitric acid. The beaker was then heated to 80°C on a hot plate, and the solution was stirred for over two hours to digest the matrix (Figure 7.4 (b)). After digestion, the acid was filtered from the remaining material, and the reinforcement (Figure 7.4 (c)) was washed with deionized water. The wet carbon fiber was then dried in an oven at 100°C for 60 minutes. Finally, the mass of the dry material was measured to determine the FVF (Figure 7.4 (d)).



(a) (b) (c) (d)

Figure 7.4: Acid digestion procedure conducted with one HP-RTM sample: (a) initial sample weight measurement, (b) acid digestion in nitric acid bath on a hot plate in a fume hood, (c) sample partially digested in nitric acid, and (d) final weight measurement of the acid-digested sample.

7.3.4 Microscopic sample preparation

To capture cross-sectional microscopic images, samples with dimensions of approximately 20 mm × 20 mm were extracted from the central region of the WCM and HP-RTM panels

(Figure 7.5a) using an abrasive waterjet cutting machine (ProtoMAX, OMAX). Next, the microscopy samples were mounted in a two-part cold-mounting epoxy resin, namely Lecoset 7008 (Leco) (Figure 7.5b). To ensure high-quality microscopy images, the surface of each sample designated for examination was meticulously sanded and polished through a four-step process, including two grinding and two polishing steps, using an automatic polishing machine (Tegramin, Struers) (Figure 7.5c). The initial step involved the use of a 120-grit grinding surface pad with SiC abrasive in a resin bond (Primo 120, Struers) to perform coarse grinding with water for three minutes. The second step employed a surface pad (MD-Allegro, Struers) for finer grinding using a 9 μm diamond solution for six minutes. The third step used a satin-woven acetate polishing cloth (MD-Dac, Struers) to facilitate coarse polishing with a 3 μm diamond solution for six minutes. The final step utilized a short synthetic nap polishing cloth (MD-Nap, Struers) to provide the finishing polish with a 1 μm diamond solution for three minutes. Following the final polishing step, samples were cleaned with acetone and subsequently cleaned with ethanol.



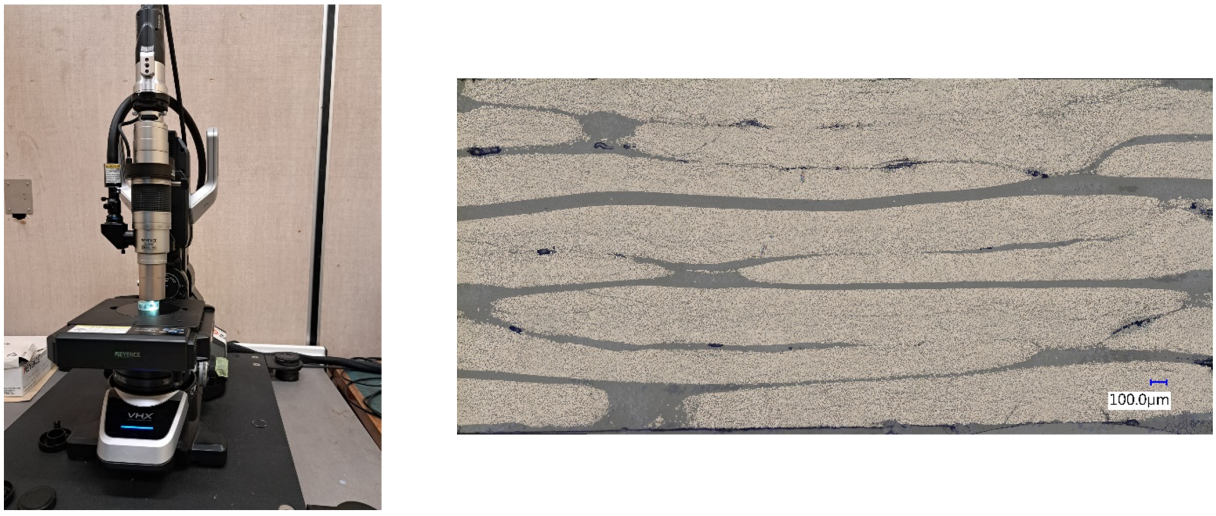
(a) (b) (c)

Figure 7.5: Procedure to prepare samples for microcopy: (a) panel regions where samples were extracted, (b) cold-mounted sample, (c) Struers automatic polisher used to grind and polish the cold-mounted samples.

7.3.5 Microscopic assessment

The polished samples were assessed with a VHX-5000 opto digital microscope (Keyence) equipped with a 500-5000× lens. Using the lowest magnification of 500×, a set of images

was taken and stitched, creating mosaic figures (Figure 7.6) large enough to include the full sample thickness and up to 20,000 pixels in width, which is the limit of the microscope.



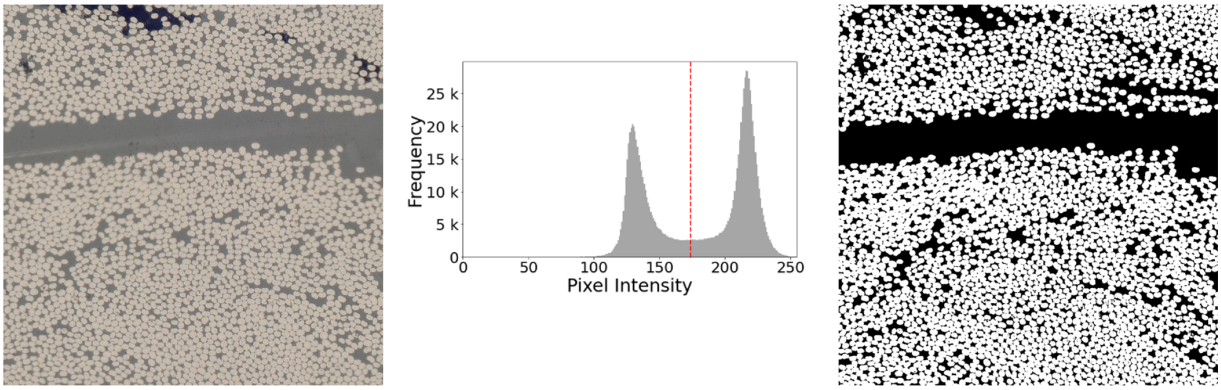
(a) (b)

Figure 7.6: (a)Microscope used to assess the cold-mounted samples (Keyence VHX-5000 microscope) and (b) mosaic-image made through several microscopic figures assessed with an optical-digital microscope.

7.3.6 Digital image processing

The extracted high-resolution microscopic images were digitally stitched together utilizing the Python library OpenCV [29] to generate an expanded view of the sample. These mosaic images facilitated the identification of carbon fibers through the full thickness of the UD-NCF composite laminate, where a custom Python script that uses the NumPy [30] and OpenCV [29] libraries was employed. Initially, the script converted the image to grayscale, assigning reflectance values to each pixel and storing them in an array [9]. Subsequently, a Gaussian filter was used to mitigate visual noise and enhance the differentiation between carbon fibers and resin regions. A threshold line was then established to distinguish high-intensity pixels associated with carbon fibers from those associated with the resin regions and the stitching yarns [10], as shown in Figure 7, and the array was sorted by values greater than or lower than a threshold. Pixels with a value greater than the threshold (i.e., those associated with carbon fibers) were assigned a value of 1; otherwise, they were assigned

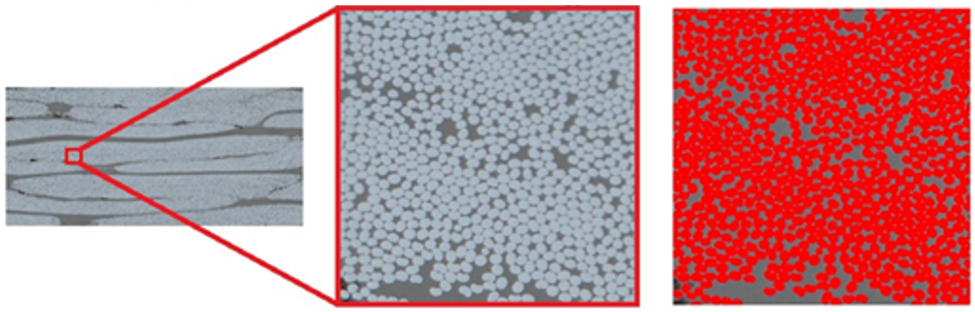
a value of 0. Given the variability in lighting conditions, Otsu's thresholding method was adopted to determine optimal threshold values. Ultimately, the algorithm computed the ratio of pixels exceeding the threshold by summing their values and dividing by the total number of pixels within the analyzed image, thereby determining the proportion of pixels identified as carbon fibers. This procedure enabled the determination of the FVF of the carbon fiber UD-NCF composite material in one step by using pixels for the entire cross-sectional image, in lieu of a two-step process, which is more prone to error.



(a) (b) (c)

Figure 7.7: Image filtering process: (a) raw microscopic image, (b) definition of the pixel intensity threshold, (c) identification of the pixels that represent fibers.

Following the acquisition of the images and development of the Python script, the images were examined to confirm whether the appropriate pixels had been selected to represent carbon fibers. This verification was conducted by highlighting all selected pixels in red. Figure 8 displays a magnified image with all carbon fibers rendered in a lighter shade. The fibers, identified by the script, are colored red to demonstrate the accuracy of the process method (Figure 8 (c)).



(a) (b) (c)

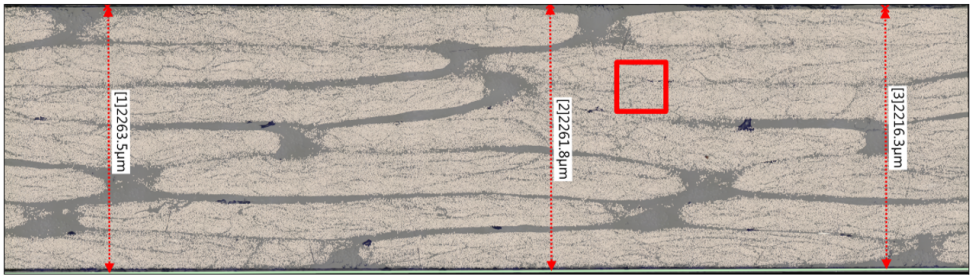
Figure 7.8: Verification procedure for pixel selection: (a) the original microscopic image; (b) a magnified region within the original microscopic image, and (c) the visualization of pixels identified as carbon fiber, highlighted in red.

7.4 Results and discussion

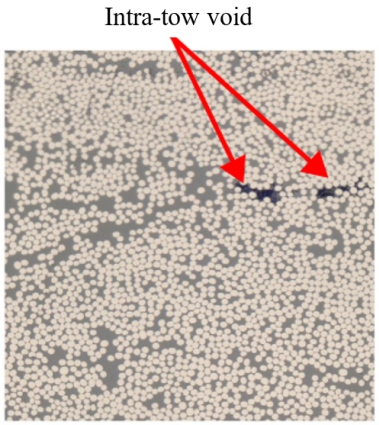
7.4.1 Microstructural assessment of WCM and HP-RTM materials

Microstructural assessment was performed on two HP-RTM and three WCM carbon fiber UD-NCF composite samples, with representative microscopic images shown in Figures 7.9 and 7.10, respectively. Although both sets of samples consisted of the same reinforcement fabric and resin system, the manufacturing process played a crucial role in establishing the microstructure of the sample. It is observed in the HP-RTM sample that the fiber tows exhibited a more uniform and rectangular shape, whereas tows in the WCM sample were distorted. The increased deformation in the WCM specimens can be attributed to greater compaction pressure during production, leading to more tow spreading and distortion. The average ply thickness and tow height values listed in Table 7.1 indicate that the WCM specimens experienced greater compaction.

Another key difference in the microstructure of the presented samples is the greater presence of inter- and intra-layer voids in the WCM sample, which can be partially attributed to lower cavity pressure associated with the WCM process. A low-pressure gradient characteristic of the WCM process may result in microscopic flow behaviour that impregnates the fiber tows but poorly fills the spaces between them, leading to the formation of large voids between fiber tows [20, 31]. Also, a vacuum was used to draw air from the mold



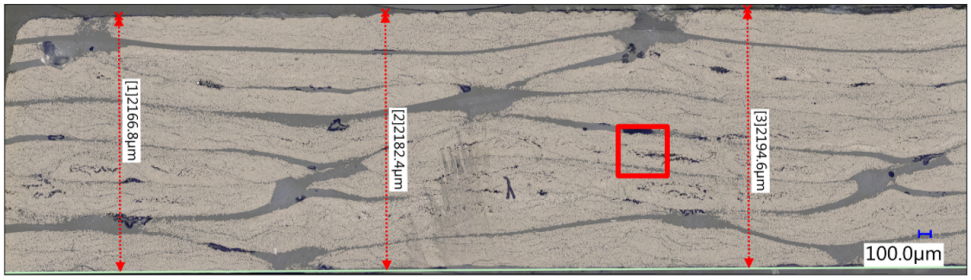
(a)



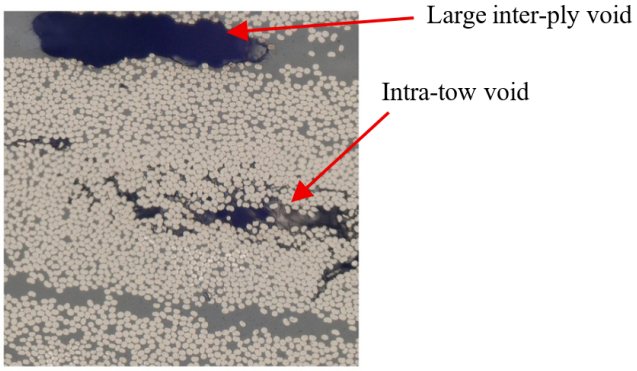
(b)

Figure 7.9: Microscopic assessment of a $[0]_7$ HP-RTM sample: (a) cross-sectional micrograph with laminate thickness measurements and region of interest indicated, and (b) magnified view of the region of interest.

prior to resin infiltration for the HP-RTM panels; however, a vacuum was not used for the WCM panels, which contributed to increased void content within these panels. Figures 7.9 (b) and 7.10 (b) show the fiber distribution in the HP-RTM and WCM specimens, respectively, where the reduced inter-fiber spacing and void morphology within the latter sample is clear. On the other hand, fewer and smaller intra-tow voids were observed in the HP-RTM sample (Figure 7.10 (b)).



(a)



(b)

Figure 7.10: Microscopic assessment of a $[0]_8$ WCM sample: (a) cross-sectional micrograph with laminate thickness measurements and region of interest indicated, and (b) magnified view of the region of interest.

7.4.2 Fiber volume fraction estimation using the acid digestion method

Prior to estimating the FVF via DIP, the acid digestion method was conducted using a sample from an HP-RTM panel with a mass of 0.6904 g (Figure 7.4 (a)). At the conclusion of the process, the mass of the sample was 0.5933 g (Figure 7.4 (d)), representing more than 85% of the initial mass. Noting that FVF values exceeding 70% are atypical even for unidirectional composites [1], the acid was clearly unable to fully digest the matrix and stitching yarns, despite an extensive and time-consuming process. Furthermore, the FVF for the same material system was determined in a previous study using a two-step imaging technique, where for samples comprising an average tow height of 0.29±0.07 mm, the FVF was reported to be 54% [27]. The FVF was also estimated using the density-based approach for further comparison. The areal weight of the fabric, excluding the supporting

Table 7.1: Characteristics of the indicated samples, including panel thickness, average ply thickness, tow height, and tow width. Mean and standard deviation of all values are provided.

	Panel thickness [mm]	Average ply thickness [mm]	Tow height [μm]	Tow width [μm]
HP-RTM	2.25 ± 0.02	0.32 ± 0.02	292 ± 40	4263 ± 214
WCM	2.18 ± 0.01	0.27 ± 0.01	240 ± 50	3866 ± 200

glass fibers, stabilizing binder, and polyester stitching, was 309 g/m^2 [32]. Additionally, the product of the laminate density and thickness was derived from multiplying the mass by the area of the sample, resulting in an FVF of 52%.

7.4.3 Fiber volume fraction estimation using DIP technique

The FVF of samples extracted from the HP-RTM and WCM panels was subsequently estimated using the procedure described in Section 7.3.6. Beginning with samples from the HP-RTM panel, images with widths spanning three tows (Figure 7.11 (a)) were analyzed. Figures 7.11 (b) and (c) illustrate a localized region highlighted in blue within Figure 7.11 (a). Figure 7.11 (b) displays the raw image, whereas Figure 7.11 (c) presents the processed image with selected pixels representing carbon fibers in white. The FVF for two HP-RTM samples is provided in Table 7.2, with an average value of approximately 56%. This outcome aligns with the FVF of 54% reported in Ref. [33] for samples extracted from HP-RTM panels with the same average ply thickness, thereby validating the DIP method. It should be noted that the FVF of the samples reported in Ref. [33] were estimated using a two-step imaging process whereby the infiltrated tow regions were defined, which is prone to error. Thus, the FVF value for the HP-RTM samples estimated herein is deemed to be more accurate.

Table 7.2: Mean and standard deviation of FVF measurement of each analyzed WCM sample with average result.

	Sample 01	Sample 02	Average
FVF	54.41%	57.55%	55.98 ± 1.57%

The same procedure was subsequently carried out to determine the FVF of the WCM panels. Images obtained from distinct samples (Figure 7.12) were analyzed using the same Python script. The red regions in these images (Figures 7.12 a, d, e) represent the resin-rich regions as well as regions comprising stitching yarns and voids, while the gray regions signify the impregnated tows, with darker shades corresponding to higher local FVF regions. The first and fourth images (Figures 7.12 (a) and (d)) depict a width spanning four fiber tows, whereas the fifth image (Figures 7.12 (e)) depicts a width spanning two fiber tows. Figure 7.12 (b) depicts a magnified raw image extracted from Figure 7.12 a (Sample 01) showing the intra-tow structure, including carbon fiber and resin-rich regions as well as voids within the upper tow. Figure 7.12 (c) illustrates the processed image by the Python script and distinguishes the carbon fiber from the rest of the microstructure. The script yielded FVF values that are listed in Table 7.3 (≈65%), which is greater than that of the HP-RTM samples owing to greater compaction.

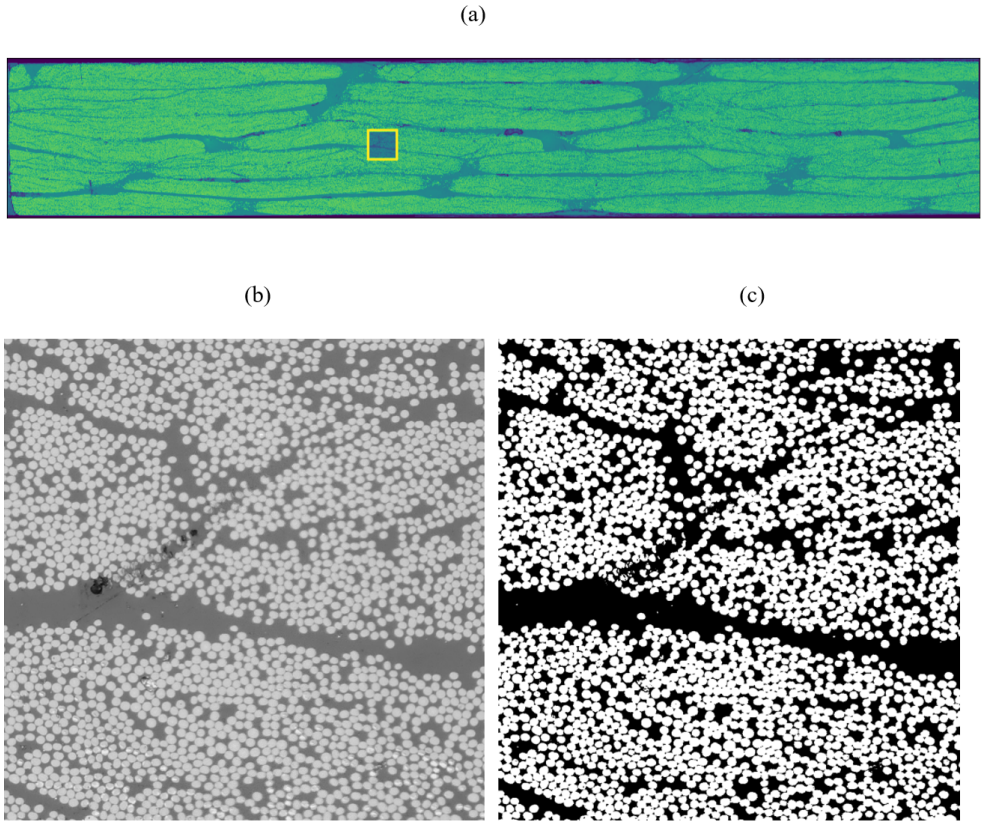
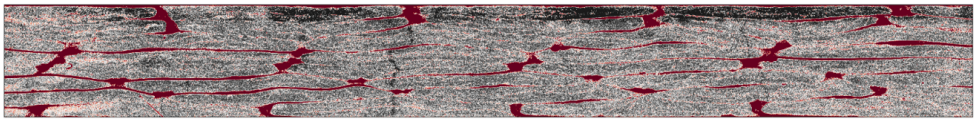


Figure 7.11: Microscopic image of the (a) HP-RTM sample 02 with a designated region of interest highlighted in blue, (b) raw image of the selected region, and (c) processed image of the same area, with the pixels corresponding to carbon fiber identified in white.

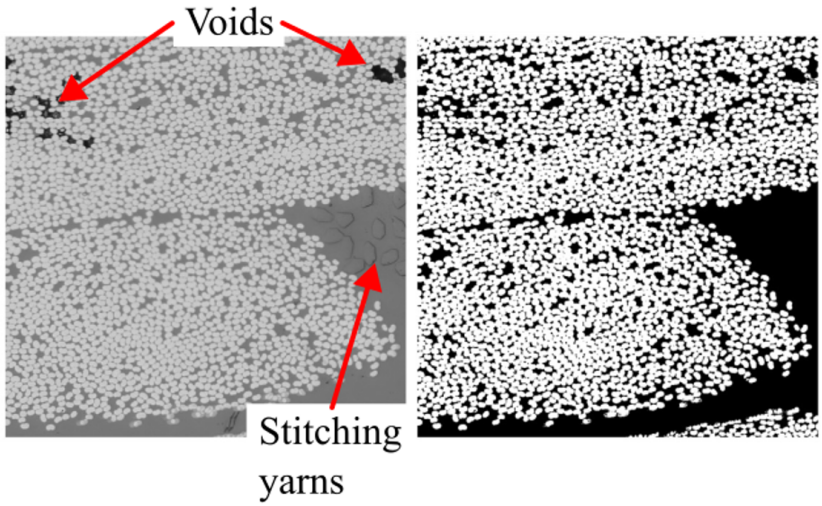
Table 7.3: Mean and standard deviation of FVF measurement of each analyzed WCM sample with average result.

	Sample 01	Sample 02	Sample 03	Average
FVF	65.13%	65.63%	65.60%	65.45 ± 0.23%

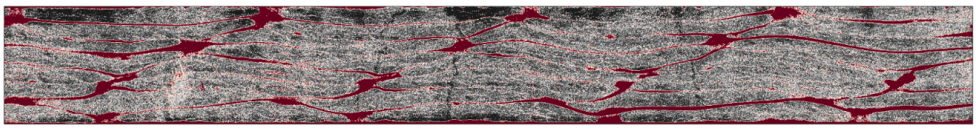
Given that stitching mosaic images is computationally demanding and the resulting images can be of substantial size (exceeding 100Mb), additional analyses were conducted to assess the FVF using regions of interest (ROI) on the samples with widths spanning one (Figure 7.13 (a)), two (Figure 7.13 (b)), or three (Figure 7.13 (c)) fiber tows. Table 7.4 lists the FVF values computed from WCM Sample 02 and HP-RTM Sample 02. In



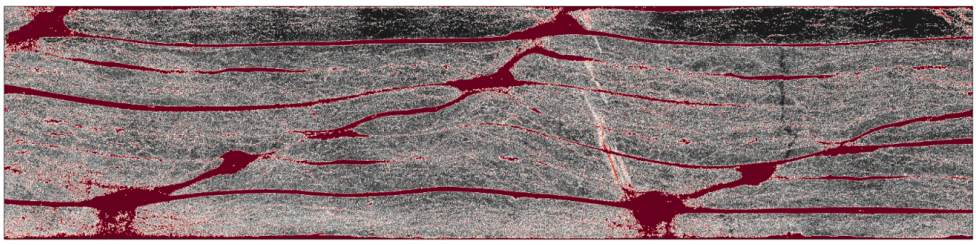
(a)



(b) (c)



(d)



(e)

Figure 7.12: Cross-sectional microscopic images of different WCM samples: (a) image of Sample 01, (b-c) magnified raw and processed images of Sample 01 with fibers identified for the latter (white regions), (d) image of Sample 02, and (e) image of Sample 03.

both cases, it was observed that an ROI with a width equivalent to one fiber tow (Figure 7.13 (a)) produced a FVF with greater deviation compared to that obtained using the entire image (i.e., 2.26% for the WCM sample and 2.80% for the HP-RTM sample). As the ROI width increased to two tows, deviation significantly reduced to 1.23% and 0.96%, respectively, for the WCM and HP-RTM samples. Lastly, when the ROI width spanned three tows, this deviation was 1.35% for the WCM sample and 0.38% for the HP-RTM sample. FVF measurements using wider regions of interest are generally deemed to be more representative of the bulk material but are more computationally expensive to process.

Table 7.4: FVF measurements of the second HP-RTM and WCM samples for regions of interest with widths spanning one, two, and three fiber tows.

	One fiber tow	Two fiber tows	Three fiber tows
WCM	64.15%	66.44%	66.52%
HP-RTM	59.16%	57.01%	57.77%

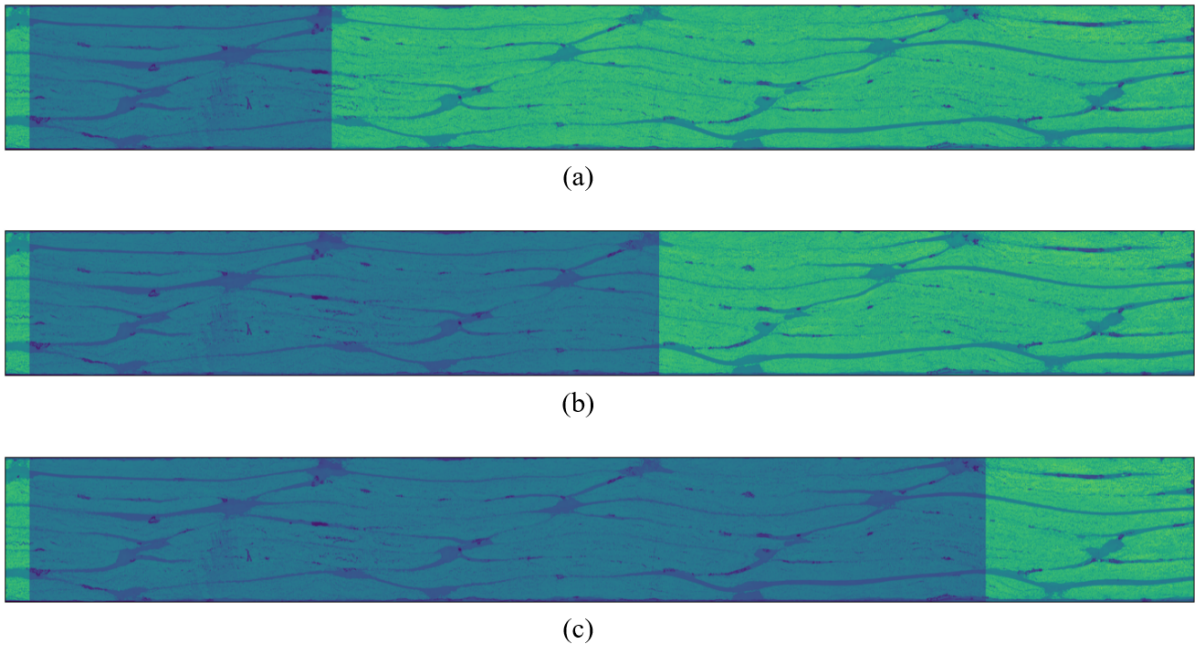


Figure 7.13: Microscopic assessment of WCM Sample 02 for regions of interest with varying widths (in blue): (a) single tow, (b) two tows, and (c) three tows.

7.5 Conclusions

This investigation has shown that the digital image processing (DIP) technique is a reliable means of measuring the fiber volume fraction (FVF) for carbon fiber unidirectional non-crimp fabric (UD-NCF) composites. A single-step analysis approach was proposed to accurately estimate the FVF for a set of associated samples. The methodology involves capturing microscopic images, converting to grayscale, assigning intensity values to each pixel, automatically establishing a threshold to differentiate pixels representing carbon fibers from those corresponding to resin-rich regions, stitching yarns, and voids. Subsequently, the ratio of pixels depicting carbon fibers to the total number of pixels was computed. The DIP technique can be more accurate and less time-consuming than standardized methods, such as the acid digestion method. Microscopic assessment of unidirectional laminates can also yield supplementary information, including fiber tow dimensions, fiber distribution, and void content, all of which influence the mechanical properties of the laminate. Regions of interest within microscopic images of UD-NCF composite samples spanning two tow widths were deemed sufficient to accurately determine the sample FVF without the need for larger images. This research has made an important contribution towards accurately estimating the FVF for carbon fiber UD-NCF through a non-destructive method.

The study also enabled assessment of the microstructure of samples produced through two distinct manufacturing processes, namely wet compression molding and high-pressure resin transfer molding. The study explored microstructural differences, including the dimensions of fiber tows and layers, and the void morphology. Future research will focus on developing a machine learning model to facilitate the rapid assessment of microscopic images and the characterization of specimen microstructure, including void content, FVF, and tow dimensions.

References

[1] E. Duernberger, C. MacLeod, and D. Lines, "Fibre volume fraction screening of pultruded carbon fibre reinforced polymer panels based on analysis of anisotropic ultrasonic sound velocity," *Composites Part B: Engineering*, vol. 254, p. 110 577, Apr. 2023, ISSN: 1359-8368. DOI: 10.1016/J.COMPOSITESB.2023.110577. [Online]. Available: https://www.sciencedirect.com/science/article/pii/S135983682300080X.

[2] Y. Kim, C. Choi, S. K. S. Kumar, C.-G. Kim, S.-W. Kim, and J. H. Lim, "Thermogravimetric analysis method to determine the fiber volume fraction for pan-based cfrp considering oxidation of carbon fiber and matrix," *Composites Part A: Applied Science and Manufacturing*, vol. 102, pp. 40–47, Nov. 2017, ISSN: 1359835X. DOI: 10.1016/j.compositesa.2017.07.024. [Online]. Available: https://linkinghub.elsevier.com/retrieve/pii/S1359835X17302828.

[3] C. N. Morales, G. Claure, J. Álvarez, and A. Nanni, "Evaluation of fiber content in gfrp bars using digital image processing," *Composites Part B: Engineering*, vol. 200, p. 108 307, 2020.

[4] "Standard test methods for constituent content of composite materials," ASTM International, West Conshohocken (PA), Tech. Rep., 2022. DOI: 10.1520/D3171-22.

[5] L. Conklin, "Tutorial for collecting and processing images of composite structures to determine the fiber volume fraction," Tech. Rep., 2017.

[6] R. E. G. Jr., K. J. Kozaczek, and C. O. Ruud, Eds., *Nondestructive Characterization of Materials VI*. Springer US, 1994, vol. Voume 1. DOI: 10.1007/978-1-4615-2574-5.

[7] S. R. Montoro, M. Y. Shiino, T. G. D. Cruz, M. O. H. Cioffi, and H. J. C. Voorwald, "Influence of voids on the flexural resistance of the ncf/rtm6 composites," in *Procedia Engineering*, vol. 10, Elsevier Ltd, 2011, pp. 3220–3225. DOI: 10.1016/j.proeng.2011.04.532.

[8] X. Li, S. Shonkwiler, and S. McMains, "Detection of resin-rich areas for statistical analysis of fiber-reinforced polymer composites," *Composites Part B: Engineering*, vol. 225, p. 109 252, 2021.

[9] H. Yang and J. S. Colton, "Quantitative image processing analysis of composite materials," *Polymer composites*, vol. 15, no. 1, pp. 46–54, 1994.

[10] L. P. Mikkelsen, S. Fæster, and V. A. Dahl, "Dataset for scanning electron microscopy based local fiber volume fraction analysis of non-crimp fabric glass fiber reinforced composites," *Data in Brief*, vol. 48, p. 109 058, Jun. 2023, ISSN: 23523409. DOI: 10.1016/j.dib.2023.109058. [Online]. Available: https://linkinghub.elsevier.com/retrieve/pii/S2352340923001762.

[11] L. P. Mikkelsen, S. Fæster, S. Goutianos, and B. F. Sørensen, "Scanning electron microscopy datasets for local fibre volume fraction determination in non-crimp glass-fibre reinforced composites," *Data in Brief*, vol. 35, p. 106 868, Apr. 2021, ISSN: 23523409. DOI: 10.1016/j.dib.2021.106868. [Online]. Available: https://linkinghub.elsevier.com/retrieve/pii/S2352340921001529.

[12] L. A. Carlsson, D. F. Adams, and R. B. Pipes, *Experimental characterization of advanced composite materials*. CRC press, 2014.

[13] M. T. Cann, D. O. Adams, and C. L. Schneider, "Characterization of fiber volume fraction gradients in composite laminates," *Journal of Composite Materials*, vol. 42, pp. 447–466, 5 Mar. 2008, ISSN: 00219983. DOI: 10.1177/0021998307086206.

[14] J. E. Little, X. Yuan, and M. I. Jones, "Characterisation of voids in fibre reinforced composite materials," *Ndt & E International*, vol. 46, pp. 122–127, 2012.

[15] Y. Nikishkov, L. Airoldi, and A. Makeev, "Measurement of voids in composites by x-ray computed tomography," *Composites Science and Technology*, vol. 89, pp. 89–97, 2013, ISSN: 0266-3538. DOI: https://doi.org/10.1016/j.compscitech.2013.09.019. [Online]. Available: https://www.sciencedirect.com/science/article/pii/S0266353813003813.

[16] P. Yang and R. Elhajjar, "Porosity content evaluation in carbon-fiber/epoxy composites using x-ray computed tomography," *Polymer-Plastics Technology and Engineering*, vol. 53, no. 3, pp. 217–222, 2014. DOI: 10.1080/03602559.2013.843700. eprint: https://doi.org/10.1080/03602559.2013.843700. [Online]. Available: https://doi.org/10.1080/03602559.2013.843700.

[17] G. W. Melenka and A. Gholami, "Fiber identification of braided composites using micro-computed tomography," *Composites Communications*, vol. 27, p. 100 813, Oct. 2021, ISSN: 2452-2139. DOI: 10.1016/J.COCO.2021.100813. [Online]. Available: https://www.sciencedirect.com/science/article/pii/S2452213921001893.

[18] C. Yang, Z. Chen, S. Yao, P. Xu, S. Li, and M. S. Alqahtani, "Quasi-static and low-velocity axial crushing of polyurethane foam-filled aluminium/CFRP composite tubes: An experimental study," *Composite Structures*, vol. 299, Nov. 2022, ISSN: 02638223. DOI: 10.1016/j.compstruct.2022.116083.

[19] X. W. Yu, H. Wang, and Z. W. Wang, "Analysis of yarn fiber volume fraction in textile composites using scanning electron microscopy and x-ray micro-computed tomography," *Journal of Reinforced Plastics and Composites*, vol. 38, pp. 199–210, 5 Mar. 2019, ISSN: 15307964. DOI: 10.1177/0731684418811943.

[20] M. Mehdikhani, L. Gorbatikh, I. Verpoest, and S. V. Lomov, "Voids in fiber-reinforced polymer composites: A review on their formation, characteristics, and effects on mechanical performance," *Journal of Composite Materials*, vol. 53, no. 12, pp. 1579–1669, 2019.

[21] P. Mitschang and K. Hildebrandt, "Polymer and composite moulding technologies for automotive applications," *Advanced Materials in Automotive Engineering*, pp. 210–229, 2012. DOI: 10.1533/9780857095466.210.

[22] M. Ghazimoradi, E. A. Trejo, C. Butcher, and J. Montesano, "Characterizing the macroscopic response and local deformation mechanisms of a unidirectional non-crimp fabric," *Composites Part A: Applied Science and Manufacturing*, vol. 156, p. 106 857, May 2022, ISSN: 1359-835X. DOI: 10.1016/J.COMPOSITESA.2022.106857.

[23] A. Schnabel and T. Gries, "1 - production of non-crimp fabrics for composites," in *Non-Crimp Fabric Composites*, ser. Woodhead Publishing Series in Composites Science and Engineering, S. V. Lomov, Ed., Woodhead Publishing, 2011, pp. 3–41, ISBN: 978-1-84569-762-4. DOI: https://doi.org/10.1533/9780857092533.1.3. [Online]. Available: https://www.sciencedirect.com/science/article/pii/B9781845697624500011.

[24] L. Kärger, S. Galkin, E. Kunze, M. Gude, and B. Schäfer, "Prediction of forming effects in ud-ncf by macroscopic forming simulation–capabilities and limitations," in *ESAFORM 2021 - 24th International Conference on Material Forming*, Liège, Belgium, 14-16 April 2021.

[25] P. Boisse, N. Hamila, E. Guzman-Maldonado, A. Madeo, G. Hivet, and F. Dell'Isola, "The bias-extension test for the analysis of in-plane shear properties of textile composite reinforcements and prepregs: A review," *International Journal of Material Forming*, vol. 10, pp. 473–492, 2017.

[26] F. Mariano, "Development of an LCM process for rapid curing CFRP parts," M.S. thesis, Politecnico di Torino, Torino, Italy, 2019.

[27] A. Cherniaev, Y. Zeng, D. Cronin, and J. Montesano, "Quasi-static and dynamic characterization of unidirectional non-crimp carbon fiber fabric composites processed by hp-rtm," *Polymer Testing*, vol. 76, pp. 365–375, Jul. 2019, ISSN: 01429418. DOI: 10.1016/j.polymertesting.2019.03.036.

[28] *Technical data sheet epikote™ resin 06150 epikure curing agent 06150*, Westlake Epoxy, Jan. 2019.

[29] G. Bradski, "The opencv library," *Dr. Dobb's Journal of Software Tools*, pp. 120–123, 25 2000.

[30] C. R. Harris *et al.*, "Array programming with numpy," *Nature*, vol. 585, pp. 357–362, 7825 Sep. 2020, ISSN: 0028-0836. DOI: 10.1038/s41586-020-2649-2.

[31] N. R. Thompson, "Void formation during liquid composite molding under varied pressure with mechanical properties validation," M.S. thesis, Brigham Young University, 2024.

[32] *Technical data sheet zoltek™ px35 uni-directional fabrics*, Zoltek, Jan. 2021.

[33] Y. Zeng and J. Montesano, "Multiscale fe modelling and ann to predict mechanical properties of non-crimp fabric composites with manufacturing-induced defects," in *38th American Society for Composites (ASC) Technical Conference*, Sep. 2023.

Chapter 8

Effect of stabilizing binder on void morphology and mechanical performance of wet compression molded rapid-curing non-crimp fabric composites

The contents of this chapter stem from the following paper: R. M. Portela, A. Soltansaleki, G. W. Melenka, A. R. de Faria, and J. Montesano, "Effect of stabilizing binder on void morphology and mechanical performance of wet compression molded rapid-curing non-crimp fabric composites," Manuscript submitted (under review).

This chapter presents the mechanical performance characterization of in-house manufactured WCM panels. Samples of these panels were extracted for microscopic assessment using DIP, as described in the previous chapter. CT scans were also conducted to quantify the fiber volume fraction (FVF), microstructure, and void content. Mechanical tests were performed on specimens of both WCM and HP-RTM panels for comparison.

8.1 Overview

The use of binder-stabilized fabrics in wet compression molding (WCM) processes may be necessary to maintain fabric integrity and improve the bending stiffness of thick fabric

stacks for improved resin management, particularly for unidirectional non-crimp fabrics (UD-NCFs). Therefore, it is essential to characterize the influence of stabilizing binder on the mechanical properties and quality of the final part. In this study, UD-NCF composite panels were manufactured with distinct processing conditions, including binder pre-activation and vacuum application during WCM, and extracted specimens were mechanically tested and microscopically assessed via microscopy and X-ray computed tomography. Pre-activation of the stabilizing binder reduced void content within the composite panels, thereby enhancing mechanical properties. Additionally, drawing a vacuum for a duration of 20 s reduced the volume of large voids and increased the fiber volume fraction and interlaminar shear strength. This study provides valuable insights into the effects of a stabilizing binder and vacuum assistance on the mechanical properties of binder-stabilized UD-NCF composites.

8.2 Introduction

8.2.1 Motivation

Wet Compression Molding (WCM) processes for continuous fiber-reinforced composites are suitable for high-volume production parts where highly reactive resins are employed. WCM serves as a potential alternative to High-Pressure Resin Transfer Molding (HP-RTM) processes given that fabric draping and resin infiltration are performed simultaneously in one step without the need for preforming, thus, contributing to reduced cycle times [1–4]. A conventional WCM process involves five main steps, as depicted in Figure 8.1. The initial stage includes cutting and stacking the dry fabric layers, which are then placed into a preheated mold. Thereafter, resin is applied to the stack of fabric before the mold is closed. In some automated systems, the resin may be applied externally, after which the impregnated fabric stack is introduced into the mold. During the molding phase, the fabric is both formed and infused simultaneously, thus removing the necessity for a separate preforming process [4, 5]. Prior to completely closing the mold, a vacuum can be pulled for a specified duration to extract any air within the mold cavity. Finally, the resin cures, allowing for the removal of the completed part from the mold.

WCM parts comprise continuous reinforcements, such as woven fabric or non-crimp fabric (NCF), and snap-cure resin when high-volume production is sought. Unidirectional non-crimp fabrics (UD-NCFs) are a type of continuous fiber reinforcement composed of parallel-oriented tows. These tows are held together by stitching yarns, which provide stability and improve handling during the manufacturing process [6, 7]. Unlike woven

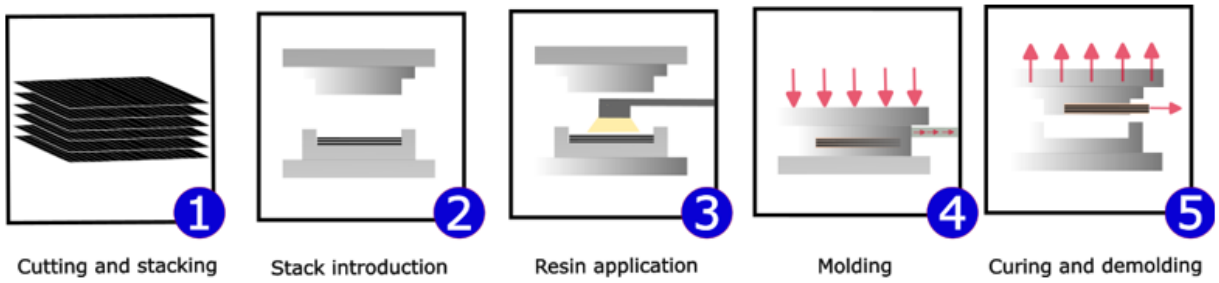


Figure 8.1: Schematic of the typical steps for a direct WCM process.

fabrics, which have interlaced yarns, NCF tows are not interlaced, resulting in improved fiber alignment and reduced crimp, leading to enhanced in-plane mechanical properties [8–11]. Rudd et al. [8] highlight that NCF composites can provide higher lightweight potential, as they can withstand up to 15% greater load compared to similar woven composites. Nevertheless, the lack of tow interlacing in UD-NCFs results in relatively low fabric stability during handling, while they are more prone to wrinkling during forming owing to low bending stiffness along the transverse direction [12].

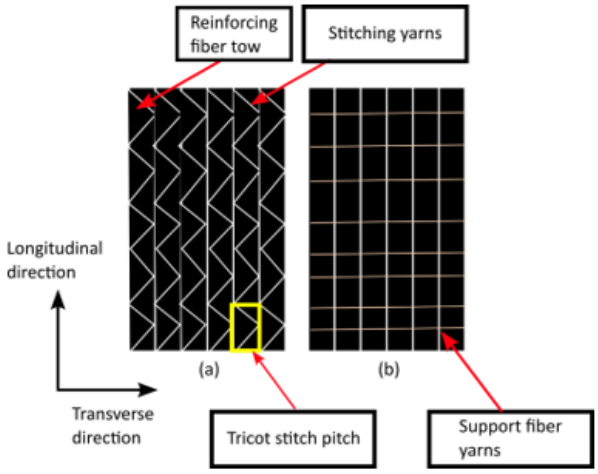


Figure 8.2: Schematic of UD-NCF: (a) stitching side with yarns in a tricot pattern, and (b) transversely oriented supporting fiber side.

The design of associated structural composite components requires multiple layers of UD-NCF, which can be oriented in different directions to achieve the desired anisotropic properties and mechanical performance. However, the fabrication of these components may

result in relatively thick stacks and a significant quantity of resin dispensed on the stack (refer to step 3 in Figure 8.1). The manufacturing of thick complex-shaped components via the WCM process in deep-cavity molds presents challenges related to resin management due to the possibility of the UD-NCF draping under gravity with a significant amount of resin applied (Figure 8.3). Premature draping of the stack prior to closure of the mold may result in resin pooling and undesired movement of the fabric stack within the mold and, consequently, defects in the final part. A potential alternative to overcome premature draping is use of binder-stabilized UD-NCF. The stabilizing binder can increase the bending stiffness of the fabric and improve resin management [13, 14].

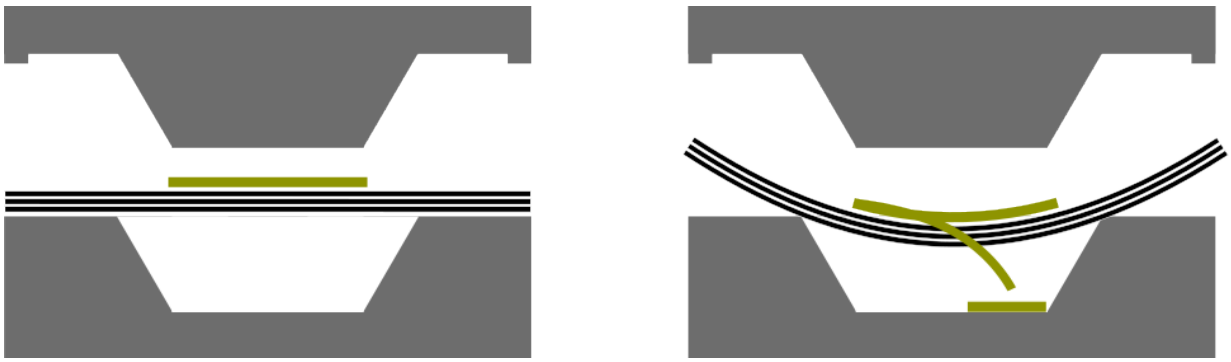


Figure 8.3: Schematic demonstrating distinct draping characteristics between: (a) binder-stabilized fabric stack, and (b) non-bindered fabric stack with lower bending stiffness.

8.2.2 State-of-the-Art

Stabilizing binders or tackifiers applied to fabrics are commonly thermoplastic or uncatalyzed epoxy resins in liquid or dry powder forms [15–17]. When activated, the stabilizing binder creates cohesion between adjacent fabric layers, preventing movement and reducing defects such as wrinkling, fiber misalignment, and fiber washout. Additionally, the stabilizing binder aids in maintaining fabric integrity during trimming and handling of the fabric layers and minimizes fiber volume fraction (FVF) variation in the final part [3, 8, 14, 15, 18–23]. On the other hand, tackifiers may have drawbacks under certain process conditions, including reducing fabric permeability, increasing resin viscosity [15–17, 24], and altering the fabric draping behavior [25–29]. Estrada et al. [15] observed a reduction in permeability with increased binder concentration. Brody and Gillespie [16] studied the effect of thermoplastic binder on vinyl ester resin and noted that the powder of the binder dissolves gradually in the resin, leading to a decrease in the binder particle size over time.

The authors also reported an increase in the resin viscosity and a delay in the curing time. Yoo et al. [17] studied the influence of epoxy binder on the permeability of fabric and reported a reduction in the permeability of up to 98%. Neunkirchen et al. [24] observed the formation of an interlayer caused by the melting of the stabilizing binder powder which blocked some capillary channels, slowing resin flow. The reduction in fabric permeability caused by a stabilizing binder may lead to higher void content in the final part [10, 18, 30].

The use of a stabilizing binder may also influence the mechanical properties of the final composite part as a result of any introduced defects. In a series of studies, Tanoğlu and Tuğrul [31, 32] investigated the effect of powder thermoplastic polyester binder concentration on the mechanical performance of vacuum-assisted resin infused E-glass/polyester composite parts. In Ref. [31], they reported a reduction in flexural strength and Mode I interlaminar fracture toughness with use of with 3% wt binder content, while interlaminar shear strength was not influenced by the presence of a binder. In Ref. [32], they stated that the compressive strength and modulus of the same material increase with up to 3wt.% binder content, and are reduced with any further addition of binder. The authors also highlight that the highest preform compaction is achieved at 3wt.% binder content, where the preform thickness increases for higher binder concentrations. Daelemans et al. [33] investigated the use of a thermoplastic polyester as an interlayer toughening system for composite laminates fabricated by vacuum-assisted resin infusion. They reported that for high concentrations the mixture of thermoplastic polyester with epoxy resin resulted in polyester-rich globules, which reduced the fracture toughness of the matrix. On the other hand, low concentrations of the polyester (i.e., up to 4.8 wt%) increased the elongation of the epoxy and the fracture toughness, resulting in up to a 60% increase in Mode I interlaminar fracture toughness. While these reported results provide valuable insight into the influence of thermoplastic binder on the mechanical properties of resin infused composite parts, they cannot be generalized for different types of fabrics (e.g., UD-NCF), fabrics with commonly employed thermosetting binders, or for parts manufactured using other liquid composite molding (LCM) processes, such as WCM, given the distinct process characteristics. Hillermeier and Seferis [34] conducted a comparison of epoxy binder in two different forms (i.e., in powder and spray) applied to resin transfer molding (RTM) preforms. They reported that the spray was more evenly distributed on the fabric surface, resulting in a more homogeneous laminate than that produced with the powder binder. Consequently, the spray-bonded composites exhibited a 30% improvement in Mode II interlaminar fracture toughness. The limited number of publications focused on studying the influence of stabilizing binder on the mechanical properties of composite materials highlights a gap in the literature, especially regarding UD-NCF composites manufactured via the WCM process.

The morphology of voids and the resulting mechanical properties of composite materials depend not only on the material system used but also on the manufacturing process [35]. In LCM processes, voids may originate due to mechanical entrapment or gases resulting from chemical reactions during resin curing [36–38]. In the case of the WCM process, resin infiltration occurs during the molding stage, simultaneously with the draping process, and it is a thickness-dominated flow under low pressure. Muthuvel et al. [39] describe a rapid resin flow through the stack thickness at the beginning of mold closure during the WCM process, regardless of the number of layers, followed by a gradual progression and stabilization of the flow across the fabric stack. However, the stabilized flow or low-pressure gradient may lead to microscopic flow behaviour that impregnates the fiber tows but poorly fills the spaces between them, resulting in the formation of large voids between fiber tows (Figure 8.4) [36, 37]. These inter-tow voids are more likely to initiate damage, in contrast to micro-voids located within the fiber tows (i.e., intra-tow voids), which are smaller and less detrimental to the mechanical properties of the composite parts.

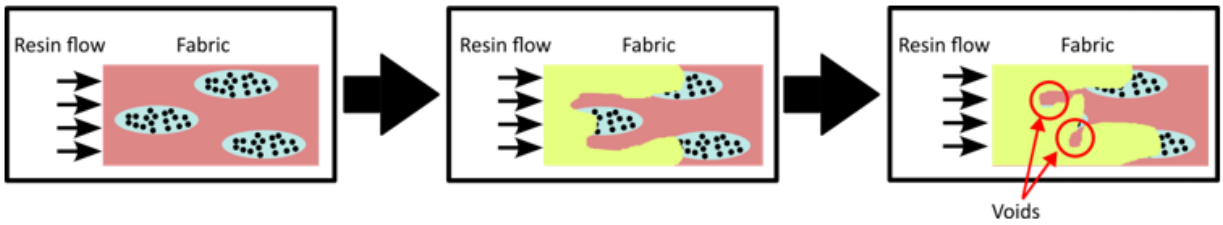


Figure 8.4: Schematic of in-plane resin flow and the resulting inter-tow void formation under low-velocity infiltration.

Voids of certain size and morphology may represent critical defects in composite materials because they can act as stress concentrators and significantly reduce matrix-dominated mechanical properties, such as interlaminar shear strength and transverse tensile strength [36, 40–43]. Ghiorse [44] reported a 20% reduction in both flexural and interlaminar shear strength in composites containing only 2% of void content. Zhang et al. [45] examined the influence of void content on the strength and ductility of composite materials and observed that a void content of 2.5% results in reductions of 34% in transverse tensile strength and 35% in ultimate strain. The authors also noted that when void content exceeds 1.5%, the composite part becomes more brittle, with lower strain at failure and decreased strength. Additionally, they stated that voids larger than 5 μm in diameter impact ductility and failure susceptibility. Luo et al. [46] reported that composites with 3% void content can experience about a one-third decrease in matrix-dominated mechanical properties.

While mitigating the formation of voids is desirable, manufacturing void-free composites

is often impractical and economically unjustified. However, the production of high-quality WCM parts can be achieved by controlling the void formation. Some strategies include degassing the resin prior to application and drawing air from the sealed mold using a vacuum pump before complete mold closure. Mehdikhani et al. [37] conducted a comprehensive review on void formation in fiber-reinforced polymer composites. They reported that the vacuum technique can improve the composite part quality in LCM processes by reducing the air pressure inside the mold and drawing the trapped air, which may result in a lower void content; however, if not properly managed, the application of vacuum in LCM processes can also promote void formation by inducing resin evaporation. Kaynak et al. [47] studied the effects of vacuum on the mechanical properties of a woven glass composite fabricated via the RTM process. They reported that the vacuum application contributes positively to the final mechanical properties due to the void content reduction, although void content was not quantified. The authors observed reductions of up to 26% in impact toughness and 5% in tensile and flexural strength in composite parts produced without vacuum application. Nevertheless, similar studies on fiber-reinforced composites manufactured using by WCM have not been reported in the literature.

Ayatollahi [48] examined the effect of process parameters, including resin temperature, mold temperature, resin set time, gap closure speed, and mold curing time, on the quality of UD-NCF carbon fiber/epoxy WCM panels. Mold temperature, resin temperature, and resin set time significantly impacted the mechanical properties, while gap closure speed and mold curing time exhibited no notable effect. Also, Sears [49] further studied the WCM process for the same material system and identified a temperature gradient across the mold, which correlated with locations where the specimens exhibited reduced mechanical properties. Although both investigations provided a significant contribution to improving the understanding of the WCM process, they did not consider the application of vacuum to the mold nor the pre-activation of binder-stabilized fabric to assess their influence on part quality and mechanical properties.

8.2.3 Objective of Study

The objective of this study is to assess the influence of a stabilizing binder and vacuum assistance on the void morphology and mechanical performance of wet compression molded carbon fiber UD-NCF snap-cure epoxy composite panels. The research involved several key tasks, including manufacturing flat panels using a WCM process, microscopic evaluation to determine FVF and qualitatively assess void formation, X-ray computed tomography scans to quantitatively assess void morphology and content, and mechanical testing to establish mechanical properties. For the latter, tensile tests were performed to measure

longitudinal and transverse Young's modulus and strength, while short-beam shear (SBS) tests were performed to assess interlaminar shear strength. The mechanical properties were correlated with the FVF and void content observed within the panels. In addition, the quality and mechanical properties of the WCM panels was compared to specimens taken from previously manufactured HP-RTM panels, which served as a benchmark for this investigation.

8.3 Materials and panel manufacturing

8.3.1 Materials

The panels used in this investigation were manufactured from a UD-NCF, specifically PX35-UD300 (Zoltek, US) [50]. The fabric was composed of axially oriented, parallel tows, each containing 50K continuous PX35 carbon fibers, which were stitched together with 76 dtex polyester yarn in a tricot pattern. The fabric also contained low linear density transversely oriented supporting glass fibers to enhance handleability. The fabric had a total areal weight of 333 g/m^2. One variant of the fabric did not include a stabilizing binder, while the other variant included a thermosetting polymer powder binder dispersed on the surface of the fabric with the stitch tricot pattern. Moreover, a three-part snap-cure resin system was used, namely Epikote 6150 (Westlake Epoxy, US). The resin system comprised a medium-viscosity snap-cure epoxy resin, a low-viscosity amine hardener, and an internal mold release agent [51].

8.3.2 Panel manufacturing

The equipment used to manufacture the WCM flat panels included a Genesis G100H-24-CPX 100-ton press (Wabash MPI, US) (Figure 8.5a), a custom two-part steel mold with a variable thickness cavity measuring 304.8 mm × 304.8 mm (Laval, Canada) (Figure 8.5b), and a Super E electronic metering unit (Michael Engineering Ltd., US) for rapid mixing and dispensing of the resin system (Figure 8.5c). The setup also included a vacuum pump and a catch pot for the subset of panels that utilized vacuum assistance for drawing air out of the sealed mold cavity. The upper mold half featured a vacuum port, while the lower half of the mold was equipped with a wiper vacuum seal that engaged prior to full mold closure and a silicon fiber pinch seal to prevent fiber wash during resin impregnation. The mold halves were mounted onto the press platens, which included integrated cartridge heating

elements. The metering unit comprised a heated tank for the resin and a second tank for the hardener, each connected to a hose that fed into an electronically controlled dispensing gun equipped with a static mixing nozzle. The resin and hardener were adequately mixed in the nozzle before being dispensed onto the UD-NCF stack. Further details of the WCM process setup are provided in Ref. [52].



(a) (b) (c)

Figure 8.5: WCM equipment utilized for manufacturing flat panels: (a) 100-ton hydraulic press with heated platens, (b) lower half of two-part mold with wiper vacuum seal visible, and (c) electronic metering unit for quick mixing and dispensing of resin and hardener.

Prior to beginning each WCM trial, the mold cavity was cleaned and sealed, and Loctite Frekote 770NC release agent (Henkle, Germany) was applied. The upper and lower press platens, and correspondingly the upper and lower tool halves, were preheated to a set temperature of 135°C and 115°C, respectively, and the temperature was maintained throughout the manufacturing trials. The resin and internal mold release were poured into the heated tank of the metering unit and premixed, and the hardener was poured into the second tank. The metering unit was programmed to automatically dispense 104.52 ml of the three-part resin mixture for each panel, following a volume ratio resin: curing agent: internal mold release = 100: 29 : 1.7.

Eight layers of UD-NCF, each measuring 300 mm × 300 mm, were cut and stacked with

a sequence $[0]_8$ and introduced into the lower cavity of the preheated mold. For panels comprising stabilizing binder that was pre-activated, the fabric stack was pre-heated in an oven at 120°C for 20 minutes. The three-part resin system was subsequently mixed and dispensed onto the center of the fabric stack, and the mold was closed with a constant force set to achieve 15 bar pressure within the mold cavity. For a subset of the panels, prior to complete mold closure, vacuum was applied for 10 seconds or 20 seconds. The panels were allowed to cure for 5 minutes prior to demolding without a cooling cycle. A total of ten panels covering five different configurations were manufactured (Table 8.1).

Additionally, flat panels made of seven layers of the same UD-NCF fabric ($[0]_7$) and epoxy resin system fabricated in a previous study [53] using an HP-RTM process were also investigated. Although the WCM panels fabricated through this study and the previously fabricated HP-RTM panels comprised the same fabric and resin system, microstructural variations were expected because of the distinct manufacturing processes.

Table 8.1: Configurations of panels fabricated using the WCM process, including fabric binder state and vacuum duration specified.

Configurations	Identifier	Stabilizing binder state	Vacuum duration	Quantity
1	UNB	None	None	2
2	IT	Inactivated	None	2
3	AT	Pre-activated	None	2
4	VAC 10s	Pre-activated	10 s	2
5	VAC 20s	Pre-activated	20 s	2

8.4 Mechanical testing and microstructural assessment

8.4.1 Tensile testing

Two sets of tensile test specimens were extracted from the manufactured panels using an abrasive waterjet cutting machine (ProtoMAX, OMAX): one set was cut along the fiber direction (longitudinal) and the other was cut perpendicular to the fiber direction (transverse) (Figure 8.6 (a)). The transverse test specimens measured 160 mm × 20 mm, while the longitudinal specimens measured 200 mm × 15 mm in accordance with test standard ASTM D3039 (Figure 8.6 (b)) [54]. After extracting the rectangular specimens from the panels, the specimens were equipped with 40 mm-long end tabs (Al 6063) bonded with Loctite 480 black, rubber-reinforced instant adhesive to mitigate the risk of end tab slippage and premature failure at or near the end tab region.

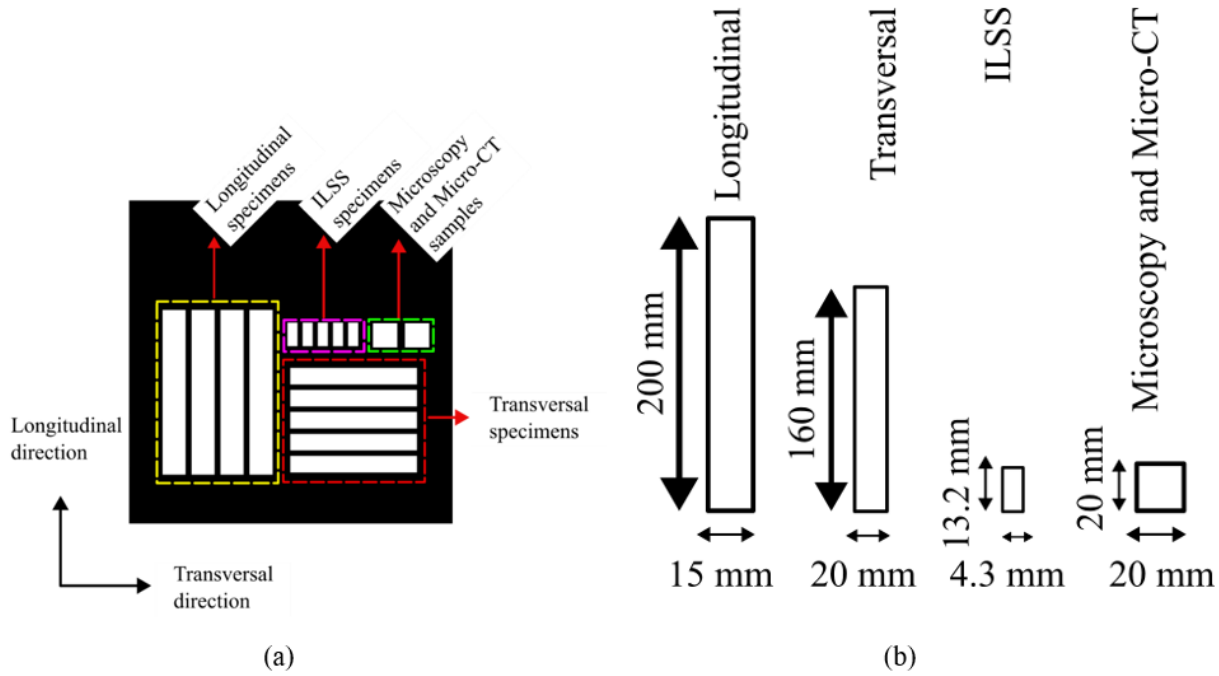
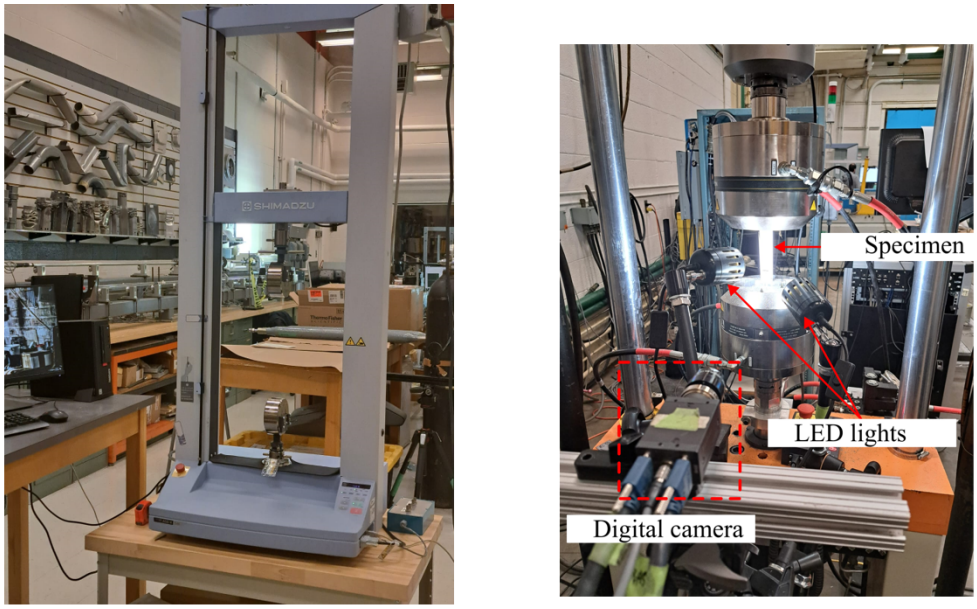


Figure 8.6: (a) Sketch of the manufactured panels showing the regions where the specimens were waterjet cut for mechanical tests and microscopic analysis, and (b) dimensions of each specimen.

Quasi-static tensile tests on the transverse and longitudinal specimens were conducted at room temperature using a Shimadzu AGS-X universal testing machine with mechanical wedge grips (±10 kN load cell capacity, Figure 8.7a) and an Instron 1331 universal testing machine with hydraulic wedge grips (±100 kN load cell capacity, Figure 8.7 b), respectively,

in accordance with ASTM D3039 [54]. All tensile tests were performed in displacement control with a crosshead speed of 2 mm/min, with 4-5 repeats per configuration to gather sufficient data for statistical analysis. For all experimental trials, a fan was used to mitigate noise in DIC strain measurements, yielding an uncertainty of 1×10^{-5} mm/mm. From these repetitions, only the specimens that failed significantly away from the end tabs were selected for analysis. For all tests the Young's modulus, ultimate tensile strength, and ultimate strain were determined. For calculating the Young's modulus, the slope of the stress-strain data was measured over the strain range of 0.2% – 0.3%.



(a) (b)

Figure 8.7: Universal testing machines used in tensile tests: (a) Shimadzu AGS-X for testing transverse specimens and (b) Instron 1331 for testing longitudinal specimens.

Two-dimensional digital image correlation (DIC) was employed to track specimen surface displacement fields using a VIC-2D 5 MP system, which includes a 5MP digital camera (Figure 8.7b). The region of interest (ROI) located at the center of each specimen, measuring 120 mm × 15 mm for the longitudinal specimens and 80 mm × 20 mm for the transverse specimens, was speckled with a fine black-on-white spray paint. The software VIC-Snap (Correlated Solutions, Inc) was used to capture the images at a frequency of at least 4 frames per second during the experimental tests. The average strain within the

ROI, which has a pixel size of 45.34 μm/pixel, was calculated using a subset of 20 pixels, a step size of 5 pixels, and a median strain filter.

To evaluate the statistical significance of the influence of the stabilizing binder, its activation, and the vacuum-assistance on the laminate mechanical properties, pairwise analyses were conducted on mechanical properties for two conditions (i.e., Young's moduli and strength data) using a two-sample T-test. The null hypothesis assumes no significant difference between the analyzed data sets and is accepted when the corresponding p-value is greater than 0.05. If this condition is not satisfied, the null hypothesis is rejected, indicating a significant difference between both data sets.

8.4.2 Short-beam shear testing

SBS tests were performed using a custom servo-hydraulic test frame equipped with a $\pm$10 kN capacity load cell and a three-point bend fixture (Figure 8.8). All tests were performed in displacement control with a crosshead speed of 1 mm/min until the desired failure mode (i.e., a delamination crack) was observed, in accordance with ASTM D2344 [55]. Five repeats were carried for each configuration to gather enough data for statistical analysis. To observe the failure mode of the specimen, a 5 MP digital camera equipped with a Schneider Kreuznach 1.9/35 mm lens and two led lamps captured images at a frequency of 1 frame per second. The load-displacement data was recorded and the shear stress was calculated using:

$$\tau_{sbs} = \frac{3\,P}{4\,b\,h} \tag{8.1}$$

where P is the load, b is the measured specimen width, and h is the measured specimen thickness. The inter-laminar shear strength (ILSS) was calculated using the maximum load, Pm, and Eq. (8.1). Analogous to the tensile tests, a two-sample T-test was performed on ILSS values of specimens from two configurations

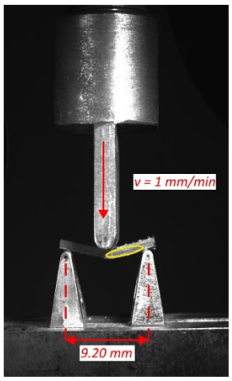


Figure 8.8: Image of an SBS test showing the support span length, the direction of displacement of the loading pin, and a delamination region near the loading pin.

8.4.3 Microscopy

Microscopic evaluation was performed on two samples extracted from panels for each configuration (Figure 8.6a) to measure the panel thickness, determine FVF, and qualitatively assess microstructure and void formation. Samples with dimensions 20 mm × 20 mm were extracted from the panels, cold-mounted in a two-part epoxy resin, namely Lecoset 7008 (Leco), sanded, and polished. To ensure high-quality microscopy images, each sample underwent a four-step polishing process using an automatic polishing machine (Tegramin, Struers). This involved coarse grinding with a 120-grit pad (Primo 120, Struers), finer grinding with a 9 μm diamond solution (MD-Allegro, Struers), coarse polishing with a 3 μm diamond solution (MD-Dac, Struers), and finishing with a 1 μm diamond solution (MD-Nap, Struers). After polishing, the samples were cleaned with acetone and ethanol. The cold-mounted samples were examined using a Keyence VHX-5000 opto-digital microscope equipped with a 500× to 5000× lens. Using the lowest magnification of this lens, mosaic images spanning the width of several tows were obtained for each sample. The FVF of the samples was estimated by digital image processing using a custom script that evaluates pixel intensity and assigns a threshold to classify each pixel as either fiber or matrix. Additional details of the imaging procedure are provided in Ref. [56].

8.4.4 Micro-CT imaging

X-ray micro-computed tomography (μCT) was employed to analyze void content and distribution, as well as to characterize the material microstructure, enabling a direct compar-

ison between microstructural characteristics and the mechanical behavior of the material for each configuration considered. Previous studies have shown that μCT is a reliable technique for qualitatively and quantitatively assessing voids in composite materials [57–59].

Samples measuring 20 mm $\times$ 20 mm extracted from panels (Figure 8.6a) for Configurations 1–3 and 5 and later machined to 10 mm $\times$ 10 mm in size, were scanned using a SkyScan 1272 μCT scanner (Bruker, Belgium) (Figure 8.9a). In this system, an X-ray beam is projected from a source onto the sample, and the transmitted radiation is captured by a flat-panel detector (Figure 8.9b). During scanning, the sample rotates incrementally, and multiple projection images are acquired at each angular step. The μCT software averages these projections to enhance image quality and stores the data. Image binning is determined by the geometric configuration, including the distances between the source, sample, and detector. Additionally, the system offers various filters to adjust the intensity of the X-ray beam; however, due to the high quality of the acquired images, the use of filters was unnecessary [60]. The binning mode was selected based on the sample size and the desired field of view. The maximum resolution capacity of the scanner was utilized to capture fine features such as voids, supporting glass fibers, and the volume corresponding to the carbon fiber, stitching yarns, and matrix. As a result, the reconstructed datasets were large in volume and required substantial computational resources. A summary of the scanning parameters is provided in Table 8.2.

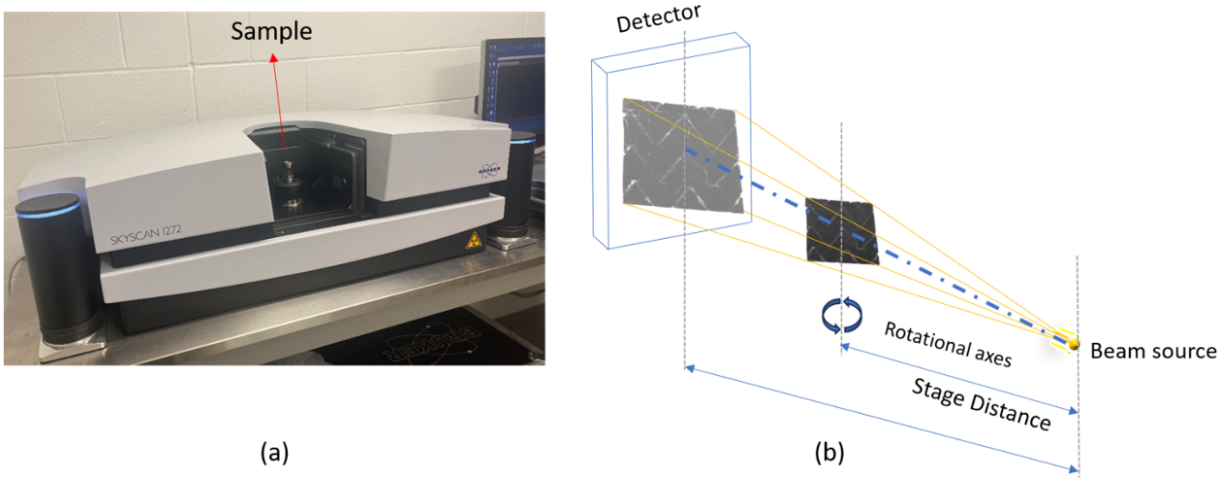


Figure 8.9: (a) μCT Sky Scan 1272 used to CT-scan the four samples, (b) schematic of the scanning procedure.

Table 8.2: Parameter used for X-ray μCT scanning of the WCM samples.

Parameter	Value
Source voltage [kV]	60
Source current [μA]	166
Image pixel size [μm]	$8 \times 8 \times 8$
Frame averaging	3
Rotation step [deg]	0.4
Depth [bits]	8
Image size	2452×1640
Filter [mm]	No filter
Scan duration	1 h : 2 m : 59 s
Flat field correction	On

After scanning, the cross-sectional images were reconstructed using the software NRecon (version 1.7.1.0, Bruker, Belgium). Figure 8.10a shows the reconstructed mid-section slice of an AT sample, which serves as a representative for all samples. To minimize ring artifacts, a ring artifact correction factor of 9 was applied during the reconstruction process. By stacking the reconstructed cross-sectional images, 3D volumetric models were generated and visualized as described in Ref. [61]. In this study, visualization and subsequent analysis were carried out using Avizo 3D (Thermo Fisher Scientific, version 2021.2).

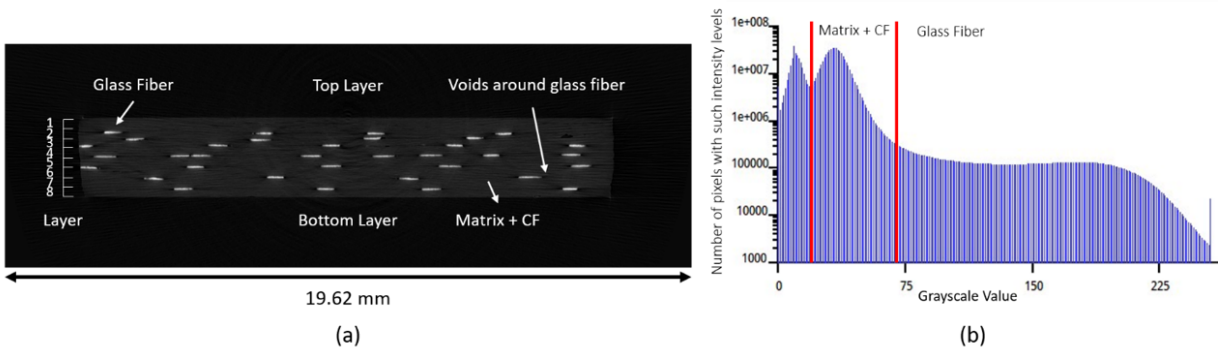


Figure 8.10: Microscopic analysis of an AT sample showing: (a) cross-sectional CT image with supporting glass fibers and voids shown, and (b) histogram with values for threshold for voids and glass fibers.

The reconstructed cross-sectional images had a voxel size of 8 μm × 8 μm × 8 μm. To enhance the quality of the analysis and reduce computational cost, a volume of interest was extracted from the full image stack after reconstruction. Background noise was filtered using a local thresholding approach applied to each cross-sectional image individually. During the segmentation process, voids, supporting glass fibers, and the volume associated with the carbon fibers, stitching, and matrix were identified based on the grayscale histogram (Figure 8.10b). However, due to similar X-ray attenuation properties of the matrix, polyester stitching, and carbon fibers, they could not be segmented separately [62]; thus, the FVF could not be calculated from the μmCT scans. The grayscale range associated with each zone for voids in each sample is summarized in Table 8.3.

Table 8.3: Gray scale classification range for segmenting each sample type for voids only.

	UNB	IT	AT	VAC 20 s
Void	<8	<10	<25	<12

Porosity analyses were also performed on the 3D datasets to quantitatively assess void fraction. The voids were classified by individual volume into three categories: small voids (<0.001 mm^3), medium-sized voids (0.001 mm^3 – 0.005 mm^3), and large voids (>0.005 mm^3). Finally, the void percentage was calculated as [63]:

$$v_{vo} = \frac{V_{vo}}{V_{vo} + V_C} \tag{8.2}$$

where V_C is the volume of the composite specimen and V_{vo} denotes the total volume of voids in the specimen.

8.5 Results

8.5.1 Microstructural Assessment

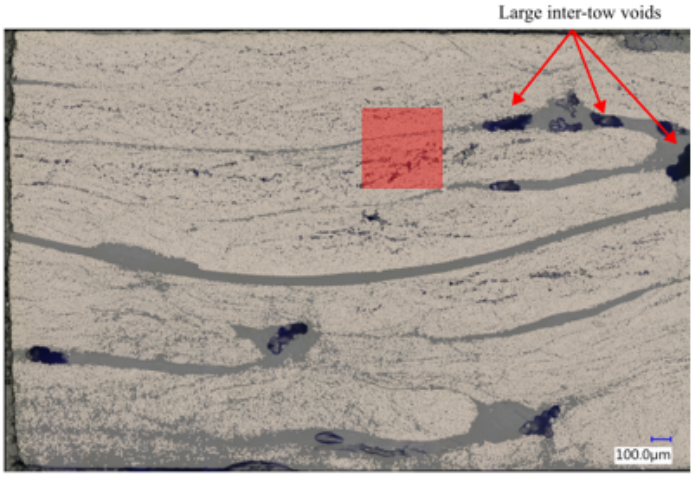
Samples extracted from WCM panels corresponding to each configuration and the HP-RTM panels were used to measure panel and average ply thicknesses and to estimate FVF (Table 8.4). The average ply thickness and, thus, the FVF was similar in magnitude for each of the WCM samples, with FVF values falling within the same range of scatter. The exception was the VAC 20 s specimen, which exhibited a slightly lower average ply thickness and higher FVF. In addition, the FVF for the HP-RTM samples was notably

Table 8.4: Panel and average ply thickness for each investigated configuration, along with FVF. Average values with standard deviation are tabulated.

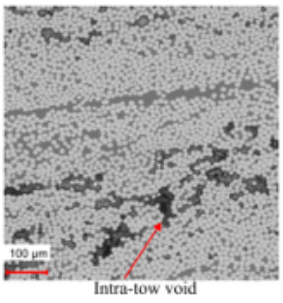
	Panel thickness [mm]	Average ply thickness [mm]	FVF [%]
UNB	2.28 ± 0.01	0.29 ± 0.01	62.17 ± 2.56
IT	2.24 ± 0.01	0.28 ± 0.01	62.06 ± 2.46
AT	2.34 ± 0.00	0.29 ± 0.00	62.63 ± 2.72
VAC 10s	2.34 ± 0.01	0.29 ± 0.02	61.54 ± 2.85
VAC 20s	2.19 ± 0.00	0.27 ± 0.01	63.60 ± 2.41
HP-RTM	2.25 ± 0.02	0.32 ± 0.02	54.71 ± 2.02

lower than that of the WCM samples, revealing that greater compaction was achieved for the WCM panels.

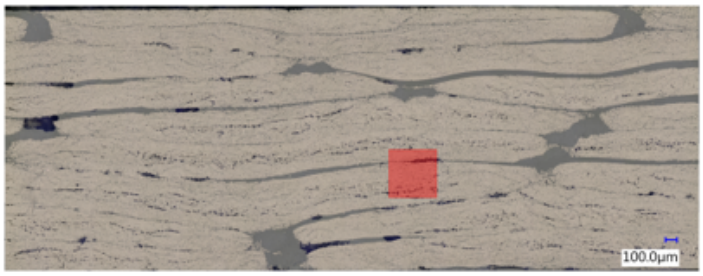
Samples were also used for qualitative assessment of the microstructure and to identify the location of voids (Figure 8.11). The UNB samples (Figures 8.11a and 8.11b) exhibited the greatest void content, characterized by notable micro-voids within the fiber tows (i.e., intra-tow voids) and between the tows (i.e., inter-tow voids). The IT samples (Figures 8.11c and 8.11d) similarly exhibited a significant number of intra- and inter-tow voids, revealing that the existence of a stabilizing binder did not influence the material microstructure. The void content and size were observed to be reduced within the AT samples (Figures 8.11e and 8.11f) relative to the UNB and IT samples, with intra-tow voids being dominant and minimal inter-tow voids observed. This finding reveals that pre-activation of the stabilizing binder has improved the quality of the material. Interestingly, the content of intra-tow voids was greater for the VAC 10 s samples (Figures 8.11g and 8.11h) when compared to the AT samples, which may be due to resin evaporation during the time air was drawn out of the mold using a vacuum pump. However, the VAC 20 s samples (Figures 8.11i and 8.11j) exhibited a notable reduction in the void content when compared to the VAC 10 s samples, which can be attributed to the fact that sufficient time was allowed for air, and possibly evaporated resin, to be removed from the mold. The HP-RTM samples (Figures 8.11k and 8.11l) exhibited limited intra-tow voids and no inter-tow voids.


Large inter-tow voids
100.0μm

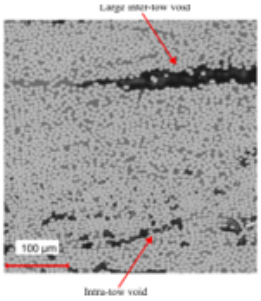
(a)


100 μm
Intra-tow void

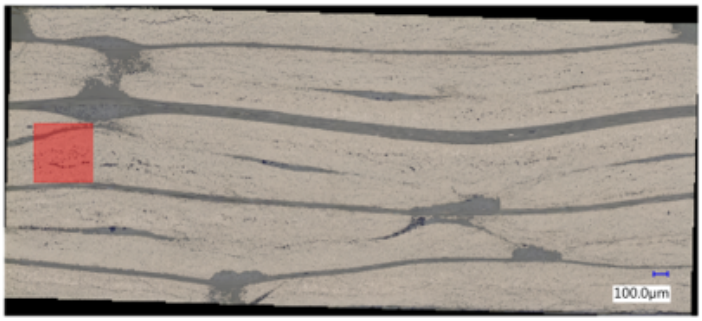
(b)


100.0μm

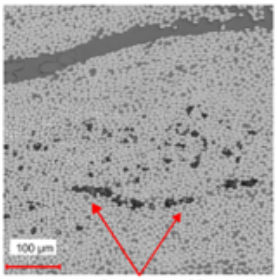
(c)


100 μm

(d)


100.0μm

(e)


100 μm
Intra-tow void

(f)

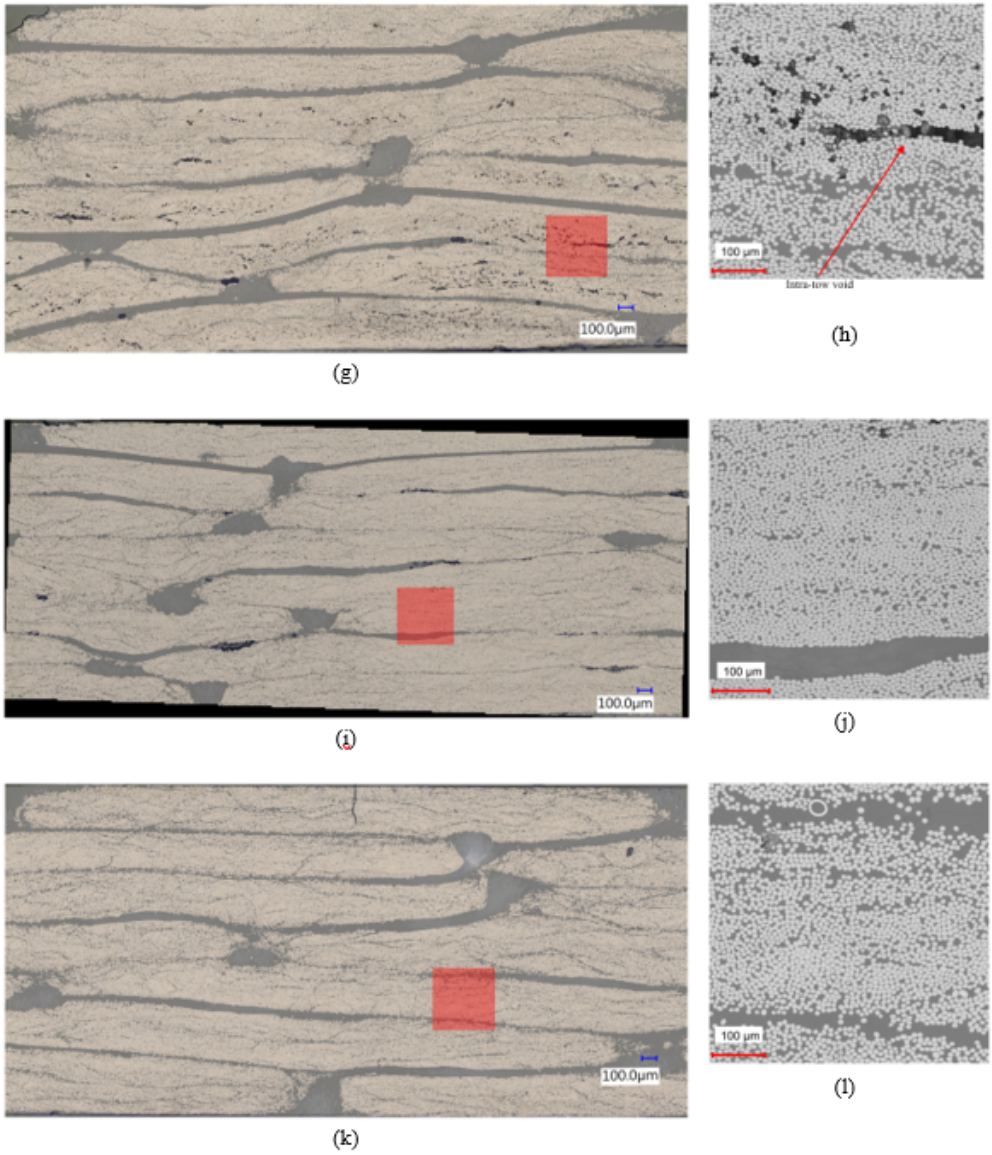


Figure 8.11: Microscopic images of samples extracted from panels manufactured by indicated processing condition, including a magnified view of a region of interest (ROI) in each image: (a-b) UNB sample, (c-d) IT sample, (e-f) AT sample, (g-h) VAC 10 s sample, (i-j) VAC 20 s sample, (k-l) HP-RTM sample.

8.5.2 Void Morphology

Figure 8.12 shows images of 3D volumetric models generated from the CT scans of samples for four configurations, showing supporting glass fibers and voids, while Figure 8.13 includes

2D images for the same samples. It is worth noting that the carbon fibers, stitching yarns, and matrix constituents could not be distinguished by the CT scanner due to similarities in their densities; therefore, the measurement of FVF was not possible using CT scans. For the UNB and IT samples, large voids were observed adjacent to the supporting glass fibers along their contours, which correspond to inter-tow voids (Figures 8.12b, 8.12c, 8.13b, and 8.13c). This important finding highlights the influence of the supporting glass fibers on void formation. The supporting glass fibers may act as a physical barrier to resin flow where air entrapment is more likely to occur. For the same samples, a significant number of small voids were observed in the regions around the glass fibers, corresponding to intra-tow voids, as shown in Figures 8.11-8.11d. The AT samples featured smaller inter-tow voids adjacent to the supporting glass fibers, as well as small intra-tow voids in the surrounding regions (Figures 8.12a and 8.13a). Finally, for the VAC 20 s samples fewer large voids were observed and instead smaller intra-tow voids were observed (Figures 8.12d and 8.13d). The UNB and IT samples exhibited a notably higher void content than the other samples, while the void content was similar for the AT and VAC 20s samples (Table 8.5). This finding further reveals that pre-activation of the stabilizing binder improved the quality of the material. One explanation may be that the pre-activated binder enhanced adhesion between the fabric layers for the AT and VAC 20 s panels, which reduced sliding between layers relative to the UNB and IT panels, leading to less air entrapment between layers.

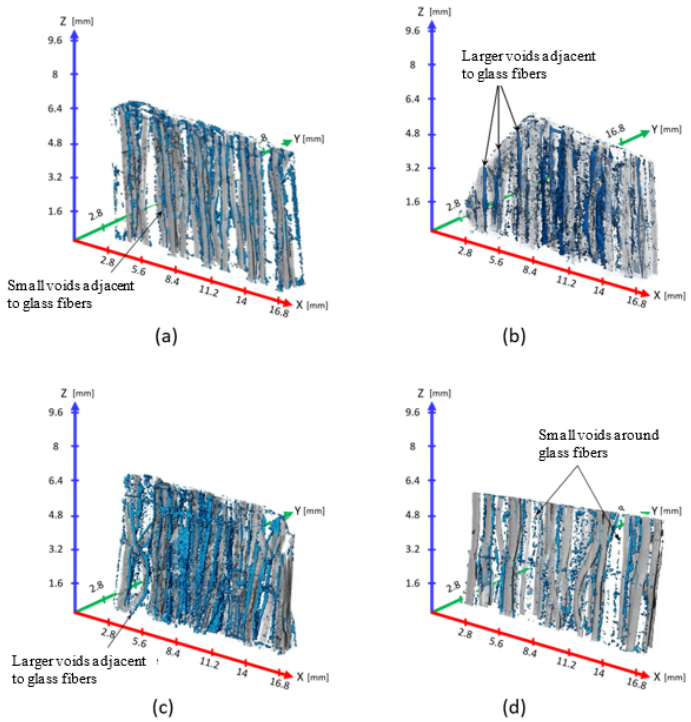


Figure 8.12: 3D volumetric models generated from the CT scans of samples showing supporting glass fibers in grey and voids in blue: (a) AT, (b) IT, (c) UNB, and (d) VAC 20 s samples.

Figure 8.14 shows the void distribution along the sample thickness for voids with volumes classified into three groups: small (<0.001 mm^3), medium (0.001 mm^3 – 0.005 mm^3), and large (>0.005 mm^3). Idealizing a void as a sphere simply for perspective, which is not necessarily accurate, a small void would be regarded as having a diameter <120 μm, while a large void a diameter >200 μm. Note that the position of 0 mm for the samples corresponds to the surface of the panel onto which the resin was poured (i.e., the panel surface in contact with the upper mold). It is noticeable that for all samples, voids from each classification group were distributed through the sample thickness. The largest voids in the UNB and IT samples exceeded a volume of 1.0 mm^3, with several voids >0.1 mm^3 (i.e., very large voids and broader variation in size). In contrast, the large voids in the AT and VAC 20 s samples did not exceed a volume of 0.1 mm^3 and exhibited a narrower variation in size relative to the UNB and IT samples, revealing the positive influence of binder pre-activation on mitigating large void formation. Moreover, the VAC 20s samples

exhibited the fewest large voids, specifically 36% fewer than the AT samples, revealing the effectiveness of vacuum assistance in mitigating large void formation.

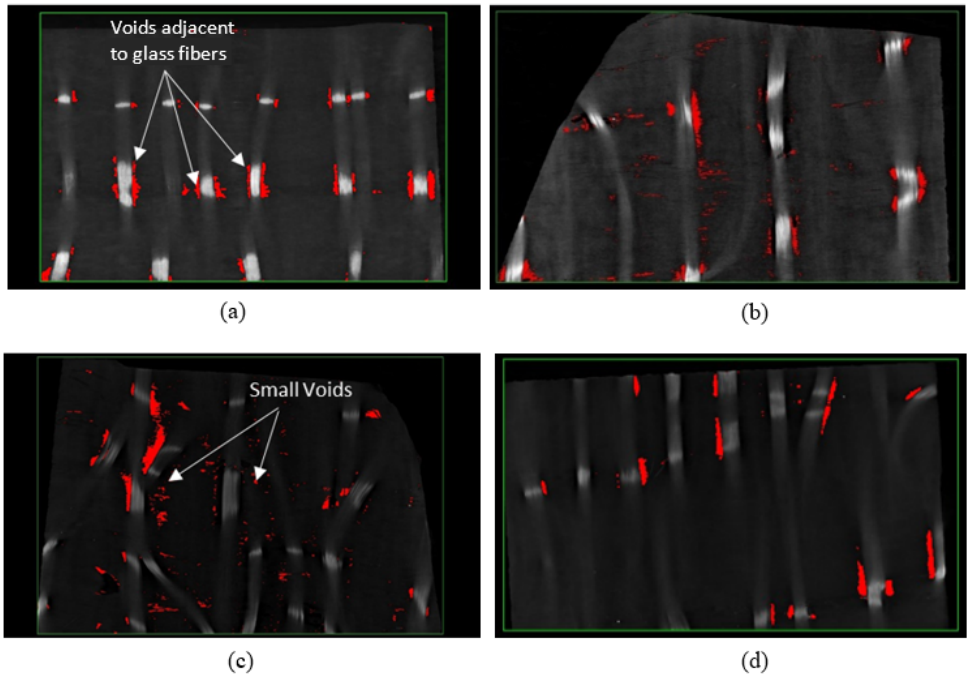


Figure 8.13: 2D images from CT scanned samples highlighting the presence of voids in red around and adjacent to the supporting glass fibers: (a) AT, (b) IT, (c) UNB, and (d) VAC 20 s samples.

Table 8.5: Void content, glass fiber volumetric fraction, and the percentage of the mix comprising carbon fiber, matrix, and stitching.

	UNB	IT	AT	VAC 20 s
Void content [%]	2.64	1.92	0.94	0.96
Glass fiber content [%]	4.86	4.68	3.10	4.45
Carbon fiber + Matrix + Stitching content [%]	92.50	93.40	95.96	94.59
Void/Glass fiber	0.54	0.41	0.30	0.22

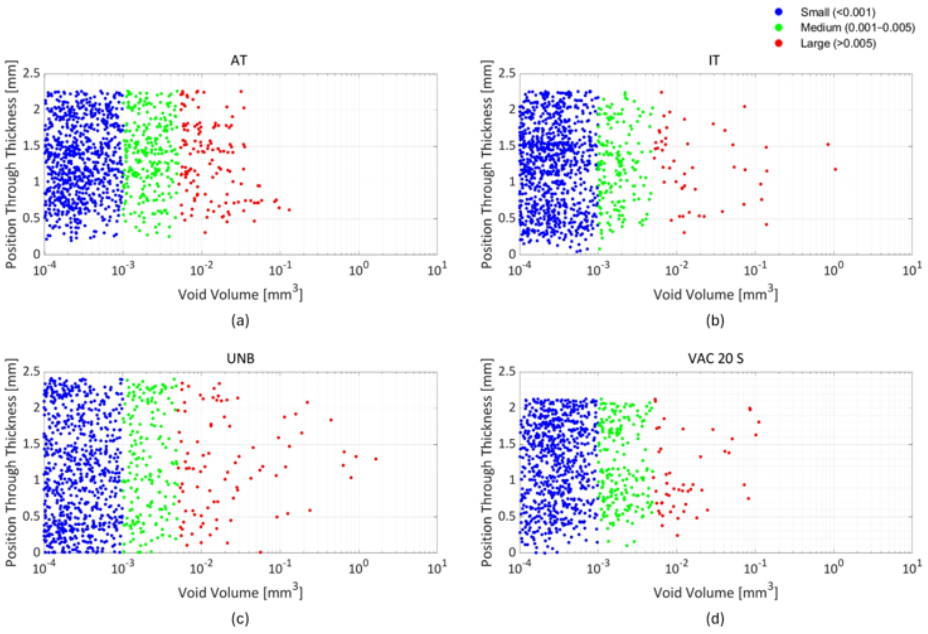


Figure 8.14: Position of the voids along the sample thickness with their volume categorized as small (<0.001 mm^3), medium (0.001 mm^3 – 0.005 mm^3), and large (>0.005 mm^3): (a) AT, (b) IT, (c) UNB, and (d) VAC 20 s samples.

The total volume of voids and number of voids categorized by size as well as the accumulated void volume by layer was analyzed for each sample (Figure 8.15). The total volume of large voids was greatest for the UNB and IT samples, particularly for the former, and lowest for the VAC 20 s samples, while the volume of small and medium voids was nearly consistent in all samples. Moreover, for the UNB and IT samples, the accumulation of void volume was highest within the central layers, whereas the accumulated void volume was consistent throughout the layers of the AT and VAC 20 s samples. This distinct result may be attributed to the influence of binder pre-activation on resin flow during the process for the latter samples.

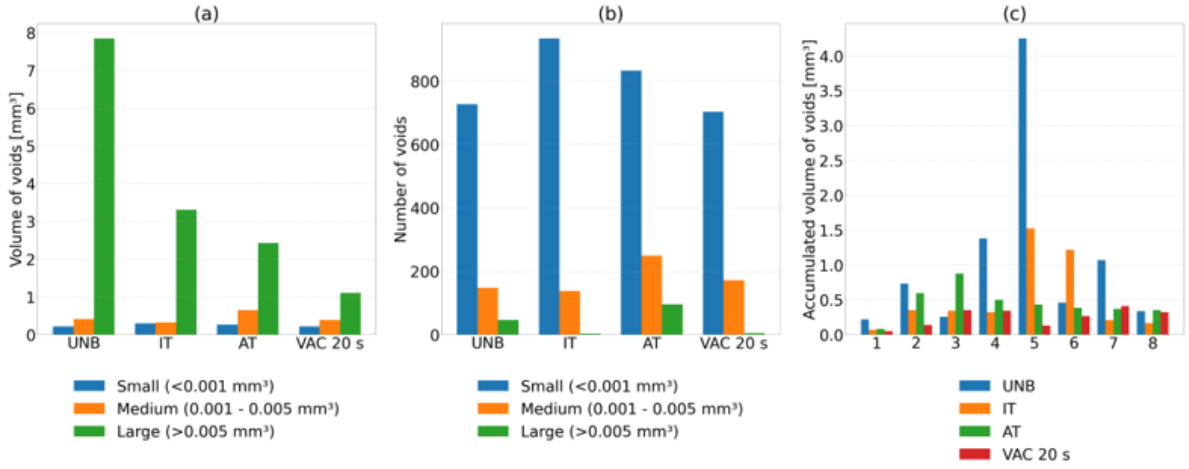


Figure 8.15: Void analysis in samples corresponding to each configuration: (a) volume of voids categorized by size, (b) number of voids categorized by size, and (c) void volume accumulation by layer.

8.5.3 Short-Beam Shear Tests

The captured shear stress-displacement data for specimens corresponding to each configuration demonstrated excellent repeatability (Figure 8.16), with the peak shear stress corresponding to the onset of delamination between the central plies. The UNB and VAC 10s specimens exhibited the lowest performance among the six configurations, with an average ILSS of 58 MPa and 55 MPa, respectively (Table 8.6). The AT and IT specimens demonstrated improved mechanical performance, with an average ILSS of 63 MPa and 66 MPa, respectively. A pairwise t-test revealed that the performance of the IT specimens differed significantly from that of the AT specimens (Table 8.7). Lastly, the VAC 20 s and HP-RTM samples achieved similar average ILSS values of 72 MPa (statistically comparable, see Table 8.7), which was a 15% increase compared to the AT specimens.

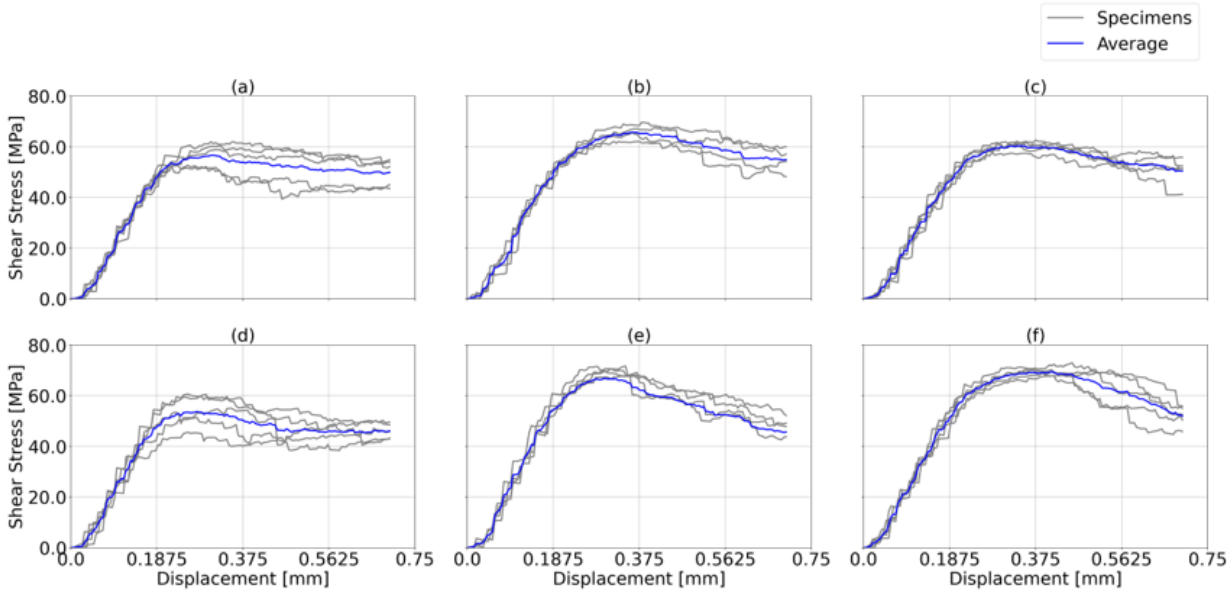


Figure 8.16: SBS test shear stress-displacement plots for configurations: (a) UNB, (b) IT, (c) AT, (d) VAC 10 s, (e) VAC 20 s, and (f) HP-RTM.

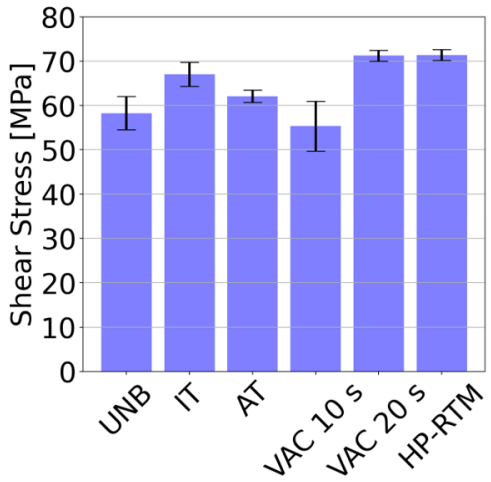


Figure 8.17: ILSS obtained from SBS tests for indicated conditions.

Table 8.6: Average ILSS with standard deviation for each studied configuration.

	UNB	IT	AT	VAC 10s	VAC 20s	HP-RTM
Shear Stress [MPa]	58.27 ± 3.78	67.03 ± 2.70	62.05 ± 1.40	55.32 ± 5.60	71.21 ± 1.26	71.37 ± 1.22

Table 8.7: P-values obtained through T-Test comparing the maximum shear stress values for different manufacturing parameters.

	UNB	IT	AT	VAC 10 s	VAC 20 s	HP-RTM
UNB	-	9.06×10^{-3}	1.19×10^{-1}	4.12×10^{-1}	1.17×10^{-2}	1.38×10^{-3}
IT		-	4.09×10^{-2}	1.04×10^{-2}	5.83×10^{-1}	6.19×10^{-2}
AT			-	7.31×10^{-2}	5.47×10^{-2}	9.31×10^{-6}
VAC 10 s				-	7.52×10^{-3}	3.80×10^{-3}
VAC 20 s					-	3.64×10^{-1}
HP-RTM						-

8.5.4 Transverse Tension Tests

Similar to the ILSS, the transverse tension properties are regarded as matrix-dominated and more susceptible to degradation due to the presence of voids. The stress-strain data for specimens of all configurations reveal a near linear elastic response until failure, apart from the VAC 20 s specimen which exhibited minor nonlinearity prior to failure (Figure 8.18). The magnitude of the average Young's modulus was statistically consistent for all configurations (Figure 8.19a, Tables 8.8 and 8.9). While the average transverse tensile strength was statistically consistent for the WCM specimens, the the HP-RT specimens exhibited a notably greater strength and strain to failure (Figures 8.19b and 8.19c, Tables 8.8 and 8.10). Given that the WCM samples has a greater FVF (i.e., lower inter-fiber spacing), and thus greater stress concentrations at the fiber-matrix interface, when compared to the HP-RTM specimens, it is not surprising that their transverse tensile strength was lower in magnitude. Furthermore, the HP-RTM samples exhibited minimal void content, which contributed to increased transverse tensile strength. It is worth noting that the transverse properties for the HP-RTM specimens were consistent with those reported by Suratkar for the same material system [64].

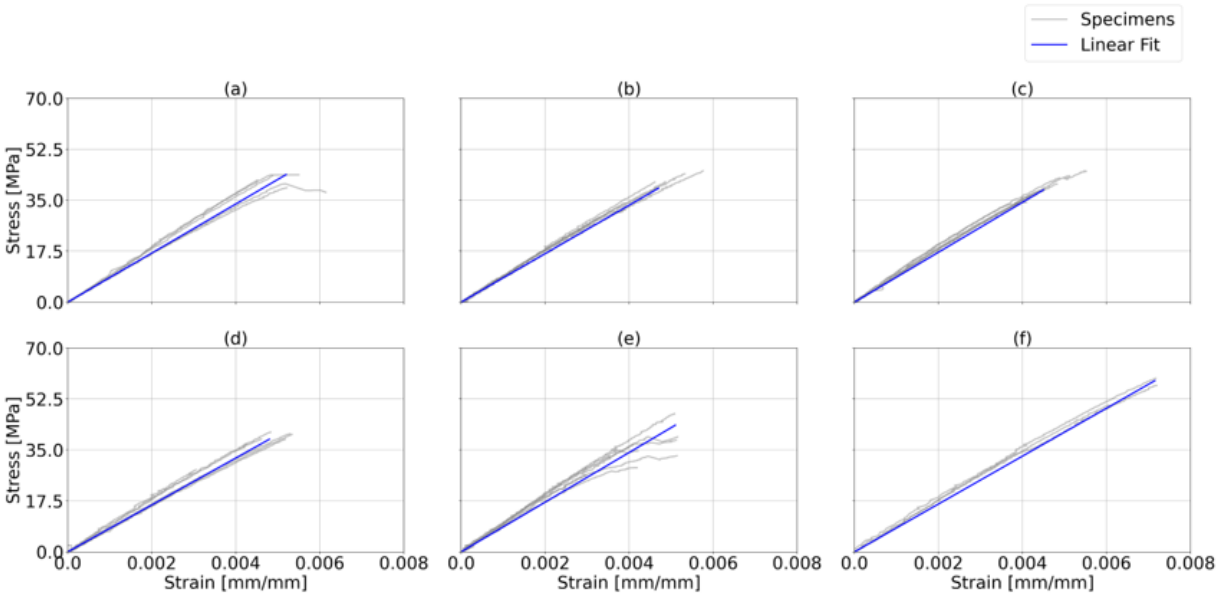


Figure 8.18: Transversal tensile test stress-strain plots for configurations: (a) UNB, (b) IT, (c) AT, (d) VAC 10 s, (e) VAC 20 s, and (f) HP-RTM.

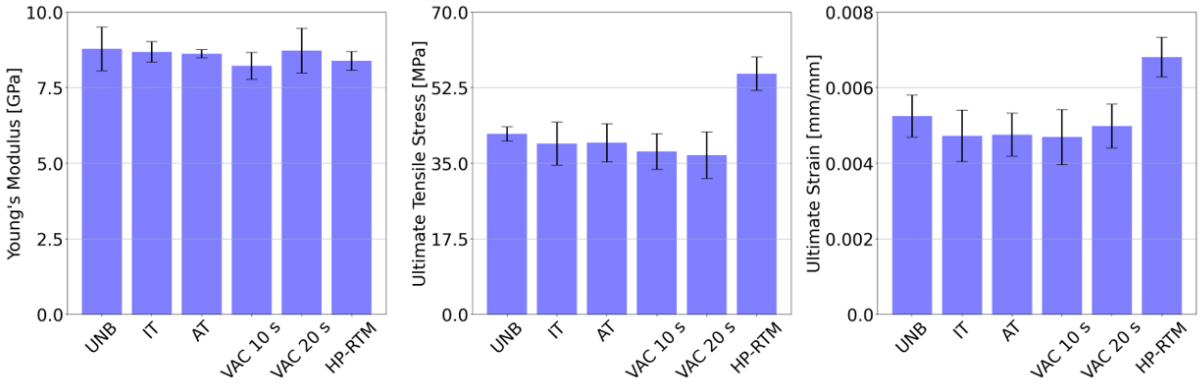


Figure 8.19: Mechanical properties in the transverse direction.

Table 8.8: Average and standard deviation of Young's modulus, ultimate tensile strength, and ultimate strain values for each studied condition in the transverse direction.

Property	UNB	IT	AT	VAC 10s	VAC 20s	HP-RTM
Young's Modulus [GPa]	8.79±0.72	8.68±0.34	8.63±0.14	8.22±0.44	8.72±0.74	8.39±0.31
Ultimate Tensile Strength [MPa]	41.81±1.67	39.57±4.99	39.77±4.43	37.74±4.13	36.89±5.42	55.74±3.89
Ultimate Strain [$\times 10^3$ mm/mm]	5.23±0.56	4.73±0.68	4.76±0.57	4.70±0.73	4.99±0.48	6.81±0.52

Table 8.9: P-values obtained through T-Test comparing the Young's modulus in the transverse direction for different manufacturing parameters.

	UNB	IT	AT	VAC 10 s	VAC 20 s	HP-RTM
UNB	-	8.06×10^{-1}	6.81×10^{-1}	2.14×10^{-1}	9.02×10^{-1}	3.84×10^{-1}
IT		-	7.19×10^{-1}	7.73×10^{-2}	9.06×10^{-1}	3.28×10^{-1}
AT			-	6.99×10^{-2}	7.52×10^{-1}	3.93×10^{-1}
VAC 10 s				-	1.86×10^{-1}	5.88×10^{-1}
VAC 20 s					-	3.94×10^{-1}
HP-RTM						-

Table 8.10: P-values obtained through T-Test comparing the ultimate tensile strength in the transverse direction for different manufacturing parameters.

	UNB	IT	AT	VAC 10 s	VAC 20 s	HP-RTM
UNB	-	3.81×10^{-1}	2.31×10^{-1}	6.00×10^{-2}	7.29×10^{-2}	2.81×10^{-2}
IT		-	9.41×10^{-1}	5.29×10^{-1}	4.13×10^{-1}	7.01×10^{-3}
AT			-	3.71×10^{-1}	2.96×10^{-1}	1.25×10^{-2}
VAC 10 s				-	7.67×10^{-1}	6.76×10^{-3}
VAC 20 s					-	3.56×10^{-3}
HP-RTM						-

8.5.5 Longitudinal Tension Tests

The longitudinal tension stress-strain response was linear elastic until failure for specimens of all configurations (Figure 8.20). The WCM specimens exhibited a statistically similar longitudinal modulus, while the longitudinal modulus of the HP-RTM specimens was notably lower in magnitude (Figure 8.21a, Tables 8.11 and 8.12). This result is primarily due to the fact that the HP-RTM specimens had a lower FVF than the WCM specimens, and that the presence of voids had minimal impact on the fiber-dominant material behaviour. Moreover, the UNB specimens exhibited the lowest longitudinal strength owing in part to premature failure near the tabs, which was not exhibited by the other test specimens; thus, the influence of adding a stabilizing binder is inconclusive. It is interesting to note that the VAC 20 s specimens exhibited a greater longitudinal strength when compared to the other WCM specimens and the HP-RTM specimens (Figure 8.21b, Tables 8.11 and 8.13). While the latter results is expected given the higher FVF of the WCM specimens, the former result shows a positive influence of vacuum assistance during the WCM process.

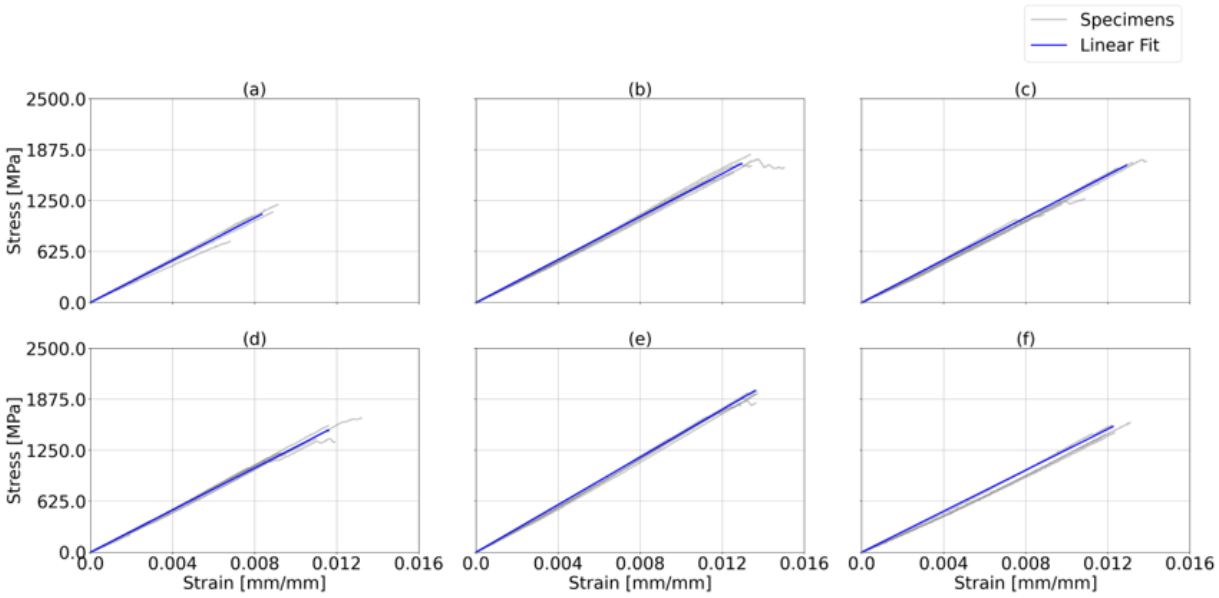


Figure 8.20: Longitudinal tensile test stress-strain plots for configurations: (a) UNB, (b) IT, (c) AT, (d) VAC 10 s, (e) VAC 20 s, and (f) HP-RTM.

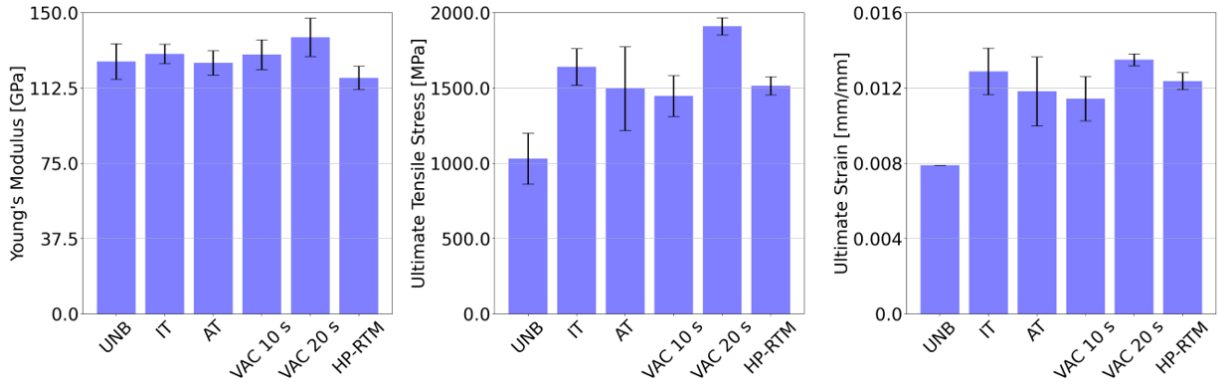


Figure 8.21: Mechanical properties in the longitudinal direction.

Table 8.11: Average and standard deviation of Young's modulus, ultimate tensile strength, and ultimate strain values for each studied condition in the longitudinal direction.

Property	UNB	IT	AT	VAC 10s	VAC 20s	HP-RTM
Young's	125.70	129.50	125.03	129.11	137.80	117.59
Modulus [GPa]	±8.84	±4.83	±6.10	±7.40	±9.55	±5.81
Ultimate Tensile	1031.35	1640.70	1496.72	1447.90	1909.65	1514.91
Strength [MPa]	±169.45	±121.70	±277.99	±135.55	±56.97	±60.47
Ultimate Strain	7.90	12.88	11.83	11.44	13.50	12.37
[$\times 10^3$ mm/mm]	±0.00	±1.23	±1.83	±1.17	±0.32	±0.44

Table 8.12: P-values obtained through T-Test comparing the Young's modulus in the longitudinal direction for different manufacturing parameters.

	UNB	IT	AT	VAC 10 s	VAC 20 s	HP-RTM
UNB	-	5.30×10^{-1}	9.12×10^{-1}	5.97×10^{-1}	1.29×10^{-1}	2.40×10^{-1}
IT		-	2.02×10^{-1}	9.23×10^{-1}	1.68×10^{-1}	2.76×10^{-2}
AT			-	3.48×10^{-1}	5.44×10^{-2}	1.23×10^{-1}
VAC 10 s				-	1.76×10^{-1}	4.24×10^{-2}
VAC 20 s					-	1.11×10^{-2}
HP-RTM						-

Table 8.13: P-values obtained through T-Test comparing the ultimate tensile strength in the longitudinal direction for different manufacturing parameters

	UNB	IT	AT	VAC 10 s	VAC 20 s	HP-RTM
UNB	-	3.09×10^{-3}	1.32×10^{-2}	1.38×10^{-2}	1.75×10^{-3}	1.12×10^{-2}
IT		-	2.84×10^{-2}	3.98×10^{-2}	2.82×10^{-3}	8.86×10^{-2}
AT			-	7.13×10^{-1}	1.02×10^{-2}	8.83×10^{-1}
VAC 10 s				-	2.29×10^{-4}	3.68×10^{-1}
VAC 20 s					-	9.79×10^{-5}
HP-RTM						-

8.5.6 Discussion

The microscopic assessment of the material samples for different configurations led to the realization that the stabilizing binder did not reduce the variation in FVF as was reported in previous studies [14, 15, 19–21], although the FVF slightly increased owing to reduced

panel thickness (Table 8.4, Figure 8.22). The VAC 20s samples exhibited a notably reduced thickness and higher FVF compared to the other WCM samples, including the VAC 10s samples, and less thickness variation. This important result reveals that with sufficient time, air can be drawn from the mold and greater compaction can be achieved with vacuum assistance, which is supported by the results reported in Ref. [37].

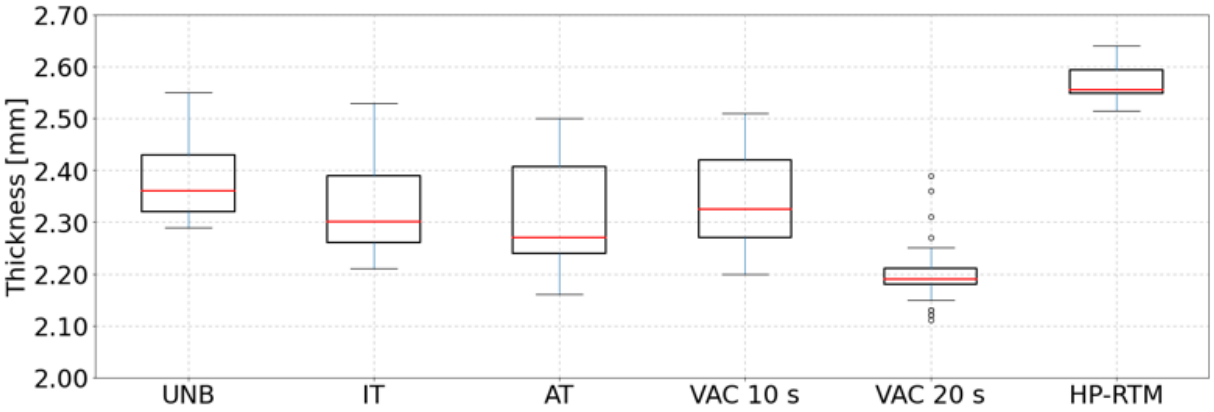


Figure 8.22: Thickness measurements taken from all WCM samples ($[0]_8$ stacking sequence) and the HP-RTM samples $[0]_7$ stacking sequence.

Many studies have reported that the stabilizing binder affects the permeability of the stack [15–17, 24]. The microscopy images and CT-scans captured herein revealed that the stabilizing binder had a positive influence on void formation, where the UNB samples exhibited the highest void content among all configurations. This important result can be explained by the relative movement of the layers, leading to higher air intake and its entrapment between the layers for the UNB samples. This relative movement is reduced when manufacturing with binder-stabilized fabric due to increased friction between the layers. As friction increases and relative movement is minimized through pre-activation of the stabilizing binder (i.e., AT samples), the size of the voids and void content decreases, possibly due to reduced air entrapment. The application of a vacuum to the mold cavity (i.e., VAC 20s samples) further reduced the air trapped in the mold, leading to a significant reduction in the number of large inter-tow voids. Qualitatively, the degree of local intra-tow void formation for the VAC 20s panels was consistent with the HP-RTM panels, which exhibited few voids in general. Another interesting observation was the formation of inter-tow voids adjacent to the supporting glass fibers of the UD-NCF fabric. It is possible that microscopic flow across the tows was impeded by the supporting glass fibers, resulting in the formation of voids at those locations.

The influence of the stabilizing binder on void formation also impacted the mechanical performance of the UD-NCF composite material. The WCM specimens (i.e., UNB, IT, AT, and VAC 10s) exhibited lower interlaminar shear strength compared to the HP-RTM specimens, which aligns with the study by Fels et al. [2]. The UNB and VAC 10s specimens exhibited the lowest ILSS, which can be attributed to the high void content, particularly the number of large inter-tow voids, and the concentration of voids near the midplane of the specimen (Figure 15c), where the shear stresses peak and delamination cracks propagated. Although applying a vacuum to the mold may reduce the number of voids in the microstructure and improve quality, the vacuum applied should build pressure in the mold and be sufficient to prevent resin evaporation and to remove excess air from the mold [65], which did not happen when pulling for 10 seconds and resulted in a significant number of voids observed in the microscopic images. This observed reduction in ILSS for the UNB specimens when compared to the VAC 20s specimens, which consisted of lower void content, aligns with the findings reported by Luo et al. [46]. Also, the ILSS of the VAC 20s was comparable to the HP-RTM specimens. Although from the CT-scans a higher void content was computed for the IT specimens compared to the AT specimens, with larger voids and higher concentration of voids near the center plies for the former (Figures 14b and 15c), the ILSS was slightly greater for the IT specimens. This result reveals that the number of voids and the void content may vary across the WCM panel, as shown in previous studies on WCM process [48, 49]. Moreover, all WCM specimens exhibited a similar transverse tension strength, where void content and morphology seems to have limited impact, which differs from previous studies that report a decrease in matrix-dominated transverse tension properties with an increase in void content [45]. Nevertheless, the transverse tension strength of the HP-RTM specimens was notable greater than that of the WCM specimens, which is attributed to the higher FVF and lower inter-fiber spacing for the WCM specimens that resulted in significant stress concentrations at the fiber-matrix interfaces and lower strength. Lastly, the fiber-dominant longitudinal tension properties were found to be relatively insensitive to void morphology, where the IT, AT, and VAC 10 s specimens exhibited similar longitudinal tension strength. The longitudinal tensile strength of the HP-RTM specimens was also similar to the IT, AT, and VAC 10 s specimens, despite having a lower FVF, which reveals that void content played a role. Interestingly, the VAC 20 s specimens had a greater longitudinal strength when compared to the HP-RTM specimens owing to a higher FVF and low void content.

8.6 Conclusions

The objective of this study was to investigate the influence of stabilizing binder and vacuum assistance on void morphology and mechanical performance of carbon fiber/snap-cure epoxy unidirectional non-crimp fabric (UD-NCF) composites manufactured by wet compression molding (WCM). Microscopy and X-ray computed tomography were employed to determine fiber volume fraction (FVF) and quantify void content, location, and morphology, while longitudinal and transverse tension tests and short beam shear tests were performed to measure the associated strengths. The results of the WCM material were also compared with that of the same material system manufactured with a high-pressure resin transfer molding (HP-RTM) process in a previous study. The main outcomes of the study are summarized as follows:

- Pre-activation of the stabilizing binder reduced the void content and size in WCM panels. Consequently, the specimens extracted from the fabricated panels exhibited an increased interlaminar shear strength (ILSS) when compared to the specimens comprising un-bindered UD-NCF.
- The application of vacuum for 20 seconds during the WCM processes reduced the void content and size, increased the compaction of the fabric stack, and consequently the FVF of the composite panel. As a result, the specimens extracted from associated panels showed higher ILSS and longitudinal tensile strength.
- Computed tomography scans showed inter-tow voids in the vicinity of the supporting glass fibers, particularly for samples with un-bindered fabric or binder stabilizing fabric that was not pre-activated. The supporting glass fibers are deemed to influence the microscopic flow of resin and void formation.
- The HP-RTM specimens exhibited comparable ILSS compared to the WCM specimens with 20 s of vacuum assistance, which implicates a low void content. Also, the HP-RTM specimens exhibited a higher transverse tension strength compared to all WCM specimens, owing to lower fiber-matrix interfacial stress concentration caused by a lower FVF (i.e., greater inter-fiber spacing).

This was the first comprehensive investigation focused on analyzing the influence of stabilizing binder and vacuum assistance on the microstructure and mechanical performance of WCM composite materials. Given that WCM processes continue to be of interest for fabricating structural fiber-reinforced composite parts, the study is timely and fills a critical gap in the literature. The results of this study aid in understanding the capability of

the WCM process in producing high-quality parts that are comparable to that of HP-RTM parts, which will be instrumental in optimizing processes in future work.

References

[1] H. Yang, C.-C. Hsu, and C.-H. Hsu, "Three dimensional numerical simulations for wet-rtm process," in *35th Polymer Processing Society*, Cesme-Izmir, Turkey, 2019.

[2] J. Fels, G. Meirson, V. Ugresic, P. Dugsin, F. Henning, and A. Hrymak, "Mechanical property difference between composites produced using vacuum-assisted liquid compression molding and high-pressure injection resin transfer molding," in *Proceedings ACCE2017-17th Annual Automotive Composites Conference and Exhibition, Michigan*, Jun. 2017.

[3] F. Henning, L. Kärger, D. Dörr, F. J. Schirmaier, J. Seuffert, and A. Bernath, "Fast processing and continuous simulation of automotive structural composite components," *Composites Science and Technology*, vol. 171, pp. 261–279, Feb. 2019, ISSN: 0266-3538. DOI: 10.1016/J.COMPSCITECH.2018.12.007.

[4] C. T. Poppe, C. Krauß, F. Albrecht, and L. Kärger, "A 3D process simulation model for wet compression moulding," *Composites Part A: Applied Science and Manufacturing*, vol. 145, p. 106 379, Jun. 2021, ISSN: 1359-835X. DOI: 10.1016/J.COMPOSITESA.2021.106379.

[5] C. Poppe, "Process simulation of wet compression moulding for continuous fibre-reinforced polymers," Ph.D. dissertation, Karlsruhe Institute of Technology, 2021.

[6] L. Kärger, S. Galkin, E. Kunze, M. Gude, and B. Schäfer, "Prediction of forming effects in ud-ncf by macroscopic forming simulation–capabilities and limitations," in *ESAFORM 2021 - 24th International Conference on Material Forming*, Liège, Belgium, 14-16 April 2021.

[7] P. Boisse, N. Hamila, E. Guzman-Maldonado, A. Madeo, G. Hivet, and F. Dell'Isola, "The bias-extension test for the analysis of in-plane shear properties of textile composite reinforcements and prepregs: A review," *International Journal of Material Forming*, vol. 10, pp. 473–492, 2017.

[8] C. D. Rudd, A. C. Long, K. N. Kendall, and C. G. E. Mangin, *Liquid Moulding Technologies*. Amsterdam, The Netherlands: Elsevier, 1997, ISBN: 0768000165. DOI: 10.1533/9781845695446.

[9] F. J. Schirmaier, K. A. Weidenmann, L. Kärger, and F. Henning, "Characterisation of the draping behaviour of unidirectional non-crimp fabrics (UD-NCF)," *Composites Part A: Applied Science and Manufacturing*, vol. 80, pp. 28–38, Jan. 2016, ISSN: 1359-835X. DOI: 10.1016/J.COMPOSITESA.2015.10.004.

[10] J. Pourtier, B. Duchamp, M. Kowalski, X. Legrand, P. Wang, and D. Soulat, "Bias extension test on a bi-axial non-crimp fabric powdered with a non-reactive binder system," in *ESAFORM 2018 - 21st International Conference on Material Forming*, Palermo, Italy, 23. and 25. of April 2018.

[11] P. Quenzel *et al.*, "Material characterisation of biaxial glass-fibre non-crimp fabrics as a function of ply orientation, stitch pattern, stitch length and stitch tension," *Journal of Composite Materials*, vol. 56, no. 26, pp. 3971–3991, 2022. DOI: 10.1177/00219983221127005. eprint: https://doi.org/10.1177/00219983221127005. [Online]. Available: https://doi.org/10.1177/00219983221127005.

[12] B. Schäfer, S. Haas, P. Boisse, and L. Kärger, "Investigation of the membrane behavior of ud-ncf in macroscopic forming simulations," *Key Engineering Materials*, vol. 926, pp. 1413–1422, 2022.

[13] R. Kumar, K. Rashvand, A. Fraisse, A. Sarhadi, and T. L. Andersen, "Experimental testing method to characterise the drapability of ud non-crimp fabrics used in wind turbine blades," *IOP Conference Series: Materials Science and Engineering*, vol. 1293, no. 1, p. 012 020, Nov. 2023. DOI: 10.1088/1757-899X/1293/1/012020. [Online]. Available: https://dx.doi.org/10.1088/1757-899X/1293/1/012020.

[14] P. H. Broberg *et al.*, "That's how the preform crumples: Wrinkle creation during forming of thick binder-stabilised stacks of non-crimp fabrics," *Composites Part B: Engineering*, vol. 273, p. 111 269, 2024, ISSN: 1359-8368. DOI: https://doi.org/10.1016/j.compositesb.2024.111269. [Online]. Available: https://www.sciencedirect.com/science/article/pii/S1359836824000805.

[15] G. Estrada, C. Vieux-Pernon, and S. G. Advani, "Experimental characterization of the influence of tackifier material on preform permeability," *Journal of Composite Materials*, vol. 36, no. 19, pp. 2297–2310, 2002. DOI: 10.1177/0021998302036019542. eprint: https://doi.org/10.1177/0021998302036019542. [Online]. Available: https://doi.org/10.1177/0021998302036019542.

[16] J. C. Brody and J. W. Gillespie, "The effects of a thermoplastic polyester preform binder on vinyl ester resin," *Journal of Thermoplastic Composite Materials*, vol. 18, no. 3, pp. 157–179, 2005. DOI: 10.1177/0892705705043535. eprint: https://doi.org/10.1177/0892705705043535. [Online]. Available: https://doi.org/10.1177/0892705705043535.

[17] H. M. Yoo, J. W. Lee, J. S. Kim, and M. K. Um, "Influence of non-reactive epoxy binder on the permeability and friction coefficient of twill-woven carbon fabric in the liquid composite molding process," *Applied Sciences*, vol. 10, no. 20, p. 7039, 2020, ISSN: 2076-3417. DOI: 10.3390/app10207039. [Online]. Available: https://www.mdpi.com/2076-3417/10/20/7039.

[18] O. Rimmel, D. Becker, and P. Mitschang, "Maximizing the out-of-plane-permeability of preforms manufactured by dry fiber placement," *Advanced Manufacturing: Polymer & Composites Science*, vol. 2, no. 3-4, pp. 93–102, 2016.

[19] S.-B. Shim and J. C. Seferis, "Characterization of binder interactions with lightly crosslinked thermosets," *Science and Engineering of Composite Materials*, vol. 3, 3 Jan. 1994, ISSN: 2191-0359. DOI: 10.1515/SECM.1994.3.3.191. [Online]. Available: https://www.degruyter.com/document/doi/10.1515/SECM.1994.3.3.191/html.

[20] P. H. Broberg, C. Krogh, E. Lindgaard, and B. L. V. Bak, "Simulation of wrinkling during forming of binder stabilized ud-ncf preforms in wind turbine blade manufacturing," *Key Engineering Materials*, vol. 926, pp. 1248–1256, Jul. 2022, ISSN: 1662-9795. DOI: 10.4028/p-165q46. [Online]. Available: https://www.scientific.net/KEM.926.1248.

[21] S. Schmidt, T. Mahrholz, A. Kühn, and P. Wierach, "Powder binders used for the manufacturing of wind turbine rotor blades. part 1. characterization of resin-binder interaction and preform properties," *Polymer Composites*, vol. 39, pp. 708–717, 3 Mar. 2018, ISSN: 15480569. DOI: 10.1002/pc.23988.

[22] T. Grundmann, "Automatisiertes preforming für schalenförmige komplexe faserverbundbauteile. aachen, rwth aachen, fakultät maschinenwesen," Ph.D. dissertation, RWTH Aachen, 2009.

[23] L. Moser, S. Heide, I. Swentek, U. Schmidt, and M. Seiz, "Thermoset technologies for cost efficient production of lightweight composites," in *Technologies for economic and functional lightweight design: Conference proceedings 2020*, Springer, 2021, pp. 35–41.

[24] S. Neunkirchen, M. Bender, and R. Schledjewski, "Effect of binder activation on in-plane capillary flow in multilayer stacks of carbon fiber fabrics," *Applied Composite Materials*, vol. 31, pp. 709–719, 2 Apr. 2024, ISSN: 0929-189X. DOI: 10.1007/s10443-023-10198-6. [Online]. Available: https://link.springer.com/10.1007/s10443-023-10198-6.

[25] K. Wei, D. Liang, M. Mei, D. Wang, X. Yang, and Z. Qu, "Preforming behaviors of carbon fiber fabrics with different contents of binder and under various process parameters," *Composites Part B: Engineering*, vol. 166, pp. 221–232, 2019, ISSN: 1359-8368. DOI: https://doi.org/10.1016/j.compositesb.2018.11.143. [Online]. Available: https://www.sciencedirect.com/science/article/pii/S1359836818326568.

[26] R. M. Portela, B. Schäfer, L. Kärger, A. R. de Faria, and J. Montesano, "Influence of viscosity, binder activation, and loading rate on the membrane response of an infiltrated ud-ncf," in *ESAFORM 2024 - 27th International Conference on Material Forming*, Apr. 2024.

[27] P. H. Broberg, F. Shakibapour, J. Jakobsen, E. Lindgaard, and B. L. V. Bak, "Characterisation of the transverse shear behaviour of binder-stabilised preforms for wind turbine blade manufacturing," 2023. DOI: 10.17632/9m78sg3zwn.1. [Online]. Available: http://creativecommons.org/licenses/by/4.0/.

[28] C. Krogh, P. H. Broberg, J. Kepler, and J. Jakobsen, "Comprehending the bending: A comparison of different test setups for measuring the out-of-plane flexural rigidity of a ud fabric," *Key Engineering Materials*, vol. 926, pp. 1257–1267, Jul. 2022, ISSN: 1662-9795. DOI: 10.4028/p-r883x4. [Online]. Available: https://www.scientific.net/KEM.926.1257.

[29] M. Ghazimoradi, E. A. Trejo, C. Butcher, and J. Montesano, "Characterizing the macroscopic response and local deformation mechanisms of a unidirectional non-crimp fabric," *Composites Part A: Applied Science and Manufacturing*, vol. 156, p. 106 857, May 2022, ISSN: 1359-835X. DOI: 10.1016/J.COMPOSITESA.2022.106857.

[30] A. Schnabel and T. Gries, "1 - production of non-crimp fabrics for composites," in *Non-Crimp Fabric Composites*, ser. Woodhead Publishing Series in Composites Science and Engineering, S. V. Lomov, Ed., Woodhead Publishing, 2011, pp. 3–41, ISBN: 978-1-84569-762-4. DOI: https://doi.org/10.1533/9780857092533.1.3. [Online]. Available: https://www.sciencedirect.com/science/article/pii/B9781845697624500011.

[31] M. Tanoğlu and A. T. Seyhan, "Investigating the effects of a polyester preforming binder on the mechanical and ballistic performance of e-glass fiber reinforced polyester composites," *International Journal of Adhesion and Adhesives*, vol. 23, pp. 1–8, 1 Jan. 2003, ISSN: 01437496. DOI: 10.1016/S0143-7496(02)00061-1. [Online]. Available: https://linkinghub.elsevier.com/retrieve/pii/S0143749602000611.

[32] M. Tanoğlu and A. T. Seyhan, "Compressive mechanical behaviour of e-glass/polyester composite laminates tailored with a thermoplastic preforming binder," *Materials Science and Engineering: A*, vol. 363, pp. 335–344, 1-2 Dec. 2003, ISSN: 09215093. DOI: 10.1016/j.msea.2003.08.005.

[33] L. Daelemans *et al.*, "Bisphenol a based polyester binder as an effective interlaminar toughener," *Composites Part B: Engineering*, vol. 80, pp. 145–153, Oct. 2015, ISSN: 1359-8368. DOI: 10.1016/J.COMPOSITESB.2015.05.044. [Online]. Available: https://www.sciencedirect.com/science/article/pii/S1359836815003583?via%3Dihub.

[34] R. Hillermeier and J. Seferis, "Interlayer toughening of resin transfer molding composites," *Composites Part A: Applied Science and Manufacturing*, vol. 32, pp. 721–729, 5 May 2001, ISSN: 1359835X. DOI: 10.1016/S1359-835X(00)00088-9. [Online]. Available: https://linkinghub.elsevier.com/retrieve/pii/S1359835X00000889.

[35] I. R. Chowdhury, N. H. Nash, A. Portela, N. P. O'Dowd, and A. J. Comer, "Analysis of failure modes for a non-crimp basalt fiber reinforced epoxy composite under flexural and interlaminar shear loading," *Composite Structures*, vol. 245, Aug. 2020, ISSN: 02638223. DOI: 10.1016/j.compstruct.2020.112317.

[36] N. R. Thompson, "Void formation during liquid composite molding under varied pressure with mechanical properties validation," M.S. thesis, Brigham Young University, 2024.

[37] M. Mehdikhani, L. Gorbatikh, I. Verpoest, and S. V. Lomov, "Voids in fiber-reinforced polymer composites: A review on their formation, characteristics, and effects on mechanical performance," *Journal of Composite Materials*, vol. 53, no. 12, pp. 1579–1669, 2019.

[38] S. M. Sisodia, S. Garcea, A. George, D. Fullwood, S. Spearing, and E. Gamstedt, "High-resolution computed tomography in resin infused woven carbon fibre composites with voids," *Composites Science and Technology*, vol. 131, pp. 12–21, 2016.

[39] B. Muthuvel, D. Bhattacharyya, and S. Bickerton, "A parametric flow visualisation study on the impregnation and consolidation stages of the wet compression moulding process. part i: Process parameters," *Composites Part A: Applied Science and Manufacturing*, vol. 150, p. 106 634, Nov. 2021, ISSN: 1359-835X. DOI: 10.1016/J.COMPOSITESA.2021.106634. [Online]. Available: https://www.sciencedirect.com/science/article/pii/S1359835X21003523?via%3Dihub.

[40] S. Sisodia, E. K. Gamstedt, F. Edgren, and J. Varna, "Effects of voids on quasi-static and tension fatigue behaviour of carbon-fibre composite laminates," *Journal of composite materials*, vol. 49, no. 17, pp. 2137–2148, 2015.

[41] C. H. Park and L. Woo, "Modeling void formation and unsaturated flow in liquid composite molding processes: A survey and review," *Journal of reinforced plastics and composites*, vol. 30, no. 11, pp. 957–977, 2011.

[42] J.-M. Tang, W. I. Lee, and G. S. Springer, "Effects of cure pressure on resin flow, voids, and mechanical properties," *Journal of Composite Materials*, vol. 21, no. 5, pp. 421–440, 1987. DOI: 10.1177/002199838702100502.

[43] J. S. Leclerc and E. Ruiz, "Porosity reduction using optimized flow velocity in resin transfer molding," *Composites Part A: Applied Science and Manufacturing*, vol. 39, pp. 1859–1868, 12 Dec. 2008, ISSN: 1359-835X. DOI: 10.1016/J.COMPOSITESA.2008.09.008.

[44] S. R. Ghiorse, "Effect of void content on the mechanical properties of carbon/epoxy laminates," *SAMPE quarterly*, vol. 24, pp. 54–59, 2 1993, ISSN: 0036-0821.

[45] "Effects of void characteristics on the mechanical properties of carbon fiber reinforced polyetheretherketone composites: Micromechanical modeling and analysis," *Polymers*, vol. 17, p. 1721, 13 Jun. 2025, ISSN: 2073-4360. DOI: 10.3390/polym17131721. [Online]. Available: https://www.mdpi.com/2073-4360/17/13/1721.

[46] L. Luo *et al.*, "Identification of voids and interlaminar shear strengths of polymer-matrix composites by optical microscopy experiment and deep learning methodology," *Polymers for advanced technologies*, vol. 32, no. 4, pp. 1853–1865, 2021.

[47] C. Kaynak, E. Akgul, and N. A. Isitman, "Effects of rtm mold temperature and vacuum on the mechanical properties of epoxy/glass fiber composite plates," *Journal of Composite Materials*, vol. 42, pp. 1505–1521, 15 Aug. 2008, ISSN: 00219983. DOI: 10.1177/0021998308092204.

[48] S. Ayatollahi, "Effect of process parameters on the mechanical properties of carbon fiber epoxy composites by wet compression molding," M.S. thesis, The University of Western Ontario, 2023. [Online]. Available: https://ir.lib.uwo.ca/etdhttps://ir.lib.uwo.ca/etd/9144.

[49] J. Sears, "Predictive modelling of the effects of processing parameters on the mechanical properties of fiber reinforced composites using liquid composite molding," Ph.D. dissertation, University of Windsor, Sep. 2024.

[50] *Technical data sheet zoltek™ px35 uni-directional fabrics*, Zoltek, Jan. 2021.

[51] *Technical data sheet epikote™ resin 06150 epikure curing agent 06150*, Westlake Epoxy, Jan. 2019.

[52] F. Mariano, "Development of an LCM process for rapid curing CFRP parts," M.S. thesis, Politecnico di Torino, Torino, Italy, 2019.

[53] A. Cherniaev, Y. Zeng, D. Cronin, and J. Montesano, "Quasi-static and dynamic characterization of unidirectional non-crimp carbon fiber fabric composites processed by hp-rtm," *Polymer Testing*, vol. 76, pp. 365–375, Jul. 2019, ISSN: 01429418. DOI: 10.1016/j.polymertesting.2019.03.036.

[54] A. International, "Astm d3039/d3039m – standard test method for tensile properties of polymer matrix composite materials," Tech. Rep., Oct. 2017. DOI: 10.1520/D3039_D3039M-17. [Online]. Available: http://www.astm.org/cgi-bin/resolver.cgi?D3039D3039M-17.

[55] A. International, "Astm d2344 – standard test method for short-beam strength of polymer matrix composite materials and their laminates," Tech. Rep., Jul. 2022, pp. 1–8. DOI: 10.1520/D2344_D2344M-22. [Online]. Available: http://www.astm.org/cgi-bin/resolver.cgi?D2344D2344M-22.

[56] R. M. Portela, A. R. de Faria, and J. Montesano, "High-fidelity fiber volume fraction estimation for ud-ncf composites using digital image processing technique. manuscript submitted (under review).,"

[57] J. E. Little, X. Yuan, and M. I. Jones, "Characterisation of voids in fibre reinforced composite materials," *Ndt & E International*, vol. 46, pp. 122–127, 2012.

[58] Y. Nikishkov, L. Airoldi, and A. Makeev, "Measurement of voids in composites by x-ray computed tomography," *Composites Science and Technology*, vol. 89, pp. 89–97, 2013, ISSN: 0266-3538. DOI: https://doi.org/10.1016/j.compscitech.2013.09.019. [Online]. Available: https://www.sciencedirect.com/science/article/pii/S0266353813003813.

[59] P. Yang and R. Elhajjar, "Porosity content evaluation in carbon-fiber/epoxy composites using x-ray computed tomography," *Polymer-Plastics Technology and Engineering*, vol. 53, no. 3, pp. 217–222, 2014. DOI: 10.1080/03602559.2013.843700. eprint: https://doi.org/10.1080/03602559.2013.843700. [Online]. Available: https://doi.org/10.1080/03602559.2013.843700.

[60] A. Soltansaleki and G. W. Melenka, "Digital twin modelling for 3d-printed composite structures manufactured by fused filament fabrication method: Mesoscale geometry simulation," *https://doi.org/10.1117/12.3050858*, vol. 13438, C. Niezrecki and S. Farhangdoust, Eds., pp. 68–78, May 2025. DOI: 10.1117/12.3050858. [Online]. Available: https://www.spiedigitallibrary.org/conference-proceedings-of-spie/13438/134380C/Digital-twin-modelling-for-3D-printed-composite-structures-manufactured-by/10.1117/12.3050858.full%20https://www.spiedigitallibrary.org/conference-proceedings-of-spie/13438/1343.

[61] A. Dondish and G. Melenka, "Assessment of low-velocity impact response of a hybrid carbon-aramid braided composite by algorithmic quantification of volumetric structures," *Tomography of Materials and Structures*, vol. 4, p. 100 022, Mar. 2024, ISSN: 2949-673X. DOI: 10.1016/J.TMATER.2023.100022. [Online]. Available: https://www.sciencedirect.com/science/article/pii/S2949673X23000207.

[62] Y. Li, Y. Chi, S. Han, C. Zhao, and Y. Miao, "Pore-throat structure characterization of carbon fiber reinforced resin matrix composites: Employing micro-ct and avizo technique," *PLOS ONE*, vol. 16, e0257640, 9 Sep. 2021, ISSN: 1932-6203. DOI: 10.1371/JOURNAL.PONE.0257640. [Online]. Available: https://journals.plos.org/plosone/article?id=10.1371/journal.pone.0257640.

[63] G. W. Melenka and A. Gholami, "Fiber identification of braided composites using micro-computed tomography," *Composites Communications*, vol. 27, p. 100 813, Oct. 2021, ISSN: 2452-2139. DOI: 10.1016/J.COCO.2021.100813. [Online]. Available: https://www.sciencedirect.com/science/article/pii/S2452213921001893.

[64] A. P. Suratkar, "Damage in non-crimp fabric carbon fiber reinforced epoxy composites under various mechanical loading conditions," Ph.D. dissertation, The University of Western Ontario (Canada), 2022.

[65] D. Chen, K. Arakawa, and C. Xu, "Reduction of void content of vacuum-assisted resin transfer molded composites by infusion pressure control," *Polymer Composites*, vol. 36, no. 9, pp. 1629–1637, 2015.

Chapter 9

Energy absorption capability of wet compression molded binder-stabilized UD-NCF composite hat channels

9.1 Overview

Fiber-reinforced composites can be tailored to maximize their energy absorption capacity; thus, they are potential candidates for components in energy absorbing structures. While high-pressure resin transfer molding (HP-RTM) processes have been widely considered for fabricating complex-shaped automotive components, there are notable drawbacks. Wet compression molding (WCM) represents a feasible alternative for high-volume production components, particularly with unidirectional non-crimp fabric (UD-NCF) reinforcements and snap-cure resin systems. The use of a binder may be required to stabilize UD-NCFs and manage resin during WCM of complex-shaped, thick-walled components; however, the influence of stabilizing binders on the performance of such components has not been previously investigated. This study examines the impact of stabilizing binder and vacuum assistance on the energy absorption capacity of WCM UD-NCF composite hat channels subjected to axial crush loading. Channels manufactured with binder-stabilized fabric exhibited slightly higher energy absorption compared to those comprising unbindered fabric, with vacuum assistance further enhancing performance. The specific energy absorption of the vacuum assisted WCM channels was approximately 12% less than that of similar HP-RTM channels reported in a previous study, which demonstrates the feasibility of integrating WCM components into energy absorbing structures.

9.2 Introduction

Fiber-reinforced composites can be tailored to maximize their energy absorption capacity, making them strong candidates for energy-absorbing structures in automotive applications. Through progressive failure mechanisms such as delamination, fiber–matrix debonding, matrix cracking, and fiber fracture, composites can absorb significantly more energy per unit weight than metals [1], enhancing both efficiency and crash safety. As the automotive industry moves toward lightweight, high-volume production, liquid composite molding (LCM) techniques—particularly high-pressure resin transfer molding (HP-RTM) and wet compression molding (WCM)—have gained prominence. While HP-RTM enables automated fabrication of complex-shaped components, its high equipment and process costs drive interest in WCM as a more economical alternative for large-scale manufacturing [2].

WCM has emerged as a feasible alternative, particularly for high-volume manufacturing using unidirectional non-crimp fabric (UD-NCF) reinforcements with snap-cure resin systems. Depending on when fabric forming occurs, WCM can follow either a direct or indirect variant. In the direct variant, fabric forming and resin infiltration occur simultaneously during mold closure, whereas the indirect variant involves preforming the dry stack before resin application and placement into the mold [3]. The direct WCM process is generally more cost-effective due to simultaneous draping and infiltration processes without the need for a separate preforming mold [3]. Moreover, the use of UD-NCFs provides improved fiber alignment and in-plane properties, although the low crimp architecture may reduce fabric stability during handling [4].

The production of UD-NCF composite structural components involves stacking fabric layers in various orientations to achieve specific anisotropic properties. However, creating these components can lead to thick fabric stacks with substantial resin content. Using WCM to produce thick parts in complex-shaped, deep-cavity molds poses challenges with resin management, as UD-NCF can drape under gravity when excess resin is present. If the fabric stack drapes prematurely—before mold closure—it can cause resin pooling and unwanted fabric movement within the mold, resulting in defects like dry spots, voids, or wrinkles. A solution to prevent early drape is employing binder-stabilized UD-NCF, which enhances the fabric's bending stiffness and improves resin handling [5–7].

Stabilizing binders can be thermoplastic or uncatalyzed epoxy resins, available as liquids or dry powders [8–10]. When activated, their objective is to bond adjacent fabric layers, preventing movement and issues such as wrinkling, fiber misalignment, and fiber washout. They also help preserve fabric integrity during preparation steps, such as trimming and handling, and reduce fiber volume fraction (FVF) variations in the final product

[6, 11, 12]. However, binders may present drawbacks under certain process conditions, including a reduction in the permeability of fabrics compared to the raw fabric, an increase in resin viscosity [8–10, 13], alterations to fabric draping behavior (e.g., membrane, bending, and compaction responses) [14–18], and effects on mechanical properties [19]. Tanoğlu and Tuğrul [19] explored how binder concentration affects the mechanical performance of E-glass/polyester vacuum-assisted resin transfer molded composites. They found that higher binder levels decreased flexural strength but increased flexural modulus. However, they reported that the binder did not affect interlaminar shear strength (ILSS). While the impact of stabilizing binders on processing has been widely studied, their effects on microstructure—such as FVF and voids—were not analyzed microscopically in their work, even though these factors directly influence mechanical properties. Portela et al. [20] investigated the influence of the thermosetting stabilizing binder on the mechanical properties of the WCM panels. They observed that the use of binder-stabilized UD-NCF and its thermal pre-activation reduced the void content in WCM composites compared to raw UD-NCF, resulting in increased ILSS. The scarcity of studies on how stabilizing binders influence energy absorption, especially in UD-NCF composites produced by WCM, reveals a significant gap in the literature.

Despite extensive research focused on studying the energy absorption capability of fiber-reinforced composites, encompassing a wide range of variables, as summarized by Sun et al. [21], no previous investigation has specifically studied the use of a stabilizing binder in UD-NCF composites and the performance of WCM parts. Furthermore, although many studies cite the automotive industry as a primary motivation, they often employ manufacturing processes with limited large-scale applicability, such as vacuum bag molding [22, 23], autoclave curing [24], and hand lay-up [25, 26], or costly material systems like prepreg materials [27].

Feraboli et al. [22] investigated the effect of geometric features on the crush behavior of composite structures. Five sets of specimens—square tubes, small and large channels, and small and large corners—were manufactured from carbon fiber woven/epoxy prepreg designed for vacuum bag and oven curing. The authors reported that smaller, more contoured geometries (with fewer flat segments) exhibited higher specific energy absorption (SEA) than larger, flatter sections such as square tubes. Using the same manufacturing process, Mou et al. [23] produced hybrid carbon fiber reinforced plastic (CFRP)/aluminum and pure CFRP composite C-channels to compare the mechanical performance of different hybrid configurations. Fiber metal laminate (FML) C-channels, consisting of unidirectional CFRP prepreg with [$\pm 45^{\circ}$] layers and Al 2024, achieved 60.58% higher energy absorption and 15.40% higher SEA than single CFRP C-channels.

Chiu et al. [24] examined the crush response of autoclaved carbon/epoxy prepreg

composites under quasi-static and dynamic loading. They found that the specific energy absorption and steady-state crush force were independent of strain rate, attributed to the high fiber volume fraction and the dominance of reinforcement-related energy absorption over matrix fracture mechanisms. Eshkoor et al. [25] studied the influence of trigger mechanisms on the energy absorption of woven silk/epoxy hand lay-up composites. They reported that the presence of a trigger altered the failure mode from catastrophic to progressive; however, this change did not significantly affect the overall energy absorption.

Recently, Harvey [28] and Ajayi [29] investigated the axial crush response of various UD-NCF composite channels fabricated by HP-RTM with different stacking sequences ($[\pm 45/0_2]_s$ and $[0/\pm 45/90]_s$), [24, 28] under dynamic (7.5 mm/s) and quasi-static (1 mm/s) loading rates. A change in failure mode with increasing loading rate - from extensive splaying during quasi-static loading to fragmentation under dynamic loading – was reported. Furthermore, channels with a $[\pm 45/0_2]_s$ stacking sequence demonstrated superior performance owing to the increased number of 0° plies and the observed failure mode, which [29] was a combination of splaying and lamina bending.

The objective of this study is to investigate the effects of a stabilizing binder on the energy absorption capacity of wet compression molded UD-NCF carbon fiber snap-cure epoxy composite hat channels. The research involved in-house manufacturing of WCM hat channels and conducting quasi-static axial crush tests. The energy absorption capacity of the WCM hat channels was compared with results from similar HP-RTM hat channels reported in a previous study, which served as a benchmark for this investigation.

9.3 Fabric Material and Experimental Methodology

9.3.1 Materials

The WCM hat channels manufactured for this investigation were made of UD-NCF, namely PX35-UD300 (Zoltek, US), with an areal density of 333 g/m^3 [30] and a 3-part snap-cure resin (Epikote 6150 by Westlake Epoxy) [31]. The PX35-UD300 consisted of parallel-oriented tows, each composed of 50K continuous PX35 carbon fibers (CF). The CF tows were stitched together with a 76 dtex polyester stitching yarn in a tricot pattern. On the other side of the fabric, low linear density transversely oriented supporting glass fiber (GF) yarns are included to improve fabric handling. In this study, two variations of this textile were used. The difference between the two variations is the addition of a thermosetting polymer binder that was dispersed on the side of the stitched tricot pattern. The three-

component resin system consisted of a medium-viscosity snap-cure epoxy resin, a low-viscosity amine hardener, and an internal mold release agent [31].

9.3.2 Hat Channel Fabrication

The equipment used to manufacture the hat channels consisted of a Genesis G100H-24-CPX 100-ton press (Wabash MPI, US), a custom two-part steel hat channel mold (Laval, Canada), an industrial oven, and a vacuum pump. The hat channel mold was composed of two halves. The upper half featured a vacuum port for connection to the vacuum pump, while the lower half of the mold was equipped with a vacuum seal and a silicon fiber pinch seal to prevent fiber wash (see Figure 9.1 for lower mold half dimensions). For a subgroup of hat channel parts, the vacuum pump was used to remove air from the mold cavity prior to the complete closure of the mold.

Before conducting the manufacturing trials, all the necessary equipment and materials, including mold, fabric stack, and the components of the resin system, were prepared. The mold cavity was cleaned and sealed, and Loctite Frekote 770NC release agent (Henkle, Germany) was applied. The hat channel mold was mounted to the 100-tons press, which has a heating system to heat both platens separately. The press platens were preheated to 135°C and 115°C for the lower and top dies, respectively [32], and the temperature was maintained throughout the manufacturing trials. Glass beakers were used to pour each of the 3-part resins separately. The beakers that contained the additive and the resin were introduced into an industrial oven at 85°C as the supplier recommends [31] to reduce the viscosity and facilitate the elimination of air bubbles within the resin, as illustrated in Figure 9.2. The three-part resin system components were mixed manually with a glass stir rod in a disposable contained based on the volume ratio resin: curing agent: additive = 100: 29: 1.7. The total volume of the mixture of the 3-part resin, with an addition of 10% accounting for handling losses, was set to 196.62 ml.

Rectangular fabric pieces measuring 500 mm × 260 mm (see Figure 9.3(a)) were cut from a roll using a utility knife in 0°, ±45°, and 90° orientations. These layers were stacked with the sequence $[0/\pm 45°/90°]_s$, and, for parts made with binder-stabilized fabric, the fabric stacks were placed in an industrial oven at 120°C for 20 minutes to pre-activate the binder. Next, a custom T-shaped tool was used to introduce the fabric into the mold (Figure 9.3(b)) to ensure the alignment of the layers and mitigate possible misplacement of the stack into the mold. When the T-shape tool was removed (Figure 9.3(c)), the fabric stack presented a geometry similar to the hat channel. Following, the press was closed with a force of 65,000 lbf to preform the fabric stack and guarantee the stack within the resin seal area (Figure 9.3(d)).

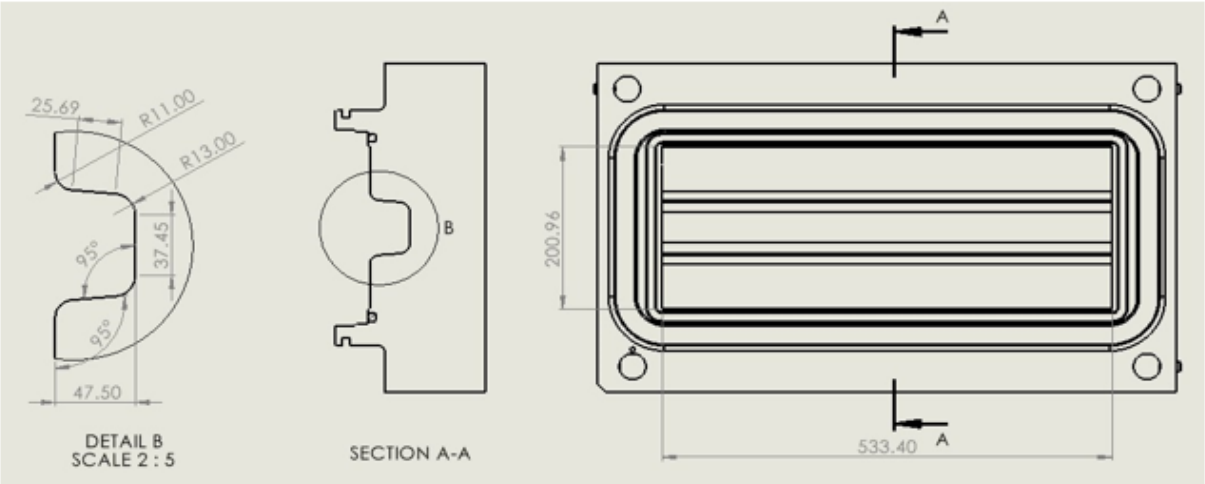


Figure 9.1: Dimensions of the hat channel lower mold used in this study.

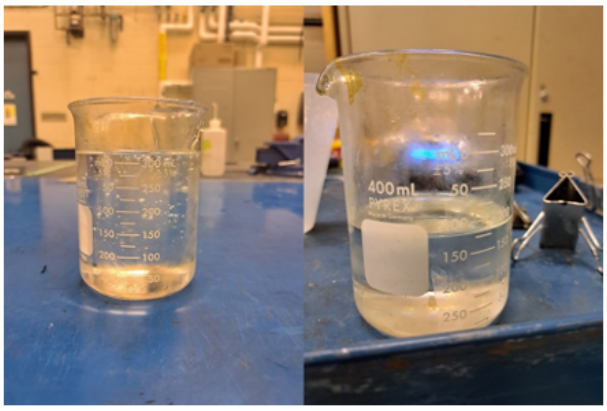


Figure 9.2: (a) Resin at room temperature with air bubbles (b) and resin heated at 85°C without air bubbles.

To manufacture the composite parts, the UD-NCF preforms were introduced into the lower cavity of the preheated mold. The second and third configurations listed in Table 1 had their binder-stabilized systems pre-activated in the preheated mold during preforming. For the last condition presented in Table 9.1, the mold was partially closed, engaging the vacuum seal, and the vacuum pump was turned on to draw air from the mold cavity for 20 seconds. The mold was then closed where the press was set to apply a force of 65,000 lbf, which was equivalent to a pressure of 20 bar. The mold remained closed for 5 minute to

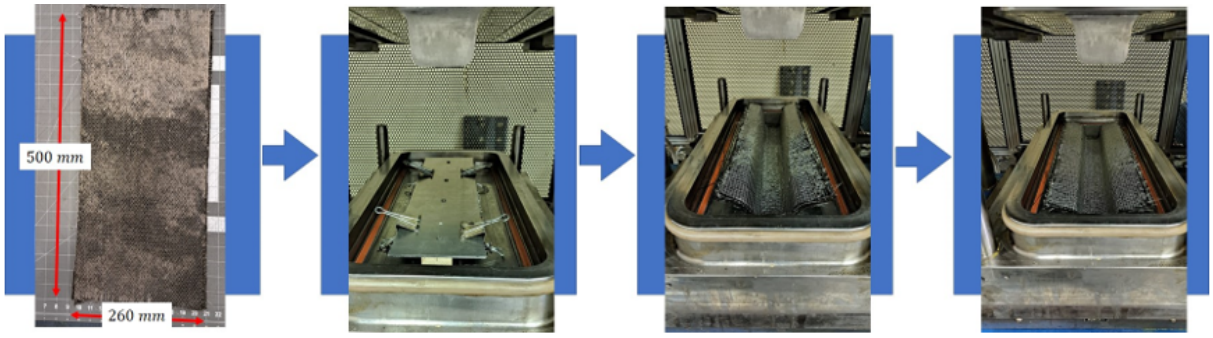


Figure 9.3: Illustration of the preform preparation steps: (a) cutting the fabric, (b) introducing it into the mold, (c) releasing from the T-shaped tool, and (d) preforming the fabric stack.

Table 9.1: Configurations of panels fabricated using the WCM process with fabric binder presence and vacuum duration specified.

Configurations	Identifier	Stabilizing binder state	Vacuum duration	Quantity
1	UNB	None	None	2
2	AT	Pre-activated	None	2
3	VAC 20s	Pre-activated	20 s	2

allow the resin to fully cure. Thereafter, the mold was opened and the part was demolded.

The molded hat channel parts underwent four steps to extract test specimens as illustrated in Figure 9.4. First, all parts were trimmed and squared with a DX-350 N tile saw (Rubi). Second, the trimmed part was divided into two parts of approximately 230 mm length and a total width of 150 mm (Figures 9.5a and 9.5b), resulting in six specimens per condition. Third, the loaded edge of the specimens was manually chamfered in 45°, as shown in Figure 9.4, to trigger progressive crushing (refer to Figure 9.6) during the tests.

9.3.3 Crushing test

Quasi-static axial crush tests were conducted using a 120-ton Macrodyne hydraulic press [33] as illustrated in Figure 9.7. The setup consisted of two steel plates; the top plate was mounted to a set of three load cells with a combined capacity of 100,000 Lbf, namely SW30-100K-B000, and a fixture, where the samples were attached, mounted on the bottom

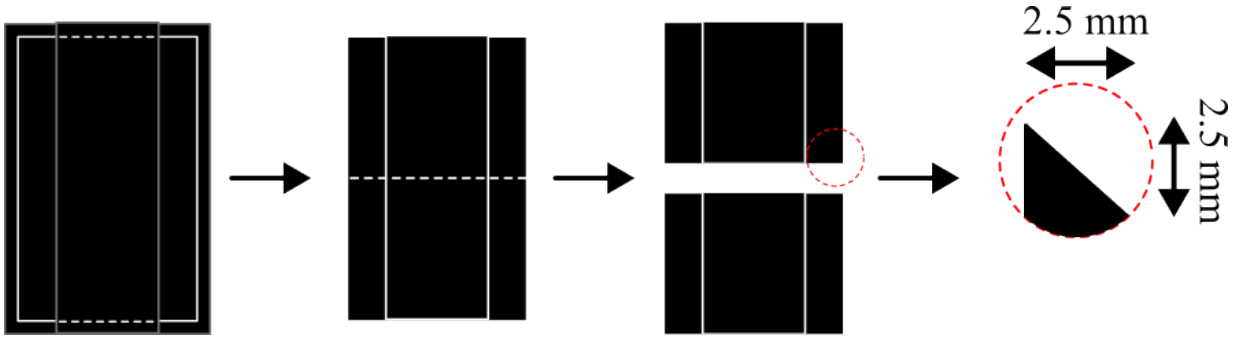


Figure 9.4: Specimen preparation steps procedure for quasi-static test.

platen. Two mid-speed cameras were positioned at the front and the back of the channel, capturing images at a rate of 40 frames per second (i.e., data was acquired at 0.04 to 0.05 seconds interval). The crush tests were performed at a velocity of 1 mm per second with the 12 chamfered samples, four per condition. The top platen was set to crush a distance of approximately 100 mm.

After the tests were conducted, the load-displacement curves were obtained for each test, similar to the progressive failure mode in Figure 9.7. The median value was then estimated for each condition. The median load-displacement curve for each condition was used to calculate the energy absorbed, which is defined by the area under the load-displacement curve [27, 34–36]. The energy absorbed is calculated by:

$$E_{\text{abs}} = \int_0^{d_c} P(\delta) d\delta, \tag{9.1}$$

where P is the load applied during the test and d_c represents the crushing distance.

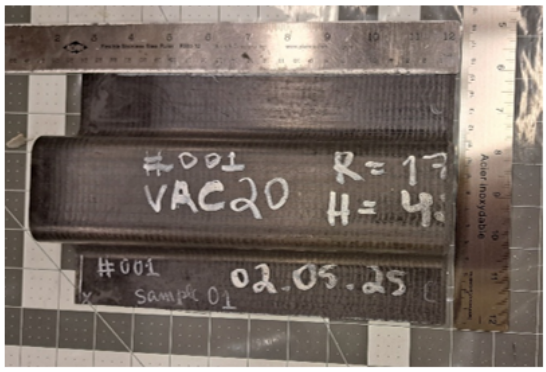
Next, the values of energy absorbed were used to compute the mean crushing force and the specific energy absorption, which are given by:

$$P_{\text{mean}} = \frac{E_{\text{abs}}}{d_c}, \tag{9.2}$$

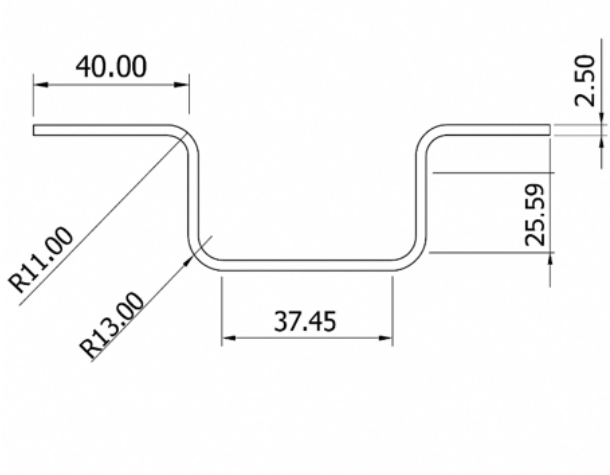
$$\text{SEA} = \frac{E_{\text{abs}}}{\text{m}} \tag{9.3}$$

where m is the crushed mass. Lastly, the crush force efficiency was estimated by the ratio between the mean crushing force and the peak force, given by:

$$\text{CFE} = \frac{P_{\text{mean}}}{P_{\text{m}}} \tag{9.4}$$



(a)



(b)

Figure 9.5: (a) WCM hat channel specimen cut from one of the hat channels manufactured with vacuum applied for 20 seconds (230 mm length), and (b) hat channel cross-sectional dimensions.

9.3.4 Microscopy

Microscopic evaluation was performed on two samples from each configuration to assess the microstructure qualitatively and to gain an overall understanding of how the different parameters affect it. These samples were cut using a Dx-350 N tile saw (Rubi) from the curvature region of a narrower section of the hat channel parts (Figure 9.8). The cut samples were cold-mounted in a two-part cold-mounting epoxy resin, namely Lecoset 7008

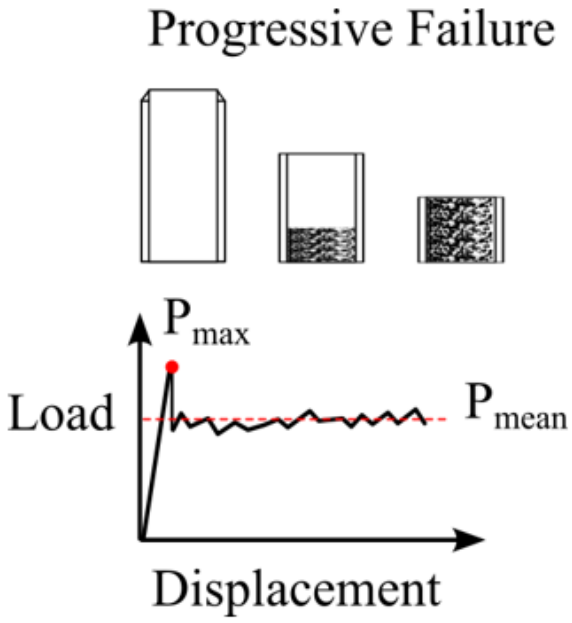


Figure 9.6: Schematic of progressive failure for a fiber-reinforced composite part subjected to axial crush load, with typical load-displacement response.

(Leco), machined, sanded, and polished. To produce high-quality microscopy images, each sample was polished through four steps using an automatic polishing machine (Tegramin, Struers). The process included coarse grinding with a 120-grit pad (Primo 120, Struers), followed by finer grinding with a 9 μm diamond solution (MD-Allegro, Struers). It then involved coarse polishing with a 3 μm diamond solution (MD-Dac, Struers), and finished with a 1 μm diamond solution (MD-Nap, Struers). After polishing, the samples were cleaned with acetone and ethanol. The samples were assessed with a Keyence VHX-5000 opto-digital microscope equipped with a 20-200$\times$lens. By using the highest magnification, a set of images was captured from each sample for a qualitative analysis.

9.4 Results and Discussion

Figures 9.9(a), (b), and (c) compare the performances of the test specimens for each condition during the quasi-static crush test. The results of individual specimens are shown in grey, while the black line represents the median of the condition. The VAC 20s hat

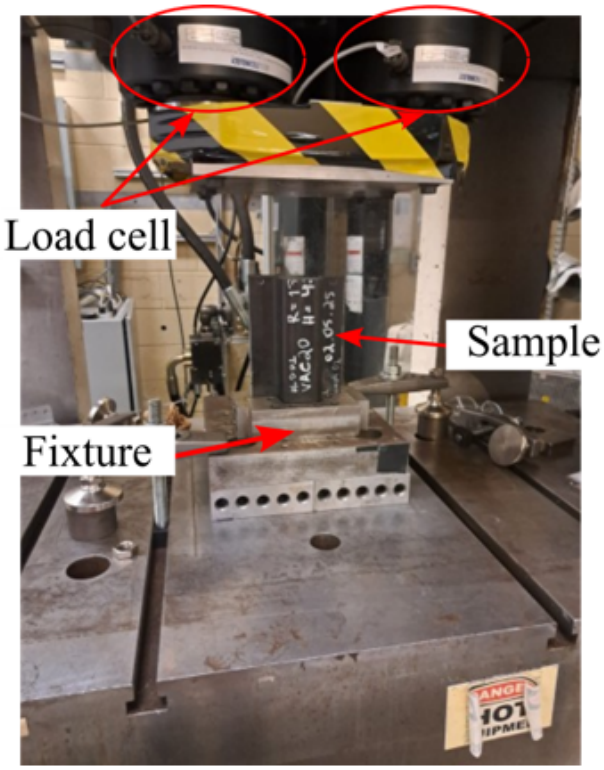


Figure 9.7: Setup for the experimental quasi-static axial loading tests showing test specimen mounted to lower press platen using a fixture and adapter plate.

channels (Figure 9.9(c)) exhibited the lowest variation, likely because better impregnation throughout the hat channels and more uniform composite parts. In contrast, the UNB and AT specimens showed incomplete impregnation in some regions (refer to Figure 9.10), which may have increased variation in crush force. This increased variation could result from significant void content, which, in turn, can affect the mechanical properties. In a previous investigation, WCM panels with the same manufacturing parameters (i.e., UNB and AT) exhibited void content of over 2% for the UNB condition and nearly 1% for the AT configuration [20].

The energy absorption of each condition was estimated using Eq. (9.1) and the median data for each condition (Figure 9.11). This comparison shows that the increase in absorbed energy - up to 5.34% at 100 mm displacement – is due to the presence of stabilizing binder and the thermal activation process. The small observed difference of 2.12% at the end of the crush stroke between the AT and the VAC 20s hat channels suggests that the application

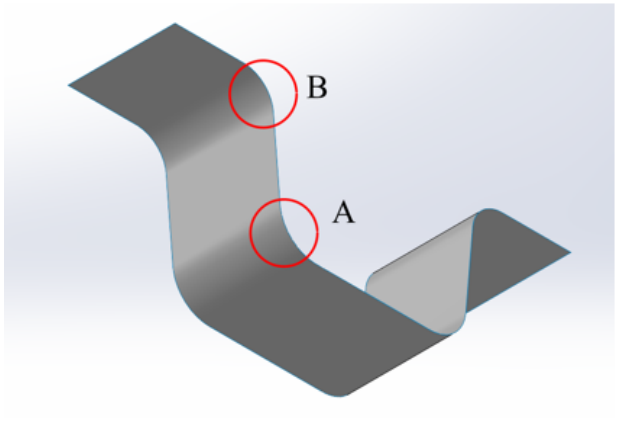


Figure 9.8: Regions in hat channel parts where samples were extracted for microscopy.

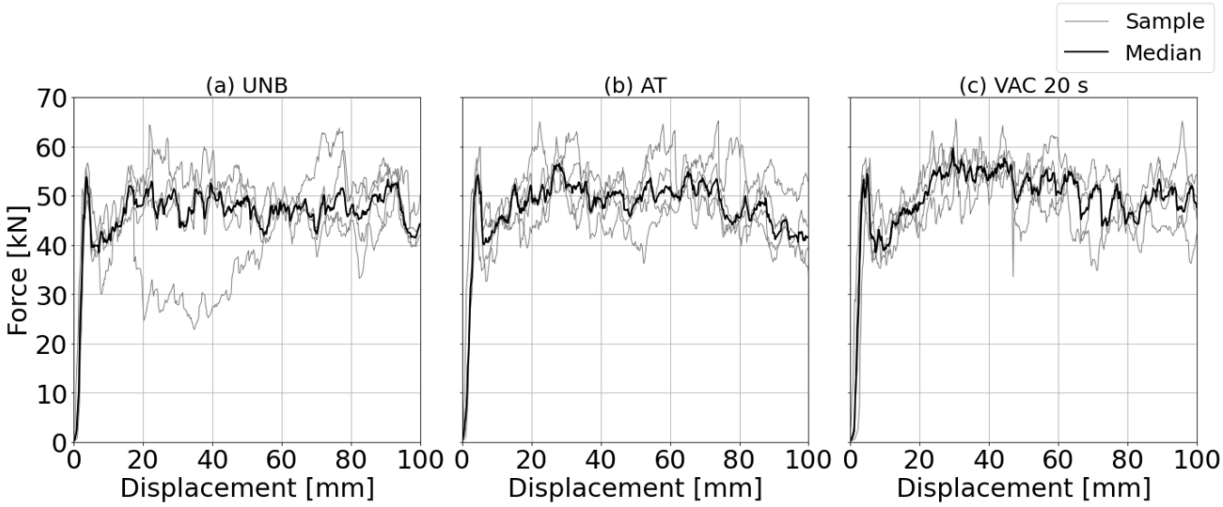


Figure 9.9: Load-displacement responses obtained from quasi-static axial crush tests for each composite laminate configuration: (a) UNB, (b) AT, and (c) VAC 20s.

of vacuum to the mold is not a significant influencing parameter.

The axial crush performance of the WCM hat channels was compared with that of similar HP-RTM hat channels reported by Harvey [28] and Ajayi [29]. The HP-RTM channels comprised the same UD-NCF carbon fiber snap-cure resin material system and the same stacking sequence of $[0/\pm 45/90]_s$; however, the cross-sectional dimensions were slightly different than the WCM hat channels fabricated in this study (refer to Figure 9.5

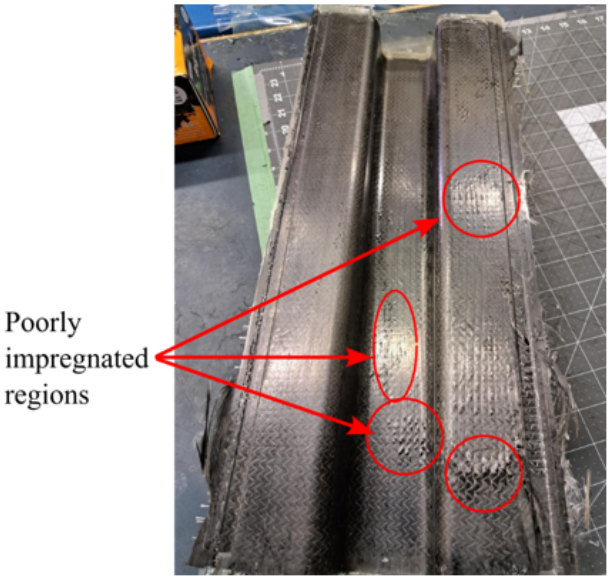


Figure 9.10: WCM hat channel with poorly impregnated regions within flanges and upper region.

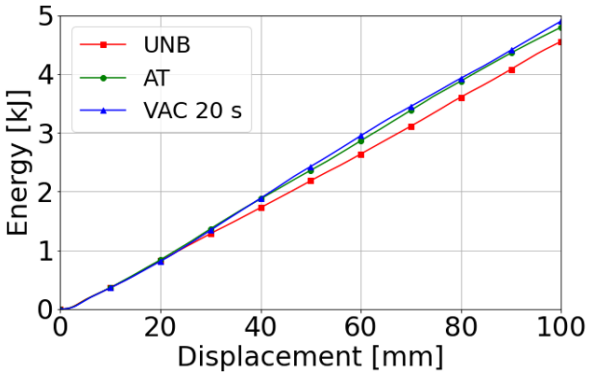


Figure 9.11: Total energy absorbed vs displacement data for each configuration during the quasi-static axial crush tests.

b). Figure 9.11 presents four comparisons between the three WCM hat channel conditions and the HP-RTM specimens [28, 29] in terms of peak crush force, mean crush force, crush force efficiency, and specific energy absorption.

First, Figure 9.12 a and Table 9.2 compare the peak crush force of these specimens;

all three WCM conditions yielded peak crush forces within a similar range. However, the median value of the UNB condition is 4.36% and 5.06% lower than the AT and VAC 20s conditions, respectively. Despite differences in peak crush force among the three configurations, these values are not statistically different, as shown in Table 9.3. Additionally, the peak force values of the AT and VAC 20s conditions differed by 16.37% and 17.14%, respectively, compared with the HP-RTM hat channels, and this difference could be partially attributed to the distinct cross-sectional geometry and the approximately 2.7 mm thickness of the HP-RTM specimens

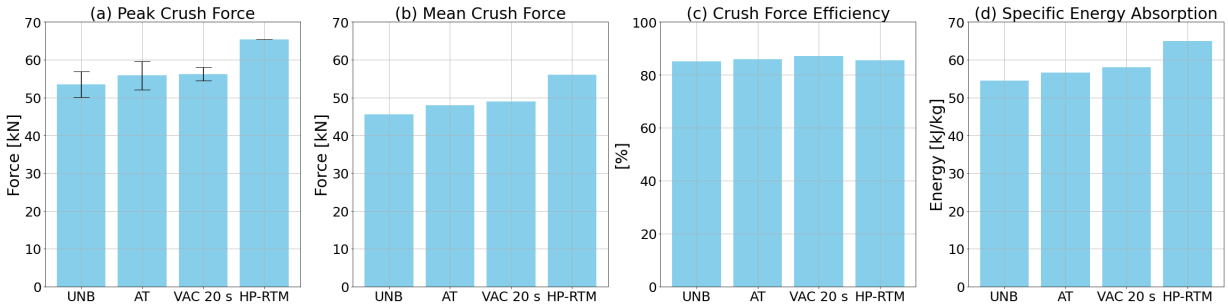


Figure 9.12: Quantitative comparison between WCM and HP-RTM [28, 29] specimens: (a) Peak Crush Force, (b) Mean Crush Force, (c) Crush Force Efficiency, and (d) Specific Energy Absorption

Second, Figure 9.12 b illustrates the mean crush force of all four conditions, calculated using Eq.(9.2). As shown in Figure 9.9 a, the UNB condition presented a lower mean value than the other WCM conditions. This may be due to the presence of a stabilizing binder, leading to higher cohesion between adjacent layers, which may require more energy to cause delamination and composite failure, and better fiber reinforcement alignment. The mean crush force difference between UNB and VAC 20s hat channels was about 7.60%. The HP-RTM hat channels also exhibited a mean crush force that was 14.30% greater than in the VAC 20s condition.

Third, Figure 9.12 presents the crush force efficiency given by Eq.(9.4). All four conditions exhibit similar crush force efficiency, due to the much higher peak crush force of the HP-RTM hat channels, which compensates for the higher mean crush force. Last, Figure 9.12 d illustrates the specific energy absorption for all four conditions, as defined in Eq. (9.3). Although the HP-RTM specimens exhibited a hat channel geometry, the mold used to produce the HP-RTM specimens had slightly different dimensions in the hat channel cavity from those shown in Figure 9.1. In the literature, specific energy absorption is the most commonly used method for comparing specimens with distinct geometries, as it nor-

Table 9.2: Peak crush force, mean crush force, crush force efficiency, and specific energy absorption of each WCM hat channel and HP-RTM hat channel specimens.

	UNB	AT	VAC 20s	HP-RTM
Peak crush force [kN]	53.50 ± 3.38	55.84 ± 3.70	56.21 ± 1.75	65.41 ± 0.00
Mean crush force [kN]	45.55	47.98	49.00	54.00
Crush force efficiency [%]	85	86	87	86
Specific energy absorption [kJ/kg]	54.45	56.67	57.99	64.89

Table 9.3: P-values obtained through T-Test comparing the peak crush force for the different WCM hat channel specimens.

UNB × AT	UNB × VAC 20S	AT × VAC 20s
0.3876	0.2209	0.8649

malizes the total energy absorbed by the crushed mass. The UNB condition exhibited the lowest specific energy absorption among all the conditions ($54.45kJ/kg$). Next, the AT and the VAC 20s hat channels reached a value of 56.67 and $57.99kJ/kg$, respectively. Lastly, the HP-RTM hat channels absorbed $64.89kJ/kg$, approximately 12% more than the VAC 20s condition

Figure 9.13a, 9.13b, and 9.13c depict the UNB, AT, and VAC 20s crushed hat channels. It is interesting to observe that all images illustrate the same failure mode, characterized by bending of the layers and the formation of debris as the press progresses. A similar failure mode was reported by Harvey [28] and Ajayi [29] in quasi-static tests using HP-RTM channels, with lamina fragmentation and considerable bending.

Next, a qualitative microscopic assessment was conducted with two microscopic samples of each investigated configuration. Figure 9.8 illustrates the assessed regions A and B, where the samples were extracted. Samples from these regions were assessed due to the higher likelihood of manufacturing-induced defects arising from the shearing and stretching of the fabric layers during the forming process, such as voids or thickness variation. Thickness measurements were taken at several points of the sample to investigate potential misalignment. Ajayi [29] reports a thickness difference of 36% between regions, which

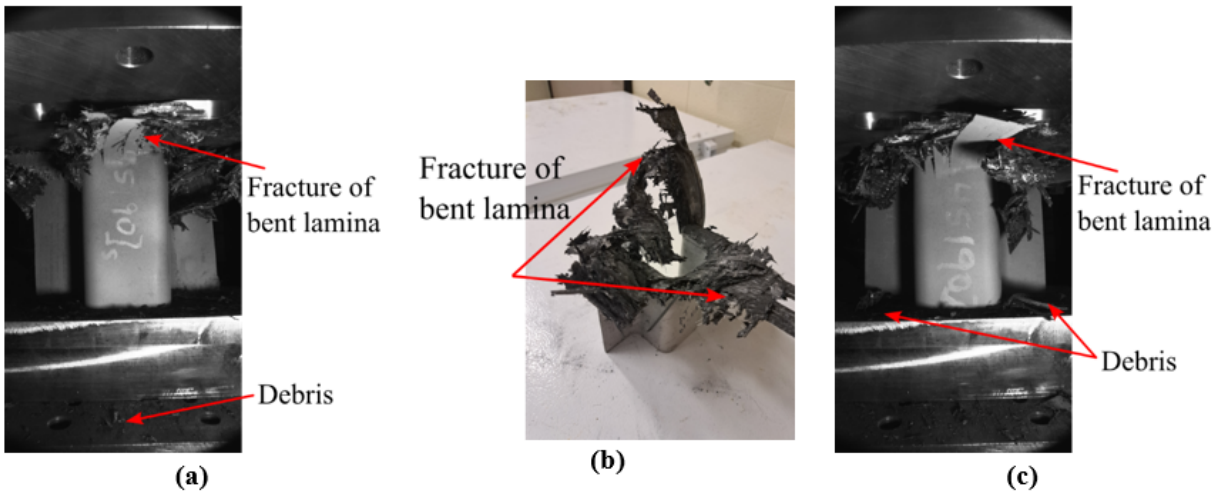


Figure 9.13: Images of the $[0/45/90]_s$ WCM hat channels after quasi-static axial loading, showing similar brittle fracture in the (a) UNB (b) AT, and (c) VAC 20s hat channel configurations.

Table 9.4: Thickness measurements obtained from regions A and B for each WCM sample.

	Region A	Region B
UNB	2.47 mm	2.50 mm
AT	2.54 mm	2.59 mm
VAC 20s	2.26 mm	2.28 mm

they attribute to a higher pressure at the bottom corner of the channel cavity during the manufacturing. Figures 9.14a and 9.14b show UNB samples at regions A and B, respectively. Both images exhibit similar thickness measurements (see Table 9.4), indicating that the part thickness was likely consistent throughout. In section A (Figure 9.14a), a void is located between the 90-degree layers, which may affect the mechanical property. Similar to the UNB samples, the thickness measurements of the AT samples were comparable between both regions (see Table 9.4). Lastly, the VAC 20s condition yielded the thinnest specimens (Table 9.4), due to the vacuum applied to the mold, which increased the compaction and reduced the stack thickness during manufacturing [20]. The reduction in thickness implies an increase in the part's FVF, which might affect the SEA [37] of the VAC 20s hat channels and explain the difference in mechanical performance between the HP-RTM specimen, which had an average thickness of 2.70 mm.

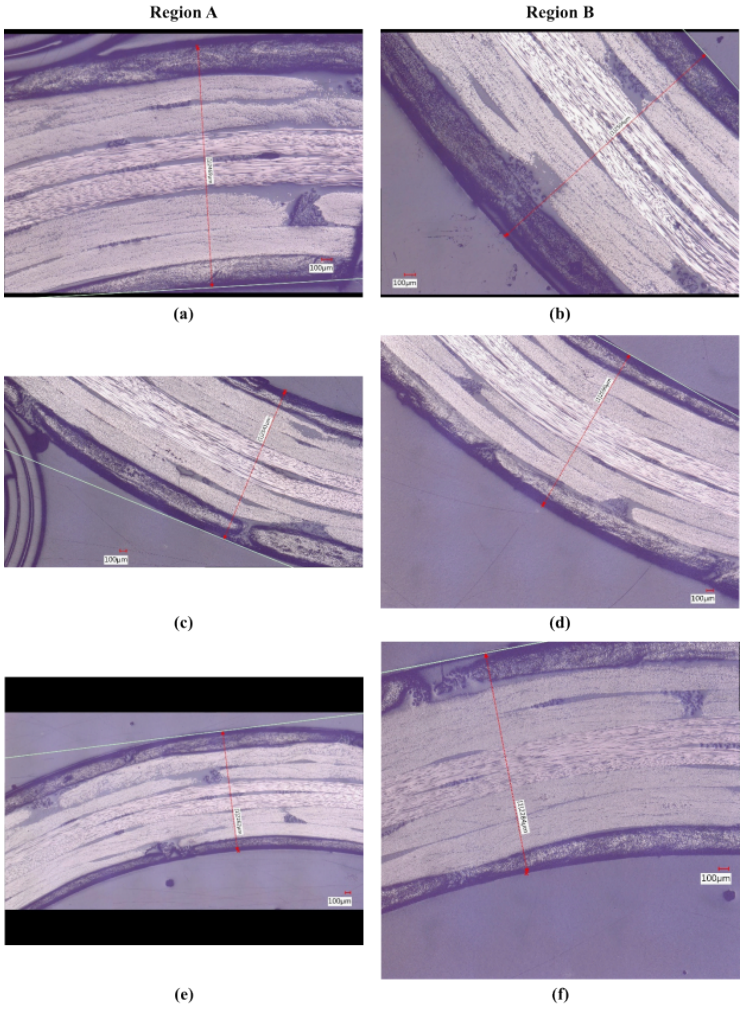


Figure 9.14: Microstructure of $[0/\pm 45/90]_s$ hat channels for three WCM manufacturing configurations: (a,b) UNB, (c,d) AT, and (e,f) VAC 20s, at regions A and B.

9.5 Conclusions

The goal of this investigation was to study how the presence of a stabilizing binder on the non-crimp fabric and the application of vacuum to the mold influence the quality and the energy absorption capability of the WCM component. The effects of the stabilizing binder and vacuum assistance were assessed through microscopy and quasi-static axial crush tests. The performance of the WCM hat channels was compared with that of similar HP-RTM component reported in a previous study.

- The use of binder-stabilized NCF increased the peak crush force and the energy absorbed during the crush test, possibly due to improved reinforcement alignment and reduced void content. However, statistical analysis did not indicate a significant difference between the configuration using raw fabric and that with pre-activated binder.
- The application of a vacuum to the mold enhanced the superficial quality of the final composite (Figure 9.5 a) and improved preform compaction, resulting in a higher FVF [20]. The crush test results indicated better performance for the configuration with vacuum assistance, likely due to lower void content.
- Similar to the HP-RTM hat channels, the WCM hat channels exhibited a brittle fracture failure mode under quasi-static axial crushing, characterized by fragmentation and bending of the lamina bundles.
- The HP-RTM hat channels demonstrated higher energy absorption compared to the VAC 20s configuration, which may be explained by the higher FVF of the WCM hat channels caused by vacuum application, resulting in a thinner fabric preform.

The results obtained in this investigation have shown that WCM hat channels can achieve energy absorption levels comparable to those of HP-RTM hat channels, indicating the feasibility of using the WCM process for producing energy-absorbing structures. Future work will focus on assessing the influence of different types and concentrations of stabilizing binders on the energy absorption capacity of UD-NCF composite parts.

References

[1] X. Liu *et al.*, "Experimental investigation of energy absorption behaviour of circular carbon/epoxy composite tubes under quasi-static and dynamic crush loading," *Composite Structures*, vol. 227, Nov. 2019, ISSN: 02638223. DOI: 10.1016/j.compstruct.2019.111266.

[2] F. Henning, L. Kärger, D. Dörr, F. J. Schirmaier, J. Seuffert, and A. Bernath, "Fast processing and continuous simulation of automotive structural composite components," *Composites Science and Technology*, vol. 171, pp. 261–279, Feb. 2019, ISSN: 0266-3538. DOI: 10.1016/J.COMPSCITECH.2018.12.007.

[3] C. Poppe, "Process simulation of wet compression moulding for continuous fibre-reinforced polymers," Ph.D. dissertation, Karlsruhe Institute of Technology, 2021.

[4] B. Schäfer, R. Zheng, N. Naouar, and L. Kärger, "Membrane behavior of uni-and bidirectional non-crimp fabrics in off-axis-tension tests," *International Journal of Material Forming*, vol. 16, no. 6, p. 68, 2023.

[5] R. Kumar, K. Rashvand, A. Fraisse, A. Sarhadi, and T. L. Andersen, "Experimental testing method to characterise the drapability of ud non-crimp fabrics used in wind turbine blades," *IOP Conference Series: Materials Science and Engineering*, vol. 1293, no. 1, p. 012 020, Nov. 2023. DOI: 10.1088/1757-899X/1293/1/012020. [Online]. Available: https://dx.doi.org/10.1088/1757-899X/1293/1/012020.

[6] P. H. Broberg *et al.*, "That's how the preform crumples: Wrinkle creation during forming of thick binder-stabilised stacks of non-crimp fabrics," *Composites Part B: Engineering*, vol. 273, p. 111 269, 2024, ISSN: 1359-8368. DOI: https://doi.org/10.1016/j.compositesb.2024.111269. [Online]. Available: https://www.sciencedirect.com/science/article/pii/S1359836824000805.

[7] R. M. Portela, B. Schafer, L. Karger, A. R. de Faria, and J. Montesano, "Effect of loading rate, viscosity, and binder activation on the bending response of an infiltrated ud-ncf," *Composites Part A: Applied Science and Manufacturing*, vol. 200, p. 109 347, Jan. 2026, ISSN: 1359-835X. DOI: 10.1016/J.COMPOSITESA.2025.109347. [Online]. Available: https://www.sciencedirect.com/science/article/pii/S1359835X25006414.

[8] G. Estrada, C. Vieux-Pernon, and S. G. Advani, "Experimental characterization of the influence of tackifier material on preform permeability," *Journal of Composite Materials*, vol. 36, no. 19, pp. 2297–2310, 2002. DOI: 10.1177/0021998302036019542.

eprint: https://doi.org/10.1177/0021998302036019542. [Online]. Available: https://doi.org/10.1177/0021998302036019542.

[9] J. C. Brody and J. W. Gillespie, "The effects of a thermoplastic polyester preform binder on vinyl ester resin," *Journal of Thermoplastic Composite Materials*, vol. 18, no. 3, pp. 157–179, 2005. DOI: 10.1177/0892705705043535. eprint: https://doi.org/10.1177/0892705705043535. [Online]. Available: https://doi.org/10.1177/0892705705043535.

[10] H. M. Yoo, J. W. Lee, J. S. Kim, and M. K. Um, "Influence of non-reactive epoxy binder on the permeability and friction coefficient of twill-woven carbon fabric in the liquid composite molding process," *Applied Sciences*, vol. 10, no. 20, p. 7039, 2020, ISSN: 2076-3417. DOI: 10.3390/app10207039. [Online]. Available: https://www.mdpi.com/2076-3417/10/20/7039.

[11] P. H. Broberg, C. Krogh, E. Lindgaard, and B. L. V. Bak, "Simulation of wrinkling during forming of binder stabilized ud-ncf preforms in wind turbine blade manufacturing," *Key Engineering Materials*, vol. 926, pp. 1248–1256, Jul. 2022, ISSN: 1662-9795. DOI: 10.4028/p-165q46. [Online]. Available: https://www.scientific.net/KEM.926.1248.

[12] L. Moser, S. Heide, I. Swentek, U. Schmidt, and M. Seiz, "Thermoset technologies for cost efficient production of lightweight composites," in *Technologies for economic and functional lightweight design: Conference proceedings 2020*, Springer, 2021, pp. 35–41.

[13] S. Neunkirchen, M. Bender, and R. Schledjewski, "Effect of binder activation on in-plane capillary flow in multilayer stacks of carbon fiber fabrics," *Applied Composite Materials*, vol. 31, pp. 709–719, 2 Apr. 2024, ISSN: 0929-189X. DOI: 10.1007/s10443-023-10198-6. [Online]. Available: https://link.springer.com/10.1007/s10443-023-10198-6.

[14] K. Wei, D. Liang, M. Mei, D. Wang, X. Yang, and Z. Qu, "Preforming behaviors of carbon fiber fabrics with different contents of binder and under various process parameters," *Composites Part B: Engineering*, vol. 166, pp. 221–232, 2019, ISSN: 1359-8368. DOI: https://doi.org/10.1016/j.compositesb.2018.11.143. [Online]. Available: https://www.sciencedirect.com/science/article/pii/S1359836818326568.

[15] R. M. Portela, B. Schäfer, L. Kärger, A. R. de Faria, and J. Montesano, "Influence of viscosity, binder activation, and loading rate on the membrane response of an infiltrated ud-ncf," in *ESAFORM 2024 - 27th International Conference on Material Forming*, Apr. 2024.

[16] P. H. Broberg, F. Shakibapour, J. Jakobsen, E. Lindgaard, and B. L. V. Bak, "Characterisation of the transverse shear behaviour of binder-stabilised preforms for wind turbine blade manufacturing," 2023. DOI: 10.17632/9m78sg3zwn.1. [Online]. Available: http://creativecommons.org/licenses/by/4.0/.

[17] C. Krogh, P. H. Broberg, J. Kepler, and J. Jakobsen, "Comprehending the bending: A comparison of different test setups for measuring the out-of-plane flexural rigidity of a ud fabric," *Key Engineering Materials*, vol. 926, pp. 1257–1267, Jul. 2022, ISSN: 1662-9795. DOI: 10.4028/p-r883x4. [Online]. Available: https://www.scientific.net/KEM.926.1257.

[18] M. Ghazimoradi, E. A. Trejo, C. Butcher, and J. Montesano, "Characterizing the macroscopic response and local deformation mechanisms of a unidirectional non-crimp fabric," *Composites Part A: Applied Science and Manufacturing*, vol. 156, p. 106 857, May 2022, ISSN: 1359-835X. DOI: 10.1016/J.COMPOSITESA.2022.106857.

[19] M. Tanoğlu and A. T. Seyhan, "Investigating the effects of a polyester preforming binder on the mechanical and ballistic performance of e-glass fiber reinforced polyester composites," *International Journal of Adhesion and Adhesives*, vol. 23, pp. 1–8, 1 Jan. 2003, ISSN: 01437496. DOI: 10.1016/S0143-7496(02)00061-1. [Online]. Available: https://linkinghub.elsevier.com/retrieve/pii/S0143749602000611.

[20] R. M. Portela, A. Soltansaleki, G. Melenka, A. R. de Faria, and J. Montesano, "Effect of stabilizing binder on void morphology and mechanical performance of wet compression molded rapid-curing non-crimp fabric composites. submitted nov 2025 (under review).,"

[21] G. Sun, D. Chen, G. Zhu, and Q. Li, "Lightweight hybrid materials and structures for energy absorption: A state-of-the-art review and outlook," *Thin-Walled Structures*, vol. 172, p. 108 760, 2022, ISSN: 0263-8231. DOI: https://doi.org/10.1016/j.tws.2021.108760. [Online]. Available: https://www.sciencedirect.com/science/article/pii/S0263823121007564.

[22] P. Feraboli, B. Wade, F. Deleo, and M. Rassaian, "Crush energy absorption of composite channel section specimens," *Composites Part A: Applied Science and Manufacturing*, vol. 40, no. 8, pp. 1248–1256, Aug. 2009, ISSN: 1359835X. DOI: 10.1016/j.compositesa.2009.05.021.

[23] H. Mou, Y. Chen, J. Xie, and H. Liu, "Crashworthiness analysis of single cfrp, hybrid cfrp/al and fiber metal laminate c-channels: Quasi-static crushing tests and numerical simulations," *Thin-Walled Structures*, vol. 213, Aug. 2025, ISSN: 02638231. DOI: 10.1016/j.tws.2025.113226.

[24] L. N. Chiu *et al.*, "Crush responses of composite cylinder under quasi-static and dynamic loading," *Composite Structures*, vol. 131, pp. 90–98, Nov. 2015, ISSN: 02638223. DOI: 10.1016/j.compstruct.2015.04.057.

[25] R. A. Eshkoor *et al.*, "Failure mechanism of woven natural silk/epoxy rectangular composite tubes under axial quasi-static crushing test using trigger mechanism," *International Journal of Impact Engineering*, vol. 64, pp. 53–61, 2014, ISSN: 0734743X. DOI: 10.1016/j.ijimpeng.2013.09.004.

[26] S. Palanivelu *et al.*, "Comparative study of the quasi-static energy absorption of small-scale composite tubes with different geometrical shapes for use in sacrificial cladding structures," *Polymer testing*, vol. 29, no. 3, pp. 381–396, 2010.

[27] Z. Xiao, F. Mo, D. Zeng, and C. Yang, "Experimental and numerical study of hat shaped cfrp structures under quasi-static axial crushing," *Composite structures*, vol. 249, p. 112 465, 2020.

[28] B. Harvey, "Characterization of the axial crush and bending response of carbon fiber non-crimp fabric/snap-cure epoxy under different loading rates," University of Waterloo, Waterloo, Canada, Internal Report (Composites Research Group), Tech. Rep., 2022.

[29] V. A. O. Ajayi, "Experimental characterization and numerical modelling of the energy absorption capacity of ud-ncf carbon fibre/epoxy composite channels," M.S. thesis, University of Waterloo, 2025.

[30] *Technical data sheet zoltek™ px35 uni-directional fabrics*, Zoltek, Jan. 2021.

[31] *Technical data sheet epikote™ resin 06150 epikure curing agent 06150*, Westlake Epoxy, Jan. 2019.

[32] F. Mariano, "Development of an LCM process for rapid curing CFRP parts," M.S. thesis, Politecnico di Torino, Torino, Italy, 2019.

[33] A. Mamalis, M. Robinson, D. Manolakos, G. Demosthenous, M. Ioannidis, and J. Carruthers, "Review Crashworthy capability of composite material structures," *Composite Structures*, vol. 37, no. 2, pp. 109–134, 1997, ISSN: 0263-8223. DOI: https://doi.org/10.1016/S0263-8223(97)80005-0. [Online]. Available: https://www.sciencedirect.com/science/article/pii/S0263822397800050.

[34] C. Yang, Z. Chen, S. Yao, P. Xu, S. Li, and M. S. Alqahtani, "Quasi-static and low-velocity axial crushing of polyurethane foam-filled aluminium/CFRP composite tubes: An experimental study," *Composite Structures*, vol. 299, Nov. 2022, ISSN: 02638223. DOI: 10.1016/j.compstruct.2022.116083.

[35] M. Capretti *et al.*, "Crashworthiness of flax and hybrid composite tubes subjected to quasi-static axial crushing: Experimental and numerical results," *Composite Structures*, vol. 354, Jan. 2025, ISSN: 02638223. DOI: 10.1016/j.compstruct.2024.118785.

[36] S. Z. Shah, P. S. Megat-Yusoff, R. S. Choudhry, Z. Sajid, and I. U. Din, "Experimental investigation on the quasi-static crush performance of resin-infused thermoplastic 3d fibre-reinforced composites," *Composites Communications*, vol. 28, Dec. 2021, ISSN: 24522139. DOI: 10.1016/j.coco.2021.100916.

[37] A. Esnaola, I. Tena, J. Aurrekoetxea, I. Gallego, and I. Ulacia, "Effect of fibre volume fraction on energy absorption capabilities of e-glass/polyester automotive crash structures," *Composites Part B: Engineering*, vol. 85, pp. 1–7, Feb. 2016, ISSN: 13598368. DOI: 10.1016/j.compositesb.2015.09.007.

Chapter 10

General Discussion

As stated in Chapter 3, the overall goal of this study was to investigate the effects of the stabilizing binder on the draping mechanisms of the UD-NCF, as well as the microstructure, and, consequently, the mechanical performance of the WCM UD-NCF composites.

The first task considered the characterization of draping mechanisms in the context of the WCM manufacturing process, in which the textile is impregnated, and the use of binder-stabilized fabric as an alternative to address the challenge of resin management in the manufacturing of thick components in complex, deep-cavity molds. The investigation of fabric behavior demonstrated that friction between fiber tows and stitching yarn, as well as fiber-fiber friction, plays an important role in the draping mechanism. The use of thermosetting binder powder, with its pre-activation, results in a physical coating that enhances cohesion among the constituents of the UD-NCFs. This enhanced cohesion protects the fabric's integrity during preparation steps and increases stiffness, as seen in membrane (Chapter 4) and bending (Chapter 5) mechanisms. The increased bending stiffness addresses the resin management challenge in manufacturing thick components. In the fabric stack, the stabilizing binder reduced relative layer movement, thereby increasing resistance to compaction (Chapter 6). In contrast to the effect of the pre-activation of the stabilizing binder, the impregnation of the fabric layers facilitated the movement between the fabric constituents by reducing friction and decreasing bending and membrane stiffness, as was previously indicated by Poppe [1], as well as influencing the compaction relaxation as stated by Li et al. [2]. Last, it was observed that the loading rate influences the bending stiffness as it is governed by the friction between different constituents of the textile (e.g., stitching-tows), while the membrane response is given by the fiber tow or stitching deformation, limiting the stiffness as indicated by Schäfer et al. [3].

The study with the WCM panels indicated changes in the microstructure and, consequently, in the mechanical properties, caused by the use of binder-stabilized fabric and vacuum application to the mold. The microscopic images show a higher fiber density in WCM panels than in HP-RTM panels, due to differences in the number of layers in panels with similar thickness (Chapter 7). These images also showed lower void content in WCM panels manufactured with binder-stabilized textiles. The reduction in void content and size—particularly in large inter-tow voids—resulted in enhanced void-sensitive properties, such as intralaminar shear strength. This is because inter-tow voids near the midplane of the specimens are more likely to cause delamination (Chapter 8), leading to results comparable to those of HP-RTM specimens. However, the transverse tensile properties, which are also void-sensitive, showed no variation with reduced void content due to the high compaction and lower inter-fiber spacing in the WCM panels. Lastly, the vacuum-assisted technique produced greater compaction of the fabric preform, resulting in parts with the lowest and most consistent thickness. The lowest thickness and, in consequence, the highest FVF resulted in higher longitudinal tensile properties.

Lastly, the manufacturing of high-quality WCM hat channels demonstrated the feasibility of producing composite parts with greater geometrical complexity, as required by the automotive industry. Although the microscopic assessment showed some voids in the UNB sample, the void content of the hat channel component was not quantified and may differ from that of the panels assessed in the second task (Chapter 8) due to differences in geometry. As the curved regions—which may be the most critical areas in terms of impregnation—exhibited few voids, it can be assumed that the overall void content was low across all three conditions, resulting in enhanced mechanical properties with limited influence from voids.

Additionally, the quasi-static axial crush tests indicated the feasibility of using the WCM process as an alternative for manufacturing energy-absorbing components. The axial crush test results showed no significant difference in energy absorption between non-binder-stabilized and binder-stabilized fabrics, nor between configurations with and without vacuum application. A significantly higher specific energy absorption (SEA) was observed for the HP-RTM hat channels compared to the WCM parts, which can be attributed to differences in fiber volume fraction (FVF), as well as geometry, specimen length, and crush distance. Although some mechanical properties may increase with increasing FVF, there is an optimal value beyond which further increases may negatively affect performance. Finally, geometric differences, in addition to specimen length and crush distance, may have influenced the results, making a direct comparison between HP-RTM and WCM hat channels less reliable.

Bibliography

[1] C. Poppe, "Process simulation of wet compression moulding for continuous fibre-reinforced polymers," Ph.D. dissertation, Karlsruhe Institute of Technology, 2021.

[2] L. Li, Y. Zhao, J. Yang, J. Zhang, and Y. Duan, "An experimental investigation of compaction behavior of carbon non-crimp fabrics for liquid composite molding," *Journal of Materials Science*, vol. 50, pp. 2960–2972, 7 Apr. 2015, ISSN: 15734803. DOI: 10.1007/s10853-015-8860-0.

[3] B. Schäfer, S. Haas, P. Boisse, and L. Kärger, "Investigation of the membrane behavior of ud-ncf in macroscopic forming simulations," *Key Engineering Materials*, vol. 926, pp. 1413–1422, 2022.

[4] B. Schäfer, R. Zheng, N. Naouar, and L. Kärger, "Membrane behavior of uni-and bidirectional non-crimp fabrics in off-axis-tension tests," *International Journal of Material Forming*, vol. 16, no. 6, p. 68, 2023.

[5] F. J. Schirmaier, K. A. Weidenmann, L. Kärger, and F. Henning, "Characterisation of the draping behaviour of unidirectional non-crimp fabrics (UD-NCF)," *Composites Part A: Applied Science and Manufacturing*, vol. 80, pp. 28–38, Jan. 2016, ISSN: 1359-835X. DOI: 10.1016/J.COMPOSITESA.2015.10.004.

[6] C. Krogh, P. H. Broberg, J. Kepler, and J. Jakobsen, "Comprehending the bending: A comparison of different test setups for measuring the out-of-plane flexural rigidity of a ud fabric," *Key Engineering Materials*, vol. 926, pp. 1257–1267, Jul. 2022, ISSN: 1662-9795. DOI: 10.4028/p-r883x4. [Online]. Available: https://www.scientific.net/KEM.926.1257.

Chapter 11

Conclusions and Recommendations

11.1 Conclusions

The goal of this study was to understand how the stabilizing binder influences the formability, microstructure, and mechanical performance of wet compression-molded UD-NCF composites. The research comprised three main objectives. The first was to investigate how the stabilizing binder affects the formability of infiltrated carbon fiber UD-NCF, specifically the membrane, bending, and compaction behaviors. The second objective was to study the influence of the stabilizing binder on the microstructure and mechanical properties of carbon fiber UD-NCF composites manufactured via WCM. Finally, the third objective focused on assessing the effect of the stabilizing binder on the energy-absorption performance of WCM UD-NCF composite hat channels.

In Task 1, a dry, infiltrated binder-stabilized unidirectional non-crimp fabric was characterized for its membrane, bending, and compaction responses during the draping phase of the WCM process. The membrane was tested with a horizontal bias-extension test (BET) setup with a reservoir, in which silicone oil was poured to fully impregnate the samples before each trial. Bending tests were conducted with a rheometer bending test (RBT) setup. Last, the compaction tests were performed with a punch-to-plate setup. All three experiments generated a valuable dataset through physical laboratory experimentation. The experimental work yielded important insights into the influence of the stabilizing binder and fabric infiltration on the fabric draping mechanism responses, addressing a critical gap in the literature concerning binder-stabilized UD-NCF draping mechanisms. Based on the experimental results, the following conclusions were drawn:

- The experimental results obtained from the UD-NCF characterization are specific to this textile, stabilizing binder type, and binder concentration. A generalization rule can be formulated in the future by characterizing the same textile with different binder types and concentrations. However, in general, binder-stabilized fabric exhibits higher membrane and bending stiffness as well as compaction peak response compared to non-binder-stabilized fabric.

- The membrane response is the dominant mechanism during the forming phase. During the characterization of this mechanism, it was planned to obtain the shear angle; however, the speckling technique was not effective for the textile, as the fibres absorbed the ink and the DIC system was unable to track the deformation of the specimens. A suggestion for future characterization is to adopt the approach presented in Ref. [4]. Although the shear angle was not measured, the force–displacement results can be used in an inverse modelling approach to identify the parameters under the different conditions. The results also indicated an increase in membrane force with binder pre-activation, which may influence local deformation mechanisms, including reduced tow sliding and increased wrinkle size.

- The draping mechanisms are mainly ruled by the friction between fiber tows and between fiber tow-stitching yarn. The activation of the stabilizing binder involves heating the thermosetting polymer, which melts and coats the tows, increasing cohesion between the fiber tows and the stiffness/force of the mechanisms. On the other hand, the infiltration of the fabric lubricates the tows, decreasing friction between them and reducing stiffness/force mechanisms.

- The loading rate elicited different responses across mechanisms. For membrane behavior, the loading rate did not differ significantly. For bending behavior, stiffness increased with loading rate because there was less time to overcome static friction at higher loading rates.

- Regarding compaction behavior, the stacking sequence did not affect the compaction force, as expected from previous investigations. This similarity is due to the supporting fibers, which prevent the layers from greater nesting and result in a similar compaction force response.

- The characterization of engineering textiles is important to understand their behavior during forming. The use of BET setups is recommended when characterizing UD-NCF instead of PFT, as stated in Ref. [5]. Additionally, the use of RBT is more consistent as highlighted in [6] and allows the characterization of the bending behavior, considering parameters like temperature, hysteresis, and loading rates.

In Task 2, a comprehensive study was performed to characterize the mechanical properties considering different materials and manufacturing parameters. Key factors evaluated included the presence of the stabilizing binder, its activation, and the vacuum application to the mold. To extend this evaluation, HP-RTM samples were also tested and analyzed for comparison with WCM specimens and their respective mechanical performances. Based on the experimental results, several conclusions can be drawn:

- The WCM process was effective in producing high-quality composite panels. This was proven by microscopically assessing samples from the different studied conditions, delivering high FVF (approximately 60%) and low void content (<2%).
- CT scan images indicated that the UNB sample exhibited the highest void content (approximately 3%) and the highest number of large inter-tow voids near the midplane, where shear stresses peak and delamination cracks tend to form. In contrast, the microstructure of the VAC 20s exhibited lower void content (< 1%) with fewer large voids.
- The transverse tensile test is mainly governed by the matrix. However, differences between conditions were not observed as the FVF of these conditions was above 60%.
- Similar to the transverse tension test, the SBS test is sensitive to void content and is recommended for capturing the presence of inter-tow voids near the midplane of the specimen, which contribute to laminate delamination. As some studies indicate that the use of binder-stabilized fabrics may affect stack permeability and resin viscosity, mechanical evaluation of the specimens is recommended.
- Compared with HP-RTM, some tested WCM conditions yielded ILSS values similar to those of HP-RTM. This comparable strength is mainly due to two factors: both used the same material system, with ILSS primarily governed by the matrix system, and certain conditions yielded void contents below 1%, thereby enhancing the composite's ILSS.

In Task 3, a set of quasi-static crush tests was conducted with WCM hat channels using a hydraulic press. A simple testing fixture was designed to hold the composite part in position during the impact test. The manufactured hat channels were trimmed at the flanges, cut in half, and chamfered at the inside end to prevent catastrophic failure of the sample. Repeatable data were generated across the four test repeats for each condition, which can be used to validate numerical models for crush-test simulation. The following conclusions were drawn:

- The stabilizing binder has an increase in energy absorption during impact of more than 5%. This is attributed to the stabilization method, which enhances the cohesion between adjacent fabric layers and improves fiber alignment during manufacturing, thereby enhancing mechanical properties. The use of the vacuum-assisted technique increased the FVF of the composite part, resulting in an energy absorption 2% higher than that of the binder-stabilized fabric.

- WCM has proven to be a reliable manufacturing process for producing composite parts with fairly complex geometries, such as a hat channel. In general, the part visually reached good quality, and later it was possible to confirm microstructural impregnation by microscopic assessment. Compared with HP-RTM parts, the WCM specimens exhibited 12% lower energy absorption.

11.2 Contributions

The first task improved understanding of the effect of the stabilizing binder state and of UD-NCF infiltration on the textile response, filling a critical gap in the literature. This understanding is important for future studies focused on engineering textile characterization and UD-NCF forming simulations.

The second task offered a detailed understanding of how the stabilizing binder and its condition affect the material, as well as how applying a vacuum impacts the microstructure and mechanical performance of WCM UD-NCF composites. It demonstrated the effectiveness of digital image processing in analyzing the laminate's microstructure and estimating the fiber volume fraction of $[0]_n$ laminates. Furthermore, this task clarified the reasons for early interlaminar and transverse tensile failure in some WCM configurations. This study addresses a critical gap in the literature on WCM and UD-NCF composites, and the results will serve as an important database for the design and manufacturing of composite parts using the WCM process.

The final task demonstrated the capability to manufacture complex-shaped, thick parts using the WCM process and the capacity of those to absorb energy during impact. Furthermore, the impact tests with WCM parts yielded results comparable to those of parts produced with well-established manufacturing processes, such as HP-RTM. As a result, the dataset generated provides a foundation for future research in impact and energy absorption, which can be used in the automotive industry.

11.3 Recommendations for Future Work

11.3.1 Future material characterization work

This study characterized the viscous draping mechanisms—including membrane, bending, and compaction behaviors—under varying loading rates, binder activation conditions, and oil viscosities. To gain a more comprehensive understanding of fabric behavior, future work should address mechanisms not covered in this study, such as the rate-dependent bending response of the UD-NCFs, which is relevant for developing rate-dependent forming models, and inter-ply mechanisms of infiltrated binder-stabilized UD-NCFs (tool-ply and ply-ply friction), which can affect the preform with defects, including fiber breakage. Additionally, the interactions among the draping behaviors should be assessed (i.e., compaction/bending, compaction/membrane, and bending/membrane), as these mechanisms occur simultaneously and may influence one another. Finally, it is recommended to extend the investigation of NCFs by considering various stitching patterns, fiber tow counts, stabilizing binder types, and their concentrations, as these factors influence the draping mechanisms.

11.3.2 Future process studies work

In this investigation, a comprehensive understanding of the process studies was achieved, considering the presence of a stabilizing binder, its activation, and the use of the vacuum-assisted technique across different time ranges. For future work, the study should also explore how to control the WCM part thickness with the vacuum-assisted technique, as it directly affects the FVF of the final part and its mechanical performance, as well as the impact of this technique on composite parts with lower FVF. Finally, it is recommended to extend the investigation of how NCF parameters, such as stitching patterns and stabilizing binder concentrations, influence mechanical performance, since they can affect the microstructure of the final part.

11.3.3 Future crush test work

This study conducted a crush test characterization considering different manufacturing parameters, such as the presence of stabilizing binders and vacuum assistance techniques, and their effects on energy absorption during impact. However, it only examined the quasi-static test in the axial direction. In real-world scenarios, impacts occur at much higher

speeds and are not always aligned axially. To better understand how automotive parts respond during a car crash, it is recommended to perform dynamic tests and consider off-axis directions. The data generated can be used to validate physically-based models used to simulate impact tests. Finally, it is recommended to extend the investigation of how different stabilizing binder types and their concentrations influence the energy absorption capacity.

Letters of Copyright Permission

In accordance with the author rights policy of Government of Canada, Elsevier, Sage, Springer, CSIR, and Cambridge University Press, individuals retain the right to include their article in a thesis/dissertation without the need for prior formal request. In the preparation of Chapters 4 to 9, the following journals have been referred to as the original source, either in their entirety or in parts.

R. M. Portela, B. Schäfer, L. Kärger, A. R. de Faria, and J. Montesano, "Influence of viscosity, binder activation, and loading rate on the membrane response of an infiltrated UD-NCF," ESAFORM Conference, Toulouse, France, April 24-26, 2024. In: Materials Research Proceedings 2024;41:494-502.

R. M. Portela, B. Schäfer, L. Kärger, A. R. de Faria, and J. Montesano, "Effect of loading rate, viscosity, and binder activation on the bending response of an infiltrated UD-NCF," Composites Part A: Applied Science and Manufacturing, vol. 200, p. 109347, 2026, doi: 10.1016/j.compositesa.2025.109347

R. M. Portela, B. Schäfer, L. Kärger, A. R. de Faria, and J. Montesano, "Characterizing and modelling the time-dependent compaction response of an infiltrated binder-stabilized unidirectional non-crimp fabric," (Submitted to a journal - Under review).

R. M. Portela, A. R. de Faria, and J. Montesano, "High-fidelity fiber volume fraction estimation for UD-NCF composites using digital image processing technique," (Submitted to a journal - Under review).

R. M. Portela, A. Soltansaleki, G. W. Melenka, A. R. de Faria, and J. Montesano, "Effect of stabilizing binder on void morphology and mechanical performance of wet compression molded rapid-curing non-crimp fabric composites," (Submitted to a journal - Under review).

Copyright permission has been duly granted for the following materials along with their respective right holders. The agreements have been established between the University of

Waterloo (represented by Renan Miranda Portela) and the respective right holders, each assigned with unique license numbers or by written approvals:

Table 11.1: Permissions, rights holders, and references for all figures used in the thesis.

Figure number	Rights holder	Reference	License / Permission
1.1	Government of Canada	"Greenhouse gas emissions: 2021 annual report." Accessed 2025-11-07, Transport Canada (2021). Available online.	Not needed
1.2	Christian Poppe	C. Poppe, "Process simulation of wet compression moulding for continuous fibre-reinforced polymers," PhD dissertation, KIT, 2021.	By email
2.1	Elsevier	C. D. Rudd, A. C. Long, K. N. Kendall, and C. G. E. Mangin, Liquid Moulding Technologies. Elsevier, 1997. doi:10.1533/9781845695446.	6151400665271
2.2	Elsevier	S. V. Lomov, Ed., Non-crimp fabric composites. Woodhead Publishing, 2011. isbn: 9781845696566.	6151400473524
2.3	Elsevier	S. V. Lomov, Ed., Non-crimp fabric composites. Woodhead Publishing, 2011. isbn: 9781845696566.	6151400473524
2.4	Elsevier	N. Razali et al., "Chapter 15 - out-of-autoclave as a sustainable composites manufacturing process for aerospace applications" in Design for Sustainability, Elsevier, 2021, pp. 395–413. doi:10.1016/B978-0-12-819482-9.00011-3.	6147590579673
2.5	Elsevier	F. Henning et al., "Fast processing and continuous simulation of automotive structural composite components " Composites Science and Technology, 2019. doi:10.1016/J.COMPSCITECH.2018.12.007.	6147590883435

Figure number	Rights holder	Reference	License / Permission
2.6	Christian Poppe	C. Poppe, "Process simulation of wet compression moulding for continuous fibre-reinforced polymers," PhD dissertation, KIT, 2021.	By email
2.7	Christian Poppe	C. Poppe, "Process simulation of wet compression moulding for continuous fibre-reinforced polymers," PhD dissertation, KIT, 2021.	By email
2.8a, 2.8b	Elsevier	F. J. Schirmaier et al., "Characterisation of the draping behaviour of unidirectional non-crimp fabrics (UD-NCF)," Composites Part A: Applied Science and Manufacturing, vol. 80, pp. 28–38, Jan. 2016, issn: 1359-835X. doi: 10.1016/J.COMPOSITESA.2015.10.004.	6147590982720
2.8c, 2.8d	Elsevier	E. A. Trejo et al., "Assessing strain fields in unbalanced unidirectional non-crimp fabrics," Composites Part A: Applied Science and Manufacturing, vol. 130, Mar. 2020, issn: 1359835X. doi: 10.1016/J.COMPOSITESA.2019.105758.	6147591063393
2.9	Elsevier	C. Krogh et al., "Pure and simple: Investigating the inplane shear kinematics of a quasi-unidirectional glass fiber non-crimp fabric using the bias-extension test," International Journal of Material Forming, vol. 14, pp. 1483–1495, 2021.	6147600201124
2.10	Christian Poppe	C. Poppe, "Process simulation of wet compression moulding for continuous fibre-reinforced polymers," PhD dissertation, KIT, 2021.	By email

Figure number	Rights holder	Reference	License / Permission
2.11	Elsevier	P. Boisse et al., "Simulation of wrinkling during textile composite reinforcement forming . Influence of tensile , in-plane shear and bending stiffnesses," Composites Science and Technology, vol. 71, no. 5, pp. 683–692, 2011, issn: 0266-3538. doi: 10.1016/j.compscitech.2011.01.011. [Online]. Available: http://dx.doi.org/10.1016/j.compscitech.2011.01.011.	6147591352148
2.12	Elsevier	B. Liang et al., "Analysis of thermoplastic prepreg bending stiffness during manufacturing and of its influence on wrinkling simulations" Composites Part A, 2014.	6147591413624
2.13	Elsevier	M. Ghazimoradi et al., "Characterizing the macroscopic response and local deformation mechanisms of a unidirectional noncrimp fabric," Composites Part A: Applied Science and Manufacturing, vol. 156, p. 106 857, May 2022, issn: 1359-835X. doi: 10 . 1016 / J . COMPOSITESA . 2022 . 106857.	6147591474972
2.14	Elsevier	C. Poppe et al., "Comparative experimental and numerical analysis of bending behaviour of dry and low viscous infiltrated woven fabrics," Composites Part A: Applied Science and Manufacturing, vol. 124, p. 105 466, Sep. 2019, issn: 1359-835X. doi: 10.1016/J.COMPOSITESA.2019.05. 034.	6151411316979
2.15	Christian Poppe	C. Poppe, "Process simulation of wet compression moulding for continuous fibre-reinforced polymers," PhD dissertation, KIT, 2021.	By email

Figure number	Rights holder	Reference	License / Permission
2.18	Andrew Hrymak	J. Fels et al., "Mechanical property difference between composites produced using VALCM and HP-IRTM," Proceedings ACCE2017, Michigan, 2017.	By email
2.19	Elsevier	C. Yang et al., "Quasi-static and low-velocity axial crushing of polyurethane foam-filled aluminium/CFRP composite tubes: An experimental study," Composite Structures, vol. 299, Nov. 2022, issn: 02638223. doi: 10.1016/j.compstruct.2022.116083.	6147600027869

Bibliography

[1] C. Poppe, "Process simulation of wet compression moulding for continuous fibre-reinforced polymers," Ph.D. dissertation, Karlsruhe Institute of Technology, 2021.

[2] L. Li, Y. Zhao, J. Yang, J. Zhang, and Y. Duan, "An experimental investigation of compaction behavior of carbon non-crimp fabrics for liquid composite molding," *Journal of Materials Science*, vol. 50, pp. 2960–2972, 7 Apr. 2015, ISSN: 15734803. DOI: 10.1007/s10853-015-8860-0.

[3] B. Schäfer, S. Haas, P. Boisse, and L. Kärger, "Investigation of the membrane behavior of ud-ncf in macroscopic forming simulations," *Key Engineering Materials*, vol. 926, pp. 1413–1422, 2022.

[4] B. Schäfer, R. Zheng, N. Naouar, and L. Kärger, "Membrane behavior of uni-and bidirectional non-crimp fabrics in off-axis-tension tests," *International Journal of Material Forming*, vol. 16, no. 6, p. 68, 2023.

[5] F. J. Schirmaier, K. A. Weidenmann, L. Kärger, and F. Henning, "Characterisation of the draping behaviour of unidirectional non-crimp fabrics (UD-NCF)," *Composites Part A: Applied Science and Manufacturing*, vol. 80, pp. 28–38, Jan. 2016, ISSN: 1359-835X. DOI: 10.1016/J.COMPOSITESA.2015.10.004.

[6] C. Krogh, P. H. Broberg, J. Kepler, and J. Jakobsen, "Comprehending the bending: A comparison of different test setups for measuring the out-of-plane flexural rigidity of a ud fabric," *Key Engineering Materials*, vol. 926, pp. 1257–1267, Jul. 2022, ISSN: 1662-9795. DOI: 10.4028/p-r883x4. [Online]. Available: https://www.scientific.net/KEM.926.1257.

Appendix 1

Table 2: P-values obtained through the T-Test comparing the maximum compression stress values of inactivated and pre-activated binder-stabilized specimens under different impregnation conditions, for each stacking sequence in both first and second compaction phases (Phases I and VI).

Stacking Sequence	Dry IT x Dry AT	Dry IT x 20 cSt AT	Dry IT x 100 cSt AT	Dry AT x 20 cSt AT	Dry AT x 100 cSt AT	20 cSt AT x 100 cSt AT
$[0]_8$ (1st)	0.1858	0.9637	0.3012	0.1911	0.7885	0.2111
$[0/45]_4$ (1st)	0.1528	0.9221	0.4093	0.1517	0.0791	0.3727
$[0]_8$ (2nd)	0.1710	0.8810	0.3500	0.1616	0.6517	0.2252
$[0/45]_4$ (2nd)	0.1203	0.9280	0.3865	0.1214	0.0612	0.3537

Table 3: P-values obtained through T-Test comparing the maximum compression stress values for the first and second compaction phases (Phases I and VI), for each specimen condition.

Configuration	$[0]_8$	$[0/45]_4$
Dry IT	0.1225	0.0617
Dry AT	0.2435	0.1557
20 cSt AT	0.1386	0.0184
100 cSt AT	0.1211	0.1489

Table 4: : P-values obtained through the T-Test comparing the normalized relaxation stress values of inactivated and pre-activated binder-stabilized specimens under different impregnation conditions, for each stacking sequence in both first and second relaxation (Phases II and VI).

Stacking Sequence	Dry IT x Dry AT	Dry IT x 20 cSt AT	Dry IT x 100 cSt AT	Dry AT x 20 cSt AT	Dry AT x 100 cSt AT	20 cSt AT x 100 cSt AT
$[0]_8$ (1st)	5.85×10^{-3}	1.40×10^{-2}	4.82×10^{-4}	2.18×10^{-3}	8.30×10^{-7}	3.99×10^{-6}
$[0/45]_4$ (1st)	1.06×10^{-6}	5.84×10^{-5}	4.99×10^{-4}	4.53×10^{-3}	7.58×10^{-7}	1.90×10^{-5}
$[0]_8$ (2nd)	5.64×10^{-3}	8.63×10^{-1}	5.50×10^{-7}	5.20×10^{-3}	9.86×10^{-7}	1.60×10^{-5}
$[0/45]_4$ (2nd)	5.56×10^{-5}	2.88×10^{-3}	2.89×10^{-4}	2.21×10^{-3}	2.21×10^{-5}	1.32×10^{-4}

Table 5: : P-values obtained through T-Test comparing the stress relaxation ratio values for the first and second relaxation cycles (Phases II and VI), for each specimen condition.

Configuration	$[0]_8$	$[0/45]_4$
Dry IT	5.29×10^{-3}	4.94×10^{-7}
Dry AT	5.91×10^{-3}	2.89×10^{-5}
20 cSt AT	5.84×10^{-4}	3.78×10^{-4}
100 cSt AT	1.03×10^{-7}	1.08×10^{-4}

Table 6: P-values obtained through the T-Test comparing the elastic recovery values of inactivated and pre-activated binder-stabilized specimens under different impregnation conditions, for each stacking sequence, during Phase IV.

Stacking Sequence	Dry IT x Dry AT	Dry IT x 20 cSt AT	Dry IT x 100 cSt AT	Dry AT x 20 cSt AT	Dry AT x 100 cSt AT	20 cSt AT x 100 cSt AT
$[0]_8$	6.49×10^{-3}	1.92×10^{-1}	1.30×10^{-3}	1.22×10^{-1}	7.00×10^{-2}	4.44×10^{-3}
$[0/45]_4$	2.50×10^{-2}	8.56×10^{-4}	1.44×10^{-3}	1.04×10^{-1}	2.68×10^{-2}	1.16×10^{-1}

Table 7: P-values obtained through T-Test comparing the maximum compression stress values of the specimens with different stacking sequences in both first and second compaction cycles (Phases I and V), for each condition.

Configuration	$[0]_8 \times [0/45]_4$ (1st cycle)	$[0]_8 \times [0/45]_4$ (2nd cycle)
Dry IT	0.2280	0.2549
Dry AT	0.3782	0.4004
20 cSt AT	0.1573	0.1678
100 cSt AT	0.4238	0.4225

Table 8: P-values obtained through T-Test comparing the stress relaxation ratio values of two specimens with different stacking sequences in both first and second compaction cycles (Phases I and V), for each condition.

Configuration	$[0]_8 \times [0/45]_4$ (1st cycle)	$[0]_8 \times [0/45]_4$ (2nd cycle)
Dry IT	2.34×10^{-1}	3.80×10^{-1}
Dry AT	9.52×10^{-2}	4.03×10^{-2}
20 cSt AT	1.28×10^{-1}	6.09×10^{-2}
100 cSt AT	1.82×10^{-4}	3.18×10^{-3}

Table 9: P-values obtained through the T-Test comparing the elastic recovery rate values for specimens with different stacking sequences, for each condition, during Phase IV.

Configuration	$[0]_8 \times [0/45]_4$
Dry IT	1.47×10^{-3}
Dry AT	1.05×10^{-1}
20 cSt AT	6.97×10^{-2}
100 cSt AT	6.87×10^{-1}

Appendix 2

Table 10: Material parameter values for the fractional Zener model for each condition (Phase II).

Conditions	E_0 ($\times 10^5$) [Pa]	E_1 ($\times 10^{11}$) [Pa]	α	p ($\times 10^5$) [Pa.s^α]	f(x) (R^2)
1	2.172	2.247	0.402	1.671	0.0215 (0.9798)
2	2.565	7.033	0.389	1.605	0.0231 (0.9894)
3	2.286	5.878	0.431	1.545	0.0207 (0.9143)
4	2.084	7.751	0.508	1.722	0.0239 (0.9863)
5	1.973	6.391	0.417	1.495	0.0180 (0.9608)
6	2.368	9.473	0.396	1.486	0.0226 (0.9849)
7	2.023	6.096	0.444	1.461	0.0203 (0.9274)
8	2.321	5.321	0.486	1.898	0.0280 (0.9769)

Table 11: Material parameter values for the Maxwell model for each condition (Phase II).

Cond.	E_0 ($\times 10^5$) [Pa]	E_1 ($\times 10^4$) [Pa]	τ_1 [Pa.s]	E_2 ($\times 10^4$) [Pa]	τ_2 [Pa.s]	E_3 ($\times 10^3$) [Pa]	τ_3 [Pa.s]	f(x) (R^2)
1	2.266	2.047	67.72	4.781	4.71	9.071	99.64	0.0296 (0.9744)
2	2.266	4.423	32.72	2.570	52.82	9.354	83.33	0.0174 (0.9363)
3	2.306	0.105	70.23	4.188	3.35	31.259	86.94	0.0244 (0.9655)
4	2.058	2.379	99.81	5.148	3.88	4.600	79.01	0.0247 (0.9429)
5	1.999	0.359	97.32	4.200	2.79	28.913	92.61	0.0320 (0.9875)
6	2.403	3.210	81.89	0.040	70.01	40.976	4.12	0.0284 (0.9729)
7	2.045	0.040	98.61	4.399	3.67	28.437	86.96	0.0387 (0.9444)
8	2.163	0.437	95.38	5.029	3.14	33.36	99.15	0.0316 (0.9749)

Table 12: Material parameter values for the fractional Zener model for each condition (Phase VI).

Conditions	E_0 ($\times 10^5$) [Pa]	E_1 ($\times 10^{11}$) [Pa]	α	p ($\times 10^5$) [Pa.s^α]	f(x) (R^2)
1	3.721	4.086	0.349	2.194	0.0096 (0.8076)
2	3.989	8.276	0.318	1.816	0.0104 (0.9736)
3	3.538	6.795	0.395	2.008	0.0095 (0.8906)
4	3.715	4.933	0.317	1.566	0.0095 (0.8107)
5	3.500	5.366	0.395	2.161	0.0113 (0.8925)
6	3.724	2.686	0.383	1.900	0.0126 (0.8385)
7	3.115	6.962	0.256	1.243	0.0071 (0.8341)
8	3.932	9.871	0.296	1.741	0.0130 (0.8571)

Table 13: Material parameter values for the Maxwell model for each condition (Phase VI).

Cond.	E_0 ($\times 10^5$) [Pa]	E_1 ($\times 10^4$) [Pa]	τ_1 [Pa.s]	E_2 ($\times 10^4$) [Pa]	τ_2 [Pa.s]	E_3 ($\times 10^3$) [Pa]	τ_3 [Pa.s]	f(x) (R^2)
1	3.949	1.607	69.43	2.040	62.26	46.277	6.41	0.0094 (0.9662)
2	4.247	2.477	42.04	1.387	62.33	30.884	4.54	0.0083 (0.8786)
3	3.705	4.995	9.86	0.074	99.18	19.554	68.53	0.0245 (0.7607)
4	3.940	0.564	82.58	3.042	37.81	23.091	1.18	0.0098 (0.5426)
5	3.636	1.325	63.12	3.997	5.58	25.579	76.95	0.0154 (0.8880)
6	3.901	3.183	47.05	0.676	35.05	30.005	1.33	0.0110 (0.7316)
7	3.362	1.155	64.13	1.394	69.47	25.365	5.90	0.0084 (0.9397)
8	4.198	0.009	71.76	3.828	57.19	29.75	1.76	0.0100 (0.8043)

Table 14: Material parameter values for the nonlinear Maxwell model for each condition (Phase I).

Cond.	A	B	a_1	b_1	τ_1	a_2	b_2	τ_2	a_3	b_3	τ_3	R^2
1	394.07	0.22	205.55	57.74	714.79	551.56	73.45	884.58	956.24	87.26	991.15	0.7826
2	234.82	24.56	10.01	78.06	774.41	52.81	4.83	505.24	832.72	76.11	897.55	0.5775
3	456.61	22.51	36.27	2.69	854.27	53.58	12.71	717.58	494.55	7.72	820.84	0.9105
4	474.06	21.33	13.80	1.71	317.88	295.11	35.29	391.69	588.32	25.30	257.40	0.84184
5	255.67	23.09	43.76	63.21	666.38	70.92	0	737.68	938.10	42.52	357.21	0.9803
6	275.71	25.31	4.18	39.63	523.24	146.30	47.57	907.66	233.36	0.67	997.32	0.7341
7	379.37	22.51	238.61	0	508.07	236.88	1.36	408.77	788.20	36.39	495.48	0.8757
8	470.43	22.53	4.20	5.17	358.60	393.38	0.61	230.53	995.24	0	386.00	0.9340